

Advanced Friction Modeling and Simulation of Temperature Dependent Friction in Metal Forming Processes



Master Research Project
Industrial Engineering and Management

Written by: Robbert Nienhuis
IEM-PTL-APE s2039060

First Supervisor: prof. dr. Antonis Vakis
Second Supervisor: prof. dr. ir. Jan Post
External Supervisor: Mark Veldhuis, MSc



**university of
 groningen**



Interreg 
North-West Europe
ASPECT
European Regional Development Fund

Preface

The subject of this research project was offered to me by prof dr. A. Vakis at the request of the Engineering and Technology Institute of Groningen and in collaboration with the Metal forming department of Philips Drachten.

The project proposal with the subject of “Advanced friction modeling and simulation of temperature dependent friction in sheet metal forming processes”, fitted in my interest area concerning the research and development process by finite element method simulations. Nevertheless, this project introduced more knowledge, expectations and challenges than expected beforehand.

The multi-aspect nature of this research project forced the development of both my general knowledge as my level of specific knowledge to certain aspects. Consequently, this research project was most certainly a good experience to take with me to future scientific endeavors.

In my collaboration with Philips, I would like to thank the whole metal forming department for their helpfulness and their unprecedented amount of specialized knowledge. The metal forming team introduced me deeper into the business side of research and a mindset that differs from the educational side of research.

In particular, I want to thank my external supervisor ir. Mark Veldhuis for guiding me towards a complete deliverable. During this integration project, Mark acted as a strict but fair mentor helping me reach a new level of knowledge and gain new insights in both the project and myself. His thoroughness and structured manner of working in this science-business context can be seen as a personal goal for me to work towards.

I would like to thank my supervisor, prof dr. Antonis Vakis for guiding and supporting me during this research project. The useful remarks and calm guidance throughout the process helped in further developing the inner scientific mentality and allows for positive development.

Also I would like to thank my second supervisor, prof. dr. ir. Jan Post for guiding me towards a proper deliverable and for the entertaining conversations at the office.

This research project provided an experience that expanded my knowledge and gave me new insights in the multi aspect nature of friction in metal forming processes and also in myself.

I am very content with my final draft and I hope you find this report enjoyable and informative!

Robbert Nienhuis

Groningen, 21 September 2018

Summary

In conventional metal forming processes, normal loading and sliding motions occur which generate frictional forces that can significantly affect the quality of the process and the product. The frictional behavior at the tool-workpiece interface shows to be especially prone to temperature variations. During the warm-up period, variations in temperature are occurring more frequently compared to the steady state period, making this an especially hard process to predict and control.

Traditional FEM studies in companies, generally apply a standard friction model such as Coulomb's friction law in their simulations. The simple friction models are easy to use and enable fast calculations, however, these models lack the complexity to fully encompass the total frictional behavior that is present. This especially holds during the warm-up period.

This research project aims to implement and validate a simulation model that correctly captures the impact of a temperature dependent friction coefficient in a metal forming process. Accurately forecasting the frictional behavior enables to compensate for the rising temperatures during start-up via a control system.

An adaptation on the model of J. Hol is provided, using the modified Bergström van Liempt model that describes friction as a function of the local nominal pressure, strain, sliding velocity and temperature. The advanced friction model aims at an optimum between output accuracy and computation time and is implemented to study the temperature-induced frictional behavior in a two-step deep draw process.

In order to determine the impact of temperature on the deep draw process, subsequent numerical studies were performed to determine the flange and hole diameter development for temperature increments of 293K at room temperature up to 373K, where the process is assumed to develop into a steady state.

The results of the sensitivity analysis confirm the dominance of temperature on the frictional behavior over the influence of material properties, which is concluded to be minimal for the current deep draw set-up. The total temperature dependency of friction alone takes up ~80% of the total variation and the other ~20% accounts for the strain hardening in the development of the flange and hole diameter.

The results of the Bergström van Liempt model with full frictional table show that an increase in temperature will result in an increase of friction and a decrease in temperature will result in a decrease of friction. Consequently, a higher amount of friction during the deep draw process results a relative decrease of the final hole diameter and a relative increase in the final flange diameter.

The results of the alternative Erichsen stretching validation show that a good fit is determined for the 323K temperature increment between the deformation of the workpiece in the FEM simulation and the real life workpiece. This concurs with the expectation that the best fit is reached for the temperature value closest to the steady state period, from which the real life workpiece sample was taken.

In conclusion, the simulations of the modified Bergström van Liempt model show promising results in the prediction the frictional behavior during the warm-up period of a deep draw process. The roughness and lubrication variations together with alternative validation add to the applicability of the FEM model in other metal forming processes. However, a full validation is still required to completely validate the model and enable the development of control parameters that can minimize the product variations in the warm-up period.

Table of Contents

<i>Preface</i>	1
<i>Summary</i>	2
<i>Table of Contents</i>	3
<i>Introduction</i>	5
<i>Problem Context</i>	7
<i>Stakeholder Analysis</i>	10
<i>Resources and Data Acquisition</i>	12
<i>Research Goals</i>	13
Scope.....	13
<i>Methodology</i>	14
<i>Research Questions</i>	16
<i>Theoretical Framework</i>	17
Macroscopic	17
Microscopic	17
FEM Solver	17
Metal Forming Processes	18
Deep Drawing Process.....	19
Possible Failures	20
Control Parameters	22
Macroscopic Models of Friction	27
Demonstrator Line	33
Tribological Framework.....	36
Coupling Macroscale and Microscale Material Behavior.....	38
Microscopic Models of Friction	40
I - Surface Properties	48
II - Material Properties	51
III - Boundary Lubrication Friction Modeling	55
IV - Process Parameters.....	57
Modelling Evolution of Friction	67

<i>FEM Analysis</i>	71
Micro-scale Four Dimensional Look-up Table	71
Subroutine.....	73
Simulation	76
<i>FEM Results</i>	79
Study 1 - Frictional Models MSC Marc	81
Study 2 - Temperature Induced Frictional Model.....	86
Study 3 - Bergström van Liempt Model	89
Study 4 - Friction Model Variations - Roughness, Lubrication	94
<i>Validation</i>	97
<i>Conclusion</i>	98
<i>Discussion</i>	101
<i>Appendix</i>	102
Appendix 1 – Tooling Two-Step Deep Draw Process	102
Appendix 2 – Adhesion Formula’s	104
Appendix 3 – Deformation Formula’s.....	105
Appendix 4 – Material Behavior AISI 420	108
Appendix 5 – Boundary Shear Tests	110
Appendix 6 – Temperature Dependent Dynamic Viscosity Tests	113
Appendix 7 – Four Dimensional Look-up Table	114
Appendix 8 – FEM Analysis - Dimensional Parameters.....	115
Appendix 9 – FEM Analysis – Matlab Routine	117
Appendix 10 – MSC Marc Standard Frictional models.....	118
Appendix 11 – FEM Study 1 – Frictional Models	119
Appendix 12 – FEM Study 2 – Sensitivity Analysis	132
Appendix 13 – FEM Study 3 – Bergström van Liempt Model	134
Appendix 14 – FEM Study 4 – Bergström Variations	152
Appendix 15 – Pressto Case – Alternative Point Validation.....	172
<i>References</i>	173

Introduction

New product development teams are constantly looking for new innovative manufacturing technologies that offers improved product performances at lower costs and better serves customer demands. At Philips, the Research and Development department aims to realize a better shaving experience by focusing on new and improved manufacturing technologies for high-precision metal key-components.

Mass-manufacturing tens of millions of high-precision parts for global consumption within strict specifications is extremely challenging. Variations within the production process can lead to large rejection rates and a lower yield. This is deemed highly undesirable since it leads to unnecessary amounts of wasted materials, energy and costs.

In order to be able to predict and control possible manufacturing variations more accurately and reduce the amount of rejected parts, Philips participates in the Advanced Simulation and Control of Tribology - ASPECT project.

The ASPECT project is funded by the Interreg North-West Europe program and consist of 13 companies and research organizations that focus on the innovation and the development of accurate and computationally efficient simulation models that are able to predict the tribological effects in metal forming processes [1].

In particular, the friction variation with temperature during the start-up of the production line, that is estimated to be responsible for a yield loss of 25-40% [2]. A three-phase structure can be identified within the project, which is shown in Figure 1.

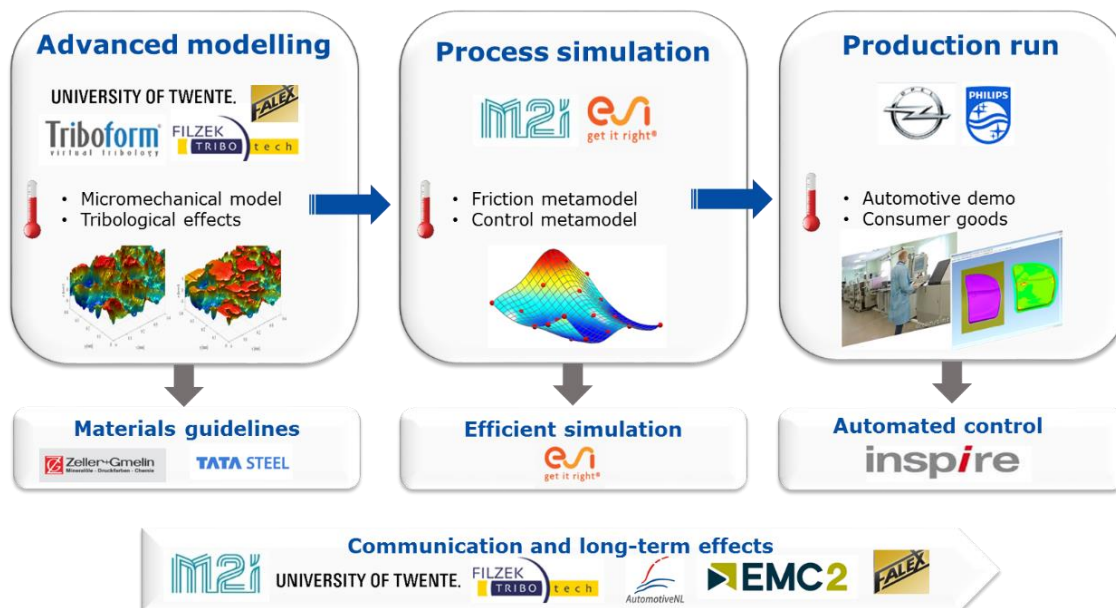


Figure 1 - An overview of the phases within the Aspect project [3]

This research project is conducted within the Production run phase where the main focus will lie on generating new knowledge and insights concerning the control of temperature induced friction variations during the warm-up period of a two-step deep draw process.

Warming-up effects have a considerable effect on the metal-forming process; especially friction is identified as being the dominant effect that influences the output quality of the product. During the warm-up period, variations in temperature are more frequent compared to the steady state period. In order to accurately predict and minimize the effect of the warm-up period within a deep draw process, an accurate model of the relation between the temperature and friction is required [1] [3].

To establish a basic framework of the temperature induces friction, a thorough understanding of the material behavior and production techniques is required. Modelling and simulating the complex behavior between tool and workpiece can help to contribute to a better understanding of the temperature-friction impact in metal forming processes.

This research project will provide a comprehensive tribological overview that incorporates a multi-aspect approach, translating frictional mechanisms on a micro scale into the tool-workpiece behavior on a macro scale. A tribological system is introduced that illustrates the multi-aspect nature of the mechanisms that underlie the tool-workpiece behavior on a micro-scale that influences friction. Resulting in a look-up table, which couples friction coefficients to the parameters of nominal contact pressure, strain, temperature and relative velocity. Enabling the coupling of microscopic based friction effects to macroscopic behavior, resulting in geometrical changes of the processed workpiece.

Problem Context

Metal forming is regarded as one of the most important manufacturing processes that is widely adopted within production industries. The metal forming techniques are applied in mass manufacturing set-ups for a large variety of products, however, tribological phenomena that occur during contact between the tool and workpiece are still insufficiently considered.

In conventional sheet forming processes, normal loading and sliding motions occur which generate frictional forces that can significantly affect the quality of the process and the product. The frictional behavior during tool-workpiece contact, being prone to temperature variations during start-up, is especially hard to predict and control [3].

Coulomb's friction law [4], traditionally applied in companies for modeling frictional effects within a metal forming process. The friction model assumes a constant friction coefficient, which is dependent on the relation between the normal force and the contact forces between tool and workpiece. The simple nature of the model makes it easy to use and enables fast calculations, however, it lacks the complexity to fully encompass the frictional behavior found in the real case.

The ASPECT project aims to construct, implement and validate a simulation model that captures the impact of a temperature dependent friction coefficient on the complete metal forming process. Accurately forecasting the frictional behavior enables to compensate for the rising temperatures during start-up via a control system [1] [3].

This research project is performed during the production run phase of the ASPECT project and will focus on the tribological phenomena regarding the temperature dependent friction model in a two-step deep drawing process. The main elements of importance that can be for this study are given in [Figure 2](#).

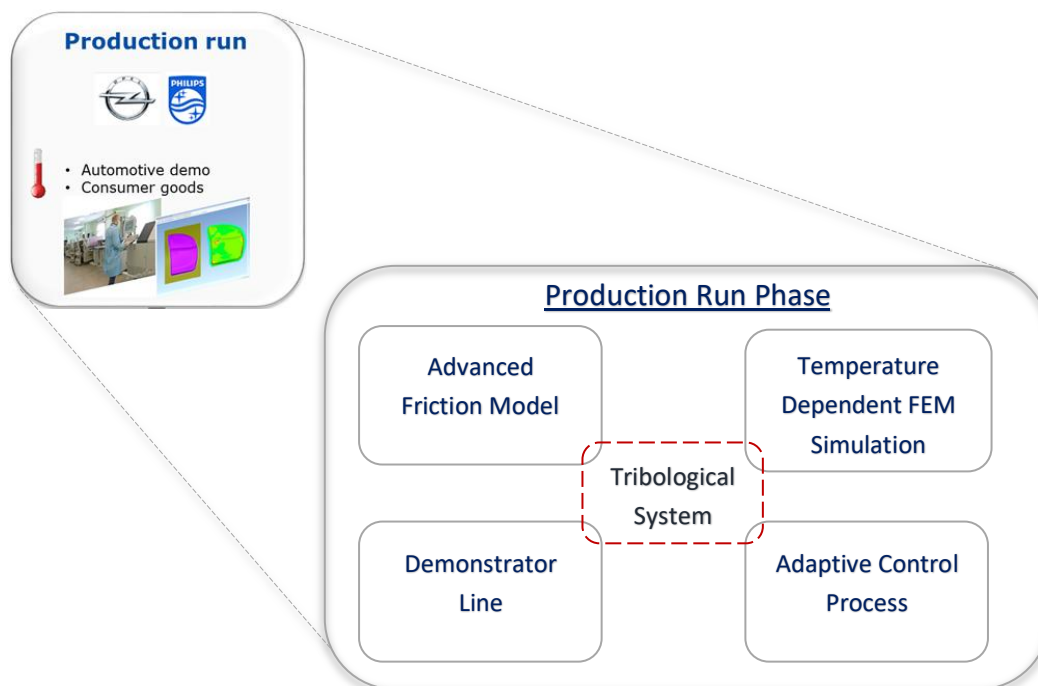


Figure 2 - The main elements identified within the Production run phase of the Aspect Project [5]

In order to study the impact of temperature variations on the advanced friction model, FEM simulations are performed. The results of the FEM simulations can be validated by running a deep draw demonstrator line. Any offset between the outcomes of the model and the demonstrator line can be adjusted accordingly. Finally, the results of the advanced friction model, FEM simulations and production line result in the building blocks for an adaptive control system. Counteracting the negative effects of temperature variations during the warm-up period [1] [3].

The connecting element of the ASPECT project is the tribological system that is valid for a specific combination of tooling, blank material, lubricant and type of metal forming process. Experimental and theoretical studies are performed to identify the friction coefficients at the tool-workpiece contact that vary during the metal forming process. In the ASPECT project, the advanced friction model of J. Hol [6] is combined with the adapted Bergström von Liempt [7] [8] [9] model to translate the micro-mechanisms of friction into a calibrated meta-model, in the form of a look-up table as a function of local pressure, strain, sliding velocity and temperature. The determined frictional values in turn are either directly implemented in FEM studies or indirectly as input for generating Stribeck [10] [11] curves, providing a soft coupling between the frictional mechanisms on the micro scale and macro-mechanical behavior of friction in a two-step deep draw process [6].

Translating the specific frictional results into a general context will decrease the veraciousness of the simulation outcomes, only partly grasping the actual mechanisms that are present. FEM studies that focus on determining the micro-mechanical aspects that influence the friction coefficient, are considered more accurate. However, the increase in accuracy also drastically increase the computation time, which is regarded as unwanted and too cumbersome in large-scale simulations. The model of J. Hol [6] provides a middle way by approximating the real area of contact, using stochastic methods, to describe the surface height distribution on a micro scale and assuming that the microscopic surface height distribution represents the surface texture on a macro scale [12].

The tribological parameters within a tool-workpiece contact situation that influence the forming behavior of the workpiece depend on a complex combination of tribological factors such as material properties, surface parameters, lubricant properties and process conditions [3] [6]. In order to study the multi-dimensional influence of the underlying mechanisms accordingly, a tribological system of friction is introduced in [Figure 3](#).

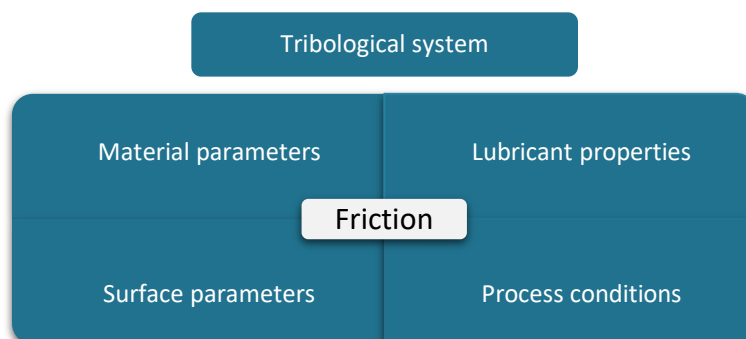


Figure 3 - A tribological system for friction in sheet metal forming

To establish a basic framework of substantiated knowledge, a thorough understanding of the work hardening behavior in the workpiece material and the hardness of the tooling is required. Understanding the complex behavior between tool-lubricant-workpiece contact points can help to contribute to better controlling the temperature-friction impact in metal forming processes.

The type of lubricant, its viscosity and the layer thickness will all influence the friction at contact patches. Different surface topologies will also show a different outcome regarding to friction and resistance to deformation. Overall conditions also need to be distinguished in order to be able to compare the FEM results with the demonstrator product.

Stakeholder Analysis

The ASPECT project consisting of companies and research organizations in the North-West of Europe, focusses collectively on the innovation and development of accurate and computationally efficient simulation models in metal forming processes. Within the project, direct and indirect partnerships between the collaborating entities are established for each of the three phases [1] [3] [5].

The direct stakeholders are identified from the direct collaborations within the production run phase, and can be coupled to the element overview, which is illustrated in Figure 4. The main stakeholders that are connected to this research project can be identified as [3] [5]

- The University of Groningen,
- Philips
- TriboForm Engineering
- M2i
- Inspire AG

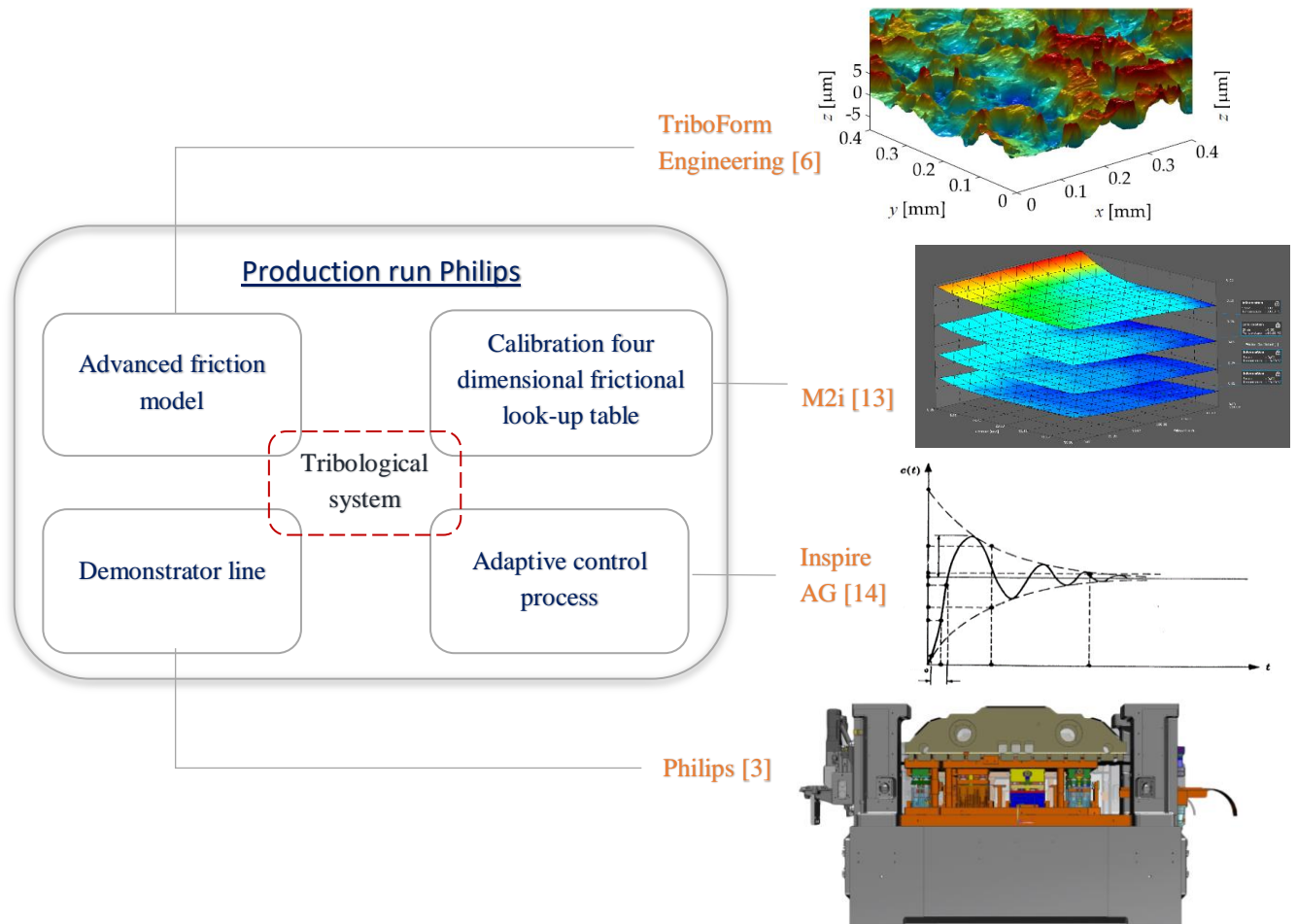


Figure 4 - Stakeholders coupled to the research context in the production run phase

University of Groningen

The Advanced Production Engineering group under supervision of Prof Dr. Antonis Vakis mainly focusses on generating new knowledge and improving the current state of the Tribological field. Different approaches are undertaken to couple the micro-mechanical mechanisms of friction into macro-mechanical behavior, with this research project being part of it [2].

Triboform

Within the ASPECT project, the main task of Triboform is to provide the advanced friction meta-model which is mainly based on the work of Johan Hol [6]. The advanced friction model has been created with the help of the University of Twente, Falex and M2i and it provides a finite element method tool that can implement, combine and simulate a large number relevant tribological parameters. The simulation software reduces the time and costs that ‘normally’ would be needed to provide friction coefficients with a similar level of accuracy in industrial simulations. Therefore, Triboform is interested with the outcome of the ASPECT project, concerning the data fit between the theoretical model and the real-life demonstrator results [5].

M2i

The physics-based friction model of Triboform is further developed by M2i which incorporates the temperature dependency within the advanced friction meta-model by incorporating the Bergström van Liempt model. The coupling software act as a tool which provides a four dimensional frictional look-up table for a specified tribology system that consists of the parameters:

1. Nominal pressure,
2. Strain,
3. Velocity,
4. Temperature

M2i is also responsible for further developing the accuracy of the temperature dependent model to enable that the model can be implemented into metal forming lines at Philips in Drachten [5].

Philips

The study will be performed at the Philips Shaver department in Drachten under supervision of Mark Veldhuis MSc where the knowledge of manufacturing processes, material behavior and friction is combined with the processing and application of simulation data and a demonstrator line. The main contribution within the ASPECT project will be the generation of new insights concerning the metal forming process, data processing and implementation of control parameters in the demonstration line [5].

Inspire AG

Within ASPECT, inspire will use the outcomes of the production run phase to develop an adaptive process control that is widely applicable in metal forming lines. The temperature dependent behavior that was studied through numerical simulations will be made controllable by integrating the FEM predictions into the control system. Inspire AG is concerned with the quality of the simulation outcomes compared to the real-life out comes of the demonstrator line because this will determine their ability to predict and control the temperature dependent behavior during start-up. Inspire is invested within the production run phase of the ASPECT project. The quality of the control parameters will primarily be defined by the differences between the FEM simulations and the demonstrator line [5].

Resources and Data Acquisition

At the start of this Research project, a large amount of data has been made available that was developed in the previous phases of the Aspect project. The following data sources can be used for reaching the main research goals:

- Research papers from previous phases of the Aspect project concerning numerical and mathematical models that can be used as foundation for this Research project.
- A list of several literature articles concerning a variety of frictional models and Finite element method routines.
- Tutorial slides provided by MSC Marc that offers insight in the FEM solver models that are used.

The data acquisition for the rest of the integration project is expected as followed:

Theoretical framework

- Aspect articles
- Literature

FEM Simulation

- MSC Marc files given
- Friction lookup table
- MSC Marc tutorial
- Own findings during simulations

Demonstrator line

- Parameters from measurements previous phases
- Paper of Mark Veldhuis
- Own findings during production runs

Research Goals

The research project is performed during the Production run phase and is performed at the Research and Development department within the Philips Shaver branch. The research project will be performed considering the control of the temperature induced friction variation in a two-step deep draw process. In this project, the main focus will be:

- ❖ To acquire a validated finite element model that accurately predicts the effect of the temperature induced friction on the workpiece during the warm-up period of a deep draw process.

From this main focus the following goals can be formulated:

- ❖ Verification of the process' sensitivity for temperature induced friction within the MSC Marc solver by application of the temperature extension on the tribological model of J. Hol [6].
- ❖ Validation of the temperature induced friction simulation by comparing the simulation results of the MSC Marc solver with empirically obtained parameters from a two-step deep draw demonstrator process.
- ❖ Further refinement or expansion of the friction subroutine within the MSC Marc solver by explaining the results of the validation step based on theoretical tribological knowledge.

Scope

The general scope of this research is considered as very broad, since the total system of the metal forming process during the demonstrator run incorporates various aspects of different fields of study. Each of the individual aspects need to be understood and investigated individually as well in order to be able to explain for possible deviations between the FEM simulations and the product run outcomes. An overview of the scope in this study is given in [Figure 5](#) below.

Modeling and Validation of Demonstrator Product				
Tribology	Fluid Dynamics (lubricant flow on micro scale)	Metal Forming Process	Material Behaviour	Finite Element Analysis

Figure 5 - An overview of the main elements included within the scope of the demonstration product in this research project [3]

Methodology

Design science research iterates between design problems and knowledge questions where novel solutions are generated through fundamental research. The focus of this research project will be knowledge based in order to provide a generalized framework of knowledge that can be implemented in metal forming processes and enhances innovative development on a transnational level. Wieringa [15] states that:

“Design and empirical research both require theoretical knowledge in the form of conceptual frameworks and theoretical generalizations, which enhance our capability to describe, explain, and predict phenomena and to design artifacts that produce these phenomena.”

From this it can be noted that in order to be able to design artifacts in relation to specific phenomena, which in this research can be identified as the temperature-friction relation within the warm-up period, a specific theoretical framework needs to be constructed and validated. The specific theoretical framework can be linked to the tribological system provided for friction in a two-step deep draw process, which is given in section - [Tribological Framework](#).

The innovative goal of the ASPECT project can be seen as a holistic goal of the higher system that is met by the results of each of the three phases of the project, the holistic goal is stated as [1]:

“Improving the innovation capacity and competitiveness of SMEs or other enterprises from North-West Europe. This priority also involves social innovation, which includes innovative solutions for social needs and problems.”

In order to keep in touch with the top-level goal of the research, the suiting validation method that is implemented within the research can be determined by identifying which phenomena is studied and how it is studied. Based on [Figure 6](#) below, it can be seen that single-case mechanism experiments are best suited to investigate the temperature-friction relation (mechanism) within a two-step deep draw process (single case).

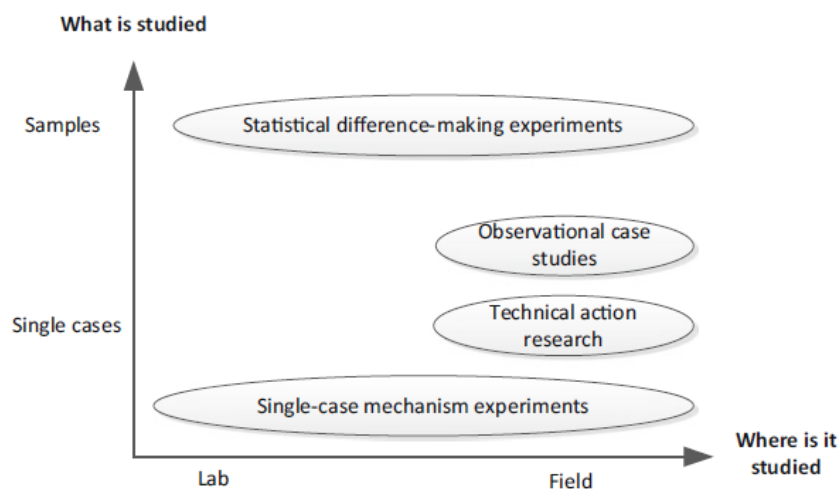


Figure 6 - Two dimensions along which to classify research methods [15]

In single-case mechanism experiments, individual parameters are studied which focus on the investigation of how a phenomena or mechanism relates to this specific case and how its behavior is related to the system architecture of the system. An important characteristic of single-case mechanism experiments is that during the conduction of research, the system architecture around the mechanism is varied.

In this study, the single-case mechanism validation process can be seen as an iterative method which encompasses the empirical cycle. Temperature variations within the tribological architecture of friction are performed in FEM simulations and validated with the demonstrator line. The methodological cycle is given in [Figure 7](#) below, where the focus of this research project will lie on the empirical cycle which provides the validated knowledge [15] [16] [17] [18].

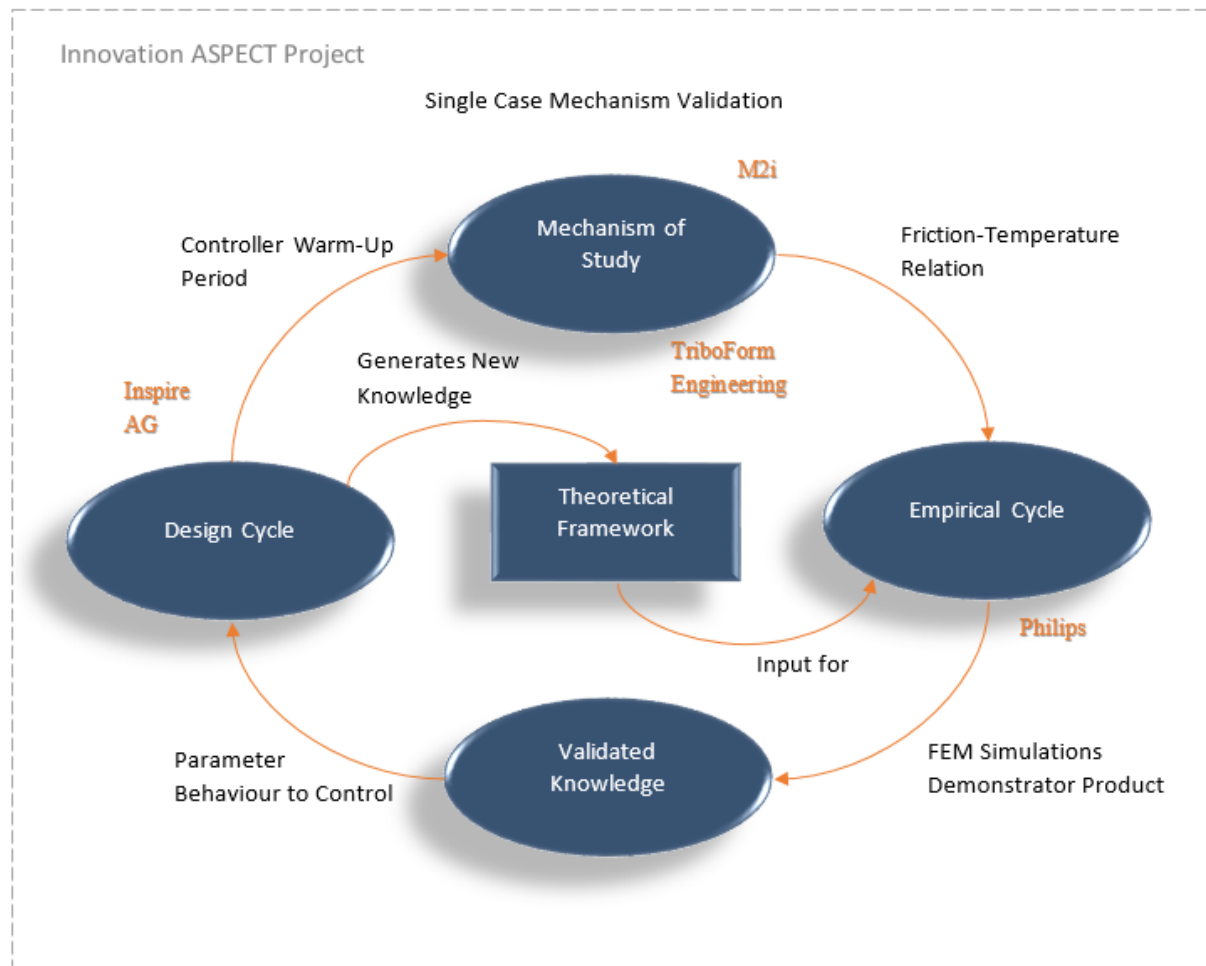


Figure 7 - The methodological cycle applied to provide validated knowledge

Research Questions

Defining a proper research question will consequently attribute to the achievement of the determined research goals [2]. Based on the tribological system and the goals formulated, the main question is formulated as:

- ❖ What is the impact of the temperature-induced friction on the output parameters of the two-step deep drawn cup?

To be able to answer the main research question, the following sub-questions can be defined:

- I. What are the dominant parameters that influence the tribological system of friction in a deep draw process?
- II. What is the sensitivity of friction to temperature changes for a specific two-step deep draw process?
- III. What is the fit between the results of the FEM simulations and the real case validation within the demonstrator line?

Theoretical Framework

This theoretical framework provides an overview of the most important mechanisms that are related to the temperature induced frictional behavior in a deep draw process. One of the main issues in the simulation and validation of frictional behavior is the disconnection between mechanisms on the macro and microscale [19]. Consequently, this theoretical framework will attempt to provide an advanced friction model that translates microscopic effects within a deep draw process into accurate macroscopic frictional behavior.

The quality of the simulation results and the translation between the micro and macroscale depends on the tradeoff between computation time and accuracy of the model that is used. In the theoretical framework chapter, a computational efficient translation of micro-scale parameters into macroscopic frictional behavior is studied.

Macroscopic

Initially, the theoretical framework will start from a macroscopic perspective, introducing the general process of deep drawing. The parameters influencing the product quality within the metal forming process will be outlined, as well as, common failures that need to be avoided. The succeeding section will provide a more in depth overview of the macroscopic frictional models that determine the coefficient of friction within the deep draw process. The focus on friction continues for the specific two-step deep draw process that is performed during the FEM simulations and the demonstrator line. The macroscopic section builds towards a tribological framework for friction within the two-step deep draw process, introducing microscopic parameters that give rise to the macroscopic frictional behavior.

Microscopic

A tribological framework is provided that introduces the micro-scale mechanisms that affect the frictional behavior in the two-step deep draw process. The identified micro-scale mechanisms are further elucidated in the subsequent sections and will form the foundation of the frictional look-up table that is used in the FEM simulations.

FEM Solver

In this section, the finite element model is explained, which is used to perform the two-step deep draw simulations. An overview of the tooling is given and the role of the look-up table within the subroutine Crystal is discussed.

In conclusion, the theoretical framework will aim to provide a holistic overview of the relation between the microscopic and macroscopic mechanisms within a two-step deep draw process. The constructed framework of knowledge will act as a foundation based on which the results of the simulations and the demonstrator test run can be validated within the subsequent chapters.

Metal Forming Processes

Metal forming processes can be distinguished in sheet and bulk forming methods. Sheet metal forming is one of the most important techniques that is applied in almost every large-scale manufacturing industry with examples being the automotive, aircraft, home appliance and food industry. The manufacturing method of sheet metal forming draws sheet metal plates into a desired geometrical shape without losing any material during the process. Examples of different metal forming processes are bending, stretching and deep drawing, which are illustrated in Figure 8 [6] [20].

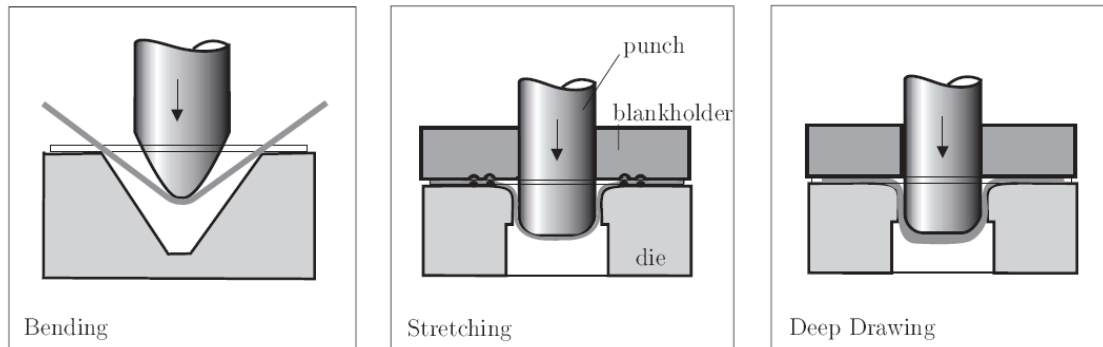


Figure 8 - Representation of different metal forming processes [21]

Stretching together with deep drawing and bending are the most common metal forming processes with their difference being the movement allowance of the blank. During bending, the blank is bent by the punch into a geometrical shape without any fixation being present at the sides of the workpiece. During stretching, the blank is clamped by the blank holder, preventing movement and promotes bulk stretching. Whereas during deep drawing, the blank will be held lightly under the blank holder, allowing for gradual movement of the blank during the process and attaining a relatively similar thickness before and after. In this research project, the main focus will be the deep drawing process where the deformation of a cylindrical shaped cup is further considered [6] [21].

Deep Drawing Process

In deep drawing, the metal sheet is drawn by the punch into the cavity of the die mold. During this process, bending and sliding mechanics occur which affect the geometry of the workpiece. The applied force of the punch stresses the blank material beyond its yield strength, causing the material to deform plastically, but not to fail. Plastic deformation dominates throughout the deep draw process by applying an external load onto the metal sheet. Sufficiently high loading forces are necessary in order to reduce the spring back and to ensure that the desired geometrical shape is retained after unloading. A general overview of the steps in a deep draw process are illustrated in Figure 9 below [22] [23].

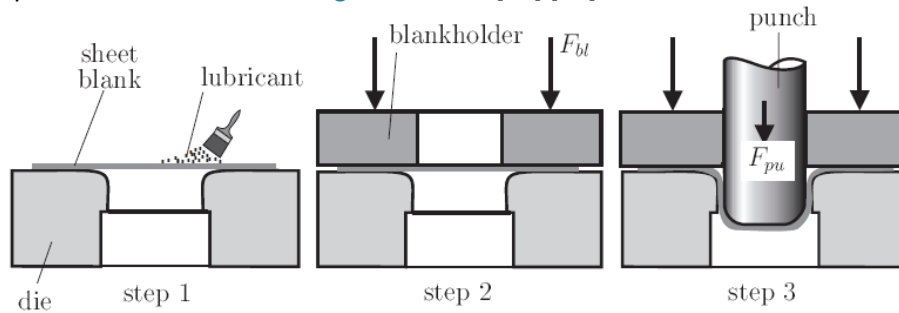


Figure 9 - Representation of different metal forming processes [21]

The main components that interact with each other during the deep drawing process can be identified as:

- Sheet Blank
- Forming Die
- Punch
- Blankholder

The quality of the deep draw product is affected by different mechanisms that occur during the interaction between each of the main components. Influencing the material behavior of the blank during the deep draw process. The different mechanisms can be divided into five different regions of interaction that are illustrated in Figure 10 below [24] [25] [26].

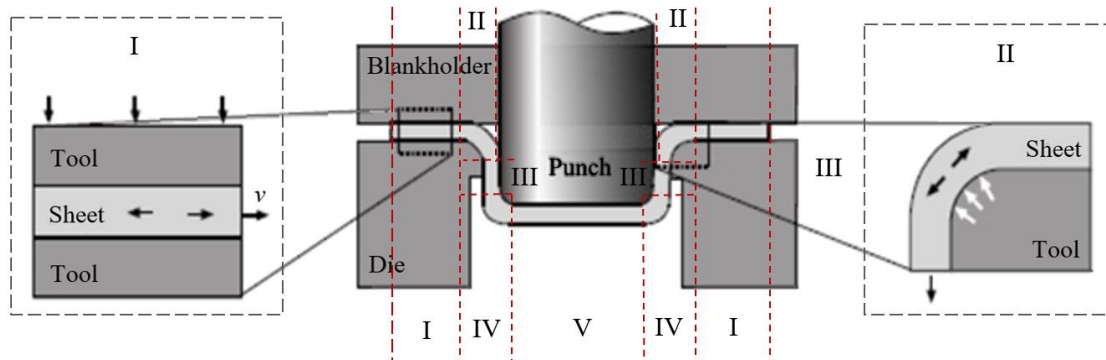


Figure 10 - Schematic illustration of the different interaction regions in the deep drawing process [26]

According to Adnan I. O. Zai [25] the different regions of interaction can be described as:

- I. Pure radial drawing between the die and the blank holder.
- II. Bending and sliding over the die profile.
- III. Stretching between the die and the punch in the clearance zone.
- IV. Bending and sliding over the punch profile radius.
- V. Stretching and sliding over the punch head.

Within each of the distinguished areas, different material behavior of the blank is expected during the deep draw process. It should be stressed that these regions require adequate control throughout the process in order to reduce any possible failures in the end product. Within this study, the main focus is to be able to control the deep draw process in order to attain a minimum amount of rejected parts during the warm-up process.

Possible Failures

Insufficient prediction and control of the mechanisms in the deep draw process can result in unwanted macroscopic effects such as necking, earing, tearing and wrinkling of material. Especially in the warm-up process, the quality of the cup varies over time, which can lead to an even increased amount of product being rejected. In order to prevent possible failures to occur, an understanding of the underlying mechanisms is required. This section will provide a broad overview of the failures which can occur during the deep draw process. An illustration of the possible failures is given in [Figure 11](#).

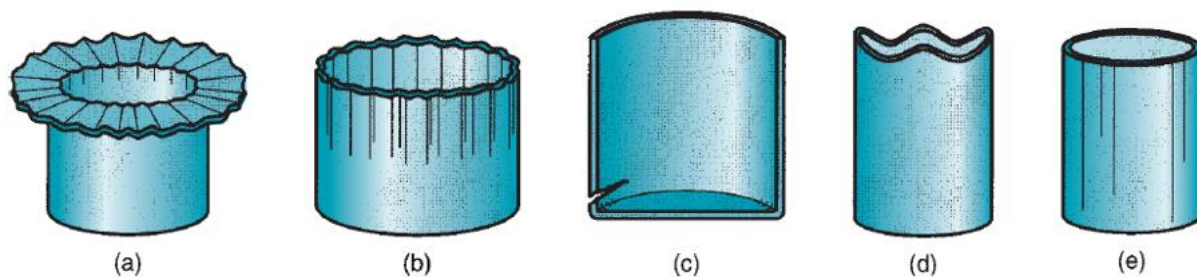


Figure 11 - Possible deep draw failures in drawn parts: (a) Wrinkling in the flange, (b) Wrinkling in the wall, (c) Tearing, (d) Earing, and (e) Surface scratches [27]

Tearing

Excessive thinning and ultimately tearing of the workpiece is caused by high tensile stresses, which develop in the bulk material can be located at different regions as identified in [Figure 10](#). The excessive forces can arise due to high blankholder pressure on the blank, preventing the flow of material between region I and II. Drawing the blank too deep in one step or applying a punch force that is too high, can also result in excessive thinning in the clearance gap of region III between the die and the punch. Frictional forces enhance the effect of the blankholder and punch on the material behavior, making the use of a lubricant important. Tearing usually occurs at the weakest spot of the blank, located at the cup wall near the base [28] [25] [29] [30].

Wrinkling

Wrinkling is another common defect of compressive buckling that causes flange instability of the blank, in region I, and will continue to grow towards the middle at region III. The wrinkle formation at the blank largely depends on the geometrical properties of the die and the punch, together with the exerted pressure of the blank holder and the thickness ratio of the blank itself. If the applied blank holder pressure is too low, disorderly material flow can occur during the deep draw process. Another element is the corner radius of both the die and the punch, if the radius is too large, excessive space enables for wrinkling of the blank material. The increasing of the coefficient of friction between the blank piece and the tool during the deep draw process can help to reduce the wrinkling phenomena [28] [25] [20] [29] [31] [30].

Earing

The formation of earing is another one of the major defects during deep drawing. This effect of wavy unevenness formed along the edges of the flange or end of the cup wall is caused by the planar anisotropic properties of the blank material. The sheet shows stronger material behavior in one direction compared to other directions in the plane sheet. The uneven material behavior in different directions can be affected by drawing the blank too deep or by the material properties of the blank itself. The formation of earing is not desirable since additional processing steps are required to trim the excess material [28] [20] [29] [25] [30].

Surface Scratches

Scratches occur on the surface of the blank material during deep drawing if the surface quality of the punch and die are not high enough or if insufficient lubrication is applied. A large roughness on the punch and die result in particles getting into contact between the tooling and the blank. During the deep draw process, contact with the particles lead to abrasion of the softer material, causing damage to the die surface. Surface scratches can be avoided by keeping the die surface in very good surface quality and reducing the friction between the tooling by applying a sufficient amount of lubricant material [28] [20] [29] [30] [32].

Control Parameters

The deep drawing process manufactures the blank material into a desired shape within strict specifications. Deep drawing, even in its basic form, involves very complicated mechanics influencing the material behavior of the product. Failures occurring within the production process can lead to large rejection rates and a lower yield. This is deemed highly undesirable since it leads to unnecessary amounts of wasted materials, energy and costs. To be able to predict and control possible manufacturing variations more accurately, the possible parameters responsible for possible failures in the deep draw process need to be identified. The parameters that affect the deep drawing process can be categorized into three general categories [33]:

- I. Geometrical parameters
- II. Material Parameters
- III. Process parameters

The geometrical parameters of the tooling, blank and the process parameters define the final shape of the product and the material flow behavior is largely dependent of the material choices in the deep draw process. Both the geometrical and material choices are predefined within this study, an overview of the chosen parameters used in the simulations and experimental setup are provided in section - [Dimensions](#). The process parameters are the focus of this study since these factors are generally used to control the deep drawing process within the metal forming industry.

An overview of the identified macroscopic parameters in the deep draw process is given in [Table 1](#) below [34] [25] [30] [3]. The most important parameters that control the forming process are further discussed in this section.

Table 1 - Overview of the identified macroscopic parameters in the deep draw process [25]

Geometrical Parameters	Material Parameters	Process Parameters
Punch Diameter	Blank Material Type	Blankholder Force
Punch Corner Radius	Blank Material Geometry	Punch force and Drawing speed
Punch-die Clearance	Young's Modulus	Lubrication Thickness
Die Opening Diameter	Material Flow Stress	Coefficient of Friction
Die Corner Radius	Anisotropy	
Initial Blank Thickness	Hardness Tooling	
Initial Blank Diameter	Drawing Ratio	

Blank Holder Force

The blank holder applies pressure onto the blank material and determines the amount of flow resistance to the blank material along the punch movement. If the blank holder force is too high, tearing behavior can occur in the cup wall and if the force is too low, wrinkling behavior in the flange region may occur. Singh and Agnihotri [33] and Jaisingh et al. [35] concluded that the amount of blank holder force influences the plastic strain ratio, which determines the thinning and thickening properties of the blank material, and the fictional behavior during the deep draw process. The applied blank holder force resides in the range of 0.5% to 1% of the ultimate tensile strength of the sheet material. The controlling properties of the blank holder force within the deep draw process will be further examined in this research project [36] [37] [38] [39] [30].

Punch Force and Drawing Speed

The punch force required for deforming the blank plastically, will increase linearly with the press speed due to increased straining forces that triggers strain hardening behavior. The required drawing pressure necessary to avoid wrinkling of the blank depends on the type of blank material used, the thickness of the blank and the limited drawing ratio. The drawing speed is of greater significance for drawing harder materials than for drawing softer, more ductile materials. Excessive drawing speeds can induce crack formation and excessive wall thinning since material has less time to react and flow into the cavity. Reducing the drawing speed also reduces the thinning effects on the blank material. The total force required in the deep draw process can be divided into 15% on bending and unbending of the blank material, 70% for the actual radial drawing of the blank material and 10% of the energy for overcoming the frictional forces. The controlling properties of the punch force and drawing speed force within the deep draw process will be further examined in this research project [40] [41] [42] [30].

Lubricant Properties

In metal forming processes, it is common practice to apply a lubrication layer between the blank-tooling material interface to reduce the friction coefficient. Lubrication is one of the process parameters, which affect the material flow during forming and the quality of deep draw product. The distribution of lubrication is dependent on the particular region of contact in the deep draw setup, influenced by surface conditions, pressure differences and sliding speeds. Therefore, different contact regions may exhibit different lubrication regimes [21] [43] [44].

Richard Stribeck introduced the Stribeck curve theory in 1901 in [11] [10] which showed the relationship between the film-forming properties of the lubrication between two surfaces. The Stribeck curve represents the contact between two fluid-lubricated surfaces with on the X-axis the Hersey number and on the Y-axis the friction coefficient, as shown in Figure 12 and Figure 13 [45] [46] [11] [10].

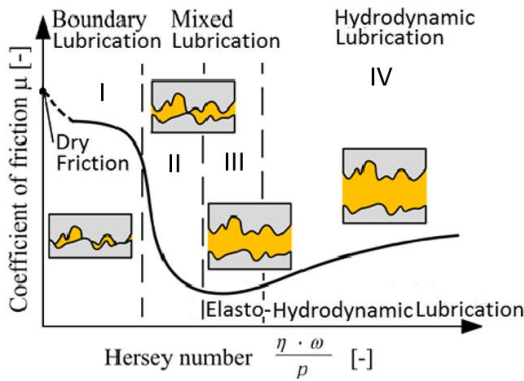


Figure 12 - Stribeck curve representing the different possible lubrication regimes [46]

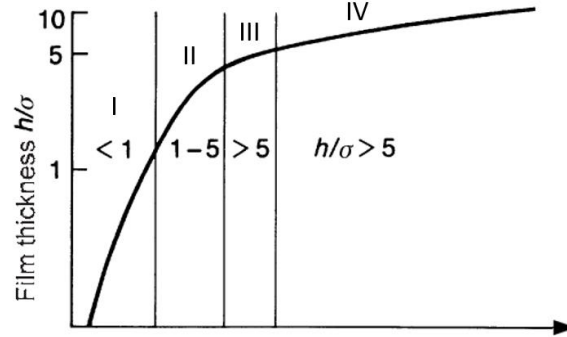


Figure 13 - Depiction of the film thickness parameter and the Hersey number linked to the possible lubrication regimes [10]

The Hersey number is identified as a dimensionless lubrication parameter, which is defined as [47]:

$$\text{Hersey number} = \frac{\eta \cdot N}{P} \quad (1)$$

Where η represents dynamic viscosity of the particular lubricant type, N is the relative velocity of the contacting surfaces, and P the normal load. A high Hersey number equals a relatively large lubricant thickness, whereas a small Hersey number represents a thin film lubricant.

Thus the Stribeck curve [11] [10] represents, for a given viscosity and load, how the friction coefficient develops for a deviating relative velocity. Along the curve in [Figure 12](#), starting from the friction coefficient in a dry contact situation, four distinctive lubrication regimes or lubrication regions can be identified:

- I. Boundary Lubrication
- II. Mixed-film Lubrication
- III. Elasto-Hydrodynamic Lubrication
- IV. Hydrodynamic Lubrication

Most of the deep drawing processes are performed between the boundary and the mixed lubrication regimes where the lower frictional values are present. Each of the distinctive lubrication regimes will be briefly discussed below where the dry contact situation will be discussed within the friction parameter.

Boundary Lubrication

Within the Boundary Lubrication (BL) regime, the normal load is carried by contacting asperities of the surface-lubrication-surface interface. Within this interface, a thin boundary layer is sheared, preventing dry contact between the surfaces. The boundary lubricant layer is often exhibited during start-up and shutdown of metal forming processes. Low production speeds and high load conditions result in the highest friction values of the lubricated regimes identified along the Stribeck curve. Boundary Lubrication and Mixed Lubrication are the most widely adapted lubrication regimes within metal forming processes [11] [10] [21] [48] [45].

Mixed Lubrication

The transition between the Boundary Lubrication regime and the Elasto-Hydrodynamic Lubrication is identified as the Mixed Lubrication (ML). This mixed regime dominates when the friction coefficient further decreases for an increased shearing velocity, film thickness and viscosity. Also a decrease in the load results in lower frictional values between the contacting surfaces. Within the Mixed Lubrication regime, the distance between the surfaces increases and less solid contact exists. Due to the increasing lubricant thickness, existing pockets within the surface become filled with the lubricant [11] [10] [21] [48] [43].

Elasto-Hydrodynamic Lubrication

Increasing the lubricant layer thickness further results in a transition into the Elasto-Hydrodynamic Lubrication regime where the surface-lubrication-surface interface is completely separated by a thin fluid film. The Elasto-Hydrodynamic Lubrication exhibits the shearing of the lubricant layers, in the form of elastic deformation, over each other lowering the friction coefficient significantly, this is generally occurring for high velocity processes. The amount of lubrication is further increased and the friction coefficient is further reduced up to a minimum value. Beyond the minimum value, internal friction within the lubricant itself becomes dominant, which in turn results in the friction coefficient increasing instead of decreasing [11] [10] [21] [48] [49].

Hydrodynamic Lubrication

Beyond the minimum value, the friction coefficient increases and the Stribeck curve further develops into the Hydrodynamic Lubrication regime. This regime is categorized by a full film lubrication layer which induces a lower normal pressure, reducing the viscosity. The internal hydrodynamic friction of the lubricant becomes more dominant, increasing the overall friction forces. Consequently, the friction coefficient develops itself beyond the optimal processing situation and increases [11] [10] [21] [48] [50].

Friction

The complex physical phenomenon of friction is generally described as a non-conservative force of resistance to the relative motion between two bodies that are in contact with one another. The friction force distribution is tangent to the true contact surface area of the apparent body under consideration with a direction that is opposite to the direction of motion. Friction can also occur within the body itself, this occurs within the air and in hydrodynamic friction. There are many, situation based sources of friction that can be identified ranging from the deformation of asperities, adhesion between surfaces to capillary and van der Waals forces [51]. Due to its complex nature and the absence of a universal theorem that is applicable at different levels of scale, the actual physics of friction and its numerical representation continue to be topics of research at this day [21].

Within the deep draw process, friction predominantly arises due to a relative motion between the blank and the tooling that are in contact. Schey [52] [53] determined six different contact regions, which exhibit different frictional behavior during the deep draw process. A brief overview of the most important regions of interest is provided below in Figure 14.

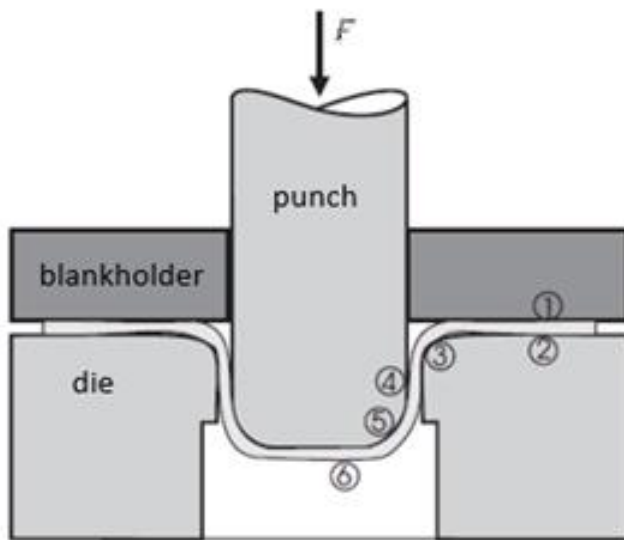


Figure 14 - Contact regions in deep drawing [53]

Region 1-2 depict the flange region which is identified by the blank being held between the blank holder and die. The blank holder lightly clamps the blank during the deep draw process. However, there is allowance for gradual movement of the blank, which results in relatively low amounts of strain and nominal pressure around region 1 and 2.

Region 3-4 depict the bending point of the blank over the die rounding. Due to the forces of the punch that deform the blank, relatively high pressure and tension forces occur, which result in material flow in the form and stretching of the blank sheet.

Region 5-6 depict the contact between the face of the punch and the blank sheet. Here the depth of the drawing influences the extent to which the blank is subjected to stretching. In general, high amounts of strain are present at region 5-6.

Friction, together with plastic deformation, is considered the dominant mechanism that impacts the forming behavior of the blank material during the deep draw process. The generated friction influences the amount of work needed to deform the sheet material, however, the impact of friction is not considered

to be uniform throughout the total process. Different contact regions exist between the punch, workpiece, blank holder and die during the deep draw process for which different frictional behavior is desired.

As seen in [Figure 14](#) and [Figure 15](#), in region 5 at the punch-blank contact, the amount of friction must be sufficiently high to induce material flow that follows the punch movement. In the regions 1, 2 and 3 however, a minimum amount of friction is required in order to reduce the resistance to the drawing direction.

Based on the control parameters, friction is considered a dominant mechanism influencing the final quality of the product and giving rise to the need of controlling its development throughout the deep draw process. However, there are multiple approaches to derive the coefficient of friction within a metal forming process. Therefore, the basic macroscopic frictional models will be introduced in the following chapter before continuing to the two-step deep draw process for the Philips demonstrator line [3].

Macroscopic Models of Friction

In this paragraph, an overview is given of the classical models of friction that are used and further developed for the specific two-step deep draw process of the Philips cup. Before the impact of different lubrication regimes will be discussed, first the classic or dry friction will be treated.

In general, for two solid surfaces in contact, a distinction between two different regimes of friction can be made, which are dependent on the relative lateral motion of both surfaces. The two regimes of friction that can be identified are *static friction* (or "stiction") and *kinetic friction* (or dynamic friction). Static friction holds for the situation of two contacting surfaces that are not in relative motion, the static friction force can be identified as the minimum force required in order to initiate motion. The static friction coefficient represents the force needed to sustain the previously initiated motion and occurs in a state where there is relative motion between contacting surfaces [54].

First the static friction models will be introduced, starting with Amontons laws of friction [55], the Coulomb friction model [4] and the Stribeck curve [11] [10] which are often referred to as the classical models of friction. Also deviations on the Coulomb model, including the effect of viscous and static friction (stiction), will be discussed. An overview of the general static friction models is shown in Figure 15 below [11] [56] [57].

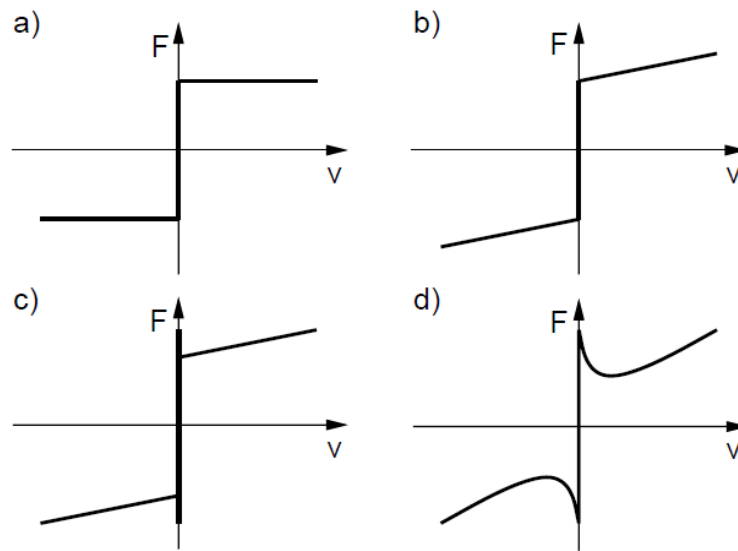


Figure 15 - Examples of static friction models a) shows Coulomb friction b) Coulomb combined with Viscous friction c) Coulomb combined with Stiction and Viscous friction d) Coulomb combined with the Stribeck effect [57]

Amontons' Laws of Friction

The foundation of friction can be traced back to the 15th century where Leonardo da Vinci discovered that the friction force is proportional to the applied loading force and is independent of the apparent contact area between two solid surfaces. These fundamental laws of friction were ultimately expanded upon and published by Amontons in the 17th century [55]. The published paper of Amontons offered a first simplified understanding of the complex phenomena of dry friction.

Amontons' Laws of Friction are stated as follows [55]:

- I. The friction force is directly proportional to the applied normal load.
- II. The friction is independent of the apparent (nominal) area of contact.

Coulomb Friction Model

The two main laws of Amontons were complemented with a third law of friction that was added by Coulomb in the 18th century. A more comprehensive understanding of the friction phenomena was developed which resulted into the third main friction law, Coulombs law [55] [58]:

III. The kinetic friction is independent of the sliding velocity.

Coulomb based his finding on a series of experiments between different sliding materials where the schematic representation is show in [Figure 16](#) below. The observed variations of friction over time are explained as a contribution of interlocking of asperities which, after a definite period of time, reach a limit value that indicated the occurrence of full deformation [58] [59].

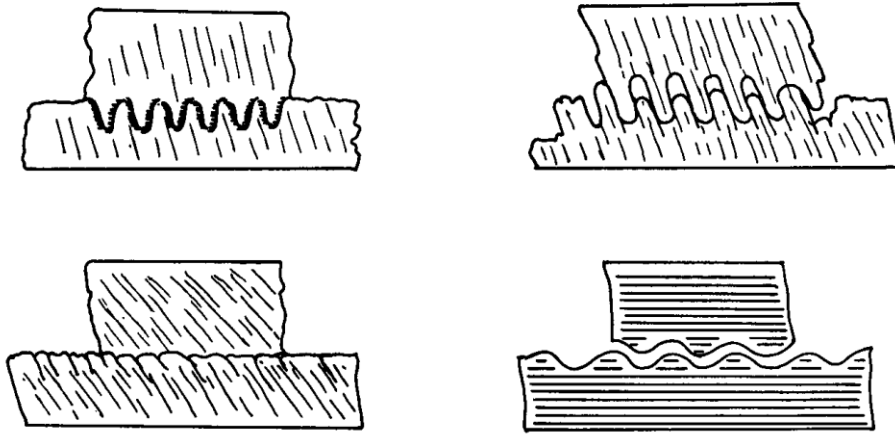


Figure 16 - Coulomb's schematics of surface interactions [58]

According to Coulomb, different behavior for the dynamic friction case was theorized due to the surface asperities of the two sliding surfaces that did not have enough time to become interlocked.

The observational results of these experiments are shown in the memoires “The theory of simple machines” and formed the foundation of the Coulomb friction model which is presented in following equation [55] [58]:

$$F_f = F_k \cdot \text{sgn}(\dot{x}) \quad (2)$$

Where F_k is the friction force that is specified for the kinetic friction case:

$$F_k = \mu_k \cdot |F_n| \quad (3)$$

Since the Coulomb friction model is an approximation of the dynamic friction regime, it only specifies for a non-zero velocity situation where it can take a value in the interval between $-F_k$ and $+F_k$. The Coulomb friction model cannot take into account the properties of (increasing) static friction motion which results, for the zero or starting velocity situation, in a friction force that becomes zero [60] [59].

Describing an undefined friction force at zero velocity is also the main reason that the Coulomb friction model can only be used to describe the behavior of friction in macro-scale situations. A schematic representation of the friction force is shown in Figure 17 and Figure 18 below [61] [59].

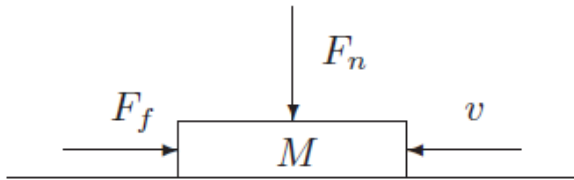


Figure 17 - Schematic representation of the friction force F_f on an object M moving relative to a flat surface [62]

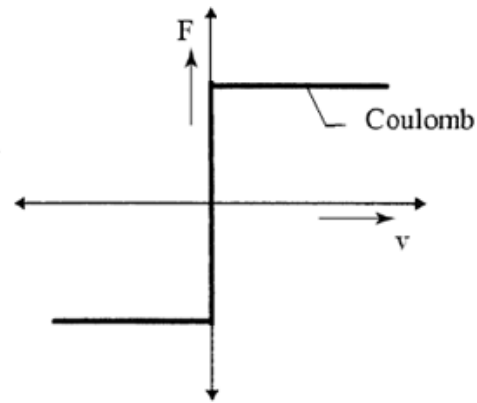


Figure 18 - The Coulomb friction model as a function of velocity [56]

After the establishment of the Coulomb model, two other facets are added that expand upon this classical friction model. Progression was made by Morin who introduced the concept of static friction in 1833 [63] and Reynolds further expanded the friction model by proposing the concept of viscous friction in 1886 [64]. Stribeck introduced the Stribeck curve in 1902 [11] [10] which provides a relation between the coefficient of friction and the contact load, lubricant viscosity and relative velocity. Consecutively, the additions of static friction, viscous friction and the Stribeck curve are now briefly discussed.

Static Friction Model

Arthur Jules Morin observed that the friction force at rest is higher compared to the kinetic friction of the Coulomb friction model. The static coefficient of can be described as a function that is equal and opposite to the applied external force on the body up to a threshold value [63]. The break-away force is required to overcome the static friction coefficient threshold in a stick situation in order to initiate motion of the body. An illustration of the difference between static and dynamic friction is shown in Figure 19 and Figure 20 below [4] [56] [57] [63] [66].

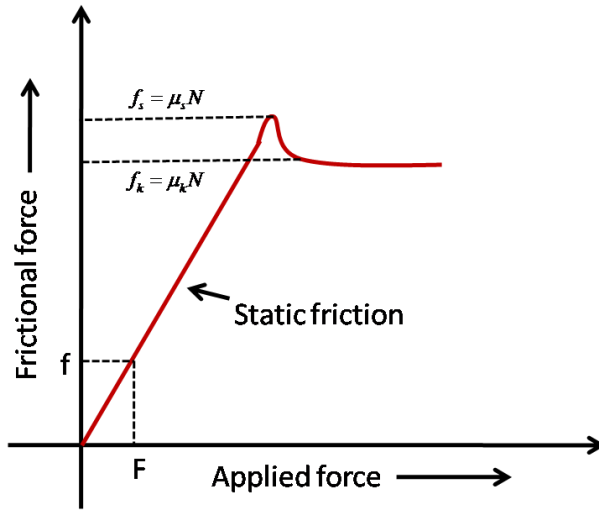


Figure 19 - The relation between friction and displacement according to Morin [65]

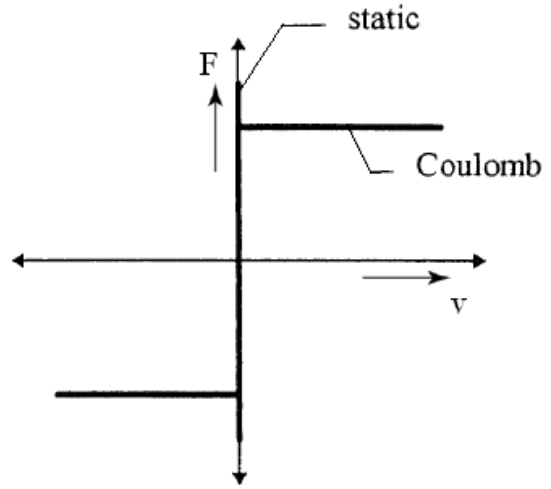


Figure 20 - The combination of static friction and the Coulomb friction model [56]

In result, the addition of Morin's static friction to the Coulomb friction model is presented in following equation [4] [56]:

$$F_f = \begin{cases} F_s & \text{if } v(t) = 0 \text{ and } |F_e| < F_s \\ F_k \cdot \text{sgn}(\dot{x}) & \text{if } v(t) = 0 \text{ and } |F_e| \geq F_s \end{cases} \quad (4)$$

Where F_s is the friction force that is specified for the static friction case [4] [56]:

$$F_s = \mu_s \cdot |f_N| \quad (5)$$

From the equation, it becomes clear that the friction force, F_f becomes equal to F_e , the external applied force, for a zero-velocity case up to the static friction threshold. When the external force exceeds the static friction threshold value, the friction force becomes dependent again on the Coulomb friction model [56].

Viscous Friction Model

After further advancements in the field of hydrodynamics, the viscous friction model was developed by Reynolds in 1866 [64]. The viscous friction can be described as the friction force caused by a combination of the internal viscous behavior of shearing fluid lubricant layers and the external viscous behavior of fluid-surface in contact. The viscous friction is proportional to the relative velocity of the surfaces and is represented in the following equation [67] [56]:

$$F_f = \sigma_v \cdot \dot{x} \quad (6)$$

Where the behavior of the lubricant is captured within a viscous coefficient, σ_v , that can be defined as the measure of a fluids resistance to flow because of its internal friction. The viscous friction model is illustrated in [Figure 21](#) below.

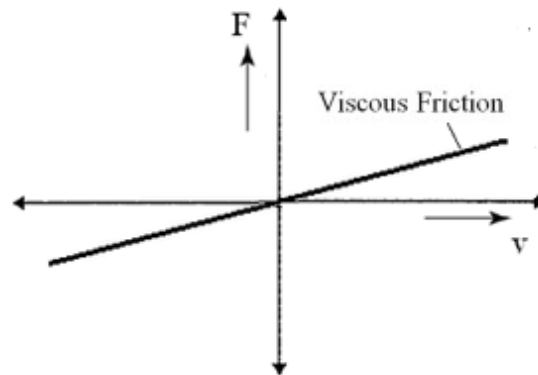


Figure 21 - The Viscous friction force as a function of the relative velocity [68]

It can be noted from the figure that the viscous friction model has a linear dependency of the relative sliding speed within a contacting fluid layer interface. Since only viscous forces of the lubricant are taken into account, application of this model for surfaces into contact is limited due to the lacking of a description of dry friction. A more encompassing frictional model, which attempts to include the frictional effects of a surface-fluid-surface interface is provided by the Stribeck friction model in the theory section below [57] [60] [69].

Stribeck Friction Model

Richard Stribeck proposed the concept of Stribeck friction which shows a decrease in the frictional coefficient for an increasing relative velocity [11] [10]. This effect occurs during the transition from static friction to kinetic friction. The addition of the velocity dependent Stribeck effect results in a more advanced friction model, including the coulomb friction and the viscous behavior. The advanced model is described as the Stribeck friction model [70] or General Kinetic Friction (GKF) [71] and is described by [72] [73]:

$$F_f(F_e, v) = \begin{cases} F_e & \text{if } v(t) = 0 \text{ and } |F_e| < F_s \\ F_s & \text{if } v(t) = 0 \text{ and } |F_e| \geq F_s \\ F_k + (F_s - F_k) \cdot e^{-a_{str} \cdot v} + F_v \cdot v & \text{if } v(t) > 0 \\ -F_k + (F_k - F_s) \cdot e^{a_{str} \cdot v} - F_v \cdot v & \text{if } v(t) < 0 \end{cases} \quad (7)$$

Where [74]:

- F_{ext} - The external applied force
- F_s - The static frictional force
- F_k - The kinetic or Coulomb frictional force
- F_v - The viscous frictional force
- v - The relative velocity
- a_{str} - The Stribeck curve coefficient

The relation between the Stribeck curve regimes and the Stribeck friction model, showing the individual influences of the different frictional forces, is depicted below [59] [75] [70].

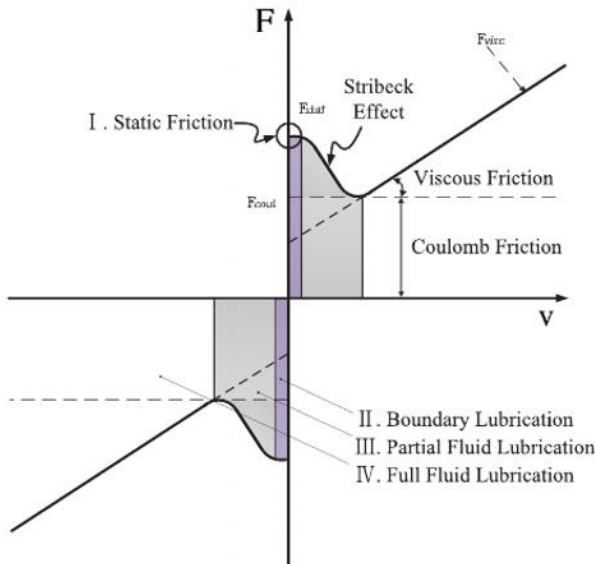


Figure 22 - Four regimes of the Stribeck curve [73]

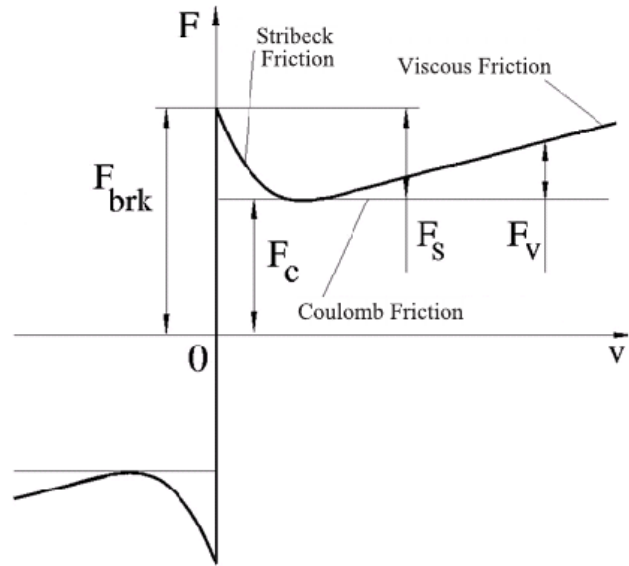


Figure 23 - Friction force simulated as a speed dependent function shown as the sum of Stribeck, Coulomb, and viscous force components [67]

The figure clearly shows the negatively sloped behavior of the Stribeck component, which occurs at low velocities. The combination of the Coulomb and Stribeck frictional forces at the zero velocity region is identified as the breakaway friction [67] [62] [59].

Demonstrator Line

Within the ASPECT project, the impact of temperature-induced friction on the quality of the end product is studied for a two-step deep draw process. This study will demonstrate the impact of the start-up effects on the end product during the specific two-step deep draw process by validating the outcomes of the FEM simulations with the results of the demonstrator line. In order to be able to compare the results of both experiments, the product geometry that is formed is relatively simple of shape and it approximates the complexity of a regular metal formed part currently produced by Philips [1] [2].

In order to be able to provide substantiated results during the experiments of this study, the demonstrator product is chosen to be highly susceptible to transient temperature and friction. Furthermore, the product should be generating a lot of heat during the deep draw process. Also, any forming behavior of the demonstrator due to other spread factors such as the flow stress, material thickness or normal anisotropy should be avoided at all costs.

As a result, it is chosen for the demonstrator product to be drawn into a cylindrical cup shape with a hole in its center, as given in [Figure 24](#). The cup approximates the geometrical properties of a Philips shaver cap that is processed within the facility in Drachten. Both the geometry of the cup as the deep draw process are highly susceptible to temperature variations during the warm-up period, making it a valid combination for the demonstrator line to be studied [3].



Figure 24 - Geometrical representation of the cup shaped demonstrator product [3]

Two-Step Deep Draw Process

The two-step deep draw process within this study consists of an initial preprocessing step and two different deep draw steps that are executed consecutively in a demonstrator line. The second deep draw step is performed in order to provide optimal sensitivity to the start-up effects. An overview of the demonstrator process is illustrated in [Figure 25](#) below.

The set-up and the geometry of the tooling within the developed two-step deep draw process is designed in Aspect Deliverable T3.1.3 [3] in order to be insusceptible to any other spread sources that may influence the material flow behavior of the cylindrical cup. Within this piloting work package, the impact of the tool fillet radii, drawing depths, ejector and blank holder forces on the cylindrical cup were studied to provide the optimal deep drawing setup that is both temperature and friction dependent. A detailed overview of the tooling used within the demonstrator line is provided in [Appendix 1 – Tooling Two-Step Deep Draw Process](#).

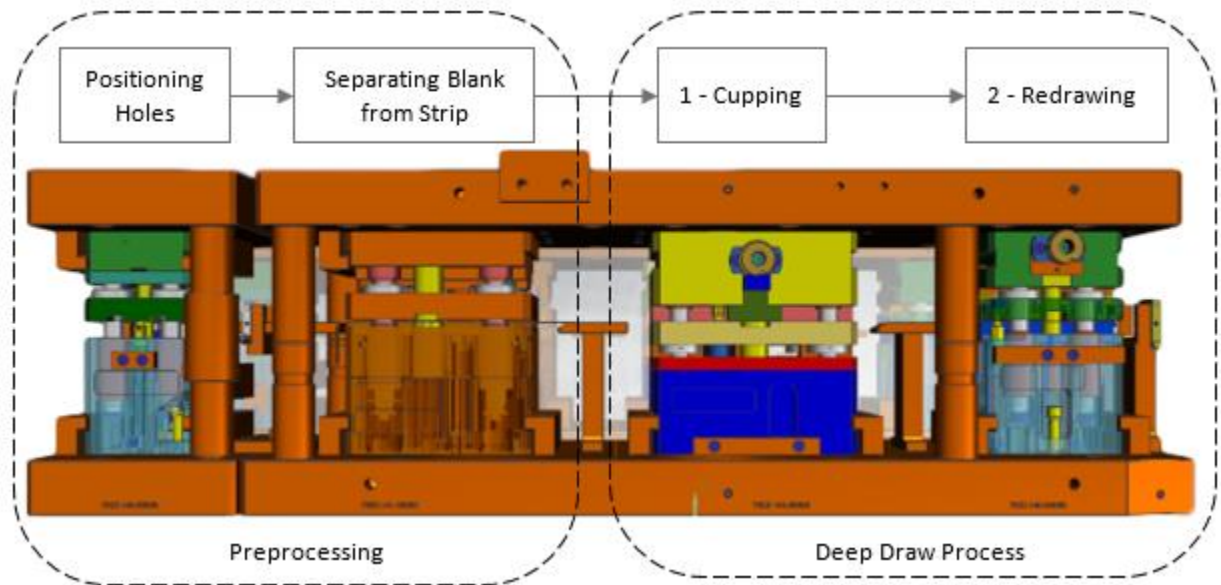


Figure 25 - Overview of the Demonstrator process [3]

Beforehand, the strip is preprocessed where a hole is punched in the middle of the blank and the blank is detached from the transportation strip with the exception of the small connectors. The first step of the deep draw process acts as a standard axisymmetric drawing step where the initial flange curve is drawn in a bottom-up movement. Deforming the blank into a cup shaped geometry [3].

The second step in the deep draw process is identified as a redrawing step that is performed in the opposite direction of the workpiece in a top-down movement. The die-punch setup is reversed, which performs a smaller indentation on the upper side of the cup [3].

The two-step deep draw process is performed sequentially within the demonstrator line within two different die sets. Consequently, a small amount of idle time between is present the two forming steps, which can affect the temperature of the blank material. This effect is approximated in the simulations by accounting for an idle time of 5 seconds between each processing step. The complete evolution of the blank during the deep draw process is illustrated in Figure 26 below.

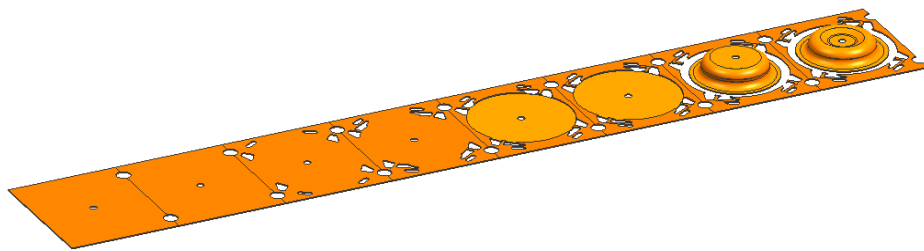


Figure 26 - Connector strip evolution for throughout process steps [3]

As can be seen in the setup of the demonstrator line in Figure 25 different tooling will interact with the blank piece in a cross-interactive fashion, resulting in a complex system to predict and simulate. The control parameters influencing the frictional behavior during the two-step deep draw process are given in Figure 27. It is determined in the Aspect Deliverable T3.1.3 that the temperature induced friction being determined to be the most dominant mechanism influencing the geometrical properties of the cup [3].

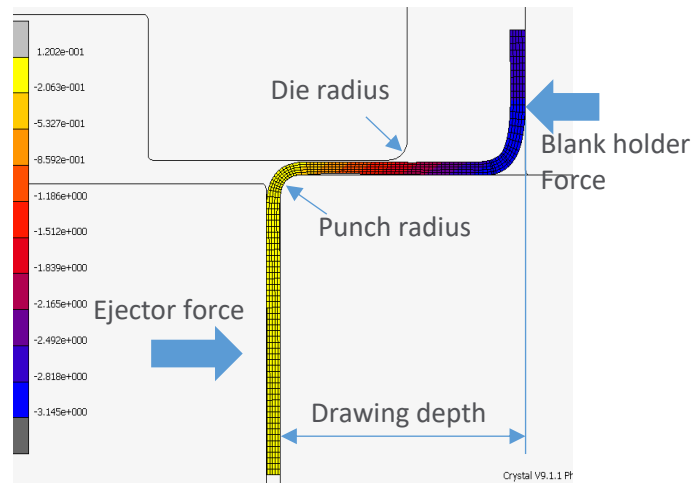


Figure 27 - Schematic overview of varied control parameters in the DACE studies [3]

In order to be able to validate the outcomes of the FEM simulations with the results of the demonstrator line, output parameters need to be defined which are reliable and fit for validation. The output parameters are required to be measurable in both the FEM simulations and the demonstrator runs for each of the two drawing steps. Also the output parameters should be sensitive to the control parameters that are identified to enable the development of controllers at Inspire AG in the last phase of the ASPECT project [1] [3].

In order to account for the temperature-induced frictional behavior during the warm-up period, first a general system overview of the most important deep draw parameters needs to be established. Each of these frictional elements contributing to the quality of the product will be further outlined in a tribological system in the next paragraph.

Tribological Framework

Being able to correctly predict and control the mechanisms that give rise to negative behavioral effects, will result in less defective parts during the warm-up period and a higher overall product quality. Therefore, the multi-scale parameters influencing the friction coefficient of the process should be studied as accurate as possible. The initial framework in Figure 3, which describes the tribological parameters related to friction in a deep draw process, is further extended in Figure 28 and will act as a foundation of the remainder of this theoretical framework [12] [13] [76] [77] [78] [79] [41].

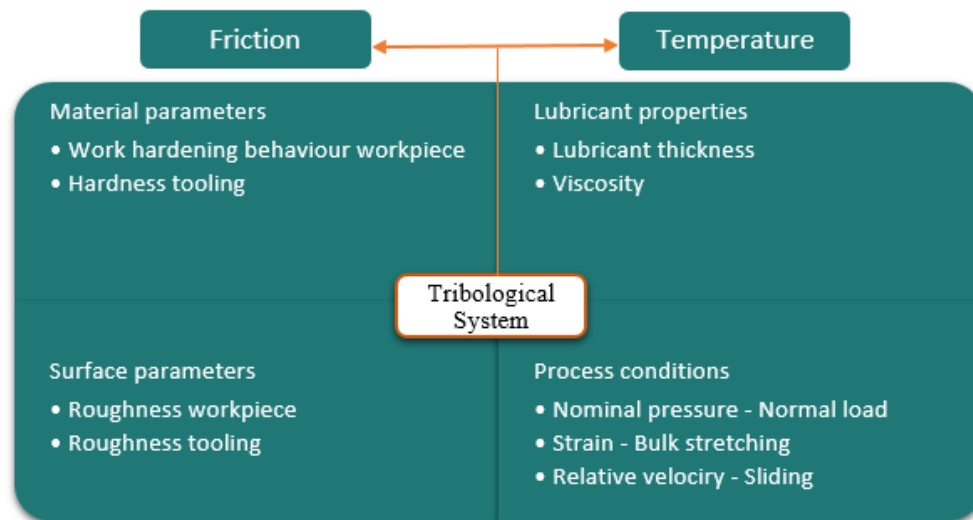


Figure 28 - A tribological system for temperature induced friction in sheet metal forming [6]

Each of the elements influences the behavior of friction during each of the metal forming steps in the deep draw process and account for the final quality of the output product. According to the suggested framework, the main aspects that influence the temperature induced frictional behavior in a deep draw process can be classified as [6] [12] [13]:

- ❖ Material parameters and its behavior during both steps of the deep draw process,
- ❖ Surface parameters of the tooling and the workpiece,
- ❖ Lubrication properties of the type used during the deep draw process,
- ❖ Process parameters and environmental conditions such as contact pressure, bulk straining and relative velocity.

Each of the elements, as identified in the framework, can be explained by mechanisms on a microscopic scale. In the end, the tribological framework will provide the four dimensional look-up table that is required during the FEM simulations in order to capture the micro-scale mechanisms that influence friction within the two-step deep draw process.

Temperature Relation

An additional effect on friction arising between the tool-blank interface is the raise in contact temperature during the two-step deep draw process. In this study, a distinction is made between the ambient temperature and the contact temperature. The ambient temperature is considered as a macroscopic parameter that is the total average of the local contact temperatures within the deep draw process.

The ambient temperature is measured and develops throughout the warm-up period of the deep draw process as seen in Figure 29 [80].

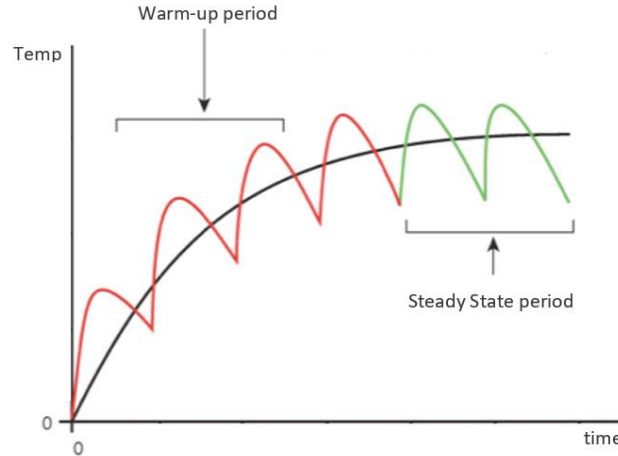


Figure 29 - Representation of standard temperature warm-up curve in a deep draw process [81]

The microscopic temperature is different throughout the process and also dependent on the contact of the tool-workpiece interface. The total average of each of the different microscopic temperature values give rise to the macroscopic temperature. Varying amounts of dissipated energy due to plastic deformation of the sheet material and different frictional contact between tool and the workpiece are the main causes of local temperature variations throughout the deep draw process. The energy dissipation in the plastic deformation and frictional contact converts into heat, significantly increasing the local contact temperature, as see in Figure 30 below [81] [82].

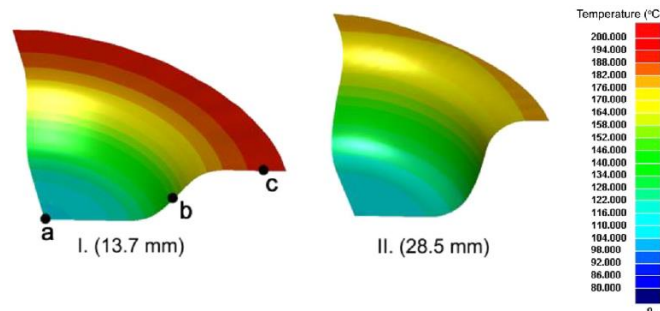


Figure 30 - Example of Temperature distribution at different deformation depths in within a deep drawing process [80]

To be able to sufficiently predict the impact of temperature on the interaction between the tool, lubricant and the workpiece within the FEM simulations, material properties, such as heat conductivity and local strain rates are accounted for in the model. All of the temperature dependencies that are included in the adapted model of J. Hol [6] will be outlined within the subsequent chapters regarding the elements described in the tribological framework of Figure 28.

The following paragraph will first provide a more in-depth overview of the microscopic mechanisms of friction and will continue to connect each of the elements mentioned above. This will ultimately lead to a four dimensional look-up table, which accurately describes the temperature-induced frictional behavior within a two-step deep draw process.

Coupling Macroscale and Microscale Material Behavior

The study of friction at contacting surfaces inherently involves the behavior of surface asperities at the micro to nanoscopic length scales. This is especially applicable for large-scale engineering applications with sliding surfaces where the real area of contact can be described by contacting asperity pairs that only take up a fraction of the apparent area of contact. Consequently, when focusing on the tool and workpiece interfaces during deep drawing, the study of a single asperity in contact can be identified as a fundamental part for describing the mechanical properties and tribological properties of surfaces. Advances within this field of science have led to the development of advanced technologies that enable a more thorough analysis of micro-tribology and nano-tribology. A general overview of the different aspects between conventional, macro-scaled, and smaller tribological scales is given in Figure 31 [83] [84].

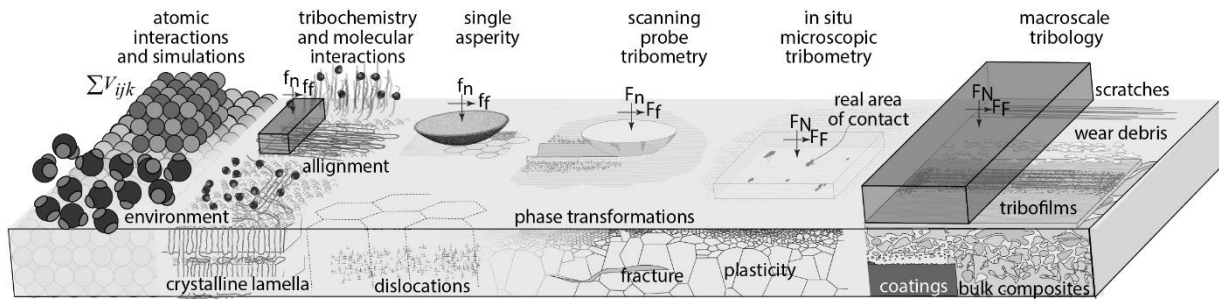


Figure 31 - A general overview of scale differences within the field of tribology [85]

Within the macroscopic scale, tribological tests are conducted with relatively large bodies of mass that are subjected under heavily loaded conditions. The relatively large normal forces and contact area inevitable leads to wear behavior, which is affected by the bulk properties of the mating components that dominate the tribological performance. Consequently, in macro-tribology, the geometrical surface contact between two bodies is approximated. Furthermore, the friction force only depends on the normal load, as given before with Coulomb's basic law of friction [4]:

$$F_f = \mu \cdot F_N \quad (8)$$

The friction force is also considered independent to the surface area in contact, as is stated by Amontons second law [55]. The macroscopic phenomena that relate to friction are elastic deformation, plastic deformation, wear mechanisms and fracture behavior. The theoretical friction

When applied to the microscale and lower, tribological tests are conducted on components with relative small masses, under mildly loaded conditions. The decrease in contact area and normal load results in a decrease of the real area of contact to only a few asperities. Surface properties, such as roughness, become more dominant within the material behavior of the contacting bodies. The microscopic mechanisms that are related to the generation of friction are (1) adhesion, (2) mechanical interaction of surface asperities such as welding, (3) plowing of harder material into softer material, (4) deformation and fracture of surface layers and (5) third body shearing causing local plastic deformation [86] [87] [88].

An overview of the mechanisms of welding (adhesion) ploughing and shearing is shown in Figure 32 below. Consequently, a dependency between friction and the real area of contact can be identified at the microscopic scale, which is based on asperity junctions that are formed due to a certain contact pressure and adhesion.

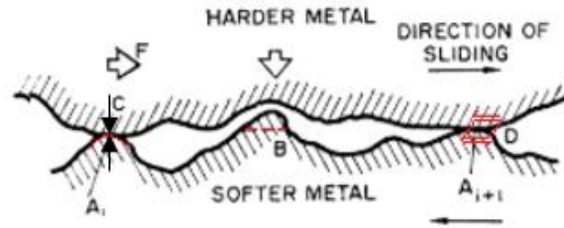


Figure 32 - Mechanisms of welding, ploughing and shearing [89]

The complexity of surface behavior on a micro scale generally leads to computation times that are too cumbersome to be useful in large-scale FE simulations. Moreover, the impact of extra micromechanical computations is generally too insignificant on macroscopic manufacturing processes. It is therefore that analysis and prediction concerning cold forming processes in general are predicted on the macro tribology, where the contact consists of millions of asperities, that the can be generalized as a single-asperity contact for simplicity [84] [83].

The main purpose of this section is to provide an overview of the micro-mechanical mechanisms that are determined to generate the coefficient of friction, which is used as a four dimensional look-up table within the FEM simulations.

First an introduction is given that couples the macro-scale frictional behavior to micro mechanisms that occur during the deep draw process. Following with a more in depth description that outlines the basic micro-mechanical friction mechanisms of adhesion, deformation and shearing.

Continuing with the proposed tribological framework, each of the elements will be discussed together with the relation to the frictional behavior of the specific two-step deep draw process. This paragraph will provide the important equations that are used in the FEM solver, which provides a physically based model that sufficiently captures the micromechanical behavior of friction for a tool-workpiece contact interface.

The equations are an adaptation on the work of J. Hol [6] that provides a middle way between the overgeneralized macroscopic and over complex microscopic simulations which enables it to be computationally attractive and still be applicable for large-scale computations [6] [90].

Microscopic Models of Friction

In the 18th century, Desaguliers [91] was the first to introduce the concept of cohesive, or now called adhesive, forces in relation to friction. The theory considers the adhesive forces, which interacts between two bodies in contact, as a universal phenomenon. It considers that friction can be largely attributed to the interaction between surface asperities that are into contact.

Tomlinson [92] expanded upon this theory in the beginning of the 20th century with the concept of molecular forces. Friction was explained as a basic property of materials, which existed through the working of fundamental bonding forces across the contact interface of the two bodies in contact.

The understanding of friction was accelerated during the mid-20th century, by the work of Bowden and Tabor [93], a firm foundation was made for the microscopic mechanisms that account for friction. Bowden and Tabor identified adhesion and deformation as the two main contributors to the energy dissipation of friction. Where adhesion occurs at the outermost contact layers, the effect of deformation is dominant in the subsurface material layers.

Applying a sliding velocity and adding an intermediate medium, such as a lubricant, between the tool-workpiece surfaces adds the shearing element of contacting asperities and lubricant layers. Assuming no interaction between the individual mechanisms, the micro-mechanical friction is written as [6]:

$$F_{friction} = F_{adhesion} + F_{deformation} + F_{shearing} \quad (9)$$

When dry materials slide against each other, a high friction coefficient of $\mu \geq 0.5$ typically can be observed. Such high values of friction will affect the performance of the process and affect the final quality of the product in metal forming practices. For the situations where high friction needs to be diminished as much as possible, lubricants will be implemented between two contacting bodies in order to dramatically reduce the friction force and wear to the surface [94]. The lubricant can be described as an intermediate medium of gas, liquid or solid between the interacting layers that contains beneficial material properties such as low shear strength. The impact of lubrication on friction in sheet metal forming is related by parameters such as [6] [95]:

- | | |
|-------------------------|-----------------------------|
| I. Material properties, | - Surface finish, |
| II. Temperature, | - Sliding velocity, |
| III. Contact pressure, | - Lubricant characteristics |

From these parameters, the impact of temperature on the lubricant will be further investigated and varied during the analysis of the temperature dependent deep draw process. In this section, the most significant liquid lubricant characteristics and lubricant regimes will be further explored [96].

Lubrication Properties

From a micromechanical perspective the tool-lubricant-workpiece contact regimes can also be identified and further outlined considering the interaction between asperities and molecular lubricant layers. The use of a lubricant in deep drawing reduces the coefficient of friction significantly and also impacts the wear of the tooling and the heat development during the process.

Each of the lubricant regimes that were identified in section - [Lubricant Properties](#), are dependent on the thickness of the lubricant in the micro-scale. The boundary, mixed and hydrodynamic lubrication regimes are based on the thickness of the lubricant layer - λ , which is defined as the ratio between the fluid thickness and the squared surface roughness [13]. An overview of the micro-scale behavior for each of the lubrication regimes is given in [Figure 33](#) below.

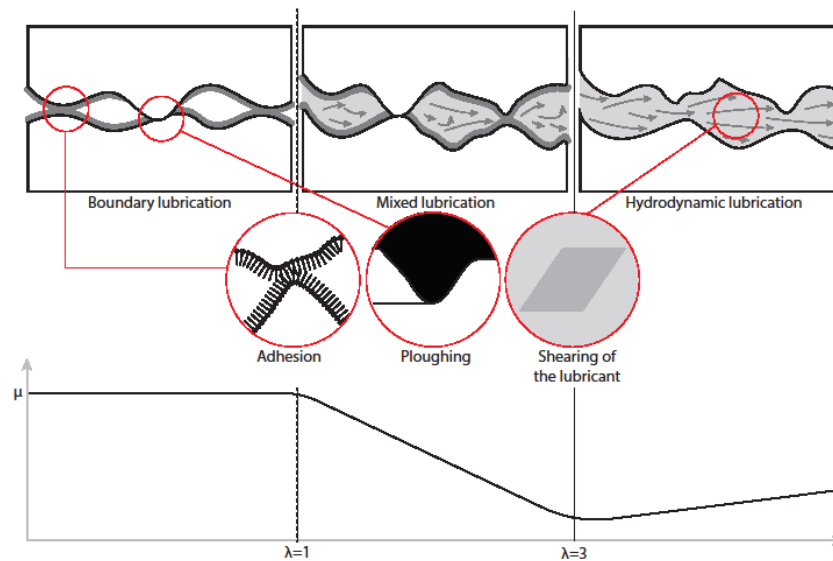


Figure 33 - Lubrication regimes and corresponding friction mechanisms compared with lubricant thickness [13]

Boundary lubrication $\lambda \leq 1$

The total nominal load is carried by the contacting asperities of the tool-workpiece surface interface with a lubricant layer in between, the boundary layer, which exhibits a thickness of a few molecules. Tangential movements of the surface interface causes deformation of the adhering asperities. Ploughing of harder asperities into the softer surface also occurs. The high pressure development at the contacting points of the surface interface cause defects in the boundary layer to occur. The boundary layer defects result in frictional behavior similar to dry friction, explaining the high coefficient of friction in this lubrication regime [11] [10] [13].

Mixed lubrication $1 < \lambda < 3$

Increasing the thickness of the lubrication layer causes for the surface interfaces to be separated further apart, decreasing the amount of contacting asperities. The total nominal load is now both carried by the lubricant as by the contacting asperities. The surfaces interfaces, or pockets, are now partially to fully filled with lubricant. This decreases the ploughing and adhesion effects in the contact interface and consequently, results in a lower coefficient of friction [11] [10] [13].

Hydrodynamic lubrication $\lambda \geq 3$

Within the Hydrodynamic lubrication regime, the nominal load is completely carried by the lubricant which fully separates the tool-workpiece contact surface. No ploughing or adhesive mechanisms occur in this regime. Tangential movements results only in shearing of the lubricant layers, where the resistant to the shearing is determined by the viscosity of the lubricant. Elastic deformation can occur at the local surfaces regions of the contact interfaces under high loads, this effect is identified as the elasto-hydrodynamic lubrication regime [11] [10] [13].

It is determined that in a situation of boundary and mixed lubrication regime micro-mechanical mechanisms concerning friction will be adhesion and ploughing. When lubricating further into the hydrodynamic contact regime, shearing forces are considered the dominant mechanism influencing the coefficient of friction. The microscopic mechanisms of adhesion, deformation, as well as shearing will now be explained consecutively [6].

Adhesion

Adhesion occurs when two surfaces are pressed together under a pure normal load or a combined load of normal and shear forces. As the two surfaces come into contact, local welding and will occur at the tips of the contacting asperities and interfacial bonds will form. This can already occur under a minimum amount of load and requires an increased amount of force to separate the surfaces again. At the contacting surfaces, the asperities with lower hardness will deform locally, as shown in Figure 34 [13] [45].

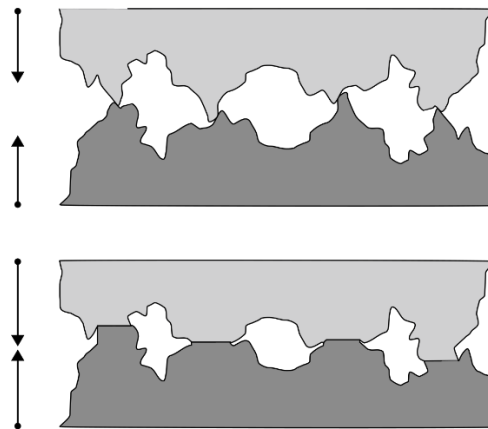


Figure 34 - Demonstration of local deformation at the asperities due to an applied load [97]

Plastic flow will occur and the asperity junctions will grow until the contact pressure can be supported by the asperities. With the assumption that plastic deformation occurs at all micro-contacts and that the stress equals to the penetration hardness, the real area contact can be determined, which primarily depend on the relation between the hardness of the softer material and the normal load applied, this relation is stated as [98] [45]:

$$A_r = \frac{F_{adhesion}}{H} \quad (10)$$

Where H is the hardness of the material, A_r the real area of contact and F_N the applied load. When tangential force on the surfaces in contact, shearing occurs at the welded junctions where the adhesive bonds must be broken [6] [45].

Overcoming the shearing strength of the bonds at the welded junctions give rise to the adhesion component of friction. Assuming that the total area of shear is given by A_r , and the relevant shear stress by τ , we can express the adhesion force as [6] [99]:

$$F_{adhesion} = A_r \cdot \tau \quad (11)$$

Where the relation between the adhesion component and coefficient of friction can be defined as [6] [99]:

$$\mu_{adhesion} = \frac{F_{adhesion}}{F_N} = \frac{A_r \cdot \tau}{A_r \cdot H} = \frac{\tau}{H} \quad (12)$$

Buckley [100] indicated the connection between the adhesion of two surfaces and the degree of matching between their crystal planes of the materials. Consequently, the highest matching values are found for contacting surfaces that consist of similar materials and the lowest values for materials with mismatching plane orientation and a high degree of insolubility towards each other [6] [99].

Other factors that influence the adhesion strength are surface interactions at the interfaces such as contaminants, fluid films and oxidation layers. These contaminations can strongly affect the impact of the adhesion component on the friction. This is also one of the main reason that lubricants are frequently applied between surfaces in order to reduce friction in cold forming processes by evolving the higher shear resistance of a solid-solid contact into a much lower shear resistance of a solid-fluid film [6] [99] [101].

For solid-solid contact that exhibits isotropic plastic flow behavior, the shear strength of approximately 1/3 of its tensile strength can be identified, where the tensile strength in turn is approximately 1/3 of the penetration hardness. Consequently, for many non-lubricated metal pairings, the coefficient of friction will give a value in the order of $\mu = 0.16-0.2$ based on a specific tool-workpiece combination [6] [102]. A more detailed overview of the general adhesion formulas is provided in [Appendix 2 – Adhesion Formula's](#).

Deformation

When a tangential movement is applied on two contacting surfaces, asperities will collide and a contact with each other, resulting in both elastic and plastic deformation. During this interaction, the relatively harder asperities will plow into the softer material, forming grooves onto the surface. The deformation initiated due to sliding or ploughing gives rise to the deformation component in the micromechanical friction [93] [98]:

$$F_{deformation} = F_{ploughing} \quad (13)$$

The ploughing effect of asperity-surface contact only occurs at discrete points at the surface interface, as can be seen in [Figure 35](#). The incoming contact angle of the harder asperities into the softer surface together with the geometrical shape of the asperities itself influence the resulting friction force [39] [103].

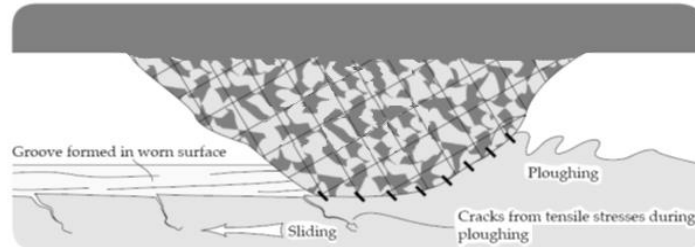


Figure 35 - The mechanism of groove formation on worn surfaces due to ploughing of asperities [104]

In order to define the component of ploughing, different geometrical model for asperities can be used. The three basic geometries generally used within micromechanical models are spherical, cylindrical and conical asperities. For each of these different geometric shapes, an expression for the coefficient of friction due to ploughing is derived.

Asperity shape

In this section, the pile-up of material during ploughing will be neglected since it has been concluded to be very difficult to assess this effect quantitatively. For each of the shapes the isotropic behavior is assumed for a situation where the asperity is grooving a path through a softer surface material with p^* defined as the local yield pressure. The real area of contact needs to be determined again, this relation is stated as [28]:

$$A_r = \frac{F_{ploughing}}{H} \quad (14)$$

We can define for the local normal load, with a load support area - A_1 , and the friction force, with the ploughing contact are - A_2 , the following relations [89]:

$$F_{normal} = p^* \cdot A_1 \quad \text{and} \quad F_{normal} = p^* \cdot A_2 \quad (15)$$

For each geometry, the sliding asperity in contact with a softer surface, the load-support and grooving areas are shown in the figure below. Consequently, an overview of the matching equations for the load support area, the ploughing contact area and the friction coefficient is shown in [Appendix 3 – Deformation Formula's](#).

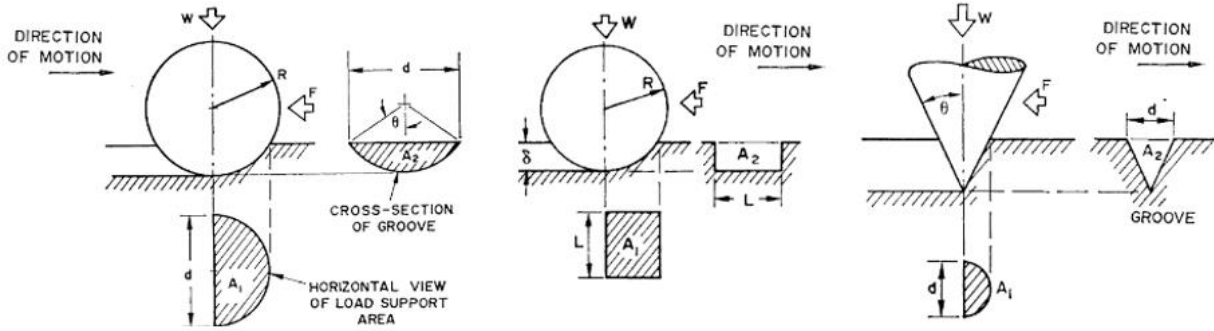


Figure 36 - Sliding of metal asperity on softer surface material, the geometrical properties given for a (1) spherical approximation, (2) cylindrical approximation and (3) conical approximation [89]

Shearing

For a lubricated conformal contact situation, as given in [Figure 37](#) where both surfaces are fully separated by a lubricant film, the general expression of the friction force can be expressed by [105]:

$$F = \tau \cdot A \quad (16)$$

Where F is the force applied on the contact surface, τ is the shear stress within the lubricant, and A is the apparent cross-sectional contact area between the lubricant and the surface. The friction force will apply on both sides of the lubricant-surface contact.

The amount of shear stress is determined by behavioral properties of the applied lubricant and the velocity and distance of the surfaces [43].

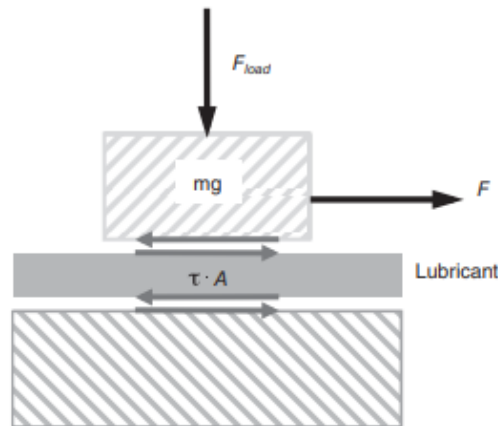


Figure 37 - Representation of shear forces between solid bodies and fluid in a lubricated contact [106]

Lubricant velocity profile

Typical velocity profiles for fully developed laminar and turbulent flows are given in Figure 38. It can be observed that the velocity profile shows a parabolic shape in the laminar fluid flow regime, for the turbulent flow regime a slightly broader parabolic profile is shown with a steep drop near the surfaces. The turbulent flow towards the wall can be considered to transfer into four different regions, based on the relative distance towards the surface. The thin fluid region close to the surface where viscous effects are dominant can be described the viscous (or laminar or linear or wall) sublayer. Here the velocity profile is approximating linear behavior, and the flow layers in this region are streamlined. The thickness of the viscous sublayer in the turbulent flow regime is very small compared to the other regions, however it plays a dominant role on the flow characteristics because of the large velocity gradients it involves [107] [108] [109].

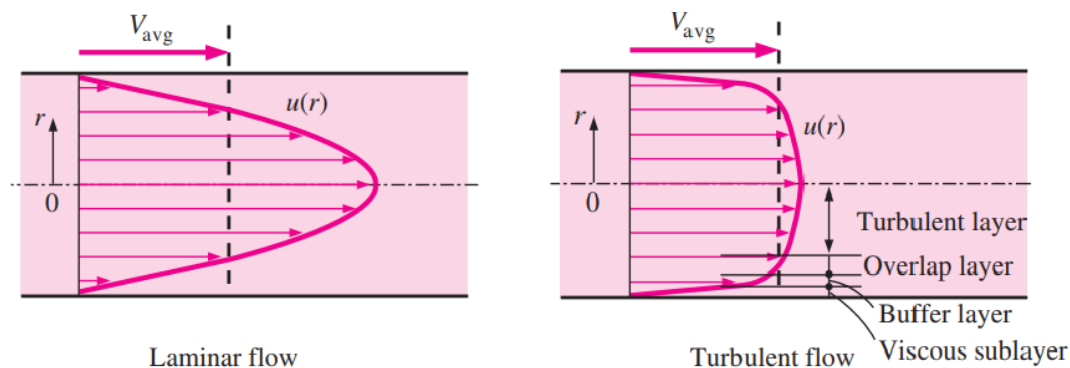


Figure 38 - The velocity profile differences for both a laminar and turbulent flow in a fluid interface [107]

The velocity profile of a fluid in a fluid interface changes from zero at the surface interface to its maximum value at the highest velocity point, which is defined Figure 38 in the center. The zero velocity between the solid surface and the adjacent fluid layers is defined as the no-slip condition which is explained by the viscous fluid properties over a solid surface. This viscous behavior of the fluid at the fluid-solid interface is not same as the wetting of surfaces by the fluids. The main difference is that the wetting property results from surface tension [117] [111].

Viscosity

Newton was the first to describe the behavior of Newtonian fluids in beginning of the 18th century, its classification is based on the behavior of the fluid describing the relation between the shearing stress and shearing strain rate. A general classification of fluid flow behavior is shown in Figure 39 and Figure 40, most of the lubricant oils that are used can be classified as Newtonian fluids [111] [112]

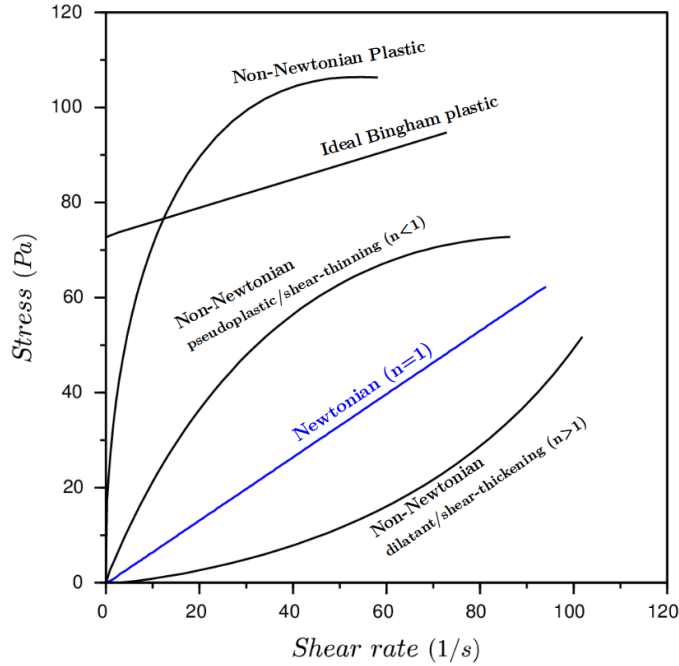


Figure 39 - Shear stress and deformation rate relationship of different fluids [111]

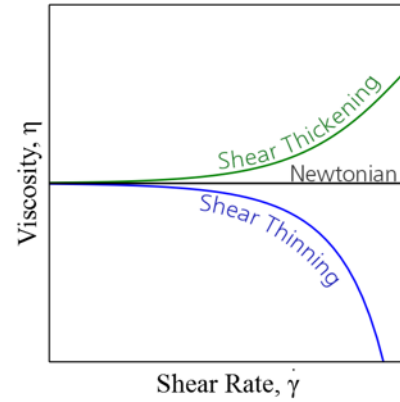


Figure 40 - The viscosity of Newtonian, Shear Thinning and Shear Thickening fluids as a function of shear rate [111]

A Newtonian fluid can be described as a “true liquid” since a linear increase in stress with increasing shear rates can be observed. The constant slope value indicates the viscosity of Newtonian fluids which can be defined as the internal resistance to relative shear motion or the internal friction of a fluid, this relationship is described as Newton's Law of Viscosity [113] [121]:

$$F = \eta \cdot A \cdot \frac{u}{y} \quad (17)$$

This relation holds for laminar flows where the shear stress τ in [Pa], as discussed in section X, can be described with the relation [106] [115]:

$$\tau = \frac{F}{A} \quad (18)$$

The rate of shear deformation $\frac{u}{y}$ or shear velocity, can be expressed by the derivative of the fluid velocity component in the direction perpendicular to the plate and is denoted by $\dot{\gamma}$ in [s^{-1}] [106] [115]:

$$\frac{\partial u}{\partial y} = \frac{\partial}{\partial y} \left(\frac{\partial x}{\partial t} \right) = \frac{\partial}{\partial t} \left(\frac{\partial x}{\partial y} \right) = \frac{\partial y}{\partial t} = \dot{\gamma} \quad (19)$$

This leads to an expression of η , the viscosity of the fluid in $[Pa \cdot s]$ or $[poise]$ which can be described by the shear stress τ in $[Pa]$ of the fluid and the shear rate $\dot{\gamma}$ in of the fluid in $[s^{-1}]$ [105] [116].

$$\eta = \frac{\tau}{\dot{\gamma}} \quad (20)$$

Translating the viscosity properties for a deep draw process where, considering the tool-workpiece interface where two surfaces are fully separated by a lubricant film. When tangential displacement is applied, which can be identified as the drawing of the punch, shearing occurs within the lubricant film layers in a similar fashion as mentioned above. The lubricant, when assuming Newtonian fluid properties, exhibits shear stress behavior that can be identified as [116] [117]:

$$\tau = \eta \cdot \dot{\gamma} \quad (21)$$

Implementing the normal pressure - p_{norm} , within the shearing formula results in a definition for the coefficient of friction and lubricant velocity for full fluid lubrication [105] [116]:

$$\mu_{shearing} = \frac{\tau}{p_{norm}} = \frac{\eta \cdot \dot{\gamma}}{p_{norm}} \quad (22)$$

Now a relation between the coefficient of friction and the viscous forces is determined, the temperature dependency needs to be implemented. Section X will describe the applied temperature dependent viscosity model in the two-step deep draw process that is analyzed [43] [117].

I - Surface Properties

The surfaces of the interacting tooling and workpiece all consist of complex structures that can exhibit different properties depending on the type of material, method of surface roughness and the type of interaction between the surface and the environment. Surface properties of materials such as roughness, influence the real area of contact, friction, the amount of wear and lubrication interaction [45] [76].

Solid surfaces, irrespective of the type of material, contain irregularities or deviations on the surface interface which prescribe the macroscopic geometrical shape of the material. Surface deviations can range from small repeating patterns to large variations with gaps and peaks. The measurement of the topography of the surface characteristics is known as metrology and is used to determine the suitability of a material regarding the specific application for which it is needed. Surface measurement is a collective term, which encompasses multiple elements [45]:

- Surface finish,
- Surface geometry or shape,
- Surface roughness profile (Ra), or in
- Surface roughness area (Sa), and
- Surface texture,

The ability to obtain the required surface roughness necessary for metal forming processes is critical for maintaining the quality of the output products. The roughness patterns are repetitive or random deviations, which can observe fractal formations that are self-similar across different scales. The most important aspects of a three-dimensional surface are the surface waviness on the macro-scale, roughness on the micro-scale, the general direction of the surface topography or lay and the flaws that are present. A general overview of the surface aspects are shown in Figure 41 [45] [118]. Surface topography can exhibit gross deviations, ranging from a nominal shape to very long surface wavelengths. Large deviations in the topography are not included within the surface texture. Different surface topology methods are used that enable a general characterization of the total surface as given in Figure 43 [45].

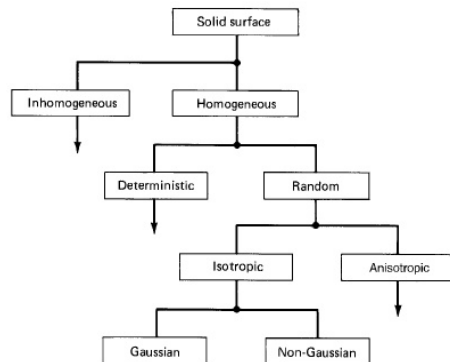


Figure 42 - Overview of general surface topology methods [45]

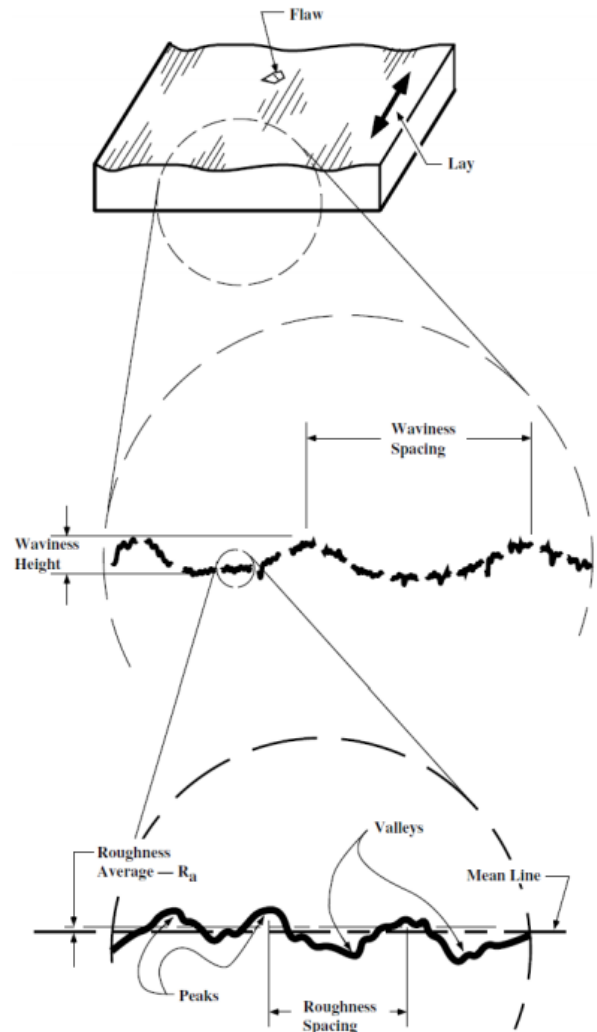


Figure 41 - Overview of surface texture elements [45]

Triboform performed confocal measurements for the surface roughness of the tooling and the workpiece as input for the four dimensional friction table in the micro-scale. A confocal sensor is used for obtaining precise thickness measurements is used for determining the gradual change of the surface topology under deformation. Where deformation of the surface topology influences the behavior of the asperities, contact patches and surface-lubricant interface and consequently affecting the coefficient friction [76] [119].

Three different sets of confocal data are presented for the tribological system of the two-step deep draw process [76]:

Sheet material	AISI420 (Euronorm: X20Cr13)
Lubricant type	Castrol Iloform FST 16
Tooling type	Ceratizid CF-S18Z

The results of the confocal data is given in [Figure 43](#) up to [Figure 46](#) below [76].

Confocal data AISI420 sheet material

For the unprocessed workpiece material surface that is used within the two-step deep draw process, it can be seen in [Figure 43](#) that the surface topology shows general grooving in the orientation of the sliding direction. A surface area - SA roughness value of $0.35 \mu\text{m}$ is measured [76].

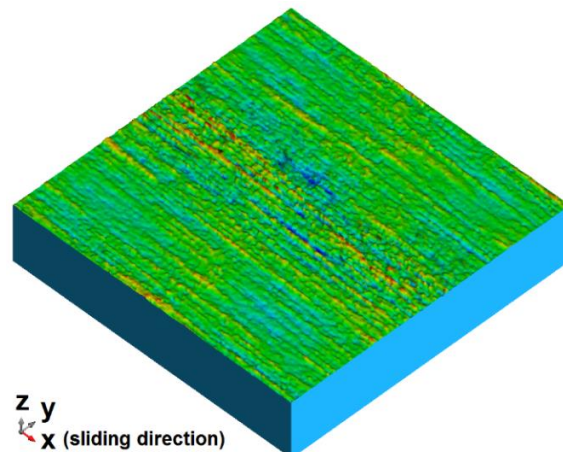


Figure 43 - Surface topography of the virgin AISI420 sheet material [76]

The unprocessed workpiece material in combination with the Castrol lubricant is mapped in [Figure 44](#), showing similar patterns as without the lubricant only less apparent. The surface is lubricated with 0.6 g/m^2 Castrol Iloform FST 16 [76].

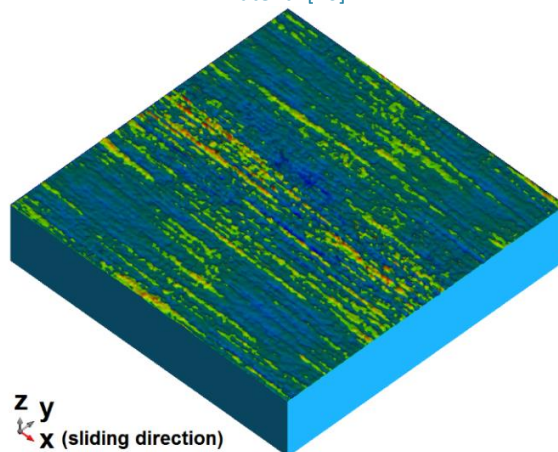


Figure 44 - Surface topography of the lubricated virgin AISI420 sheet material [76]

Confocal data Ceratizid tool material

The Ceratizid material surface is mapped in Figure 45, where it does not show a directional dependency but it does show a lower roughness value compared to the AISI420 sheet material. A surface area - SA roughness value of $0.12\text{ }\mu\text{m}$ is measured [76].

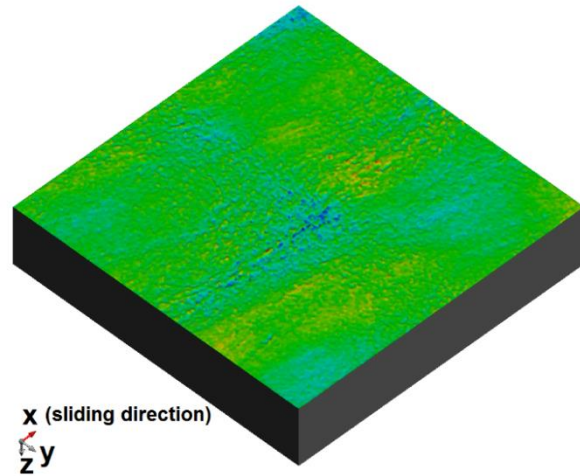


Figure 45 - Surface topography of the Ceratizid CF-S18Z tool material [76]

Confocal data PCL tool material

The Philips consumer lifestyle - PCL tool material surface is mapped in Figure 46, showing a mixed directional dependency and a low roughness value compared to the both the AISI420 sheet and the Ceratizid tool material. A surface area - SA roughness value of $0.025\text{ }\mu\text{m}$ is measured [76].

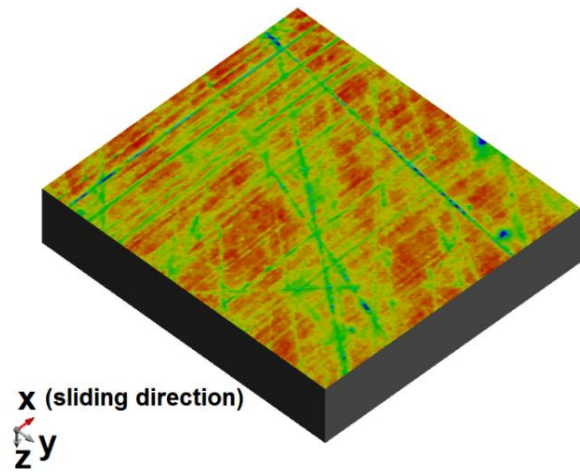


Figure 46 - Surface topography of the PCL Ceratizid CF-S18Z tool material [76]

II - Material Properties

The temperature dependent material properties from the workpiece are required input for the FEM calculations in order to correctly simulate the material flow during deep drawing. Within the two-step deep draw process, the mechanical behavior of the AISI 420 sheet metal material is captured by performing hot tensile tests under varying temperatures, strain rates and orientations. From these material tests, the basic material properties are briefly outlined below, followed by the calibrated models used in the FEM simulation [12].

Elastic Properties

For the elastic properties of the workpiece material, the stress-strain relationship is constructed by Hooke's law [12] [120]:

$$\sigma = E \cdot \varepsilon \quad (23)$$

Where σ represents the stress, ε represents the strain and the slope of the curve identifies the Young's modulus.

During the drawing process, workpiece material also is subjected to compressive and tensile forces which result in shrinking, compression and bulging effects. The material behavior can be different for axial and lateral directions which is captured by the Poisson's ratio in the FEM simulations [12] [121]:

$$\nu = \frac{\varepsilon_{Lateral}}{\varepsilon_{Axial}} \quad (24)$$

Plastic Properties

For the plastic properties of the workpiece material, the yield surface is described in a three dimensional principal stress space which can be described for any material with the matrix illustrated in Figure 47 below [12] [122].

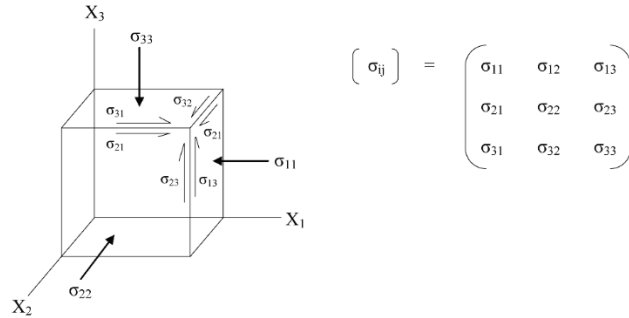


Figure 47 - The general stress tensor [123]

Based on the stress matrix, the equivalent stress is calculated with the Hill'48 anisotropic yield criterion [124]. The anisotropic behavior of the workpiece material is implemented for three orthogonal symmetry planes. The Hill'48 anisotropic yield criterion is expressed by the following equation [124]:

$$2f(\sigma_{ij}) \equiv F(\sigma_{22} - \sigma_{33})^2 + G(\sigma_{33} - \sigma_{11})^2 + H(\sigma_{11} - \sigma_{22})^2 + 2L\sigma_{23}^2 + M\sigma_{31}^2 + 2N\sigma_{12}^2 = 1 \quad (25)$$

Where f is the yield function of the parameters: F , G , H , L , M and N , which relate to a specific anisotropic state of the material.

The parameter provide the anisotropic yield functions [124]:

$$R_0 = \frac{H}{G} \quad R_{90} = \frac{H}{F} \quad R_{45} = \frac{N}{F+G} - \frac{1}{2} \quad (26)$$

Which leads to definition of the Lankford coefficient of normal plastic anisotropic behavior [125]:

$$R = \frac{1}{4} (R_0 + 2R_{45} + R_{90}) \quad (27)$$

For the workpiece material, an anisotropic R-value of 1.4 is used, representing the strains ratio in a sheet metal plane and along the thickness orientation. An R-value of 1.4 shows that no thinning of the workpiece will occur during the deep draw process.

Also the tensile strength and strain hardening properties of the workpiece material is determined to ensure that no fracturing occurs during the deep draw process. The tensile strength is determined as the maximum stress-strain value that the material can attain within the plastic regime before necking and breakdown occurs. The work hardening behavior of material increases the load-carrying capacity of the work piece material with increasing deformation [12].

Thermal Dependency

Both the elastic and plastic properties are combined with thermal expansion properties to account for the varying temperatures during the warm-up period of the two-step deep draw process.

The mechanical behavior of the AISI 420 sheet metal material under different temperatures, strain rates and orientations are shown in [Appendix 4 – Material Behavior AISI 420](#). The results are used for the calibration of the equations that are describing the material behavior during the warm-up period, the calibrated material behavior is used to describe the micro-mechanical behavior in the FEM simulations.

Calibrated Material Behavior

The models that describe the total flow stress behavior as a function of increasing plastic strain, consist of a dynamic part, and a static part. The dynamic part describes the effect of the strain rate on the flow stress behavior where the static part takes the strain itself into account. The base form of these two relations is generally represented within the Swift - Nadai hardening law [12] [126] [127]:

$$\sigma = C \cdot (\varepsilon_p)^n \cdot (\dot{\varepsilon}_p)^m \quad (28)$$

With the flow stress σ related to the strain - ε_p with a strain hardening exponent - n, the strain rate - $\dot{\varepsilon}_p$ with a strain rate dependency m and a hardening coefficient - C.

Here the dynamic part of the hardening law or the strain rate dependency is based on the activation energy needed for dislocation movements to occur. In turn, the static part of the hardening law is also related to dislocations. A dislocation cell structure develops under the surface when deformation takes place. During deformation the dislocations collide into each other with impedes further movement.

Bergström [7] developed a physical based model to describe the interaction processes between dislocations within the bulk material structure of the workpiece. The model of Bergström was later expanded by van Liempt, which added the effect of plastic strain on the change in dislocation structure. This resulted in the Bergström van Liempt model [128]:

$$\sigma_y(\bar{\varepsilon}) = \sigma_{y0} + \Delta\sigma_m \cdot \left[\beta \cdot (\bar{\varepsilon} + \varepsilon_0) + \{1 - e^{-\Omega \cdot (\bar{\varepsilon} + \varepsilon_0)}\}^{n'} \right] \quad (29)$$

Within the flow stress model, three different elements can be identified:

- First term - σ_0 denotes the basic strength of the material before any dislocations movement
- Second term - Static part which describes the strain hardening behavior
- Third term - Dynamic part which describes the strain rate dependency

Vegter [129] [130] [131] further modified the Bergström van Liempt model specifically for flow stresses occurring at high strains during sheet metal forming processes. The isotropic hardening relation is based on the theory of dislocation multiplications, which describes the resistance behavior of dislocations against movement of dislocations. The modified material behavior model introduces a Hill yield criterion and a more advanced hardening rule, which is based on a multi-axis stress state [130].

Consequently, a new formulation of the flow stress as a function of the strain and strain rate is obtained:

$$\sigma_y(\bar{\varepsilon}) = \sigma_0 + \Delta\sigma_m \cdot \left[\beta \cdot (\bar{\varepsilon} + \varepsilon_0) + \{1 - e^{-\Omega \cdot (\bar{\varepsilon} + \varepsilon_0)}\}^{n'} \right] + \sigma_0^* \cdot \left[1 + \frac{kT}{\Delta G_0} \cdot \ln \left(\frac{\dot{\bar{\varepsilon}}}{\dot{\bar{\varepsilon}}_0} \right) \right]^{m'} \quad (30)$$

In the modified Bergström van Liempt model, the dynamic strain rate dependency is combined together with the Krabiell and Dahl [132] temperature induced dislocation activity. The nomenclature of the hardening parameters in the modified Bergström van Liempt model is given in [Table 2](#) below [12].

Table 2 - Nomenclature of Bergström-van Liempt model [6]

σ_0	Static yield stress of dislocation free material
$\Delta\sigma_m$	Stress increment parameter
β	Linear hardening parameter
ε_0	Initial strain
$\bar{\varepsilon}$	Equivalent strain
Ω	Remobilization parameter
n'	Strain hardening exponent
σ_0^*	Maximum dynamic stress
k	Boltzmann's constant
T	Temperature
ΔG_0	Activation energy
$\dot{\bar{\varepsilon}}$	Equivalent strain rate
$\dot{\bar{\varepsilon}}_0$	Initial strain rate
m'	Dynamic stress exponent

The combined effects of elastic, plastic and thermal properties is provided in the calibrated Bergström-van Liempt results that are given in [Figure 48](#).

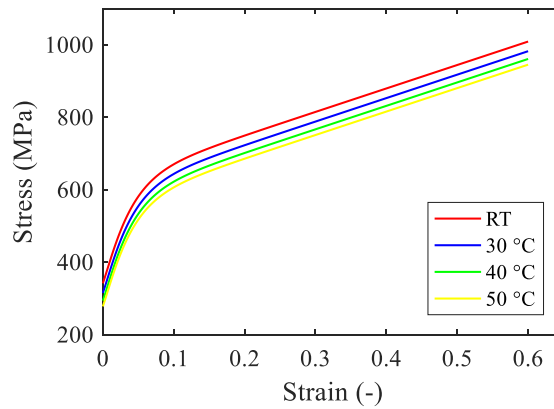


Figure 48 - Calibrated Bergström-van Liempt model for flow stresses at new temperatures and larger strains [12]

The calibrated Bergström-van Liempt model will be implemented within the micro-mechanical friction model that explains the asperity behavior under deformation of the workpiece surface. Also the FEM simulation will implement the workpiece behavior of the AISI 420 material under deformation at the component-level.

III - Boundary Lubrication Friction Modeling

By translating the discussed theory concerning rheological and viscous properties of the lubricant for a tooling-lubricant-workpiece interface. The micro-scale mechanics, which are implemented within the friction table of the FEM simulations, can be described with the addition of the temperature dependency.

The lubrication behavior is based on the different regimes described in section - [Lubricant Properties](#), which can occur during the deep draw process. Within the FEM solver, a distinction can be made between the temperature dependent behavior of the boundary layer shear strength and the shearing of the lubricant layers.

Boundary Layer Shearing

For a lubricated surface in the boundary and mixed lubrication regime, the shearing occurs between the formed boundary lubrication layers of only a few molecules thick. The layers of lubrication molecules are lifted and driven over each other and weak attractive forces work between the shearing layers. The strength of the attractive forces between the boundary layers of the tooling-lubrication-workpiece interface is identified as the boundary layer shear strength.

The temperature dependent boundary layer shear strength calculations, used for obtaining the frictional table in the FEM solver, are approximate with the relation [12] [13] [76]:

$$BLS\ factor = \frac{\tau}{k} \quad (31)$$

Where k is the shear strength of the softest surface material in the tool-lubricant-workpiece interface. The experimental BLS-data is generated by Falex for different metal-lubricant combinations.

Both test are applied for different workpiece-lubricant interfaces (9DX+PL61, DX+PL61SE, AISI420+Castrol) and temperatures of 293K, 313K, 333K and 353K at a speed of 1 mm/s. The tribology system of interest that is evaluated is given in [Table 3](#) below:

[Table 3 - Tribological system of interest for the BLS experiments \[76\]](#)

Sheet material	AISI420 (Euronorm: X20Cr13)
Lubricant type	Castrol Iloform FST 16
Tooling type	Ceratizid CF-S18Z

The results are acquired by performing temperature dependent [76]:

Shear strength test,
Cylinder-on-flat contact test
Ball-on-flat contact test

The outcomes of the calibrations for different lubricants are given in [Appendix 5 – Boundary Shear Tests](#). For the shear strength test, the approximation of the temperature dependent BLS factor is provided below. The lubricant of interest is Castrol Iloform FST 16, which is further examined in the follow-up with Cylinder-on-flat and Ball-on-flat contact experiments. The calibration of the relationship between temperature and the BLS factor relationship, for the Castrol Iloform FST 16 lubricant, is given in [Figure 49](#) [76].

Falex stated that only the measurement point of 20°C was properly determined and that the other points were constructed using a reverse engineering approach [76].

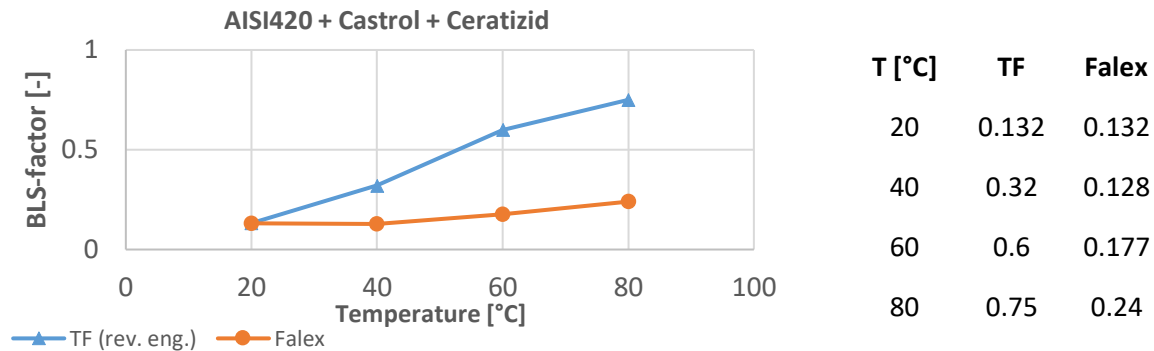


Figure 49 - Determined relation between the BLS and the temperature for Castrol Iloform FST 16 [76]

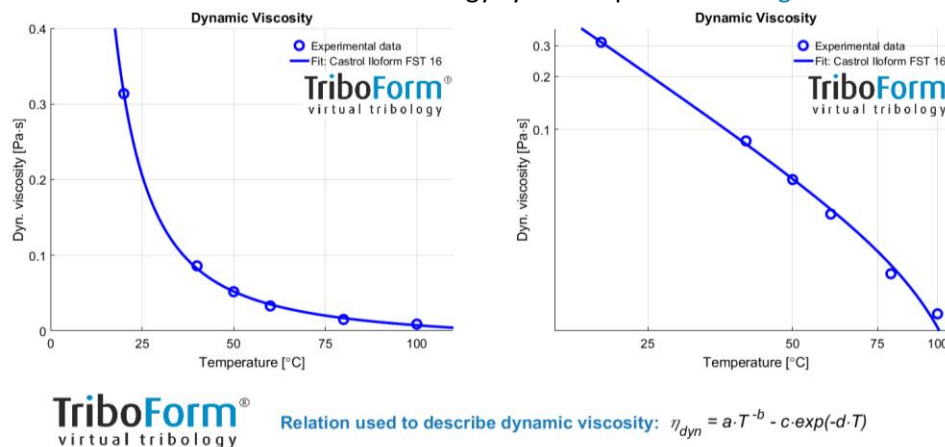
Full Lubrication Shearing

The lubrication behavior for mixed into full Hydrodynamic lubrication results into shearing mechanics that are similar to the shearing of the boundary layers. Within the Hydrodynamic lubrication regime a relative thick lubricant layer is present between the tool-lubricant-workpiece interface, which results in the shearing of individual layers within the bulk of the lubricant. The shearing of these individual lubricant layers rely on the viscosity properties of the lubricant.

Within the dynamic viscosity calculations for the frictional table in the FEM solver, the temperature dependent dynamic viscosity of the lubricant is represented by an exponential relation [13] [76]:

$$\eta_{dyn} = a \cdot T^{-b} - c \cdot e^{-d \cdot T} \quad (32)$$

The outcomes of the fully lubricated viscosity tests are given in [Appendix 6 – Temperature Dependent Dynamic Viscosity Tests](#). The calibration of the temperature dependent dynamic viscosity for the Castrol Iloform FST 16 lubricant in the established tribology system is provided in [Figure 50](#) below.



Lubricant	Cof a	Cof b	Cof c	Cof d	Density (kg/m ³)
Castrol Iloform FST 16	84.3677	1.862	0.0038724	-0.0078646	941000

Figure 50 - Temperature dependent dynamic viscosity of Castrol Iloform FST 16 lubricant [76]

IV - Process Parameters

As established within the tribological framework of friction in section - [Tribological Framework](#), another important factor influencing friction within cold forming processes is the micro-mechanical behavior of surface material in contact. The micro-mechanical behavior at the surface interface between tool and workpiece affects the flow behavior of the material, surface quality of the end product and the tool life expectancy. This specific behavior within the FEM solver is captured by the model of J. Hol [6], which defined and combined three main mechanisms on the micro scale responsible for causing surface changes of the processed material.

At the contact interface of the workpiece, surface flattening and roughening behavior contribute to the change of the real contact area. The flattening behavior primarily occurs due to normal loading, sliding and bulk deformation in cold forming processes thereby increasing the real area of contact. Consequently, the real contact area plays an important role in the characterization of friction [6].

The distribution of the contact patches is determined and expanded upon the work of Greenwood and Williams [133], which provided an initial stochastic approach to describe the surfaces roughness. Within the FEM solver, assumptions are made with respect to 3D rough surfaces in order to obtain a reasonable tradeoff between accuracy and computation time [6].

The model of J. Hol [6] embodies existing, adapted and newly developed models into a framework that provides a three stage solving methodology in order to determine the shear stresses and corresponding surface friction for tool-workpiece contact. An overview of the stages within the framework is given in [Figure 51](#) below [6].

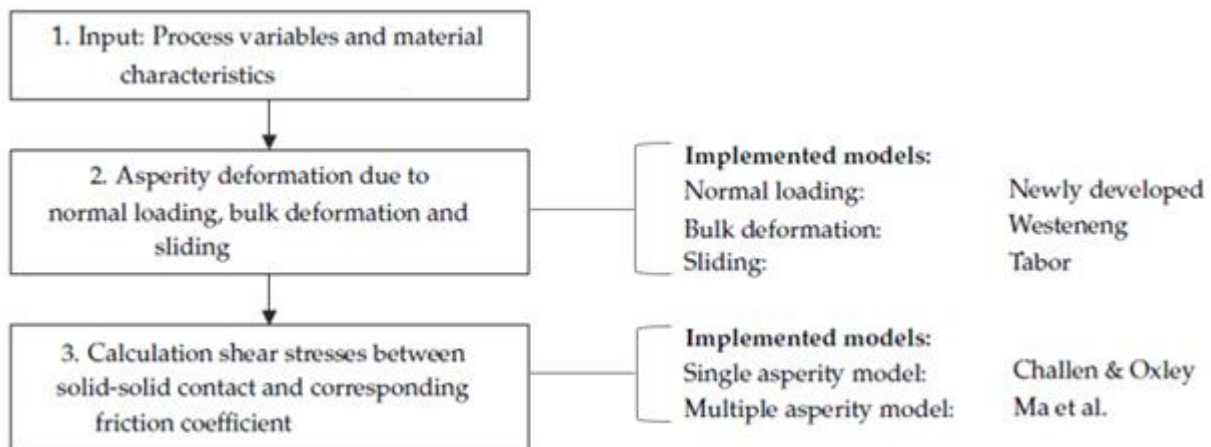


Figure 51 - Solving methodology concerning the friction look-up table [6]

In the first stage, the required process variables and material characteristics of both the tool and workpiece surface are implemented. The second stage, consist of the three mechanisms that accurately describe the behavior of asperities at the contacting surface. In this stage a, distinction is made between three different causes of deformation with their corresponding theory model:

- | | |
|---|-------------------------------|
| 1. Asperity deformation due to normal loading | – Introduced by J. Hol [6], |
| 2. Asperity deformation due to sliding | – Proposed by Tabor [134] and |
| 3. Asperity deformation due to bulk deformation | – Proposed by Westeneng [21] |

The three models together comprehend the predicted surface changes during the cold forming process and provide an expression for the fractional real area of contact. In the final stage, the shear stresses with corresponding friction coefficients are calculated. The following two models provide the coupling between the asperity deformation and shear stresses:

- I. Single asperity model – Proposed by Challen and Oxley [135],
- II. Multiple asperity model – Proposed by Ma et al [136].

The single asperity contact model of Challen and Oxley [135] [137] is implemented to predict the friction forces on individual contact points. An expansion is made upon the single asperity model by Ma et al. [136], which adds the implementation of surface contact patches and allows for the summation of all individual contact contributions to the friction coefficient.

Each of the aforementioned models will now be discussed in the following sections for the second and final stage of the solving methodology.

Flattening due to Normal Loading - J. Hol Model

In this section, a contact model is provided by J. Hol [6] which describes the flattening due to normal loading. It is proposed as an extension on the contact model of Westenberg [21] which takes the effect of work hardening into account within the deformation of asperities.

The model of Westenberg builds upon the elastic contact model introduced by Greenwood and Williams [133] which calculates the amount of asperity deformation based upon the asperity density, mean asperity radius and the *summit height* distribution. The *summit height* is based upon the peak height of an asperity, resulting in a height distribution where its accuracy is bounded by the resolution quality of the scanning method used to scan the surface. Both models describing the different approaches for the height distributions are shown in Figure 52 below.

The model of Westenberg replaces the *summit height* distribution by a *surface height* distribution, which is based on measured surface points, to predict the size of the real contact roughness. It describes plastic contact behavior that accounts for work hardening effects and shear stresses between crushing and raising asperity behavior. This results in different surface behavior, in contrast to traditional contact models, which shows a disproportional increase in surface area in relation to the nominal pressure. The flattening behavior as modelled by J. Hol [6] assumes a perfectly flat tool in contact with a rough workpiece surface that is described by the model of Westenberg [21].

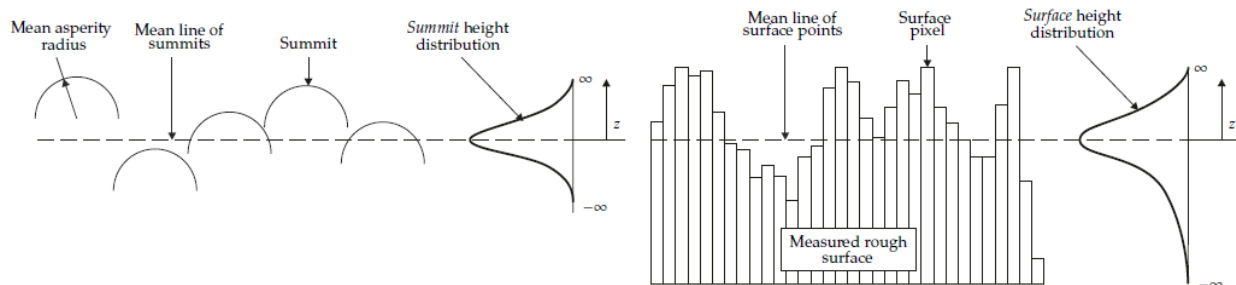


Figure 52 - Schematic view of the summit height distribution by Greenwood and Williamson [133] (left) and the surface height distribution by Westenberg [21] (right)

$$H = B \cdot \sigma_y \quad (33)$$

$$\sigma_y(\bar{\varepsilon}) = \sigma_0 + \Delta\sigma_m \cdot \left[\beta \cdot (\bar{\varepsilon} + \varepsilon_0) + \{1 - e^{-\Omega \cdot (\bar{\varepsilon} + \varepsilon_0)}\}^{n'} \right] + \sigma_0^* \cdot \left[1 + \frac{kT}{\Delta G_0} \cdot \ln \left(\frac{\dot{\bar{\varepsilon}}}{\dot{\varepsilon}_0} \right) \right]^{m'} \quad (34)$$

The reference height - λ is assumed to be constant for each asperity and depends on the surface roughness of the workpiece. Based on this constant, the total plastic strain can be calculated with the equation below [6] given below for each of the bars identified over the workpiece surface. A distinction in local strain is made for each bar, which is determined by a contact or no contact situation between the bar and the work tool.

With the given formulas, the behavior of each asperity can be determined and converted to the macroscale, resulting in the nominal pressure - p_{nom} by balancing the total internal with the total external energy applied within the tool-workpiece contact situation. This contact situation, based on the surface height distribution is introduced by J. Hol [6] and shown in [Figure 53](#) below.



J. Hol [6] describes three possible situations during tool-workpiece contact, which can occur for the bars in the boundary lubricated normal loading model:

I. Bars which are in contact with the tooling [6]

The surface bars in contact with the tooling are flattened down to the reference height; the crushing height is given by variable - Δz_i .

II. Bars which are initially not in contact with the tooling but will eventually come into contact [6]

Bars, which are initially not in contact, are lifted due to internal material flows initiated by the flattening of larger contacting asperity bars. The flattened material flows in a disproportional manner to neighboring asperities, raising the bars up which is denoted by the variable - Δu_j up to a maximum raising height - Δu_l . If the raised bars encounter the tool surface, and no equilibrium situation is reached yet, then the first situation occurs again and the raised bars are flattened. This form of secondary flattening is denoted by - Δz_j where:

$$\Delta z_j = \Delta u_l - \Delta u_j \quad (36)$$

III. Bars which that are not and will not come into contact with the tooling [6]

The bars, which are not getting in contact with the tooling can also be raised due to material flow. The raise in height however is insufficient to result in contact with the tooling, and an equilibrium is reached between the load exerted on and the support provided by the contact surface.

With the total amount of bars, for a lubricated surface contact situation, is given by the expression:

$$M = N + N^* + N^{**} \quad (37)$$

Where:

- N - The number of bars which are directly in contact with the tool,
- N^* - The number of raised bars in contact with the tooling due to material flow
- N^{**} - The number of bars which are never in contact with the tooling

These three different behavioral situations are described by an overall conservation law, which states that the total internal energy must be equal to the total external energy for the given situation. The energy equilibrium is given in the following equation as [6]:

$$W_{ext} = W_{int} \quad (38)$$

The formulas for the energy conservation law are shown in their rewritten stochastic form in order to be computationally applicable to large scale FEM simulations. Stochastic parameters are used to translate the deterministic 3D surface roughness of the tool-workpiece contact surface from a micro to macro scale. With the stochastic parameters [6]:

- $\Phi_w(z)$ - The normalized surface height distribution
- U_L - The uniform raise of the non-contacting surface area
- d_L - The separation between the tool and mean plane of the workpiece surface
- L - Refers to the normal loading increment within the simulation

Given in the stochastic form, the indentation factor (ω) and energy factors (γ, β, ψ) are rewritten by implementing the normalized surface height distribution - $\Phi_w(z)$ and taking the limit for an infinite number of bars. This results in expressions which are all depending on statistical parameters. Implementing the energy factors in the energy conservation law and introducing the nominal contact pressure provides the final relation [6]:

$$P_{nom} = \frac{F_N}{A_{nom}} = \frac{B}{A_{nom}} \cdot \left(\frac{\gamma}{\omega} + \eta \cdot \frac{\beta}{\omega} \right) + \frac{S}{A_{nom}} \cdot \frac{\psi}{\omega} \quad (39)$$

After the normal load is found, the next step is to determine the separation between the tool and mean plane of the workpiece surface - d_L and the uniform raise of the non-contacting surface area - U_L .

An expression is derived by assuming volume conservation during crushing and raising movement of asperities [6]:

$$\sum_{i=1}^N \Delta z_i \cdot \Delta A \quad \text{energy crushing asperities} = \sum_{l=1}^{N^{**}} \Delta u_l \cdot \Delta A + \sum_{j=1}^{N^*} \Delta u_j \cdot \Delta A \quad \text{energy raising asperities} \quad (40)$$

Rewritten in stochastic form results in the equation [6]:

$$U_L(1 - \alpha_L) = \int_{d_L - U_L}^{\infty} (z - d_L) \cdot \Phi_w(z) dz \quad (41)$$

This ultimately gives the [Table 4](#), which calculates the given equations for each normal loading increment, where a Newton Raphson scheme is used for solving non-linear expressions.

[Table 4 - Solving Scheme 1 – Flattening due to normal loading \[6\]](#)

Given P_{nom} :

$$P_{nom} = \frac{F_N}{A_{nom}} = \frac{B}{A_{nom}} \cdot \left(\frac{\gamma}{\omega} + \eta \cdot \frac{\beta}{\omega} \right) + \frac{S}{A_{nom}} \cdot \frac{\psi}{\omega} = 0$$

Determine d_L and solve U_L :

$$U_L(1 - \alpha_L) = \int_{d_L - U_L}^{\infty} (z - d_L) \cdot \Phi_w(z) dz = 0$$

Such that the fractional real contact area α_L :

$$\alpha_L = \int_{d_L - U_L}^{\infty} \Phi_w(z) dz$$

Output:

$$d_L, U_L, \alpha_L$$

Flattening due to Normal Loading and Sliding - Tabor

In this section, an extension on the normal loading model is provided that accounts for sliding effects in a tool-workpiece contact situation. Including a tangential movement between the tool and workpiece provides an increase of real contact area, which is captured by the junction growth theory of Tabor [134].

Mechanisms that account for the increase in the real contact area are combined. First, an increase due to normal loading as provided in the previous section is assumed which solves the energy conservation law that needs to converge to an equilibrium. Applying a normal load to the tool-workpiece contact area results in the deformation of softer workpiece asperities. However, at smaller scale, the penetration of harder tooling asperities into the workpiece surface is also included. This results in the second mechanism of deformation and junction growth due to sliding. It is assumed that the penetrated tooling asperities only have contact with the workpiece at the frontal area of the asperities

In order to provide a force equilibrium between the frontal area of the tooling asperities and sliding force, an increase of contact area is required.

The force equilibrium for the deformation due to sliding holds for an increase of real contact area by a factor of two [6]:

$$\alpha_s^1 = 2\alpha_s^0 \quad (42)$$

Where the initial area of real contact - α_s^0 is determined after reaching an equilibrium within the normal loading situation. Applying the Von Mises yield criterion, Tabor [134] provides an expression for the increase in real contact area due to tangential loading:

$$\nu = \sqrt{1 + k \cdot \mu^2} \quad (43)$$

Where the increase of fractional real contact area - ν , is related to the friction coefficient - μ and a shearing factor - k . Based on the experiments of Tabor in a 2D situation [134], the shearing factor is determined to be constant value of 3. The shearing factor for a 3D situation is provided experimentally [6].

In order to find the force equilibrium due to sliding, an iterative scheme is introduced that takes into account the relation between change of friction and change of real contact area. For each iteration, the fractional real contact area - ν , is updated up to a predefined threshold error.

After error criterion is satisfied, the next step is to account for the separation between the tool and mean plane of the workpiece surface - d_L and the uniform raise of the non-contacting surface area - U_L . As provided in the extended [Table 5](#), a Newton Raphson scheme is applied.

Table 5 - Solving Scheme 2 – Flattening due to normal loading and sliding [6]

Input:

$$\alpha_s^0$$

Solve force equilibrium:

$$\alpha_s^1 = 2\alpha_s^0$$

Real contact area ν^n iteration scheme:

```

n = 1
while (|e^n| > error) do
    Solve  $\mu^n$  for current  $\alpha_s^n$ :
     $\nu^n = \sqrt{1 + k \cdot (\mu^n)^2}$ 
    Update  $\alpha_s$ :
     $\alpha_s^{n+1} = \nu^n \cdot \alpha_s^1$ 
     $e^n = |\alpha_s^{n+1} - \alpha_s^n|$ 
    n = n + 1
end while
 $\alpha_s = \alpha_s^n$ 

```

Solve U_s and d_s for α_s such that:

$$\alpha_s = \int_{d_s - U_s}^{\infty} \Phi_w(z) dz = 0$$

$$U_s(1 - \alpha_s) = \int_{d_s - U_s}^{\infty} (z - d_s) \cdot \Phi_w(z) dz = 0$$

Output:

$$U_s, d_s, \alpha_s$$

Flattening due to Normal Loading + Bulk Stretching - Westeneng

In this section, another extension on the normal loading model is introduced where the effect of stretching in the underlying bulk material on the tool-workpiece contact is included. During normal loading on the contact surface, asperities will deform plastically. When no equilibrium has yet been reached and the asperities are already in a plastically deformed state, a strain rate is initiated in the horizontal direction of the underlying bulk material. Surrounding valleys of the asperities are stretched, as seen in Figure 54 [21]. As a result, an increase in surface contact and a decrease in the effective hardness occurs [138] [139] [140].

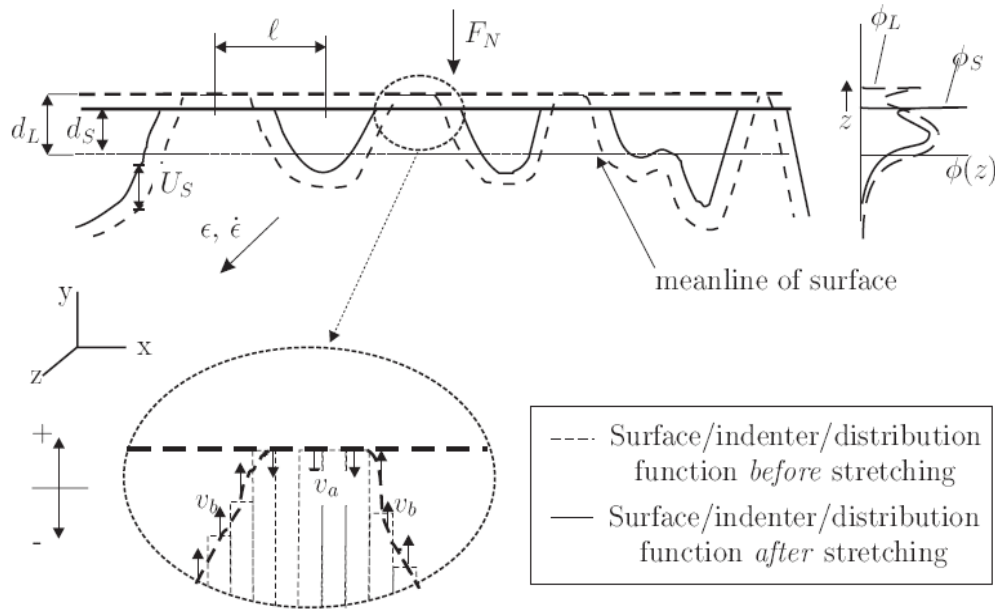


Figure 54 - Bulk stretching during surface contact under normal loading [21]

Westeneng [21] proposed an analytical contact model to determine the change in effective hardness due to bulk straining under a normal load. The effective hardness - H_{eff} can be expressed as:

$$H_{eff} = \frac{P_{nom}}{\alpha} \quad (44)$$

Where the effective hardness is based on the relation between the nominal pressure - P_{nom} and the real contact area - α . In the analytical model. Westeneng [21] introduced the impact of the planar strain - ϵ_p on the change in the fractional real surface - α_ϵ in the following expression:

$$\frac{d\alpha_\epsilon}{d\epsilon_p} = l \cdot W \cdot \frac{d\alpha_\epsilon}{d(U_\epsilon - d_\epsilon)} \quad (45)$$

Where the mean half space between neighboring asperities - l is described as [21]:

$$l = \frac{1}{2\sqrt{\rho_w \cdot \alpha_\epsilon}} \quad (46)$$

Which is based on the asperity density of the workpiece surface - ρ_w and the fractional contact area for a specific strain step - α_ϵ [21]:

Both the normal loading and sliding model are used (U_s, d_s and α_s) to implement the effect of bulk stretching within the solver. The effect of bulk stretching on the change of contact surface is expressed

within a velocity parameter - W , which expresses the velocity of the crushing and lifting motions during normal loading.

$$\alpha_\varepsilon = \int_{d_\varepsilon - U_\varepsilon}^{\infty} \Phi_w(z) dz \quad (47)$$

An empirical model is introduced by Sutcliffe [53] to account for the lack of time dependency within the velocity parameter. The performed slip line analysis resulted in a relation between the velocity parameter - W and the slip-line angle - γ , which is expressed as:

$$W = -0.184 + 1.21 e^{1.47\gamma} \quad (48)$$

$$\gamma = \frac{H_{eff}}{4k} (1 - \alpha_\varepsilon) \quad (49)$$

With the slip line angle being dependent on the relation between the effective hardness and the Von Mises criterion under pure shear - k which is given as:

$$k = \frac{H}{B\sqrt{3}} \quad (50)$$

With the hardness of the material - H and the Brinell hardness test parameter - B [134]:

$$B \approx 2.8 \quad \text{for steel materials} \quad (51)$$

For the flattening due to combined normal load and bulk stretching, an iterative scheme is introduced to solve the change in the fractional real surface - α_ε which is expressed by the differential equation [6]:

$$\frac{d\alpha_\varepsilon}{d\varepsilon_p} = l \cdot W \cdot \Phi_w(d_\varepsilon - U_\varepsilon) \quad (52)$$

For each iteration of the planar strain - ε_p , the change in the fractional real surface area - α_ε will be determined by an Euler method. A Newton Raphson method is also applied, which solves the uniform raise of the non-contacting surface area - U_ε and the separation between the tool and mean plane of the workpiece surface - d_ε . An extended procedure is shown in [Table 6](#) below.

Table 6 - Solving Scheme 3 – Flattening due to normal loading and bulk stretching [6]

Input:

$$\varepsilon_p, d\varepsilon_p, U_\varepsilon^0, d_\varepsilon^0, \alpha_\varepsilon^0$$

Real contact area ν^n iteration scheme:

$$n = 0, \varepsilon^0 = 0$$

while $\varepsilon_p > \varepsilon^n$ do

Solve $d\alpha^n$ for current $d\varepsilon_p$:

$$d\alpha_\varepsilon^n = (l \cdot W \cdot \Phi_w(d_\varepsilon^n - U_\varepsilon^n))d\varepsilon_p$$

Update α_ε :

$$\alpha_\varepsilon^{n+1} = \alpha_\varepsilon^n + d\alpha_\varepsilon^n$$

Solve U_ε^{n+1} and d_ε^{n+1} for α_ε^{n+1} such that:

$$\alpha_\varepsilon^{n+1} = \int_{d_\varepsilon^{n+1} - U_\varepsilon^{n+1}}^{\infty} \Phi_w(z) dz = 0$$

$$\begin{aligned} U_\varepsilon^{n+1}(1 - \alpha_\varepsilon^{n+1}) \\ &= \int_{d_\varepsilon^{n+1} - U_\varepsilon^{n+1}}^{\infty} (z - d_\varepsilon^{n+1}) \cdot \Phi_w(z) dz \\ &= 0 \end{aligned}$$

$$\varepsilon^{n+1} = \varepsilon^n + d\varepsilon$$

$$n = n + 1$$

end while

$$d_\varepsilon = d_\varepsilon^n, U_\varepsilon = U_\varepsilon^n, \alpha_\varepsilon = \alpha_\varepsilon^n$$

Output:

$$d_\varepsilon, U_\varepsilon, \alpha_\varepsilon$$

Modelling Evolution of Friction

The flattening models for normal loading, sliding and bulk stretching which are described in this chapter, result in a definition of the real contact area during tool-workpiece contact. Based on this, the evolution of friction can be determined for a sheet metal forming process.

In this section, first the single asperity model of Challen and Oxley [135] [137] is outlined which describes the evolution of friction on a single contact patch. Second, the single asperity contact model will act as a foundation for the multi-scale friction model introduced by Ma et al. [136], which is adapted for a metal forming process. The flattening models in section - IV - Process Parameters are combined with the adapted model for multiple contact patches. Finally, the friction coefficient is obtained for the summation of shear forces acting on the real contact area [6].

Friction Model - Individual Asperities

The single asperity model of Challen and Oxley [135] [137] describe the friction forces that act on a single contact patch based on a wear mode diagram. The wear mode diagram in Figure 55 illustrates three possible wear regimes:

1. Cutting regime
2. Ploughing regime
3. Wedge formation regime

Each of these modes are determined by a slip line analysis for a wedge shaped tooling asperity in contact with a softer workpiece surface [135] [137].

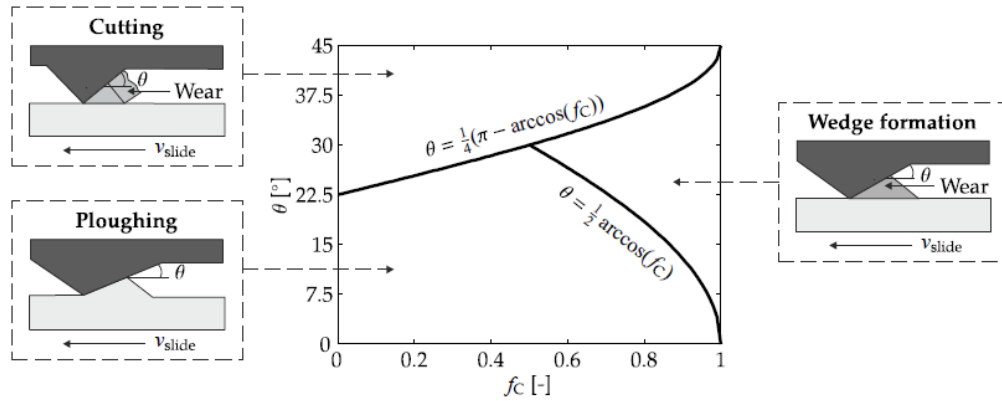


Figure 55 - Wear-mode diagram for a wedge shaped tool asperity indenting a workpiece surface [6]

The friction force as a function of the attack angle - θ of the asperity and the shearing factor - f_c between the shear strength of the interfacial boundary layer (τ) and the workpiece material (k), which can be described in the following equation [135] [137]:

$$f_c = \frac{\tau}{k} \quad (53)$$

With k being dependent on the Von Mises criterion and the shear strength of the interfacial boundary layer for full plastic deformation being defined as [6] [135] [137]:

$$\tau_{plastic} = C \cdot \left(\frac{p}{p_0}\right)^n = C \cdot \left(\frac{H}{p_0}\right)^n \quad (54)$$

With the contact pressure being equal to the hardness of the workpiece material for full plastic deformation. Each of the wear modes are represented within a different friction formula which are briefly discussed below.

Cutting regime

For sharp asperities in contact at a high attack angle the cutting regime holds, causing chip forming and groove formation on the softer surface. The expression for the friction coefficient is determined as [6] [135] [137]:

$$\mu_{cutting} = \frac{F}{N} = \tan\left(\theta - \frac{1}{4}\pi + \frac{1}{2}\arccos f_c\right) \quad (55)$$

Ploughing regime

For blunt asperities in contact at a low attack angle the ploughing regime holds, resulting in groove formation together with material accumulation at the sides. The expression for the friction coefficient is determined as [6] [135] [137]:

$$\mu_{ploughing} = \frac{F}{N} = \frac{A_1 \cdot \sin \theta + \cos(\arccos(f_c - \theta))}{A_1 \cdot \sin \theta + \sin(\arccos(f_c - \theta))} \quad (56)$$

With:

$$A_1 = 1 + \frac{1}{2}\pi + \arccos(f_c) - 2\theta - 2\arcsin\left(\frac{\sin(\theta)}{(1 - f_c)^{\frac{1}{2}}}\right) \quad (57)$$

Wedge forming regime

The wedge-forming regime holds for high shearing factors where the strength of the interfacial boundary layer is greater compared to the shear strength of the workpiece material. In this regime a wedge type of wear debris is formed. The expression for the friction coefficient is determined as [6] [135] [137]:

$$\mu_{wedge-forming} = \frac{F}{N} = \frac{\left\{1 - 2\sin(A_2) + (1 - f_c^2)^{\frac{1}{2}}\right\} \cdot \sin(\theta) + f_c \cdot \cos \theta}{\left\{1 - 2\sin(A_2) + (1 - f_c^2)^{\frac{1}{2}}\right\} \cdot \cos(\theta) - f_c \cdot \cos \theta} \quad (58)$$

With:

$$A_2 = 1 - \frac{1}{4}\pi - \frac{1}{2}\arccos(f_c) + 2\arcsin\left(\frac{\sin(\theta)}{(1 - f_c)^{\frac{1}{2}}}\right) \quad (59)$$

Friction Model – Multiple asperities

Ma et al. [136] further extends the wear regime model of Challen and Oxley [135] [137] for the total real area of tool-workpiece contact. This model provides a deterministic approach that maps both surfaces and accounts for flattening effects under normal loading, sliding and bulk stretching based on a force equilibrium. Subsequently, the multi-scale friction model prevents that its accuracy becomes dependent on the surface scanning quality or that it loses applicability under high fractional contact areas.

Instead, a translation of single asperities into a multi-asperity contact patch is performed by binary image processing techniques, excluding any possible scale dependency problems.

The contact patches are identified as a group of pixels penetrating into the opposing surface. In order to find the friction force as a function of the attack angle - θ , an elliptical paraboloid is fitted through the height characteristics of the contact patch, which is illustrated in Figure 56 [136].

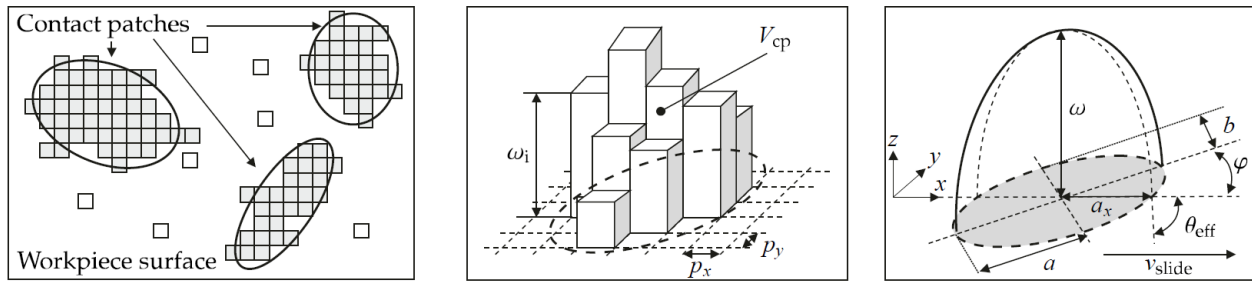


Figure 56 - Schematic overview of the mapping process to determine the angle of attack for a contact patch [6]

The elliptical paraboloid can be described as [6] [136]:

$$V_{ell} = \int_0^\omega \pi a'(z) \cdot b'(z) dz = \int_0^\omega \frac{\pi(a \cdot b)}{\omega} z dz = \frac{\pi(a \cdot b \cdot \omega)}{2} = \frac{A_{ell} \cdot \omega}{2} \quad (60)$$

With:

$$A_{ell} = \pi(a \cdot b) \quad \text{and} \quad \omega = \frac{2}{n} \sum_{i=1}^n \omega_i \quad (61)$$

With the height depending on the geometrical characteristics of the contact patch [6] [136]:

- b - The major axis
- a - The minor axis
- ω - Penetration depth of the contact patch
- φ - The orientation angle between the major and minor axis
- a_x - The characteristic length of the contact patch

Based on these geometrical characteristics, an effective attack angle - θ_{eff} between the paraboloid and the counter surface can be determined as [6] [136]:

$$\theta_{eff} = \arctan\left(\frac{2\omega}{a_x}\right) = \arctan\left(\frac{2\omega\sqrt{(b \cdot \cos \varphi)^2 + (a \cdot \cos \varphi)^2}}{a \cdot b}\right) \quad (62)$$

It is important to note that the model of Challen and Oxley [135] [137] only accounts for ploughing and adhesion effects in a 2D plane strain situation.

To translate the mechanisms of friction so that it captures the 3D nature, Hokkirigawa and Kato [141] introduced the shape factor - χ to calibrate the effective angle of attack. The shape factor can be determined by sliding experiments for a specific tool-workpiece combination. The corrected angle of attack can be determined for specific sheet metal forming processes in 3D [141]:

$$\theta = \arctan\left(\frac{2\omega}{a_x}\right) = \arctan\left(\frac{2\omega\sqrt{(b \cdot \cos \varphi)^2 + (a \cdot \cos \varphi)^2}}{\chi \cdot (a \cdot b)}\right) \quad (63)$$

Friction Model – Friction Coefficient for Contact Patches

Being able to determine the angle of attack for each contact patch together with the sliding direction. The coefficient of friction can be determine as the summation of all individual friction forces that are determined with the angle of attack divided by the summation of the normal loads carried for each of the individual contact patches. Using Coulombs friction law [4] the coefficient of friction is defined as:

$$\mu = \frac{F_w}{F_N} = \frac{\sum_{i=1}^m \mu_i (\theta_i) \cdot A_i \cdot H}{\sum_{i=1}^m A_i \cdot H} \quad (64)$$

With:

- m - The number of contact patches
- μ_i - The individual friction coefficient for a specific wear regime
- θ_i - The angle of attack for a specific contact patch

A major benefit of this multi-scale frictional approach is that anisotropic effects on individual contact patches are correctly captured by the elliptical paraboloid function, incorporating the effect of individual sliding directions into the overall coefficient of friction [6].

FEM Analysis

The multi-scale friction parameters described above are used in the simulations and provides a generic framework to predict friction in steel sheet forming processes. The model accounts for micro-mechanical behavior of the tool-sheet metal contact systems and therefore the changes in surface topography and the evolution of friction during the forming processes.

It is established in the model that the rise in tool temperature originates from:

- Plastic deformation of the sheet metal,
- Friction induced heating due to asperity deformation and
- Pressurized lubricant at blank surface pockets during mixed lubrication regimes

The temperature rise has important influence on the tribological behavior of the tool-blank contact system. The FEM analysis will study this temperature-friction relation and its impact on the material flow of the workpiece material during the specific two-step deep draw process. It is possible to perform small changes to the process during the simulations by varying the press speed and blank holder forces.

The aim of the FEM analysis is to validate the chosen frictional model for the described tribological system. Besides the validation, a pilot study is performed for exploring the control system possibilities to reduce the amount of product failure during the warm-up period. Both FEM goals will help in formulating recommendations for further research in the final stage of the ASPECT project.

Micro-scale Four Dimensional Look-up Table

The most important elements identified in the tribological system of section - [Tribological Framework](#) are used for computing the temperature induced frictional behavior of the contact interface in both boundary and mixed lubrication regimes. For the coefficient of friction, a four dimensional look-up table is generated based on [3] [6]:

Nominal contact pressure	-	P_{nom}
Temp	-	T
Relative velocity	-	v_{rel}
Strain	-	ε

Each of the calibrated parameters for the provided tribological framework are cross fitted and measured for the values given in [Table 7](#).

[Table 7 – Tribological values used in the FEM Analysis](#)

Roughness sheet [Sa]:	0.35	μm
Lubrication amount:	7.0	g/m^2
Roughness tool [Sa]:	0.02	μm
Pressure:	1, 8.33, 16.67, 25.00, 33.33, 41.67, 50	MPa
Temperature:	20, 30, 40, 50, 60, 70, 80	$^{\circ}\text{C}$
Velocity:	1, 33.33, 66.67, 100, 133.33, 166.67, 200	mm/s
Strain:	0, 0.06667, 0.13333, 0.2, 0.26667, 0.33333, 0.4	-

Cross fitting each of these values results in a 4D Triboform frictional model for AISI420 as workpiece material, Castrol Iloform FST 16 as lubricant and Ceratizid as tool material.

The micro-scale data is implemented within the FEM simulations as a four dimensional look-up table that provides the corresponding coefficient of friction for each combination. The development of the material behavior is modeled through the use of a special subroutine for each forming step within the simulation. The corresponding coefficient of friction is read from the look-up table that is based on the micro-scale mechanisms that are outlined in the [Theoretical Framework](#). An example of the Triboform frictional model for different temperatures and tool roughness variations is provided in [Figure 57](#) [76].

The generated file used in the special subroutine that contains the complete 4D-frictional look-up table is provided in [Appendix 7 – Four Dimensional Look-up Table](#). The subsequent chapter will provide a more in-depth overview of the subroutine that is used within the FEM simulation in combination with the generated 4D frictional look-up table.

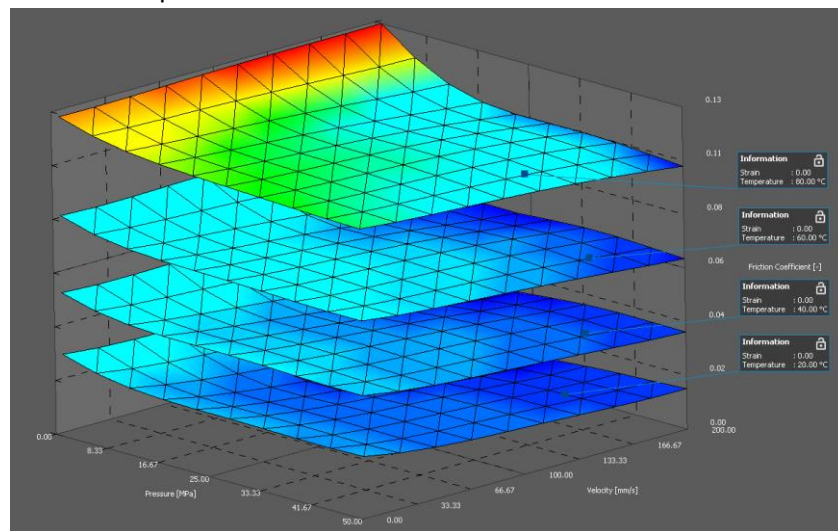


Figure 57 - Development of the friction coefficient at 20, 40, 60 and 80°C for a strain, $\epsilon=0$ [76]

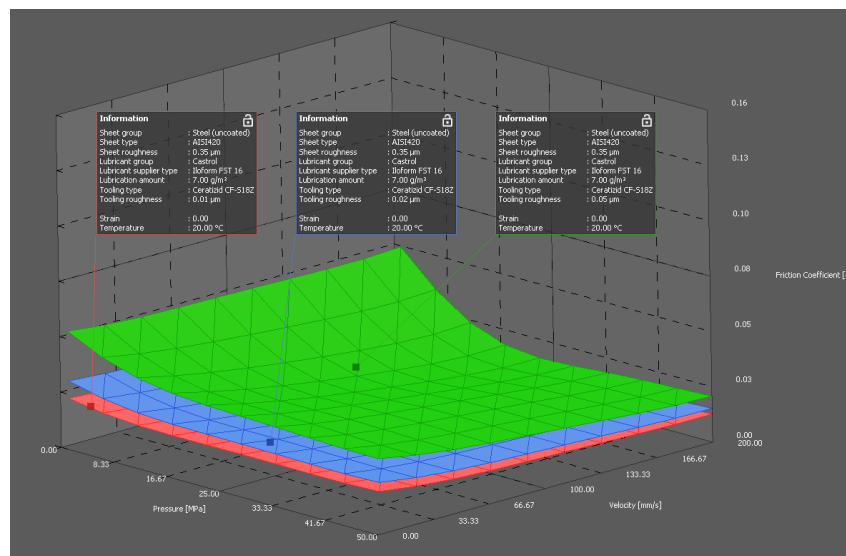


Figure 58 - Differences in μ for Sa-tool of respectively 0.01, 0.02 and 0.05 μm [76]

Subroutine

The subroutine that is used during the FEM analysis, consists of two main steps that will be performed during each increment or time step. Note that for the first increment – k , the initial temperature (room temperature) will be implemented as input into the mechanical solver. A schematic overview of the subroutine steps are illustrated in [Figure 59](#). A more in depth explanation of each step in the subroutine is provided below.

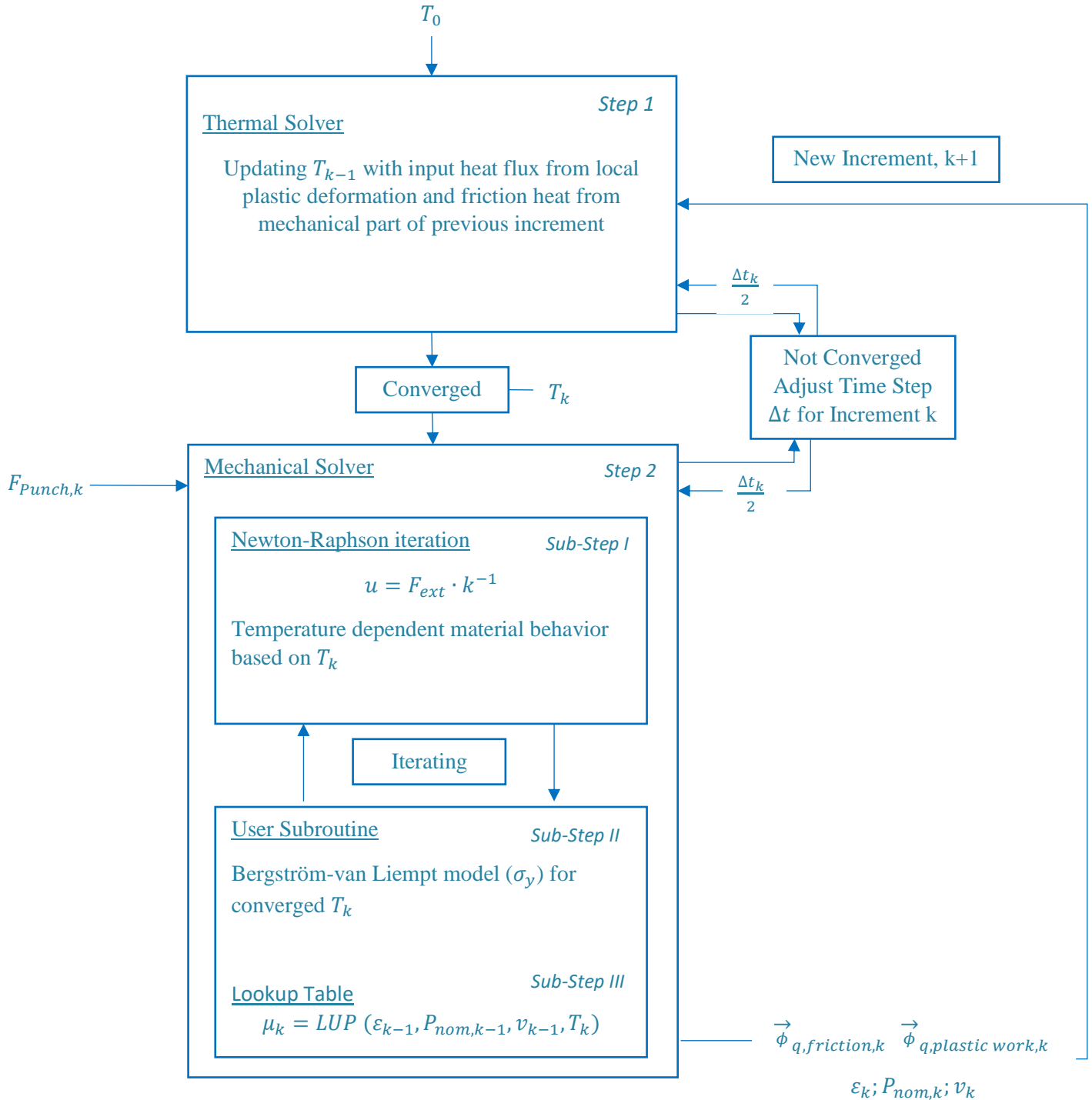


Figure 59 - Schematic overview of the subroutine steps performed at each increment during the FEM analysis

Step 1 – Thermal Solver

During the thermal solver step, the local temperature values (T_k) for that particular time step are used and implemented into the mechanical solver for each of the nodes.

Step 2 - The Mechanical Solver

Sub-Step I – Material properties update by temperature

The thermal value from the thermal solver step (T_k) is inserted, such that the strain hardening curve is only depending on $\dot{\varepsilon}$ and ε , so $\sigma_y = f(T, \dot{\varepsilon}, \varepsilon) \rightarrow \sigma_y = f(\dot{\varepsilon}, \varepsilon)$. Next a first estimation is done on the incremental increase (either positive or negative) of the tool forces and displacements. Most likely this will not provide a convergence right away due to the nonlinear nature of the material behavior. Resulting in the start of sub-step 2

Sub-Step II – Curve fitting of the Bergström-van Liempt with Newton-Raphson scheme

In order to approximate the (nonlinear) elastoplastic hardening Bergström-van Liempt curve (σ_y) [7], a Newton-Raphson (NR) Scheme [142] is initiated as an iterative solution method. The interaction between the material behavior and the displacement is provided in Figure 60 below [143].

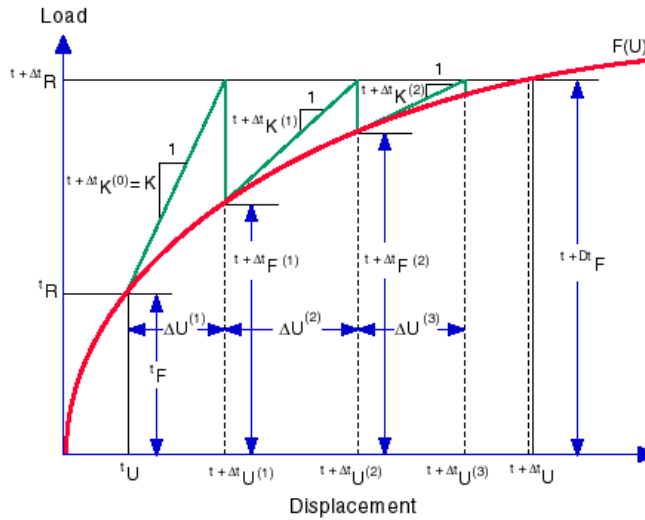


Figure 60 - Overview of the modified Newton-Raphson Scheme [142]

During each iteration the load-displacement curve ($u = F_{ext} \cdot k^{-1}$) is approximating the Bergström-van Liempt curve where the load and the displacement are based upon the material properties of the sheet.

- Here the Bergström-van Liempt curve provides the σ_y .
- The Newton Raphson iterates to approximate the Bergström-van Liempt curve to find ε_k

After each iteration, the corresponding nodal strain is found for the corresponding nodal stress. When converging takes place the following parameters are known for this increment: $\varepsilon_k, P_{nom,k}, v_k$.

Sub-Step III - 4D frictional Look-up Table

After finding the parameter needed to implement within the formula for the look-up table. The related friction coefficient (μ_k) can be found. Next increment - k+1

For the next increment, k+1, the heat flux from the friction and plastic work is inserted into the thermal solver. Together with the thermal properties of the materials specified, this will result in converged values T_{k+1} for all nodes.

Simulation

During the FEM analysis, three studies are performed to observe the behavior of temperature induced friction in the specific two-step deep draw process. The first study focusses on the different standard friction models that are possible to apply in the MSC Marc software, outlining the differences between and the influence of friction in each model that are generally used for metal forming studies. The second study will continue with the adapted Bergström van Liempt model that was introduced in the theory section and starts with a sensitivity analysis to check the temperature dependency and individual contributions of each frictional parameter. The third study will reproduce the Bergström van Liempt model results for different tooling roughness and film thicknesses lubricant film to check the robustness of the formulated calculation model. Within the FEM analysis, the material, tooling and lubricant type that are used within the FEM analysis are identified as:

Sheet material	AISI420 (Euronorm: X20Cr13)
Lubricant type	Castrol Iloform FST 16
Tooling type	Ceratizid CF-S18Z

The FEM simulations are performed in MSc Marc, simulating the specific two-step deep draw process that was described in section - [Two-Step Deep Draw Process](#). The described subroutine is used to model the temperature induced friction coefficient during each forming step. Each step of the deep draw process is separately simulated where the end result of the first drawing step will be the input of the second drawing step. The described subroutine in section - [Subroutine](#) together with the four dimensional look-up table in [Appendix 7 – Four Dimensional Look-up Table](#) will be used for every increment during the calculation of both drawing steps. A radial overview of the general set-up of the two-step deep draw process in the simulation is provided in [Figure 61](#).

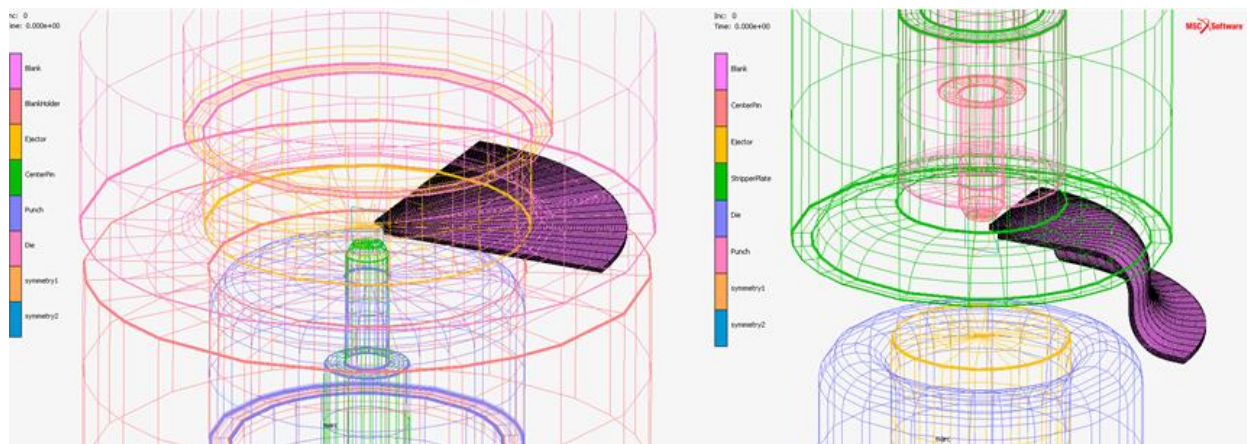


Figure 61 - General overview of the two-step deep draw process [5]

Dimensions

The determined dimensions for the FEM analyses are predetermined in the foregoing pilot study of M. Veldhuis [3] that presets the tooling within the deep draw process to be highly sensitive to temperature deviations. The tooling interaction is preset to generate heat and display a start-up behavior concerning the temperature-friction relation.

Also the impact of other unwanted spread sources, such as the influence of normal anisotropy and work hardening behavior. The most important control parameters are given below, a more detailed overview is

provided in [Appendix 8 – FEM Analysis - Dimensional Parameters](#). With the general dimensions being identified as:

- Punch fillet radius step 1: 2.00mm
- Punch fillet radius step 2: 1.00mm
- Blank holder Force in step 2: variable between 250 and 450N (set at 250N in nominal simulation)
- Redrawing depth in step 2: flexible between 1.65 and 3.65mm (set at 2.69mm in nominal simulation)

The general dimensions that enable the temperature dependency of the system is applied for each of the three performed studies. The generalization in the set-up of the process enables to analyze and compare the main results for each of the studies in the remainder of this research project. In order to do so, first the main parameters of study are specified.

Parameters of Interest

The exploratory study of M. Veldhuis [3] determined that for the FEM analysis, the main output parameters for determining the impact of temperature and friction on the process are the flange diameter, the hole diameter and the final height of the drawn cup. Primarily the geometrical dimensions of the drawn cup will be used for determining the general material flow behavior after both steps of the deep draw process. Before the metal forming process begins, the starting dimensions of the flange and the hole are identified as:

Hole Diameter	2 [mm]
Flange Diameter	29 [mm]

In general, the output parameters should be sensitive to the control parameters that are identified in to be highly susceptible for temperature changes and friction [1] [3]. The general parameters measurable in the FEM simulations are provided in [Figure 62](#) below.

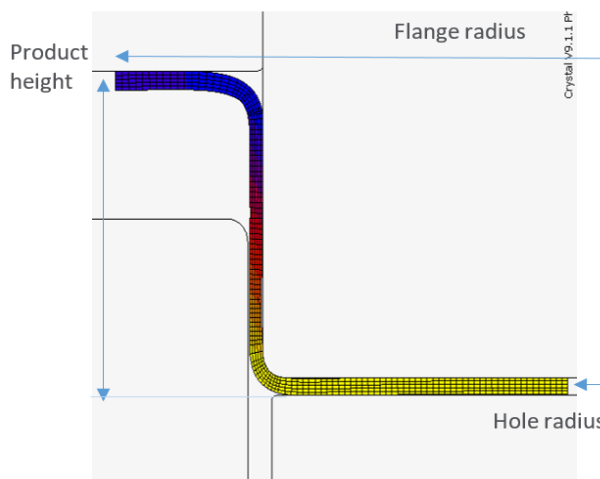


Figure 62 - Schematic overview of the general output parameters of interest [3]

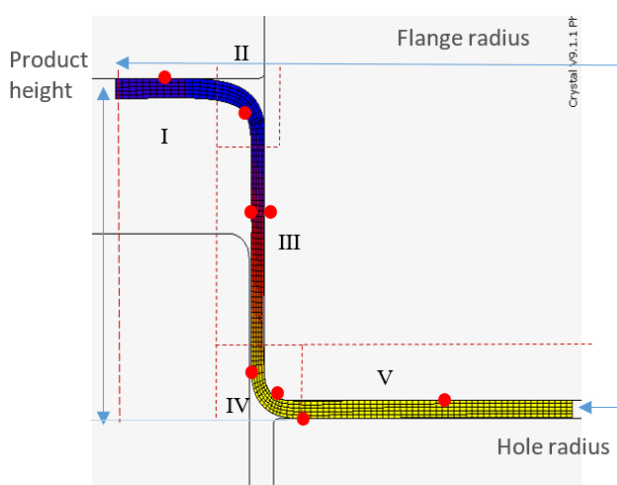


Figure 63 - Detailed overview of different material behavior regions and contact points of interest [3]

When studying each of the forming steps separately, both the radial changes of the flange and hole as the regional changes are taken into account. In order to do this, the blank material will be divided into zones, as described in [Figure 10](#).

For each particular zone, the material behavior is identified for which differences are expected in the outcomes. The material movement of the specific zones in the workpiece will be analyzed in order to provide a more in depth view of frictional impact on the local material flow behavior.

For every node in contact, the in-place plastic strain, contact normal pressure, sliding velocity and temperature are determined and within a 4D frictional look-up table, the corresponding friction coefficient is looked up and used in the next increment

The main reason to look further into each of the separate steps is to study the possibility of different effects that negate each other in the total material flow. A more detailed overview, indicating the different material behavior regions and points of interest are illustrated in [Figure 63](#).

In order to link the material flow behavior to the implemented temperature dependent frictional model, the main contact points within the workpiece-tooling interface are observed together with the frictional values and temperature development throughout the workpiece material for each increment. An overview of the gradual changes will then be plotted and provide a total overview of the observed behavior within a two-step deep draw process.

FEM Results

The FEM results will consist of four different sets of studies that are simulated within MSC Marc and will provide the outcomes of frictional behavior within the two-step deep draw process. Each of the studies are discussed in the subsequent chapters where the main findings will be used for answering the research questions.

In the first study, FEM analyses are performed for different standard adaptations on the Coulomb friction model that are available in the simulation software. The different models provide a general overview of the impact of friction within the metal forming process and will be used to compare the results of the more advanced friction models. The study is only performed at room temperature since no temperature dependency is present.

For the second study, a sensitivity analysis is performed to validate the temperature dependency for the adapted Bergström van Liempt model that is introduced in the [Theoretical Framework](#) of this research project. Also the temperature sensitivity impact for each of the frictional parameters is further examined.

The third FEM study will focus purely on the adapted Bergström van Liempt model with full frictional table and provide the friction contact points together with the temperature, equivalent stress, total plastic strain and material movement in the Y-direction for different temperature increments.

Finally, the fourth FEM study will extend on the adapted Bergström van Liempt model by analyzing the temperature dependency for different workpiece roughness values together with different lubrication thickness parameters. FEM studies are performed to analyze the frictional behavior for different temperature variations in the two-step deep draw process.

For the FEM studies performed, the results are analyzed for temperature variations that approach the warm-up curve, which is illustrated in section - [Temperature Relation](#), within the deep draw process. The temperature values of the tooling in the deep draw process is incrementally increased from 293K with steps of 10K or 20K up to the 373K mark. The temperature values within the FEM simulations are determined in order to be able to approximate the real life deep draw process as accurate as possible [3] [5].

The FEM simulations are performed in MSc Marc, the general results are retrieved by a Matlab routine that is provided in [Appendix 9 – FEM Analysis – Matlab Routine](#). The results for each of the temperature studies will consist of:

- Temperature development within the workpiece,
- Equivalent Cauchy stress development,
- Total equivalent strain development,
- Material displacement behavior.

Deep Draw Process

Both the flange and the hole dimensions are used for analyzing the material flow behavior in both steps of the deep draw process. In turn the determined behavior can be used for the validation section. For both steps in the deep draw process, a 2D axisymmetric representation is used. The 3D overview of the deep draw process in [Figure 64](#) and [Figure 65](#) is linked to the corresponding 2D representation in the illustrations below. In the performed studies, the 2D Axisymmetric results are turned 90°.

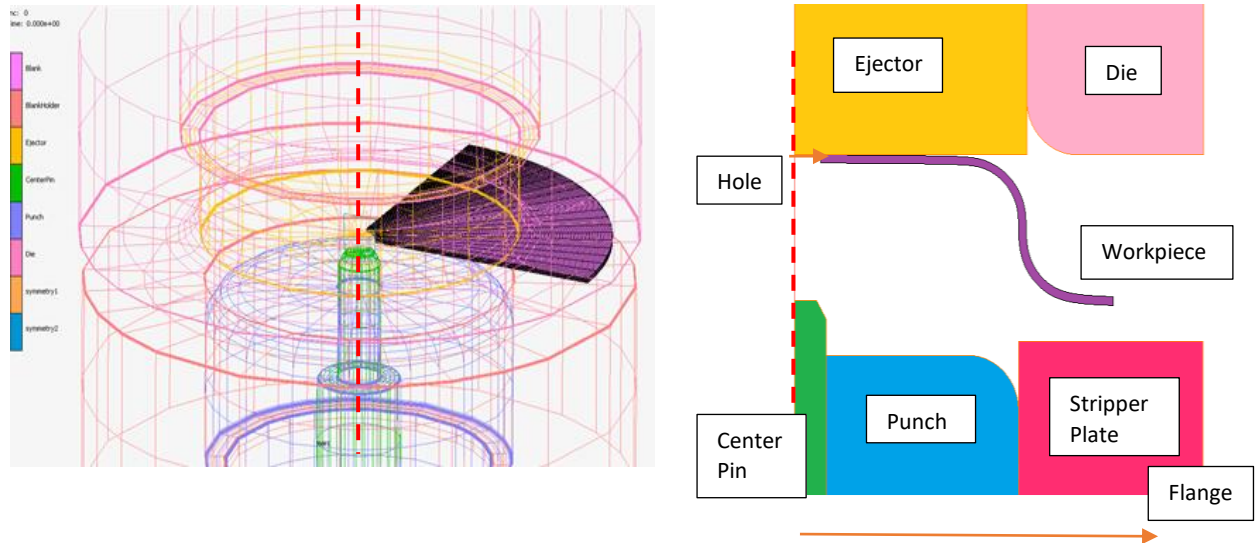


Figure 64 – 2D Axisymmetric conversion of different tooling represented in the FEM solver for deep draw step 1 [5]

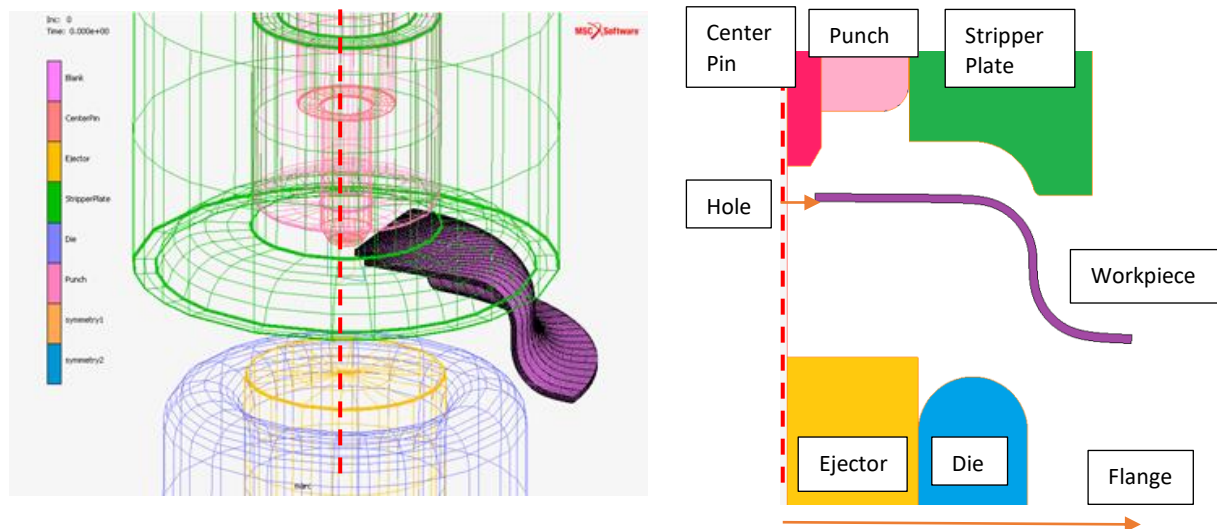


Figure 65 – 2D Axisymmetric conversion of different tooling represented in the FEM solver for deep draw step 2 [5]

Study 1 - Frictional Models MSC Marc

Different frictional models are available in the MSC Marc solver, the initial study compares the results of each frictional option to highlight their impact on the material flow behavior. The study can be seen as an introduction to the subsequent studies where the more advanced frictional model, provided in the theory section, will be analyzed. Each FEM study is performed for the room temperature of 293K since a temperature dependency is not included within the models.

Within the MSC Marc solver, two idealistic categories of models are available. For most of the metal forming simulations the Coulomb stick-slip frictional model can be used with the exception of forging processes. For this type of process, the shearing friction model is generally used in the solver. The idealistic models are further divided in the solver, based on different adaptations which are implemented to prevent any numerical issues during the transition of the step function in the simulations. A more in-depth overview of each of the available friction models is provided in.

Coulomb

For the Coulomb friction model, the arctangent, modified stick-slip and the bilinear adaptations are available in MSC Marc. The arctangent adaptation provides a smooth transition between stick and slip modes in the Coulomb model that is determined by the RVCNST variable that is based on the relative velocity. The modified step function assigns the stick or slip status to individual nodes together with additional constraints which depend on the status of the node. The bilinear model links the stick and slip modes to reversible and permanent deformation or nodal displacement that is based on the theory of elastoplasticity. A general overview of the Coulomb adaptations are provided in Figure 64 to highlight the general differences.

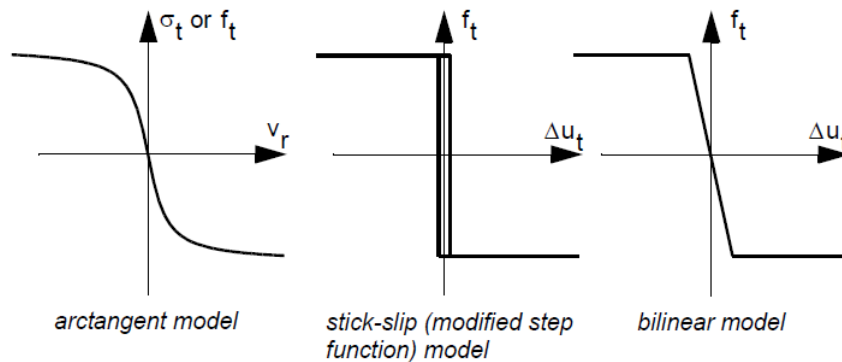


Figure 66 - Adaptations on the Coulomb friction model available in MSC Marc [144]

Shear

The frictional forces in the shearing friction model are based on the frictional stress which is determined based on the equivalent stresses in the material. The available variations on the shearing frictional model are the arctangent and the bilinear adaptations. Again, the arctangent model provides smoothing function based on the RVCNST variable that is dependent on the relative velocity. The shear bilinear adaptation determines the tangential friction stress as the minimum value of the normal shear stress and the equivalent stress where the nodal shear stress is assumed to be proportional to the applied shear force. In other words, if the friction stress stays below the flow stress of the material, the model reduces to a simple Coulomb friction law.

Applying the Matlab routine on the results of the FEM analysis provides the flange and the hole diameter development for both the steps during the two-step deep draw process. The generated results are provided in [Appendix 11 – FEM Study 1 – Frictional Models](#) and are plotted in Figure 65 and Figure 68.

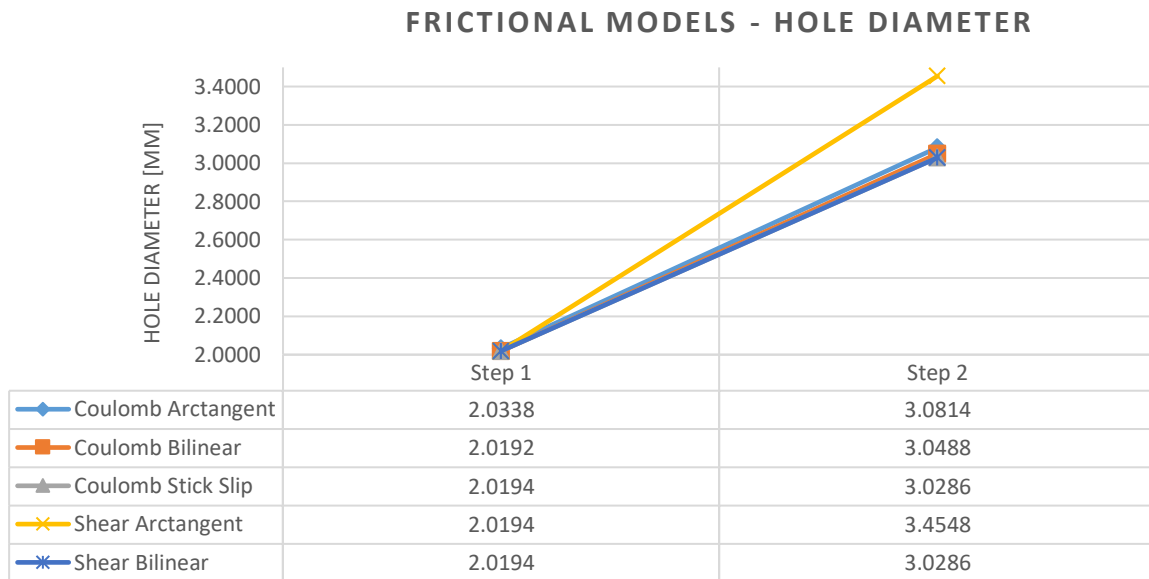


Figure 67 - Development of the hole radius for each step in the two-step deep draw process

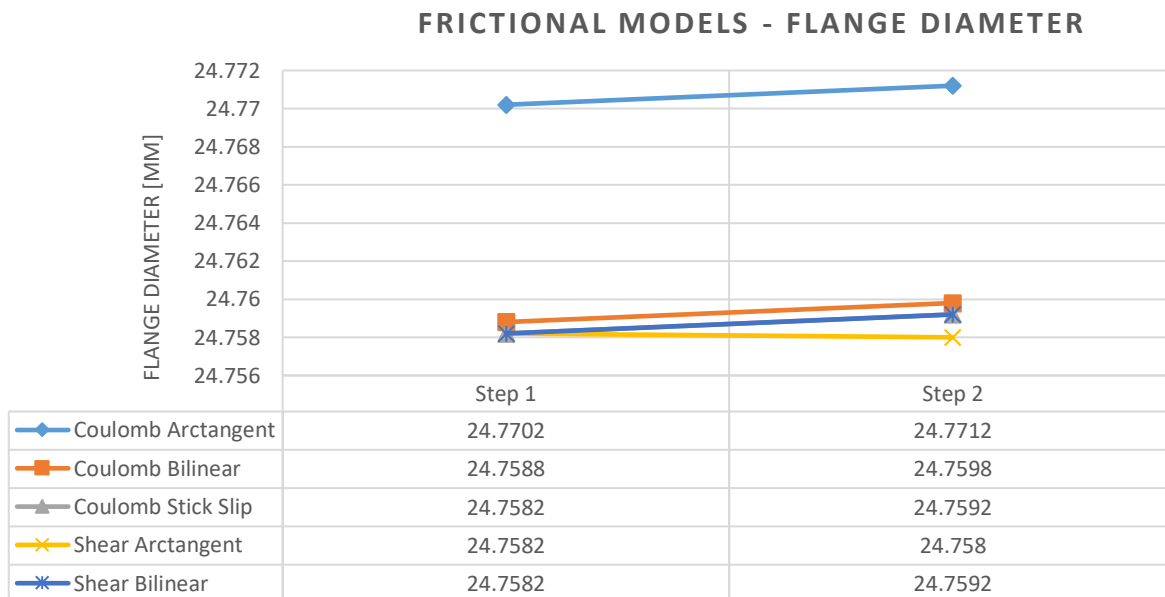


Figure 68 - Development of the flange radius for each step in the two-step deep draw process

As can be seen from [Figure 65](#) and [Figure 68](#), and when comparing with the initial values of 24 mm for the flange diameter and 2 mm for the hole diameter, it can be concluded that:

- In step 1, the flange diameter is subjected to greater changes compared to the hole diameter.
- In step 2, the hole diameter is subjected to greater changes compared to the flange diameter.

Hole diameter development

When further observing the development of the hole diameter, it can be seen that the material flow behavior is very similar for all frictional models with the exception of the Shear Arctangent model.

The hole diameter of the Shear Arctangent model grows larger during the second step in comparison to the other frictional models. This can occur for relatively lower frictional values in the region around the hole of the workpiece, marked - A in [Figure 69](#), compared to the higher frictional forces the die-workpiece contact interface, which is marked - B in [Figure 69](#). The more dominant friction effect at the region between the die and the stripper plate, the more it allows for more flow of material at the hole.

Flange diameter development

When further observing the development of the flange diameter, again it can be seen that the material flow behavior is very similar for all frictional models with the exception of the Coulomb Arctangent model. This difference is mainly a shift directly after step 1 in the deep draw process. The main explanation can be that the frictional forces at the blankholder-workpiece interface are more dominant over the frictional forces at the punch-workpiece region in the Coulomb Arctangent case compared to the other frictional models.

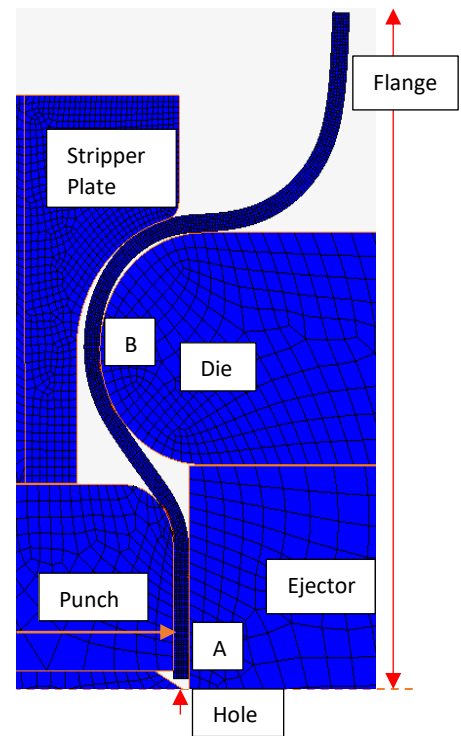


Figure 69 - Indication of hole and flange in Step 2 of the two-step deep draw process

Frictional Models – Temperature Development

An overview of the temperature development of the workpiece after each deep draw step is provided in [Appendix 11 – FEM Study 1 – Frictional Models](#). It can be seen that for both deep draw steps, the overall temperature develops similar for every friction model. Very small deviations in temperature can be noted for all friction models except for the shear arctangent model which shows temperature values of ~20K higher, as given in [Figure 70](#). This can concur with the results of the hole diameter development, the higher frictional forces present in the shear arctangent model make the hole diameter grow and in return result in a local increase of temperature.

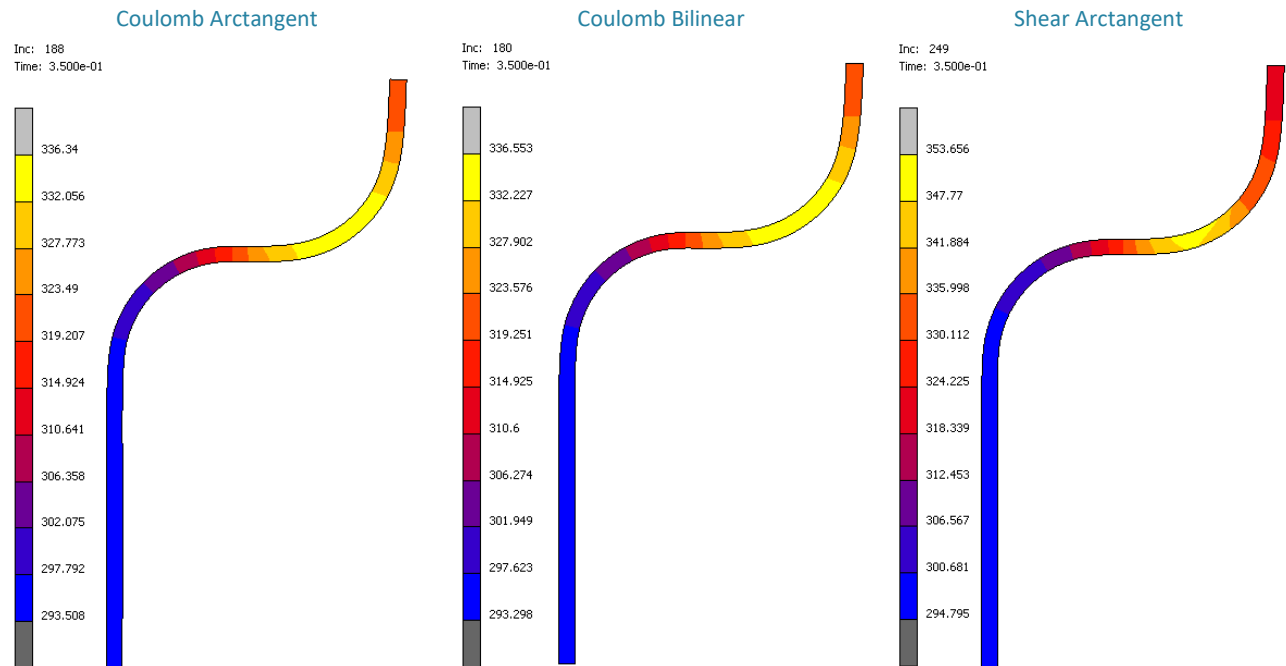


Figure 70- Overview of the temperature development for different models as stated above, it can be noted that the temperature of the Shear Arctangent model is higher compared to the other friction models

Frictional Models – Total Material Displacement Y-Direction Workpiece

An overview of the material displacement after each deep draw step is provided in [Appendix 11 – FEM Study 1 – Frictional Models](#), which is illustrated as the displacement of the material in the workpiece in the Y-direction. Comparing the main regions of material flow or displacement in each of the frictional models the observation is made that the differences in material behavior of the workpiece are minimal.

Considering the displacement values of each frictional model, it can be concluded that the largest outliers for both step 1 and step 2 originate from the shear arctangent model.

Especially when looking at the lower material displacement in the first drawing steps of this friction model, the lower negative flow values result in the increase of the hole diameter which are again confirmed in [Figure 71](#).

Another effect can be found in the shear arctangent model when comparing the difference in material displacement between both deep draw steps. In the second large difference in material displacement is observed.

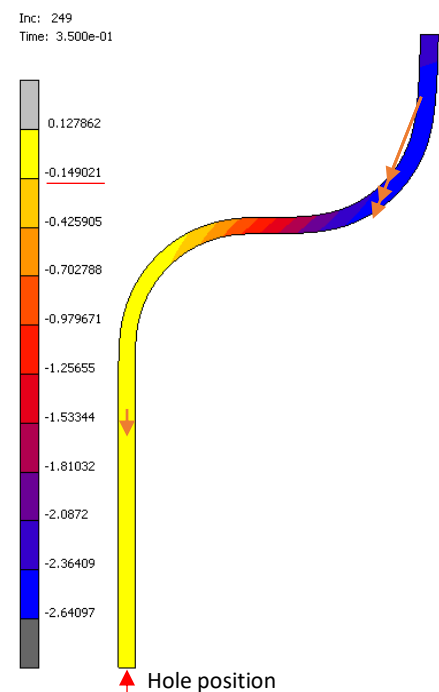


Figure 71 - Material displacement in the Y-direction after the deep draw step 1 for the shear arctangent friction model

Frictional models – Equivalent Cauchy Stress Development Workpiece

An overview of the equivalent Cauchy stresses in the workpiece after each deep draw step is provided in [Appendix 11 – FEM Study 1 – Frictional Models](#).

It can be seen that for both steps in the deep draw process, the overall stress development occurs at the die-workpiece and die-punch region for every friction model. The stress development occurs at the regions where the workpiece is drawn over the die radius by the punch movement into the desired cup shape as seen in [Figure 72](#).

Another note can be made when comparing the maximum equivalent stress values for the friction models. The highest stress values are measured before unloading occurs, it shows that the shear arctangent model displays a higher stress development in step 2 of the deep draw process.

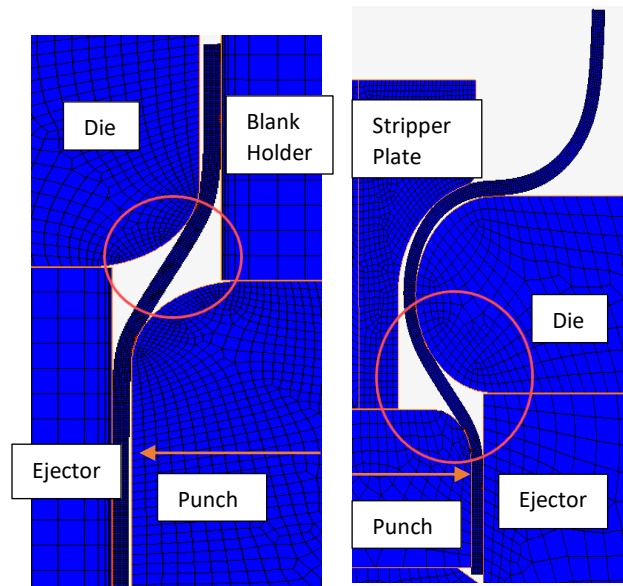


Figure 72 - Overview of Step 1 and 2 in the two-step deep draw process with the high equivalent stress regions indicated

Frictional models – Total Equivalent Strain Development Workpiece

An overview of the total equivalent strain development in the workpiece is provided in [Appendix 11 – FEM Study 1 – Frictional Models](#) for each step in the deep draw process.

It can be seen that for both steps in the deep draw process, the overall strain development is similar for each friction model. Again the maximum strain values in step 2 of the deep draw process are higher for the shear arctangent model compared to the other friction models which agrees with the higher material movement of the workpiece in the Y-direction.

In general, the higher strain values are found at the outer radius of the drawn workpiece around the die, workpiece and the punch region where tension occurs in the material. This is indicated for both steps in [Figure 73](#).

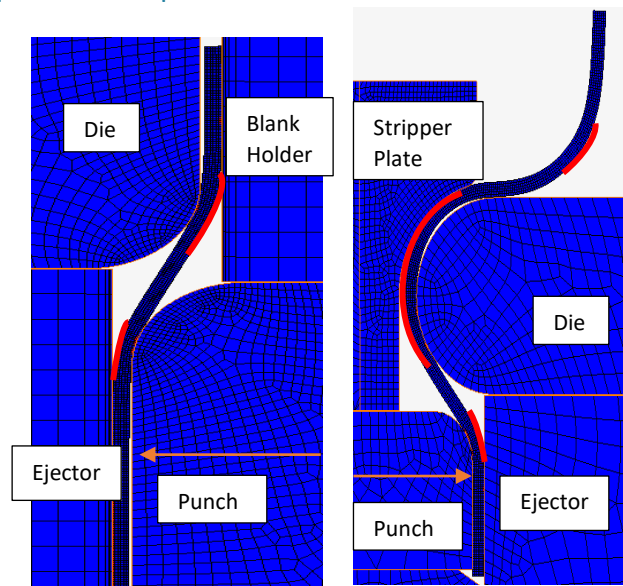


Figure 73 - Overview of Step 1 and 2 in the two-step deep draw process with the high equivalent stress regions indicated

Study 2 - Temperature Induced Frictional Model

The results of the second study are based on the adapted Bergström van Liempt model implemented within the MSC Marc software and outlined in the [Theoretical Framework](#). The adapted model introduces a temperature dependency which impacts the frictional and consequently the material behavior during the two-step deep draw process. For each increment, the local strain, nominal contact pressure, sliding velocity and temperature are determined in the workpiece, which are coupled to the corresponding coefficient of friction in the four dimensional frictional look-up table.

Within the FEM solver, the corresponding friction coefficient values are used to determine the global material flow behavior. The material flow is measured as the change in the hole and flange diameter, which is extracted for each of the two deep draw steps via the Matlab routine that is represented in.

The results of the second study are provided in a sensitivity analysis of the frictional look-up table parameters, which validates the robustness of the assumed frictional model. In addition the relative impact of the material properties over the frictional behavior, which is concluded to be minimal for the current deep draw set-up [3], is checked in the sensitivity analyses.

Sensitivity Analysis

The FEM results of the sensitivity analyses that was performed originates from variations on the adapted model from J. Hol [6] which includes the temperature dependency in the Bergström van Liempt model. The Bergström van Liempt model with full friction table should display a temperature dependency that interrelates with the frictional and consequently the material flow behavior during the two-step deep draw process.

An integral part of the adapted model and the [Theoretical Framework](#) of this research project is the coupling between the micro-scale mechanisms, which are provided in the 4D frictional look-up table, and the material behavior on the macro-scale, influenced by the coefficient of friction.

For the Bergström van Liempt model with full frictional table, the local coefficient of friction is determined by nodal parameters in the look-up table. The micro-scale look-up table depends on: nominal contact pressure, temperature, relative velocity and strain within the subroutine.

A sensitivity analysis was performed for the 4D frictional look-up table of the subroutine to study the impact of each parameter on the material flow behavior. Both the individual contribution and cross-coupled effects on the flange and hole development are provided in [Figure 74](#) and [Figure 75](#) below.

An additional iteration was performed for a constant coefficient of friction of 0.1 in order to validate the design of the deep draw process itself. The deep draw process was designed to keep the temperature induced material effects on the flow behavior as minimal as possible [3].

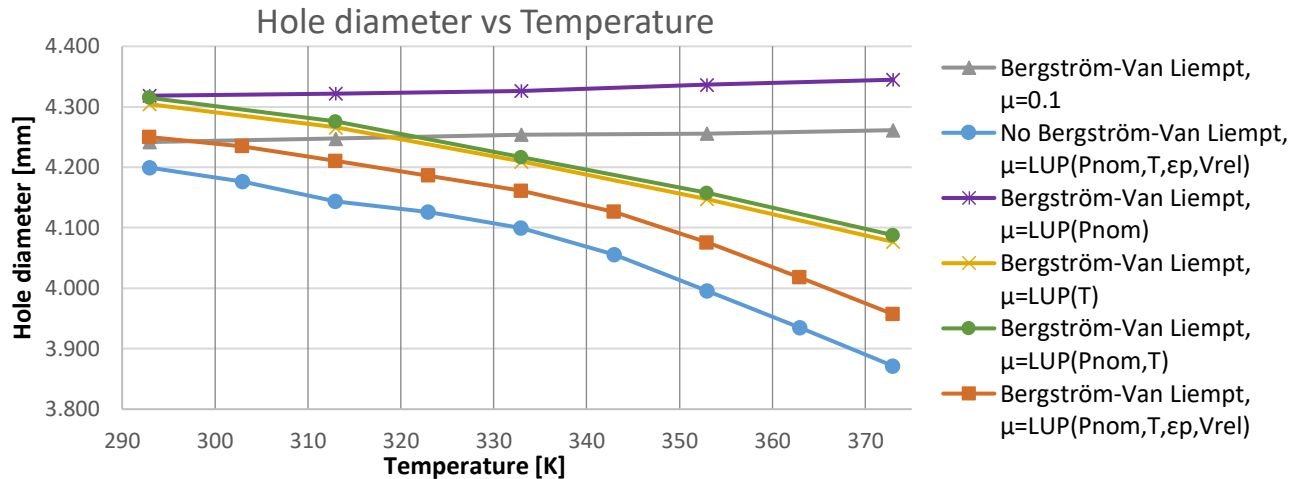


Figure 74 - Sensitivity analysis of the hole diameter development for different temperature variations

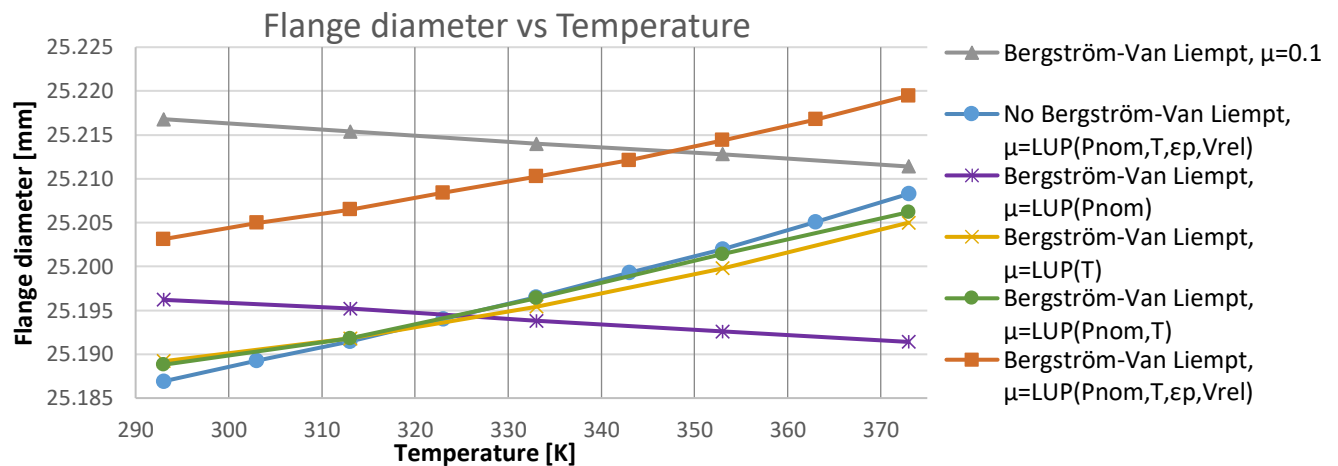


Figure 75 - Sensitivity analysis of the flange diameter development for different temperature variations

When analyzing the results of the sensitivity analysis, the following main observations can be made:

- When looking at the Bergström van Liempt model variation with only a temperature dependent friction coefficient - *Yellow line*, it can be noted that the temperature parameter of the friction accounts for ~80% of the total flange and hole development. The other 20% is estimated to be caused by the strain hardening effect of the workpiece material.
- When looking at the constant coefficient of friction variation - *Grey line*, it can be noted that the material behavior exercises a minimal influence on the development of the flange and hole diameter.
- When looking at the Bergström van Liempt model with full frictional table - *Orange line*, it can be noted that as the temperature increases the final hole diameter decreases and the final flange diameter increases relatively.

- When comparing the Bergström van Liempt model with full frictional table - *Orange line* with the No Bergström van Liempt model - *Blue line*, it can be noted that the Bergström van Liempt model with the full frictional table takes a lower amount of material hardening into account during the simulations which is seen in the shift between the two lines for both figures.
- When looking at the Pnom variation of the Bergström van Liempt model - *Purple line*, it can be noted that the nominal pressure is not influenced by the temperature deviations.

Based on the theoretic framework, an initial explanation for the material flow behavior in the adapted Bergström van Liempt model is that an increase of temperature results in a decrease of the material hardening. For the increased temperature cases compared to the original cold forming process, under constant parameters (P_{nom} , ε_p , v_{rel}), the workpiece material will deform faster. This causes an increase in surface contact which results in subsequent more adhesion, deformation and shearing between the contacting interfaces.

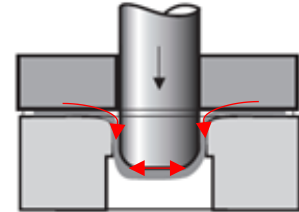


Figure 76 - Material flow in the deep draw process [21]

These micro-scale mechanisms translate at the macro-scale into an increase of surface contact and thereby surface friction. The increase in friction will oppose the material flow from the flange and hole region during the deep draw process, which is illustrated in Figure 76.

Based on the sensitivity analysis and the theoretical framework it be concluded that for the Bergström van Liempt model with full frictional table:

- I. An increase in temperature will result in an increase of friction and a decrease in temperature will result in a decrease of friction.
- II. A higher amount of friction during the deep draw process results in a smaller relative change in the final flange diameter and the final hole diameter.
- III. Consequently, a lower amount of friction during the deep draw process results in a larger relative change in the final flange diameter and the final hole diameter.
- IV. The Temperature dependency of the friction takes up already 80% of the total variation due to temperature.
- V. The remaining part of the variation is most probably coming from a strain induced effect in the friction.
- VI. The effect of the temperature on the material behavior is almost negligible.

Study 3 - Bergström van Liempt Model

The results of the temperature induced variations in the Bergström van Liempt model with full frictional table are now further examined. The temperature development of both the workpiece and the tooling will be analyzed after each step in the deep draw process. Also the flow behavior of the workpiece material is given together with the equivalent stress and strain values of the workpiece.

Full Model - Temperature Development

Given in [Appendix 13 – FEM Study 3 – Bergström van Liempt Model](#) are the temperature developments within the workpiece and the tooling after each subsequent step in the two-step deep draw process. For the original Bergström van Liempt setup, temperature results are given for increments of 20 Kelvin from 293K up to 373K. Within the appendix, the temperature variations are provided for a section of the temperature variations performed in the FEM simulations. This is mainly because the main temperature in both the workpiece and the tooling is similar for smaller temperature increments.

The main observations for the workpiece results are:

- The higher temperatures for the deep draw process in step 1 occur at the flange (top part) and for the redraw in step 2 at the hole (bottom part) of the workpiece material, due to amount of strain hardening that is mainly taking place in those regions.
- The increase in temperature after both deep draw steps is larger compared to the incremental temperature increase of the preheated tooling.
- The temperature increase of the workpiece diminishes for higher increments of 353K and 373K.

The higher temperatures in the workpiece can be concur with friction forces that occur at specific contact points during the deep draw process. At these contact points, the material is drawn and stretched over the tooling, resulting in locally elevated temperature regions, which are shown in [Figure 77](#). The plastic deformation of the workpiece, together with the friction at the contact interfaces, contribute to the increase in temperature.

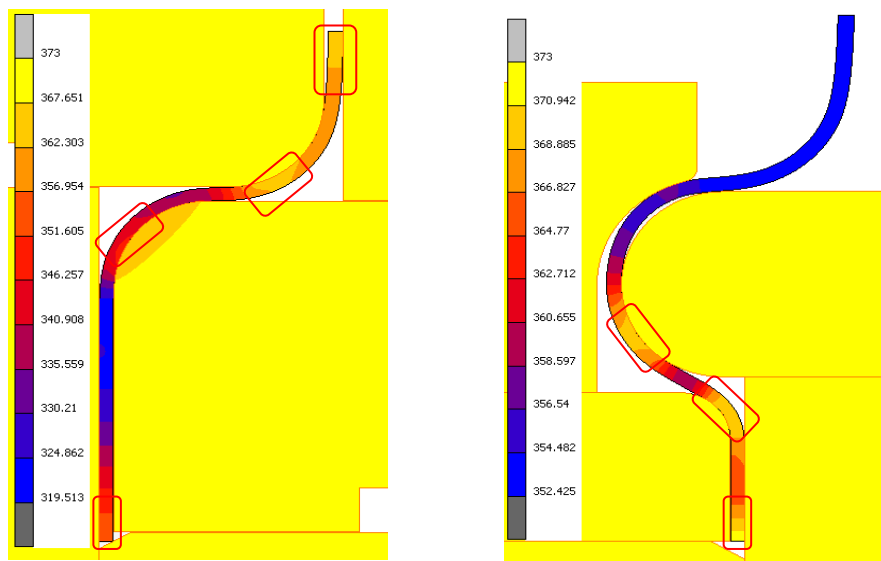


Figure 77 - High temperature areas identified in the workpiece material which correspond with high contact interfaces

For the tooling, the results show that:

- The temperature variations in the tooling after both deep draw steps can be assumed negligible, a maximum increase of approximately 1K is measured.
- The highest temperature increases are located at the die for the deep drawing step and at the punch in the redraw step.
- After step 1 of the deep draw process, a region of increased temperature is noted at the ejector for the temperature increment of 293K. For higher temperatures increments however, the heat flux decreases at the ejector region, resulting in a relatively lower temperature compared to the other tooling.

The peak temperatures in the both the die for step 1 and the punch for step 2 concur with the contact locations identified in [Figure 78](#). The conduction of heat originates from the deformation that is occurring in the workpiece material and the friction at the contact interfaces.

When looking at the temperature behavior at the tooling, it can be seen that for the 293K increment, the ejector region is heated. The main source of the heating originates from the contact interface with the workpiece. For higher temperatures increments however, the heat flux decreases at the ejector region, which occurs when the pre-heating of the tooling exceeds the temperature of the workpiece at the contact interface, resulting in a lower temperature regions as depicted in [Figure 78](#).

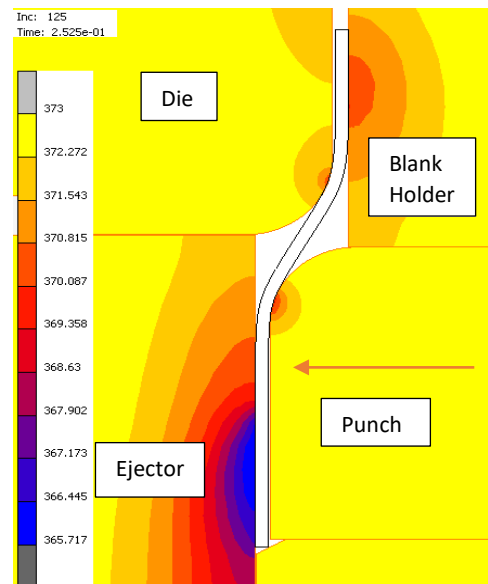


Figure 78 - Temperature decrease of the ejector for higher temperature increments

Full Model - Frictional Contact Points

The development of the main frictional contact patches are captured during the FEM analysis. An overview of the contact results is provided in [Appendix 13](#) – FEM Study 3 – Bergström van Liempt Model for the temperature variations of 293K, 333K and 373K.

When comparing the frictional contact results in [Appendix 13](#) – FEM Study 3 – Bergström van Liempt Model with the movement of the punch that is illustrated in [Figure 79](#) and [Figure 80](#), the following observations can be made:

- The main points of contact that are established and where a high coefficient of friction is developed are at the Worktool-Punch and Worktool-Die contact interface, which is mainly attributed by the movement direction of the punch and the movement of the workpiece that is drawn over the die.
- The occurring regions are identified in theoretical framework as region 3-4 and 5-6 section - [Deep Drawing Process](#), which attribute high amounts of pressure and strain occurring in these regions.

At the end of each different step in the two-step deep draw process, an overview is given together with magnified sections of importance.

As can be seen between the results at the starting temperature variations of 293K, 333K and 373K, minimal differences are noted considering the positions of the frictional contact patches with the highest coefficient values. This is also expected due to the constant geometrical properties that are used.

Consequently, by applying the theory from the adapted frictional model of J. Hol [6], relatively high strains, tangential movement and nominal pressures can account for an local temperature differences and a high coefficient of friction. These regions are identified at the contact points in [Figure 79](#) and [Figure 80](#).

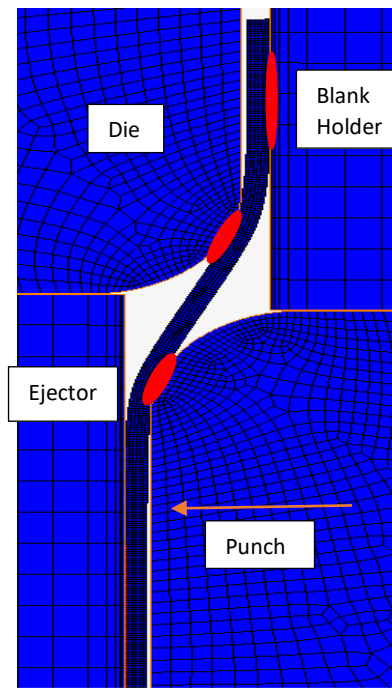


Figure 79 - Overview of Step 1 in the two-step deep draw process

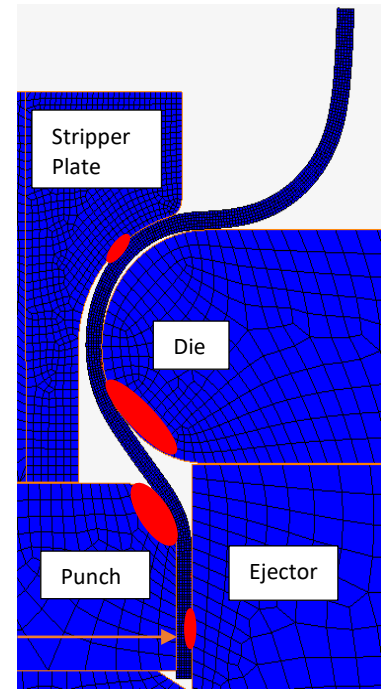


Figure 80 - Overview of Step 2 in the two-step deep draw process

Full Model - Material Displacement Workpiece

An overview of the material displacement after each deep draw step is provided in [Appendix 13 – FEM Study 3 – Bergström van Liempt Model](#), which is illustrated as the displacement of the material in the Y-direction. The temperature differences in the Y-direction is represented for the temperatures variations of 293K, 333K and 373K. When comparing the results for each temperature variation, it can be noted that:

- For the first deep draw step, the dominant region of material displacement occurs at the outsides of the blank towards the punch impacting the flange diameter, being a logical and wanted outcome of a deep drawing process.
- For the second redraw step, the dominant region of material displacement occurs at the die region (negative Y-displacement) together with material displacement from the center hole region (positive Y-direction). Both regions are showed in [Figure 81](#) and [Figure 82](#).
- For increased temperatures, the inward material displacement in the outer flange region slightly decreases and in the inner hole region slightly increases after the first deep draw steps. However, it is also noted that in the second deep draw step, the displacement in the hole region decreases for higher temperatures, overruling the effect of the first step. This effect is confirmed by looking at the trend lines of the full model of [Figure 74](#) and [Figure 75](#) in the sensitivity analysis.

The influence of different temperatures on the locations of the main displacement regions are negligible. However, the variations in temperature do impact the amount of material displacement. This can mainly be explained by the Bergström van Liempt parameter included in the FEM solver model which slightly reduces the hardness of the material and the increasing friction of material for higher temperatures.

The reduced hardness of the material will result in a more deformable material which allows for increased straining. This effect will be determined in the strain section. The increase in friction will result in more resistance of the workpiece material to the drawing movement of the punch.

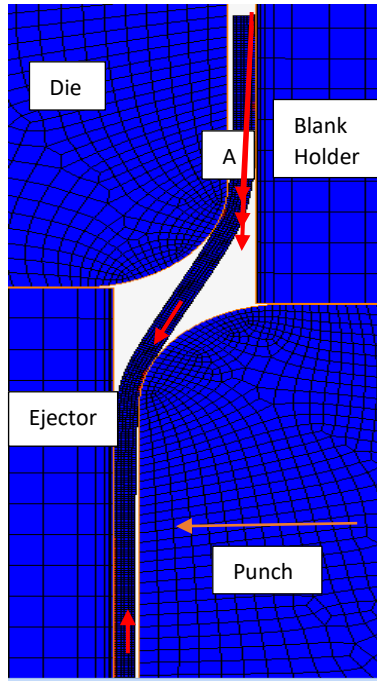


Figure 81 - Overview of Step 1 in the two-step deep draw process

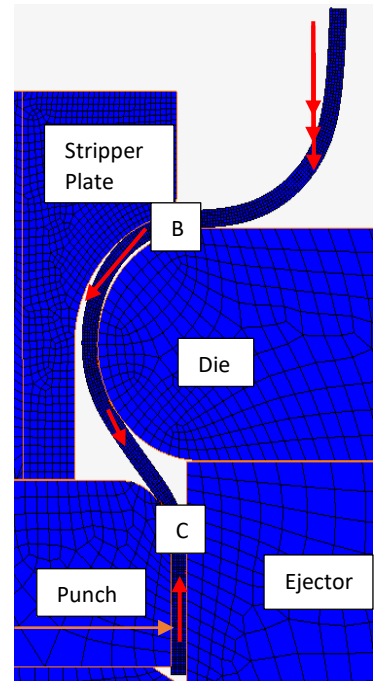


Figure 82 - Overview of Step 2 in the two-step deep draw process

The combination of both effects result, for elevated temperatures, in a decrease of the final hole diameter and an increase in the final flange diameter compared to the 293K case.

Full Model - Equivalent Cauchy Stress Development

An overview of the equivalent Cauchy stresses before and after unloading of the workpiece is provided in [Appendix 13 – FEM Study 3 – Bergström van Liempt Model](#) for the temperature variations of 293K, 333K and 373K. The main observations that are noted when comparing the results are:

- For both steps in the deep draw process, the overall stress development occurs at the die-workpiece and die-punch region for every friction model.
- The highest equivalent Cauchy stress developments occur at the regions where the workpiece is deformed when in contact with the die and the punch interface.
- The highest equivalent Cauchy stresses that develop within the workpiece decrease for higher temperature increments.

The overall stress development regions within the workpiece are similar for every FEM simulation, this is mainly due to the process parameters and the geometrical properties, which are held constant for every increment.

The high equivalent Cauchy stresses that occur within the workpiece are occurring at the places where the material is stretched over the punch or die radius. This is illustrated in [Figure 83](#) and [Figure 84](#) and is in agreement with the theoretical deep draw regions of section - [Deep Drawing Process](#).

The peak equivalent Cauchy stress values occurring within the workpiece decrease for higher temperatures. This is mainly due to the contribution of the Bergstrom van Liempt model, which reduces the hardness of the material under higher temperatures.

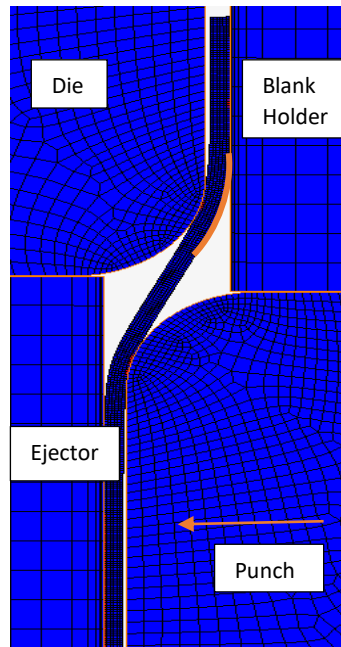


Figure 83 - Overview of Step 1 in the two-step deep draw process

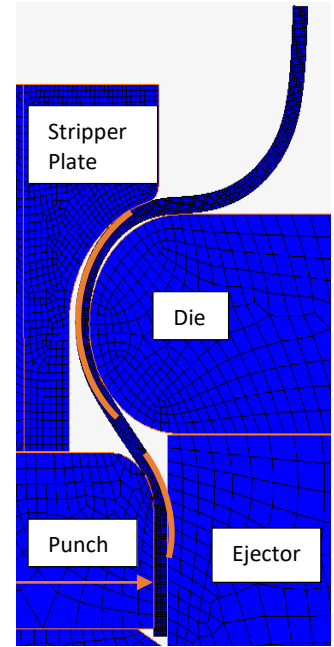


Figure 84 - Overview of Step 2 in the two-step deep draw process

Full Model - Total Equivalent Strain Development

The development of the total equivalent strain within the workpiece material is captured within the FEM analysis. When comparing the results for the temperatures variations of 293K, 333K and 373K in [Appendix 13 – FEM Study 3 – Bergström van Liempt Model](#), the following observations can be made:

- The general regions where the equivalent strain development occurs in the workpiece are similar for the temperature variations.
- The highest total equivalent strain developments occur at the regions where the workpiece is drawn into the desired shape over the die radius in step 1 and over the punch in step 2 of the deep draw process
- The highest total equivalent strains within the workpiece decrease for higher temperature increments.

An overview of the general total equivalent strain development in the workpiece is provided in [Figure 85](#) for both steps in the deep draw process.

For both steps in the deep draw process, the overall strain development is similar for each friction model. The maximum total equivalent strain values however decrease for increasing temperature variations.

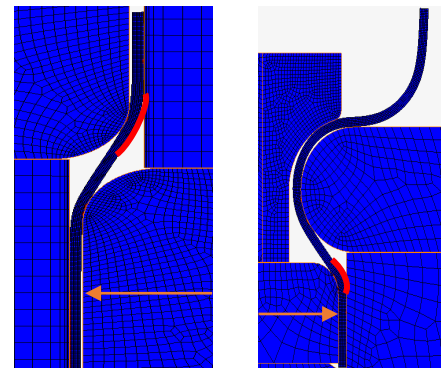


Figure 85 - The main contact interfaces provided for both steps in the deep draw process

Study 4 - Friction Model Variations - Roughness, Lubrication

This study will compare the results of the Bergström van Liempt model with full frictional table for different tribological variations, considering the impact of a different tooling roughness and lubrication thickness in for the two-step deep draw process. The Bergström van Liempt variations are provided in [Table 8](#) below.

Table 8 - Bergström van Liempt variations

Workpiece Roughness Sa [μm]	Lubricant Thickness [g/m ²]	Tooling Roughness Sa [μm]	<i>Temperature dependent contact heat transfer coefficient</i>
0.35	2	0.02	
0.35	2	0.05	
0.35	7	0.02	
0.35	7	0.02	
0.35	7	0.05	

The results of the different FEM studies, considering the impact of the workpiece roughness, lubrication thickness and the tooling roughness, will now be discussed for with the outcomes of the Bergström van Liempt model with full frictional table. First, the general impact of the roughness and lubrication variations on the change in the flange and hole diameter development will be compared. Subsequently, the temperature development, total displacement in the Y-direction, equivalent Cauchy stress and total equivalent strain development in the workpiece will be further analyzed in the sections below.

The results of the variation study on the Bergström van Liempt model is given in [Appendix 14 – FEM Study 4 – Bergström Variations](#). A general overview of both the flange and the hole development under different temperatures is provided in [Figure 86](#) and [Figure 87](#) below.

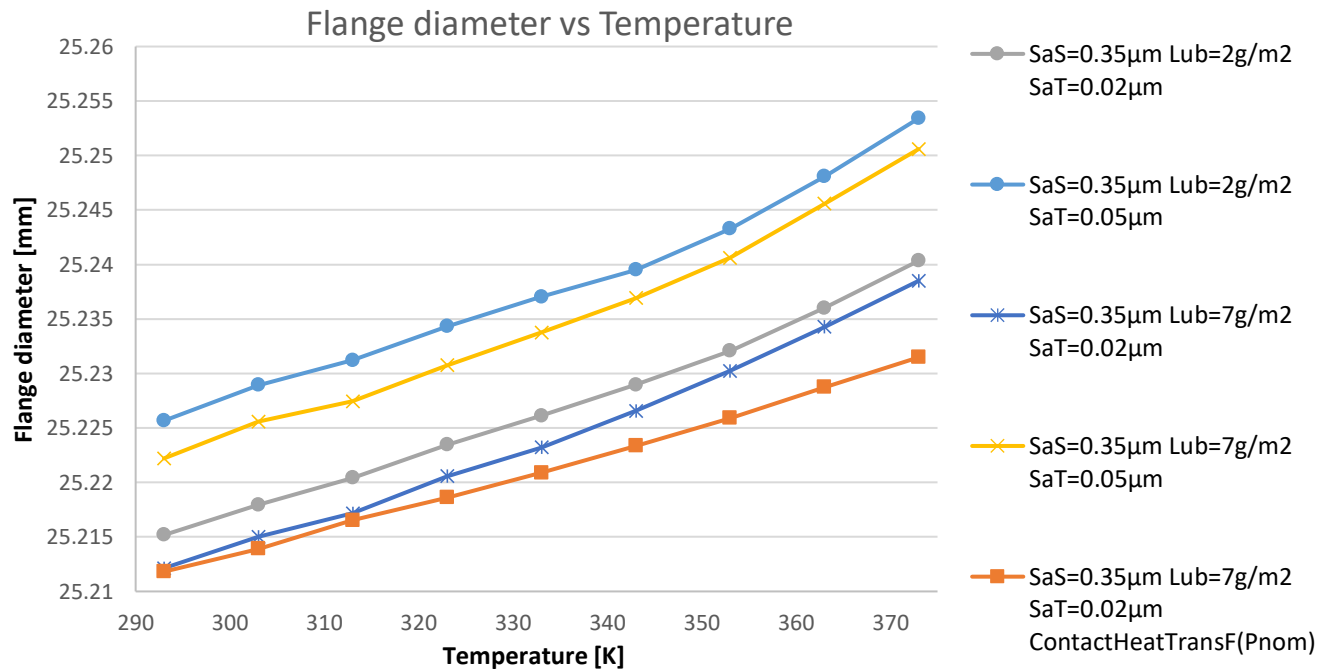


Figure 86 - Variation analysis of the hole diameter development for different temperature variations

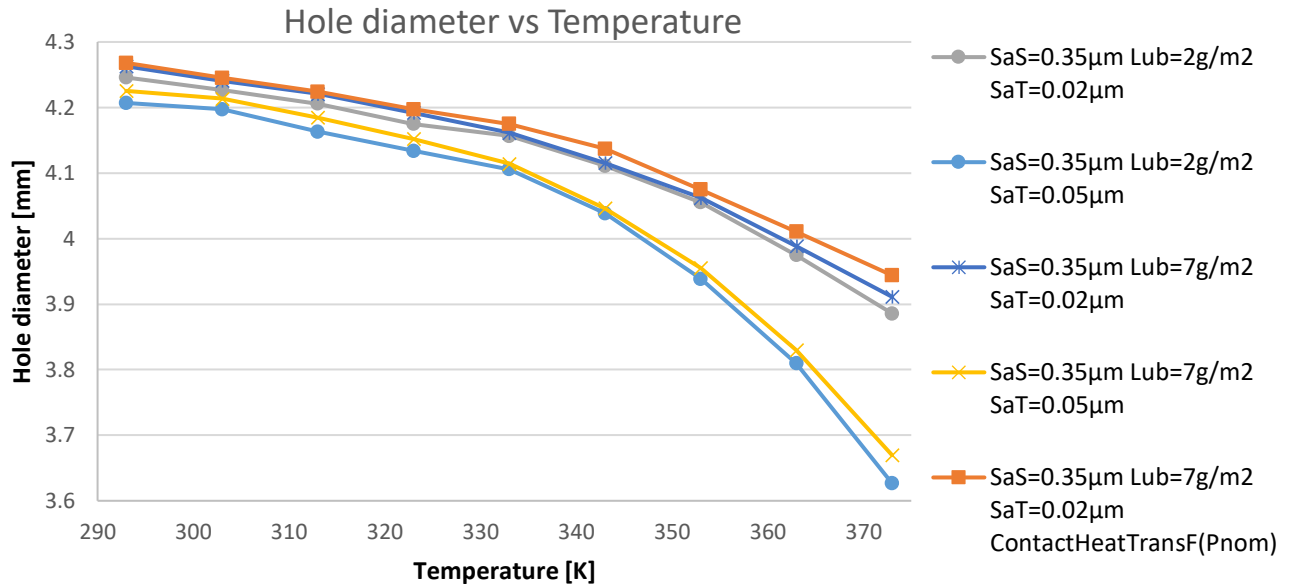


Figure 87 - Variation analysis of the hole diameter development for different temperature variations

When analyzing the results of the Bergström variations, the following main observations can be made:

- When looking at all the variations, it can be noted that for higher temperature increments the final hole diameter decreases and the final flange diameter increases.
- When looking at the overall development of both the hole and the flange diameter, it can be observed that the variations in tool roughness (the *light Blue line* and *Yellow line*) have the largest impact on the development, which seem to increase for higher temperature increments.
- When comparing the development of the flange and the hole diameter, it can be noted that the flange exhibits a relatively higher sensitivity for both the lubricant and the tool roughness variations.
- Furthermore, it can be noted that the impact of the lubricant thickness variations is less dominant compared to the impact of the tool roughness variations. This can be seen when comparing the *Yellow line*, *light Blue line*, *Grey line* and *dark Blue line*, which have the same tool and workpiece roughness values but a different lubricant thickness.

Besides the flange and hole diameter development within the deep draw process, also the results of the temperature development within the workpiece, total material displacement in the Y-direction, the equivalent Cauchy stress and the total equivalent strain are provided in [Appendix 14 – FEM Study 4 – Bergström Variations](#).

Variations – Temperature Development

The results of the temperature development within the workpiece material show very small deviations of approximately 5K for the roughness and lubrication variations. Also, all variations exhibit a similar gradual increase in the workpiece temperature for higher temperature increments.

Variations – Material Displacement

For the material displacement in the Y-direction, notable differences in material behavior are observed. The main observation is that after both deep draw steps: the maximum material displacement in the flange region (negative direction) and the hole region (positive direction) is relatively decreasing for higher temperature increments. This concurs with the behavior noted in [Figure 86](#) and [Figure 87](#), which shows that the flange increases and the hole decreases relatively for higher temperatures.

However, for the hole region this effect is reversed in the first draw step. Instead, a relative increase of the material displacement is noted at the hole region for higher temperature increments during the first deep draw step.

This shows that the hole diameter increases relatively during the first deep draw step for higher temperature increments. Consequently, this behavior is amplified within the variations with higher tooling roughness values from which it can be concluded that the contact interfaces and friction are contributing to this effect.

Variations – Equivalent Cauchy Stress

An overview of the provided equivalent Cauchy stress development of the workpiece is provided in [Appendix 14 – FEM Study 4 – Bergström Variations](#) for the temperature variations of 293K, 333K and 373K. Again, the overall stress development occurs at the die-workpiece and die-punch region for every friction model variation. The lowest stress values remain constant for both steps in the deep draw process and the stress values are not affected by any lubricant or roughness variations.

The highest equivalent Cauchy stresses that develop within the workpiece are generally decreasing for higher temperature increments. This effect is more distinct for the first deep draw step compared to the second step. Within the second drawing step, a decreasing trend is found for higher temperature increments up to 353K. For the increments of 363K and higher, the workpiece instead shows an increase in the development of maximum equivalent Cauchy stresses. An explanation for the first decreasing then increasing Cauchy stress development is that strain hardening is decreasing in the temperature region toll 353K, but for higher temperature the increased friction causes some localization in the straining, causing a peak value to increase, despite the lower strain hardening.

Variations – Equivalent Strain Development

The strain development within the workpiece for different roughness and lubrication thickness variations are provided in [Appendix 14 – FEM Study 4 – Bergström Variations](#). In the results, a general increase of the strain values is observed for the lower values in the workpiece. Consequently the higher strain values in the workpiece remain constant for the first deep draw step and are generally decreasing within the second deep draw step of the process. This effect is most notable for the higher tooling roughness variations, which concurs with the increase of frictional forces at higher temperatures. The increase of friction increases the resistance of material flow during the deep draw process and consequently has a negative effect on the amount of strain development.

Validation

Due to confidentiality issues, this page cannot be viewed.

For more information, please contact: r.m.nienhuis@student.rug.nl

Validation Results

Due to confidentiality issues, this page cannot be viewed.

For more information, please contact: r.m.nienhuis@student.rug.nl

Conclusion

The sensitivity of temperature induced frictional behavior was mapped within the MSC Marc solver by implementing an adaptation on the model of J. Hol within the FEM simulations. The 4D frictional look-up table aims towards an equilibrium between the computation time and the quality of the results. The main goal of this project was to determine the impact of the temperature-induced friction on the workpiece in the two-step deep draw process.

In order to be able to determine the impact of temperature on the deep draw process, first the general parameters affecting friction on the workpiece were identified. An initial study was performed which compared different basic frictional models available in the MSC Marc solver, for a temperature of 293K.

The results show that the flange diameter is largely influenced in the first step where the hole diameter is largely influenced during the second step. In general, both the flange and hole diameter development is influenced by friction which is prone to temperature changes, which stresses the need for complementary studies with the temperature induced Bergström van Liempt model and the 4D frictional look-up table.

In the subsequent studies, the flange and hole diameter development were simulated for temperature increments of 293K up to 373K, where the process is assumed to develop into a steady state. A sensitivity was performed to check the initial assumption for the temperature sensitivity of friction, subsequently a more in depth study of the Bergström van Liempt model with full friction table was performed.

The sensitivity analysis results confirm the dominance of temperature on the frictional behavior over the influence of material properties, which is concluded to be minimal for the current deep draw set-up.

The total temperature dependency of friction alone takes up ~80% of the total variation in the development of the flange and hole diameter. The other ~20% accounts for the strain hardening behavior all micro-contacts of the workpiece material. This can be explained by that the increase in temperature, results in softening of the material and an increase of surface contact between the tooling and workpiece material. Consequently, an increase of friction increases the resistance of material flow during the deep draw process and consequently has a negative effect on the amount of strain development.

The results of the Bergström van Liempt model with full frictional table show that an increase in temperature will result in an increase of friction and a decrease in temperature will result in a decrease of friction. Consequently, a higher amount of friction during the deep draw process results a relative decrease of the final hole diameter and a relative increase in the final flange diameter.

A more in depth analysis of the material displacement show that for increased temperatures, the inward material displacement in the outer flange region slightly decreases and in the inner hole region slightly increases after the first deep draw steps. This is mainly attributed to the dominant contact points that were identified at the die-punch interface.

Furthermore, it is also noted that in the second deep draw step, the displacement in the hole region decreases for higher temperatures, overruling the effect of the first step. This illustrates the complex behavior well of a tribological system with a wide arrange of different influencing parameters.

The highest equivalent Cauchy stress developments occur at the regions where the work piece is deformed when in contact with the die and the punch interface. Also, the highest equivalent Cauchy stresses that develop within the workpiece decrease for higher temperature increments. This coincides with the influence of the Bergström van Liempt model, lowering the workpiece material hardness for higher temperature increments.

The highest total equivalent strain developments occur at the regions where the work piece is drawn into the desired shape over the die radius in step 1 and over the punch in step 2 of the deep draw process. This coincides with the identified material behavioral regions in section - [Deep Drawing Process](#). Furthermore, it was observed that the highest total equivalent strains within the work piece decrease for higher temperature increments. Again, this coincides with the influence of the 4D frictional look-up table, where higher temperatures result in higher friction values and therefore less strain.

An additional study was performed, identifying the impact of the tooling roughness and lubricant parameters on the frictional behavior during the two-step deep draw process. It is observed that for both the hole and the flange region, the tool roughness variations have the largest impact on the diameter development, which increases for higher temperature increments. Also, when comparing the development of the flange and the hole diameter, it can be noted that the flange exhibits a relatively higher sensitivity for both the lubricant as the tool roughness variations.

Based on the theoretic framework, an explanation can be made for the obtained results of the lubrication and roughness variations. Increasing the tooling roughness results in an increase of friction at the contact interfaces with the work piece material. Less material movement is developed during the deep draw process which results in a relative increase of the flange diameter and a relative decrease of the hole diameter. Next to that, the higher temperatures cause a drop in the viscosity of the lubricant, reducing its load carrying capacity. Higher tool roughness values, result in an increased impact of the temperature on hole and flange diameter. The opposite effect is shown for the increase in lubricant thickness, when applying an increased amount of lubricant between the tool-work piece contact interface, less friction is generated during the deep draw process.

Another goal of this study was to identify the fit between the results of the FEM simulations and the real case within the demonstrator line. Unfortunately, the original demonstrator line could not be realized. Instead, an alternative validation was performed to check the quality of the implemented frictional model and indirectly the provided FEM results. For this, a one-step Erichsen stretching process in the Philips Pressto case was used, which exhibits similar workpiece deformations to the two-step deep draw process. The obtained Pressto workpiece was scanned by the Alicona measurement system and the final outline was compared with the final deformation in the simulated workpiece.

The validation results show that a good fit is determined between the deformation in the FEM simulation and the real life workpiece deformation for the 323K temperature increment. On the validation results of the Pressto case, one can state the outcomes using the ASPECT approach are exactly as expected and fit the empirical results really well.

In conclusion, the simulations of the modified Bergström van Liempt model show good results in the prediction the frictional behavior during the warm-up period of a deep draw process. The roughness and lubrication variations together with alternative validation add to the applicability of the FEM model in other metal forming processes. However, a full validation is still required to completely validate the model and enable the development of control parameters that can minimize the product variations in the warm-up period.

Discussion

As stated in the conclusion, the simulations of the modified Bergström van Liempt model show promising results in the prediction the frictional behavior during the warm-up period of a deep draw process. However, a full validation of the results is needed before a definitive conclusion can be given, considering the fit with the real-life frictional behavior in the deep draw process.

Another point of attention that needs to be considered is the multi-disciplinary approach used in ASPECT itself. Without this approach the current level of generated knowledge would not been possible, however, this working structure stresses the need for extreme caution due to it being prone of accumulating small assumptions over time. The many parameters that come together into FEM simulations are very dependable on the quality of deliverables and measurement in the pre, which can lead to unwanted behavior and fuzzy outcomes when added together.

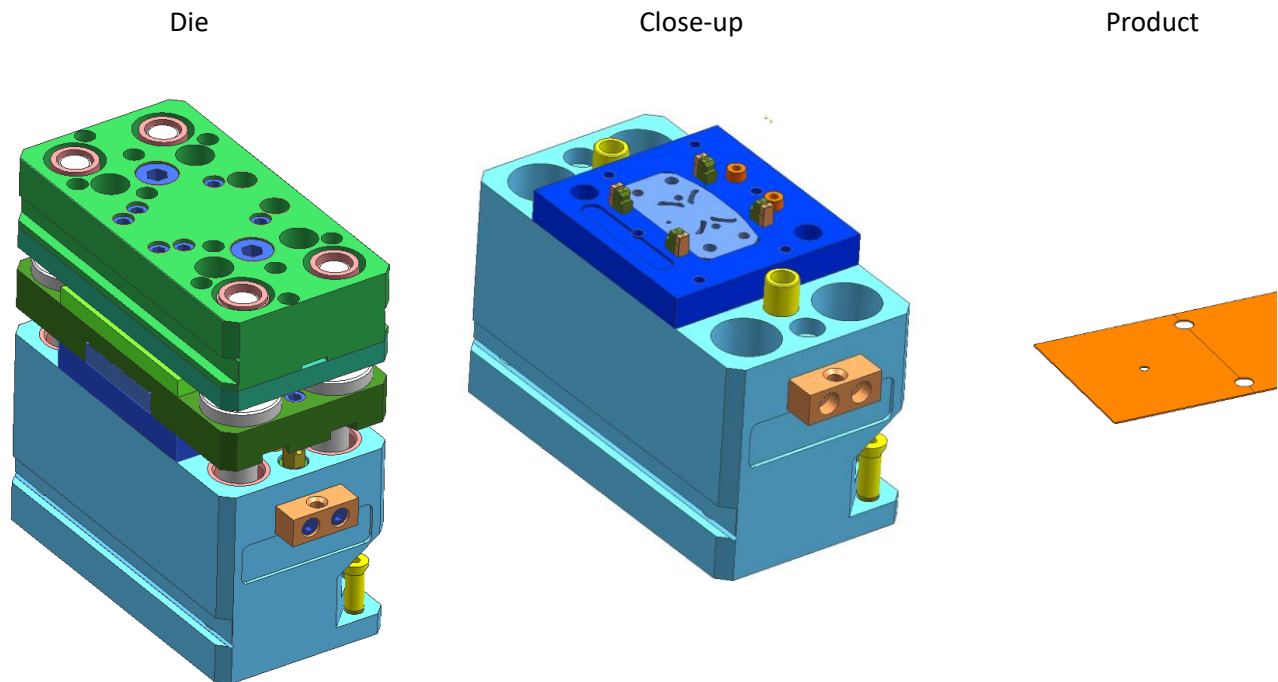
The introduced temperature-dependent frictional model can be praised for its balance between computability and complexity, this project showed in a way the main difference of the science and business development point of view. Where science has a tendency to explain everything there is to find, the business industry approaches this in a more efficient manner and is mainly focusing for the most significant contributors. This can lead, for science, to over explanation of non-existent variables and for business can lead to underestimation of important parameters. This research project provides a good balance between these two doctrines and can be seen as an excellent example of having the 'best of both worlds'.

Appendix

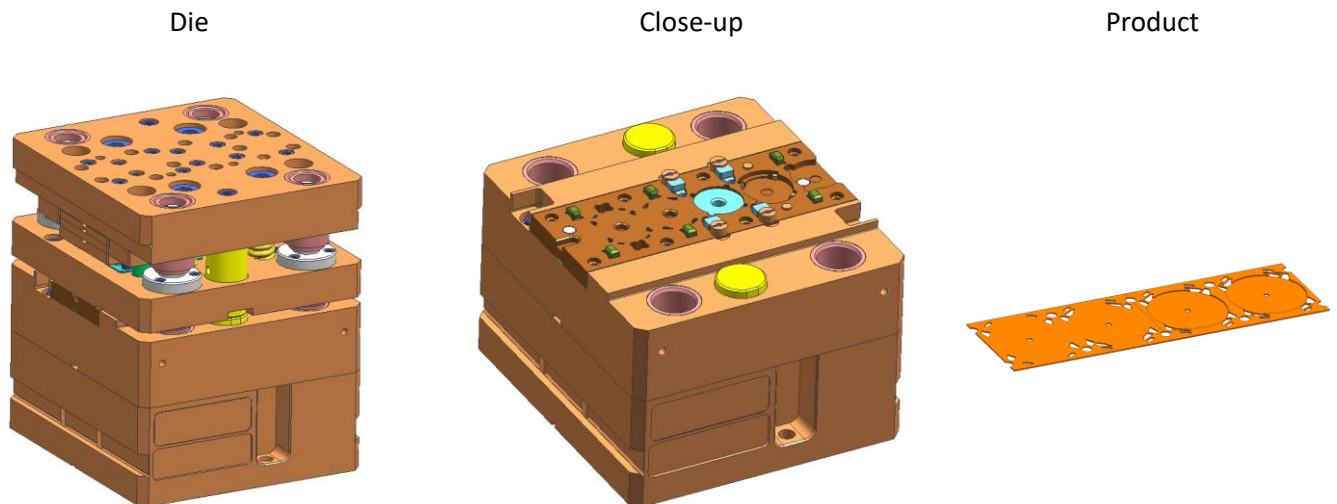
Appendix 1 – Tooling Two-Step Deep Draw Process

Preprocess

Cutting die for positioning holes and the center hole of the blank [3]:



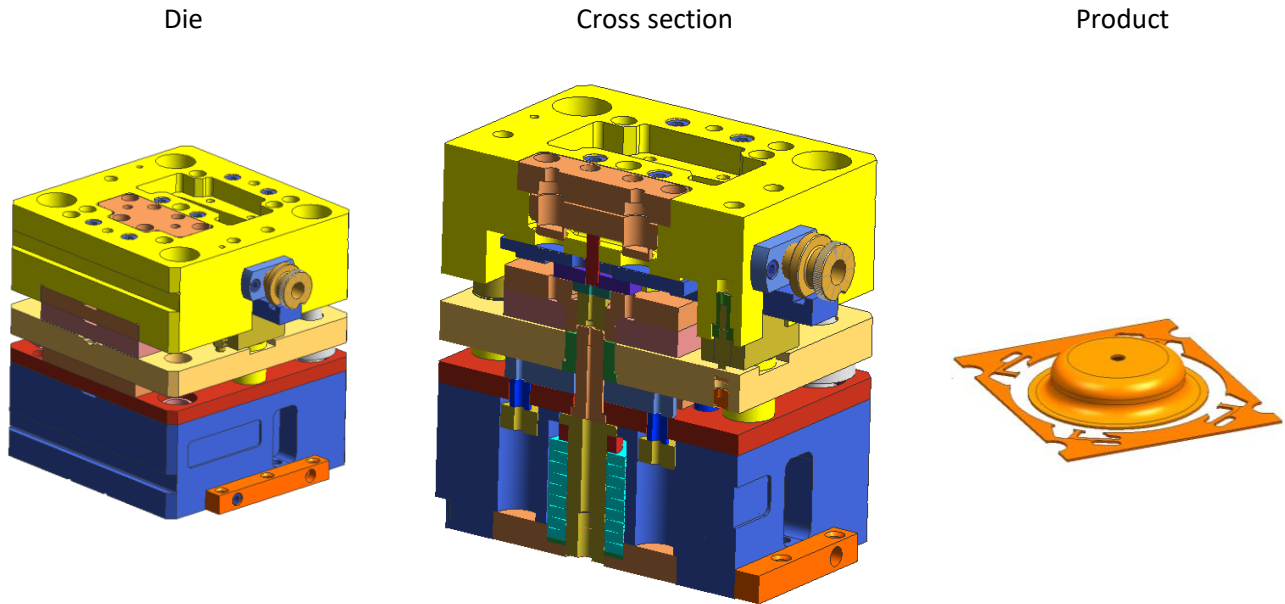
Cutting die for separating blank from strip [3]:



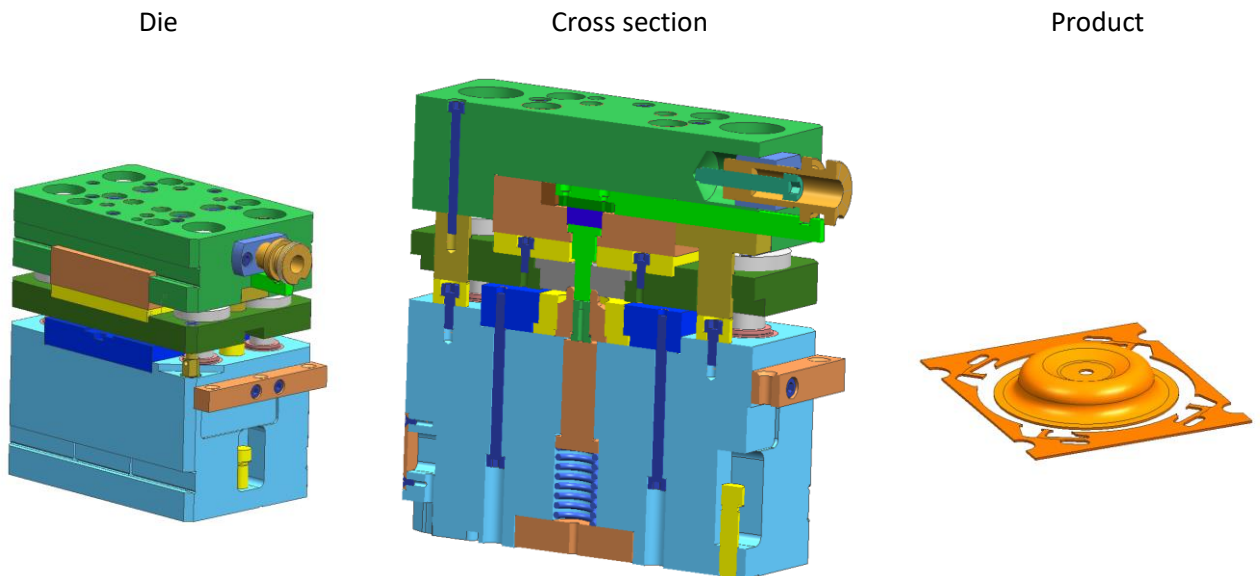
Deep draw process

Deep draw die for forming the blank material into the desired cup shape [3]:

Step 1 – Cupping step



Step 2 – Redrawing step [3]:



Appendix 2 – Adhesion Formula's

Bowden and Tabor [93] provided a rough classification to formulate the friction of coefficient for different contact pairs. In their research it was noted that for strong adhesion in a tribological contact both compression and tensile stresses are present. The tensile and compressive stresses can be defined as [93] [145]:

$$H = 3 \cdot \sigma_c \quad \text{- Compressive} \quad (65)$$

$$H = \zeta \cdot \sigma_c, \quad \text{- Tensile, where } \zeta < 3 \quad (66)$$

The following approximation results in the following formula for the coefficient of friction [93] [145]:

$$\mu_{adhesion} = \frac{\tau \cdot (A_{comp} + A_{ten})}{H \cdot (3A_{comp} - \zeta A_{ten})} \quad (67)$$

From this equation, assuming $\tau \approx \frac{H}{\sqrt{3}}$, we obtain the approximation for plastic isotropic materials [93] [145]:

$$\mu_{adhesion, approx} = \frac{1}{\sqrt{3}} \cdot \left(\frac{A_{comp} + A_{ten}}{3A_{comp} - \zeta A_{ten}} \right) \quad (68)$$

With this approximation, a rough classification can be made based on the material properties of the contact pairs combined with external factors that influence the adhesion. The three most notable situations are discussed below.

Pure metals with minimal lubrication

In this situation, the A_{ten} will become negligible due to a minimal layer of lubricant being present between the contact surfaces will inhibit the metallic adhesion. This results in a coefficient of friction which is characteristic for dry friction between metals under 'normal conditions' and can be defined as being in the order of [89] [98] [146] [147] [145] [145]:

$$\mu_{adhesion} = \frac{1}{3\sqrt{3}} \approx 0.19 \quad (69)$$

Pure metals with oxides

For this case, the adhesion force will be considered strong with a similar compressive and tensile component present. A coefficient of friction can be approximated within the range of 0.6, for hexagonal crystal lattices and up to 1.2, for cubic lattices. With the expression is [89] [98] [146] [147] [145] [145]:

$$\mu_{adhesion} = \frac{1}{\sqrt{3}} \left(\frac{2}{3 - \zeta} \right) \approx 0.6 \sim 1.2, \quad \forall \zeta = 1 \sim 2 \quad (70)$$

Pure metals with thin sheet of soft metal

For this situation the standard equation can be used. The clear difference in surface hardness results in a lower friction coefficient compared to pure metals with a value of 0.1 or smaller [89] [98] [146] [147] [145].

Appendix 3 – Deformation Formula's

Ploughing - Spherical asperities

For spherical asperities, the following ploughing effects are determined [39] [93] [148]:

Load supporting area:

$$A_1 = \frac{1}{8} \pi d^2 \quad (71)$$

Ploughing contact area:

$$A_2 = \frac{1}{2} R^2 (2\theta - 2 \sin 2\theta) \quad (72)$$

Which results in a coefficient of friction due to ploughing of spherical asperities:

$$\mu_{ploughing,conical} = \frac{F_{adhesion}}{F_N} = \frac{p^* \cdot A_2}{p^* \cdot A_1} = \left(\frac{4R^2}{\pi d^2} \right) \left(\frac{2\theta - 2 \sin 2\theta}{\pi d^2} \right) \quad (73)$$

Ploughing - cylindrical asperities

For the cylindrical asperities, two different cases can be distinguished which depends on whether the contact is applied in the transvers or upright position of the cylindrical asperity [39] [93] [148].

Load supporting area:

$$A_{1,transverse} = L \cdot \sqrt{[(2R - \delta) \cdot \delta]} \quad \text{and} \quad A_{1,upright} = \pi R^2 \quad (74)$$

Ploughing contact area:

$$A_{2,transverse} = L \cdot \delta \quad \text{and} \quad A_{2,upright} = 2R \cdot \delta \quad (75)$$

Which results in a coefficient of friction due to ploughing of spherical asperities:

$$\mu_{ploughing,transverse sphere} = L \cdot \sqrt{\left[\frac{1}{2 \left(\frac{R}{\delta} \right) - 1} \right]} \quad (76)$$

$$\mu_{ploughing,upright sphere} = \left(\frac{2}{\pi} \right) \left(\frac{\delta}{R} \right) \quad (77)$$

Ploughing - Conical asperities

For conical asperities, the following ploughing effects are determined [39] [93] [148]:

Load supporting area:

$$A_1 = \frac{1}{8} \pi d^2 \quad (78)$$

Ploughing contact area:

$$A_2 = \frac{1}{4} d^2 \cot \theta \quad (79)$$

Which results in a coefficient of friction due to ploughing of conical asperities:

$$\mu_{ploughing,conical} = \frac{F_{adhesion}}{F_N} = \frac{p^* \cdot A_2}{p^* \cdot A_1} = \left(\frac{2}{\pi} \right) \cot \theta \quad (80)$$

The total external energy for indenting the contact asperities in a boundary lubricated contact situation is given by [6]:

$$W_{ext} = F_N \cdot \omega \quad \text{with} \quad \omega = \frac{\sum_{k=1}^{N+N^*} (F_{N,k} \cdot \Delta z_k)}{F_N} \quad \text{stochastic form} \quad (81)$$

J. Hol [6] identifies three internal energy mechanisms, which together describe the total internal energy in a boundary lubricated contact situation [6]:

$$W_{int} = W_{int,ab} + W_{int,ri} + W_{int,sh} \quad (82)$$

- I. $W_{int,ab}$ - the energy absorbed by the $N + N^*$ contacting bars which are externally crushed due to normal loading is defined by [6]:

$$W_{int,ab} = B \cdot \gamma \quad \text{with} \quad \gamma = \Delta A \cdot \sum_{k=1}^{N+N^*} \sigma_{y,k} \cdot \Delta z_k \quad \text{stochastic form} \quad (83)$$

With:

- B - The experimentally obtained Brinell hardness parameter
- ΔA - The tool-workpiece contact area of the bars
- $\sigma_{y,k}$ - The yield strength of the workpiece material

To account for work-hardening effects during the crushing of asperities, the change in the yield strength is given by $\int \sigma_{y,k}(\varepsilon) d\varepsilon$. An approximation is used for computational efficiency, resulting in [6]:

$$\int \sigma_{y,k}(\varepsilon) d\varepsilon = \sigma_{y,k}(\xi \varepsilon) \quad (84)$$

Where the value of $\xi = 0$ gives the initial yield strength and $\xi=1$ gives the final yield strength including the work hardening effect.

- II. $W_{int,ri}$ - the energy required for material flow and raising the bars $N^* + N^{**}$, is given by [6]:

$$W_{int,ri} = \eta \cdot B \cdot \beta \quad \text{with} \quad \beta = \Delta A \left(\sum_{j=1}^{N^*} \sigma_{y,j} \cdot \Delta u_j + \sum_{j=1}^{N^{**}} \sigma_{y,l} \cdot \Delta u_l \right) \quad \text{stochastic form} \quad (85)$$

With:

- η - The persistence parameter based on the amount of energy required to lift the non-contacting asperity bars:
 - $\eta = 0$ – No energy required to raise non-contacting bars
 - $\eta = 1$ – Energy required to raise non-contacting bars is the as for crushing bars
- $\sigma_{y,j}$ - The yield strength of the workpiece material

- III. $W_{int,sh}$ - the energy present between contacting bars $N + N^*$ due to shearing under a relative motion, given by [6]:

$$W_{int,sh} = S \cdot \psi \quad \text{with} \quad \psi = \left(1 - \frac{A_{real}}{A_{nom}} \right) \cdot n_s \cdot w \cdot \sum_{j=1}^{N^{**}} \sigma_{y,k} \cdot \Delta s_k^2 \quad \text{stochastic form} \quad (86)$$

With:

- S - Shear parameter, determined by the Von Mises Criterion as $S = \frac{1}{\sqrt{3}}$
- n_s - Half the amount of surrounding bars
 - $n_s = 1$ – For a plain strain simulation
 - $n_s = 2$ – For a 3D simulation
- w - The width of a bar
- Δs - The shearing distance

The Shearing distance can be described by a summation of the distance between a raising bar - U_L and the neighboring crushing bar - $(z - d_L)$ giving the relation [6]:

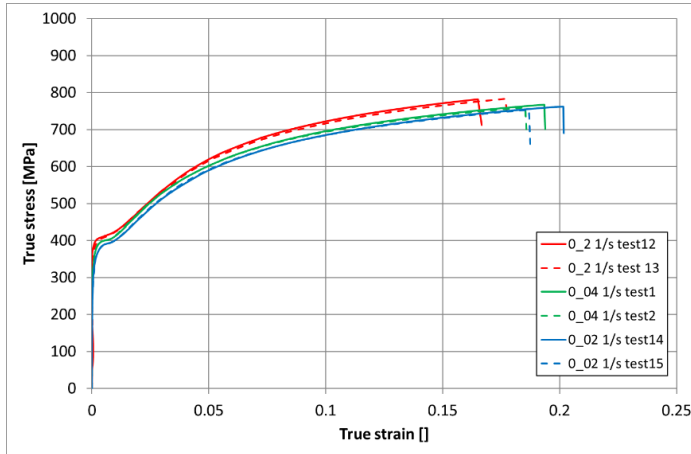
$$\Delta s = z - d_L + U_L \quad (87)$$

Appendix 4 – Material Behavior AISI 420

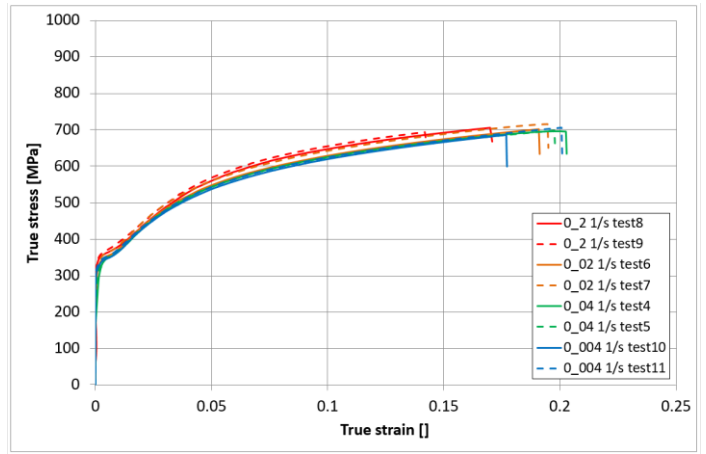
Tensile tests results

Measured material behavior of AISI 420 by Falex [12]:

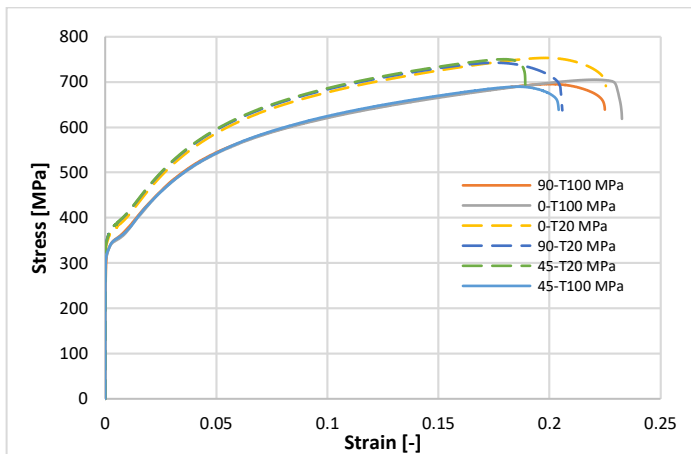
- | | | |
|------|----------------------|--|
| I. | Varying temperatures | 20°C, 60°C, 100°C and 140°C, 180°C, 220°C |
| II. | Strain rates: | 0.004 s ⁻¹ , 0.02 s ⁻¹ , 0.04 s ⁻¹ , 0.02 s ⁻¹ , 0.2 s ⁻¹ |
| III. | Orientations | 0°, 45°, 90° |



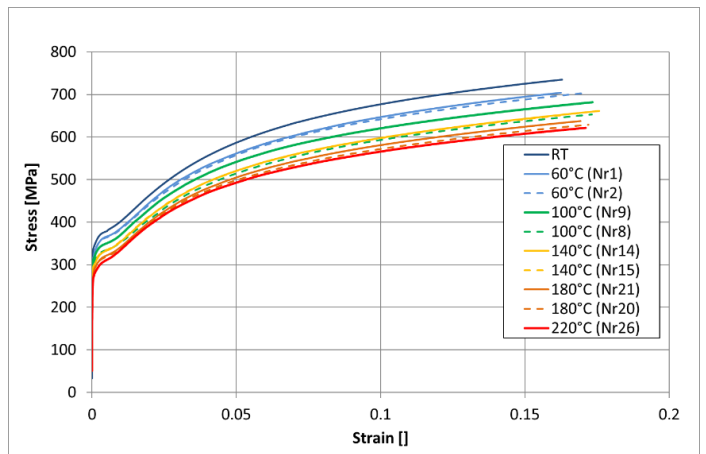
Results of tensile tests at room temperature and different strain rates (0.02-0.2 1/s) [12].



Results of tensile tests at 100°C and different strain rates (0.004-0.2 1/s) [12].



Results of tensile tests at 20°C and 100°C and different orientations at strain rate of 0.004 (1/s) [12].



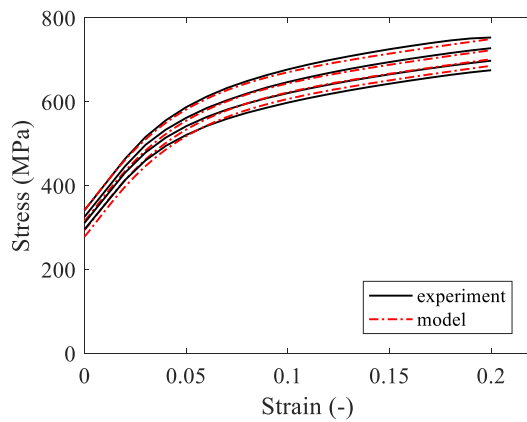
Results of tensile tests at different temperatures and the strain rate 0.004 (1/s), RT: room temperature (20°C) [12].

Calibrated Material Behavior Model

Calibrated material behavior by Falex [12]:

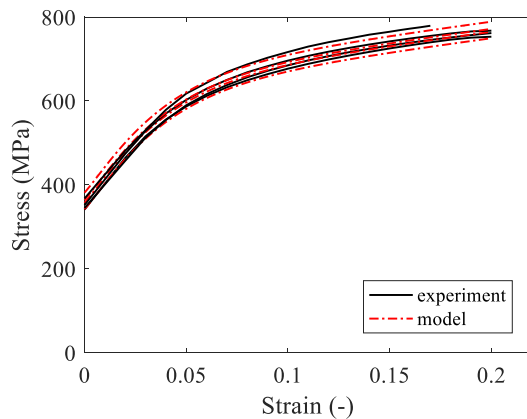
- | | |
|-------------------------|---|
| I. Varying temperatures | 20°C, 60°C, 100°C and 140°C, 180°C, 220°C |
| II. Strain rates: | 0.004 s^{-1} , 0.02 s^{-1} , 0.04 s^{-1} , 0.02 s^{-1} , 0.2 s^{-1} |

Calibrated numerical flow curves compared with experimental ones [12]:



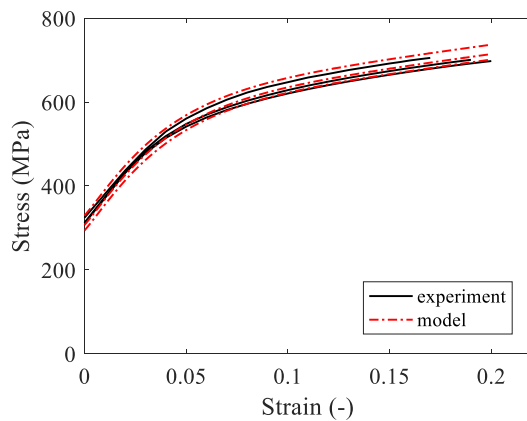
- a) Temperature effect on flow stress at a constant strain rate.

Temperature = [20 60 100 140] °C
at 0.004 s^{-1}



- b) Strain rate effect on the flow stress at room temperature.

Strain rates = [0.004 0.02 0.04 0.2] s^{-1}



- c) Strain rate effect on the flow stress at 100 °C.

Strain rates = [0.004 0.02 0.2] s^{-1}

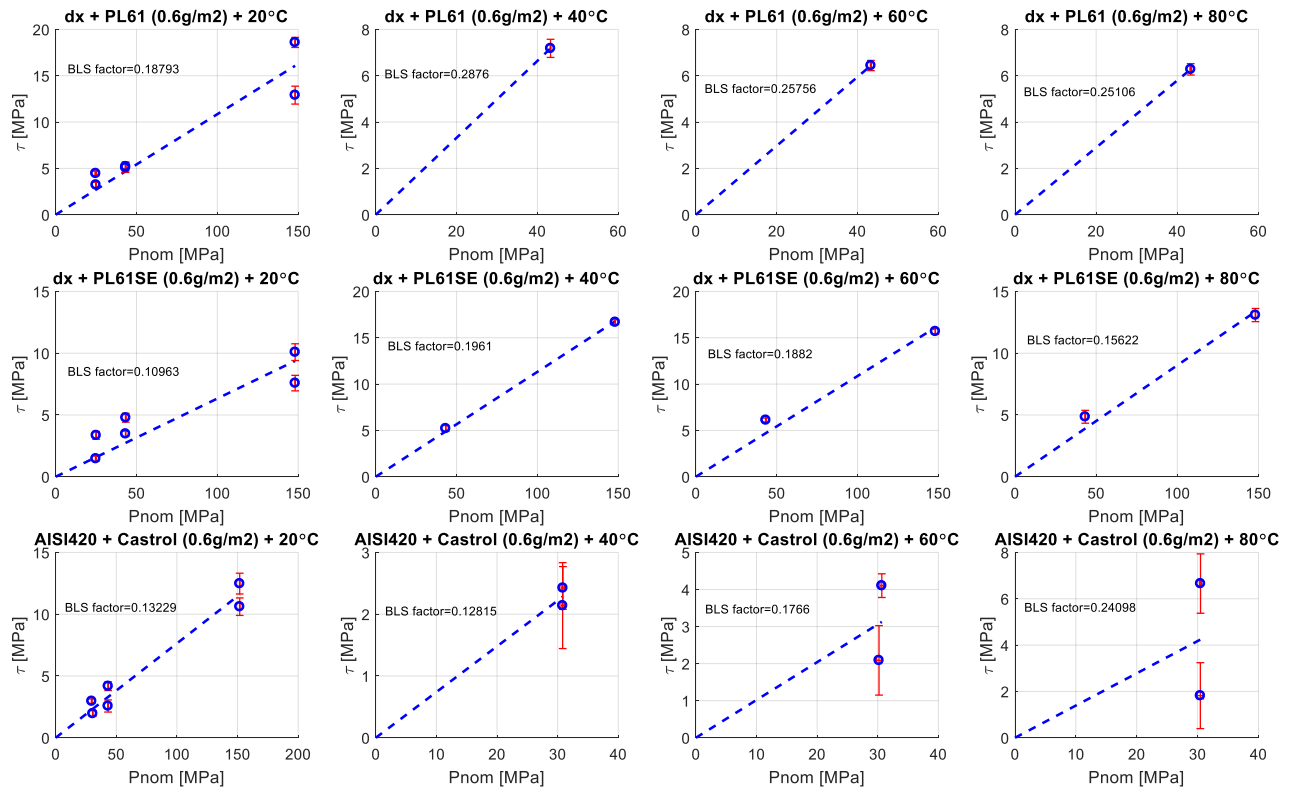
Appendix 5 – Boundary Shear Tests

Boundary layer shear strength results

Measured shear strength by Falex fitted by a linear relation [13]:

- For workpiece-lubricant interfaces: 9DX+PL61, DX+PL61SE, AISI420+Castrol and
- Temperatures: 20°C, 40°C, 60°C and 80°C

Measured shear strength by Falex, fitted by a linear relation [13]:

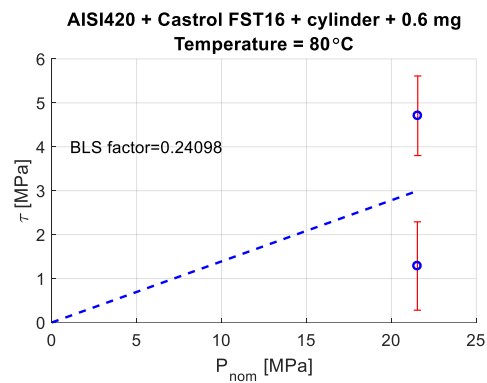
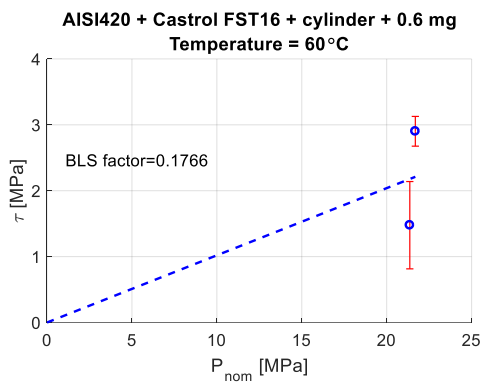
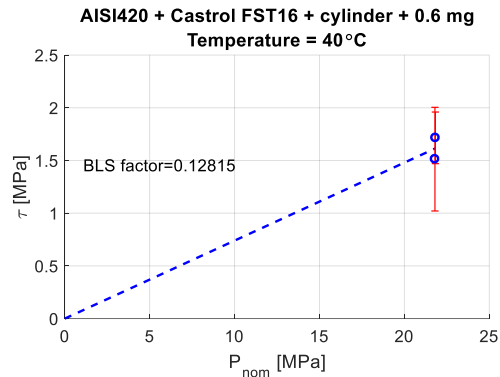
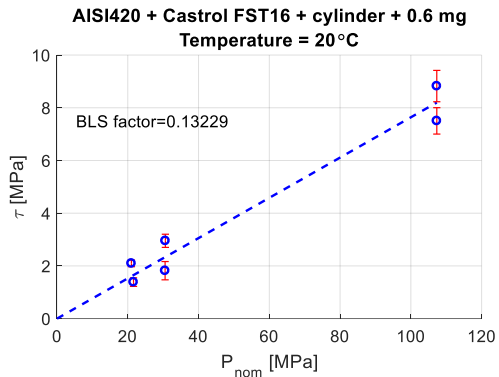


Cylinder-on-flat results

Measured Cylinder-on-flat results for a combination of [76]:

- Workpiece-lubricant interface: AISI420+Castrol lubricant and
- Temperatures: 20°C, 40°C, 60°C and 80°C

Cylinder-on-flat results of AISI420 with the Castrol lubricant [76]:

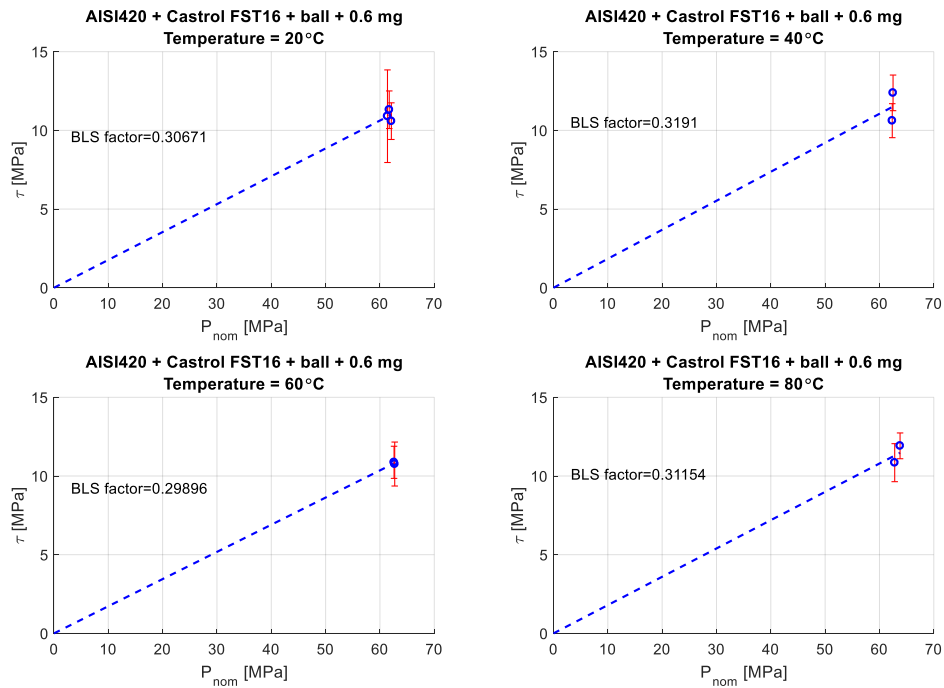


Ball-on-flat-results

Measured Ball-on-flat results of AISI420 with the AISI420+Castrol lubricant combination for [76]:

- Temperatures: 20°C, 40°C, 60°C and 80°C

Ball-on-flat results of AISI420 with the Castrol lubricant [76]:



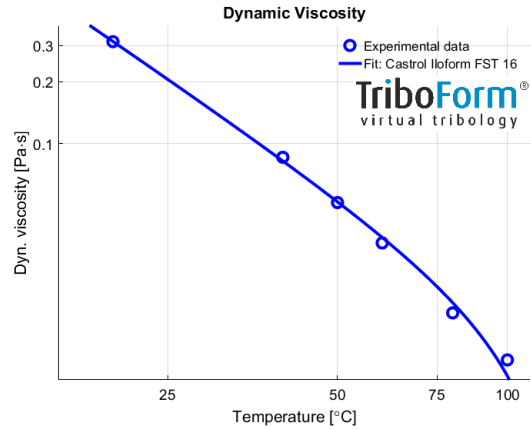
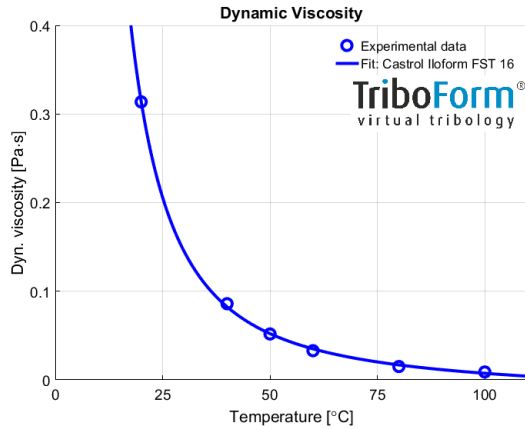
Appendix 6 – Temperature Dependent Dynamic Viscosity Tests

Measured shear strength by Falex fitted by a linear relation.

- For lubricant: Castrol Iloform FST 16
- Temperatures: 20°C, 40°C, 60°C, 80°C and 100°C

Castrol Iloform FST 16 lubricant

Temperature dependent dynamic viscosity of Castrol Iloform FST 16 lubricant [13]:



TriboForm
virtual tribology

Relation used to describe dynamic viscosity: $\eta_{dyn} = a \cdot T^{-b} - c \cdot \exp(-d \cdot T)$

Lubricant	Cof a	Cof b	Cof c	Cof d	Density (kg/m ³)
Castrol Iloform FST 16	84.3677	1.862	0.0038724	-0.0078646	941000

Appendix 7 – Four Dimensional Look-up Table

A general representation of the four dimensional frictional look-up table that is generated for each step within the FEM analysis, the total table is added as a separate file. The frictional table depends on the determined nominal contact pressure, temperature, relative velocity and strain parameters within the subroutine. General depiction of the Triboform four dimensional frictional look-up table [149]:

```
...RESULT FILE FRICTION EVALUATION TriMM...
Release: V2.0
Last revision:
Simulation executed:







Explanation column data
Column 1: Nominal contact pressure
Column 2: strain
Column 3: temp
Column 4: vrel

Length_columns: 2401

Evaluated files:
INPUT/trimm/surfaces/wp_A2_assembly_150x_500x500.asc
INPUT/trimm/surfaces/tool_die_150x_300x300mm_skip1.asc
OUTPUT:

pressure strain    temp    vrel    FRICTION
1.00    0.00000    20    1.00000    0.03191
1.00    0.06667    20    1.00000    0.02817
1.00    0.13333    20    1.00000    0.02632
1.00    0.20000    20    1.00000    0.02550
1.00    0.26667    20    1.00000    0.02492
1.00    0.33333    20    1.00000    0.02457
1.00    0.40000    20    1.00000    0.02537
1.00    0.00000    20    33.33333    0.03026
1.00    0.06667    20    33.33333    0.02622
1.00    0.13333    20    33.33333    0.02420
1.00    0.20000    20    33.33333    0.02332
1.00    0.26667    20    33.33333    0.02267
1.00    0.33333    20    33.33333    0.02209
1.00    0.40000    20    33.33333    0.02250
1.00    0.00000    20    66.66667    0.02983
1.00    0.06667    20    66.66667    0.02581
1.00    0.13333    20    66.66667    0.02393
1.00    0.20000    20    66.66667    0.02328
:        :        :        :        :
:        :        :        :        :
```

Deviations on the frictional look-up table are generated and are added as separate files:

					
TriMM_fric_original. txt	TriMM_fric_Friction_ Constant_0.1.txt	TriMM_fric_Pnom_a nd_Temp_Dependen	TriMM_fric_Pnom_D ependent.txt	TriMM_fric_Pnom_T emp_vrel_Dependen	TriMM_fric_Temp_D ependent.txt

Appendix 8 – FEM Analysis - Dimensional Parameters

Dimensions Blank

Cutting out blank (29.5mm diameter) with a hole of 2mm in diameter

Dimensions Process – Step 1

Deep drawing step:

Die: Inner diameter of 18.36mm and a fillet radius of 2.0mm

Punch: Outer diameter of 17.7mm with a fillet radius of 2.00mm

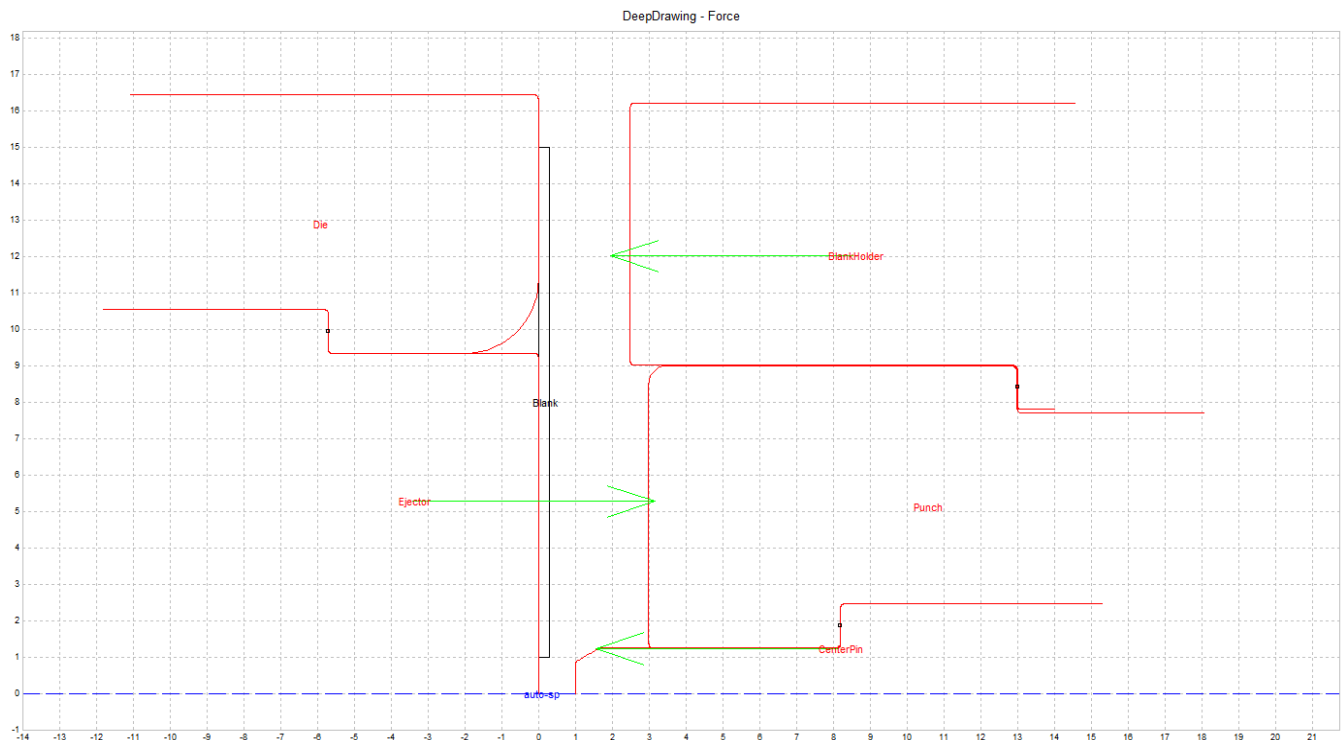
Centering pin: Conical shape of around 60 degrees.

Ejector: Force to be controllable in range from 50 to 250N

Blank Holder: Force to be controllable in range from 250 to 450N

Drawing depth: 5mm (top die surface to top punch surface)

An overview of the dimensional properties for the deep draw process step [3]:



Dimensions Process – Step 2

Re-drawing step (with smaller diameter in reverse direction)

Die:

Outer diameter 17.60mm

Die fillet radius: same as punch fillet radius from step 1 = 2.0mm

Die inner diameter: $17.6\text{mm} - 4 \times \text{die fillet radius} = 9.6\text{mm}$

Punch:

Outer diameter: Die inner diameter step 2 – $2 \times 0.33\text{mm} = 8.94\text{mm}$

Punch fillet radius: 1.0mm

Centering pin:

Conical shape of around 60 degrees.

Ejector:

Force to be controllable in range from 50 to 250N

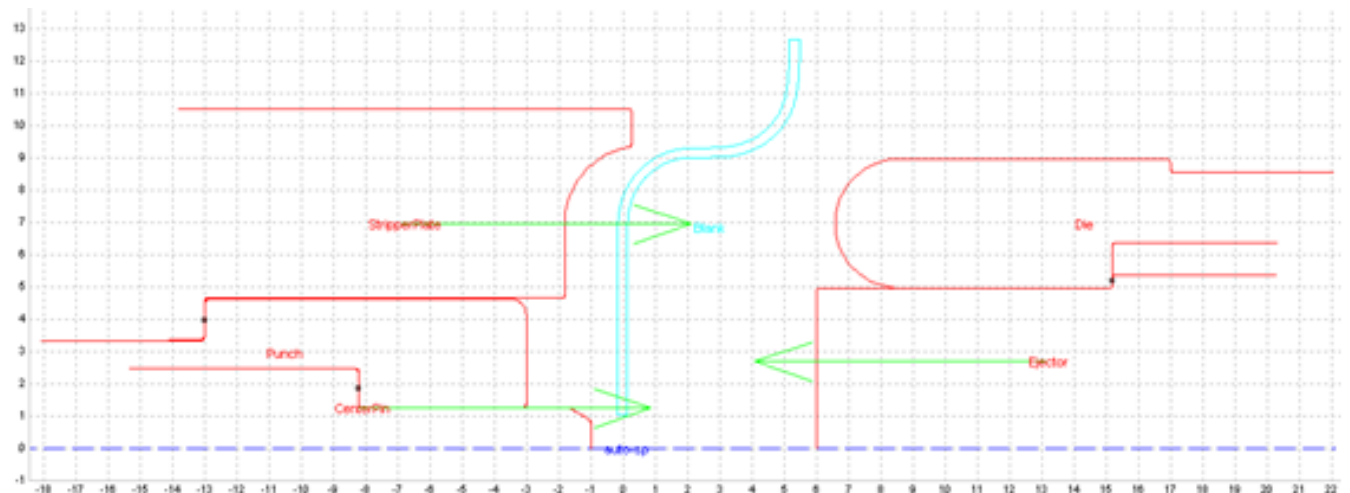
Blank Holder:

Force to be controllable in range from 250 to 450N

Drawing depth:

Flexible between 1.65 and 3.65mm (top die surface - top punch surface)

An overview of the dimensional properties for the redraw process step [3]:



Appendix 9 – FEM Analysis – Matlab Routine

General Routine:

```
for i=1:5
```

```
    T=273+20*i
```

```
    [miny,maxy] = get_ctq_aspect(['PH_Demo_DeformableTools_muT_' num2str(T) '\02-Redraw\02-Redraw_export.sec'])
```

```
    FullUSersub(i,1) = miny
```

```
    FullUSersub(i,2) = maxy
```

```
end
```

Routine File:



Routine.m

Additional Files :



get_ctq_aspect.m



get_nodal_data.m



Location_nodes.fig



plot_mesh.m



plot_sec.m



read_sec.m

Appendix 10 – MSC Marc Standard Frictional models

An overview of the available FEM adaptations in MSC Marc on the Coulomb frictional model is provided below, giving an overview of each of the main formulas.

Frictional models - Equations

1. Coulomb-Bilinear friction model

$$\sigma_t = -\mu \cdot \sigma_n \cdot \tan^{-1} \left(\frac{\|v_r\|}{RVCSNT} \right) \cdot t \quad (88)$$

2. Coulomb-Arctangent friction model

$$\dot{f}_t = \left(D - \frac{D \cdot \frac{d\psi}{df_t} \cdot \left(\frac{d\Phi}{df_t} \right)^T \cdot D}{\left(\frac{d\Phi}{df_t} \right)^T \cdot D \cdot \frac{d\psi}{df_t}} \right) \cdot \dot{u}_t = (D - D^*) \cdot \dot{u}_t \quad (89)$$

The shear based friction model derives the frictional stress based on a fraction of the equivalent stress - $\bar{\sigma}$ in the bulk material [144]:

1. Shear-Bilinear friction model

$$\sigma_t = \min \left(m \cdot \sigma_n, m \cdot \frac{\bar{\sigma}}{\sqrt{3}} \right) \quad (90)$$

2. Shear-Arctangent friction model

$$|\sigma_t| < m \cdot \frac{\bar{\sigma}}{\sqrt{3}} \text{ (Stick) and } \sigma_t = -m \cdot \frac{\bar{\sigma}}{\sqrt{3}} \cdot t \text{ (Slip)} \quad (91)$$

Appendix 11 – FEM Study 1 – Frictional Models

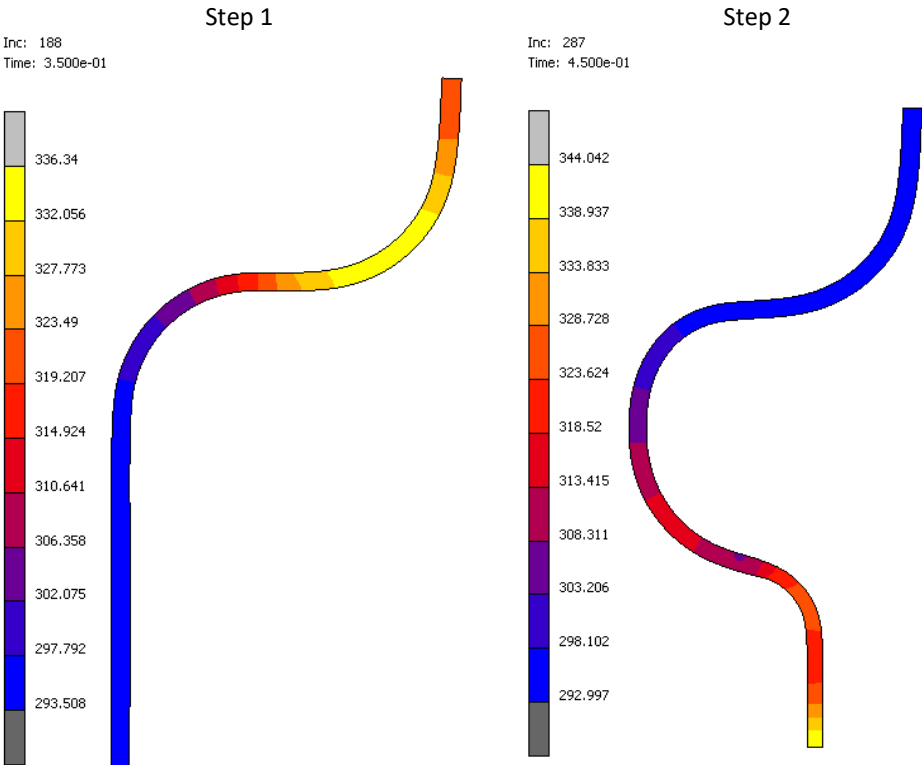
Frictional models - Result Table

The end hole and flange development for each standard friction model variation of both steps in the two-step deep draw process is provided below:

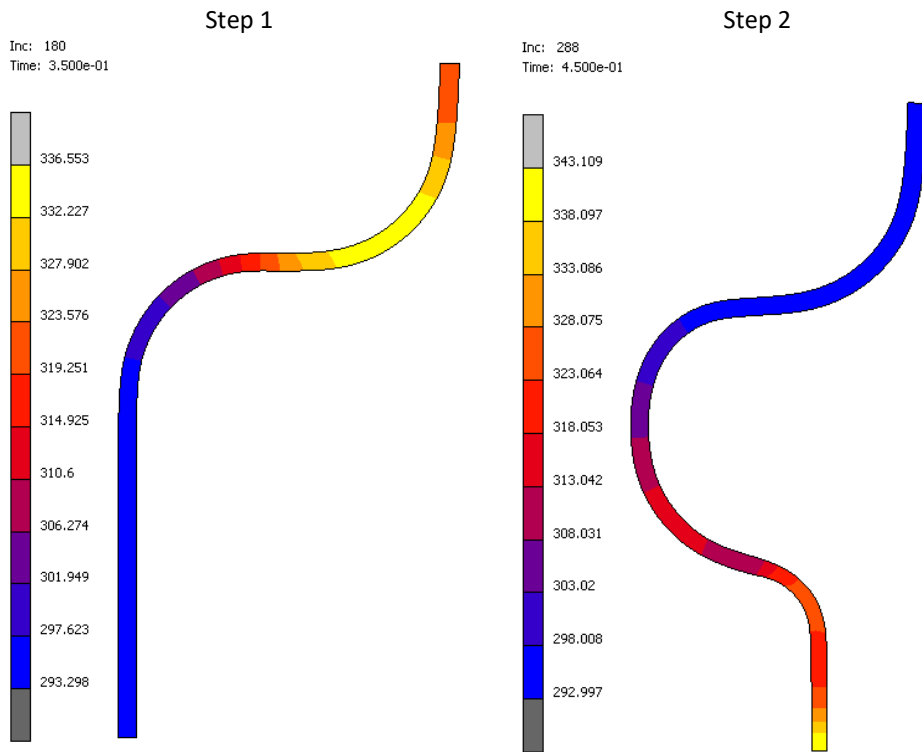
Results MSC Marc Frictional models		
Frictional model	Step 1	
	Hole Diameter	Flange Diameter
Run 1 - Coulomb Arctangent	2.0338	24.7702
Run 2 - Coulomb Bilinear	2.0192	24.7588
Run 3 - Stick Slip	2.0194	24.7582
Run 4 - Shear Arctangent	2.0194	24.7582
Run 5 - Shear Bilinear	2.0194	24.7582
Frictional model	Step 2	
	Hole Diameter	Flange Diameter
Run 1 - Coulomb Arctangent	3.0814	24.7712
Run 2 - Coulomb Bilinear	3.0488	24.7598
Run 3 - Stick Slip	3.0286	24.7592
Run 4 - Shear Arctangent	3.4548	24.7580
Run 5 - Shear Bilinear	3.0286	24.7592

Temperature Development Workpiece

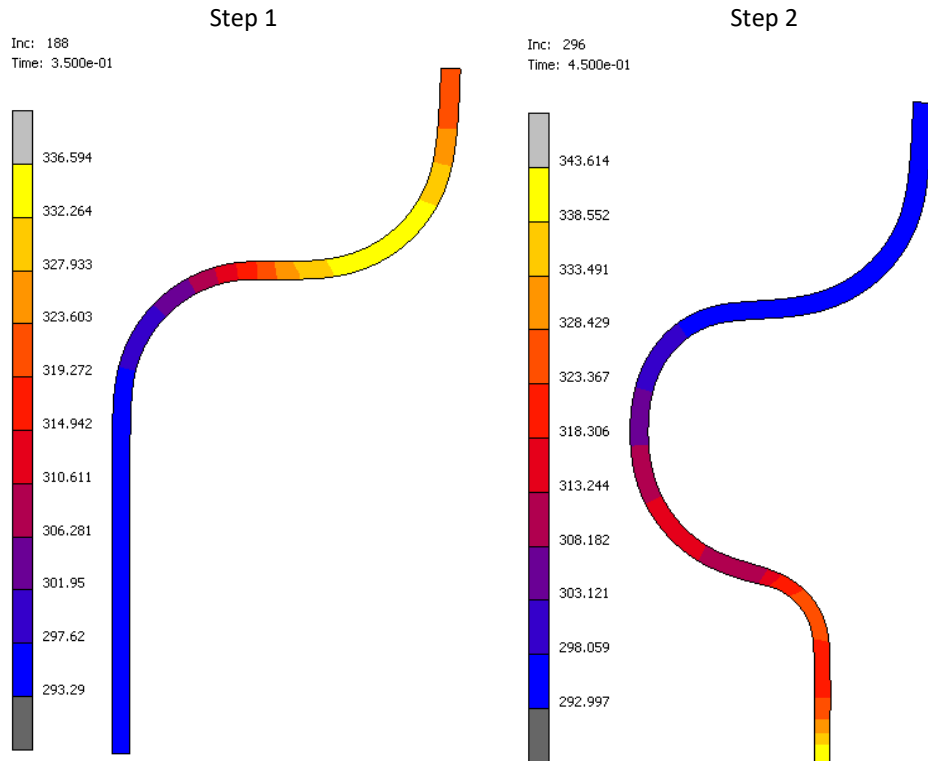
1 – Coulomb Arctangent



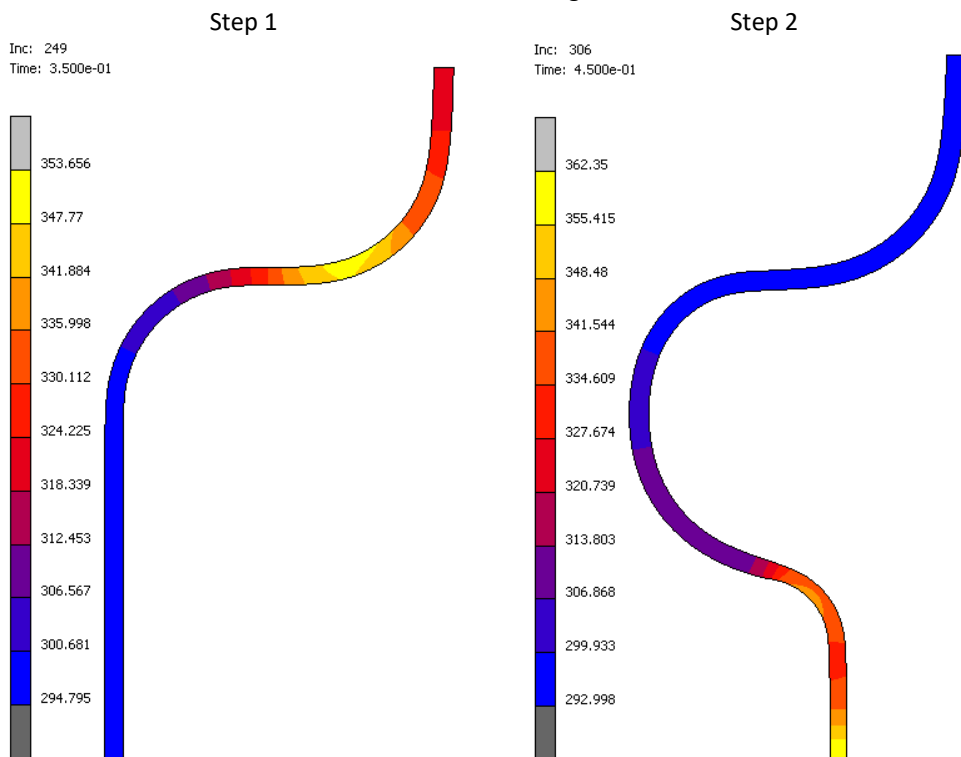
2 – Coulomb Bilinear



3 – Coulomb Stick-Slip



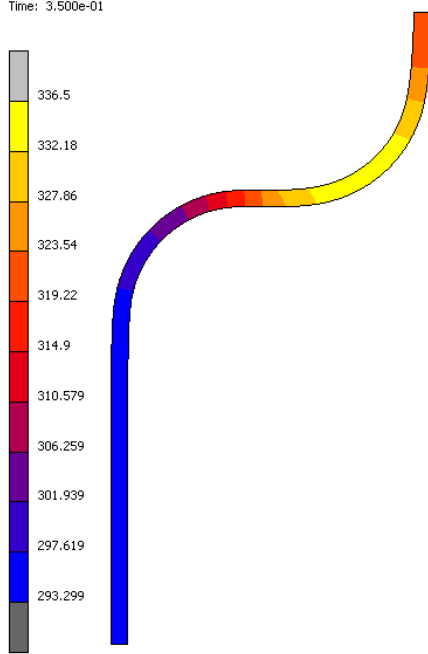
4 – Shear Arctangent



5 – Shear Bilinear

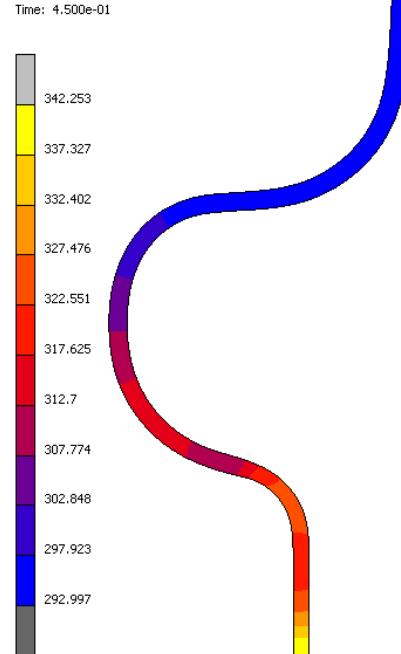
Step 1

Inc: 180
Time: 3.500e-01



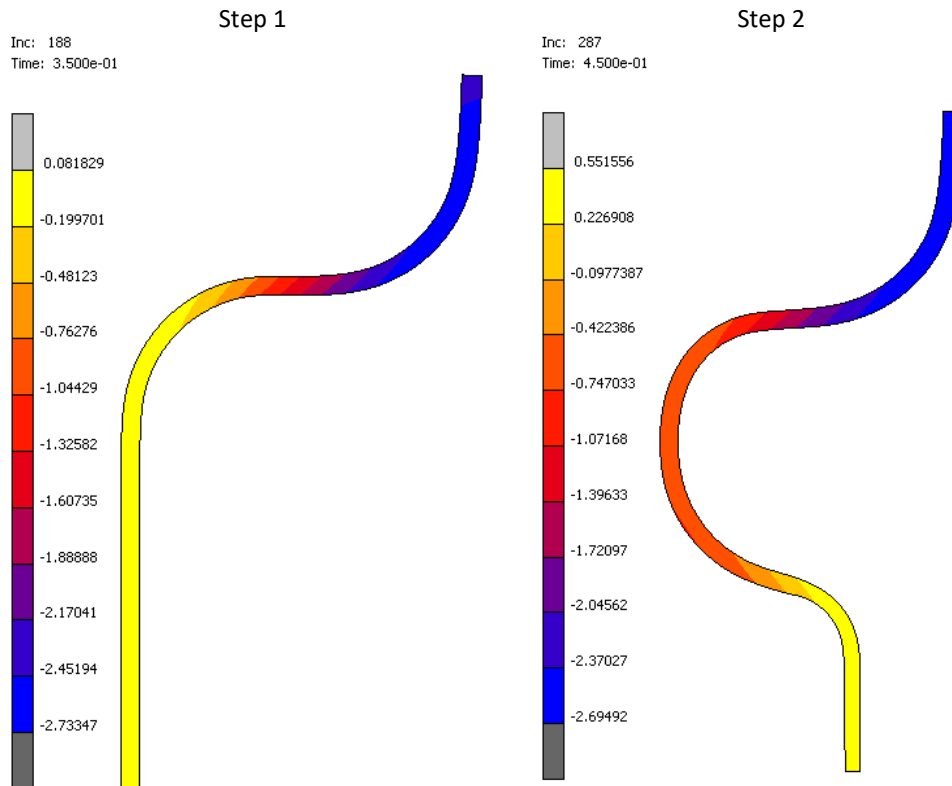
Step 2

Inc: 290
Time: 4.500e-01

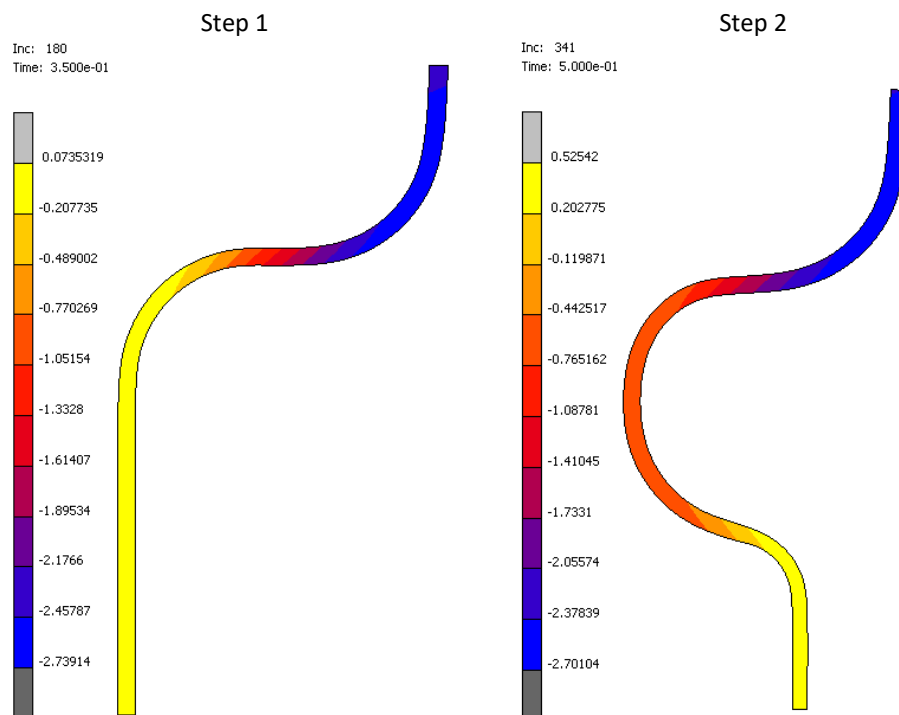


Total Displacement Y-Direction

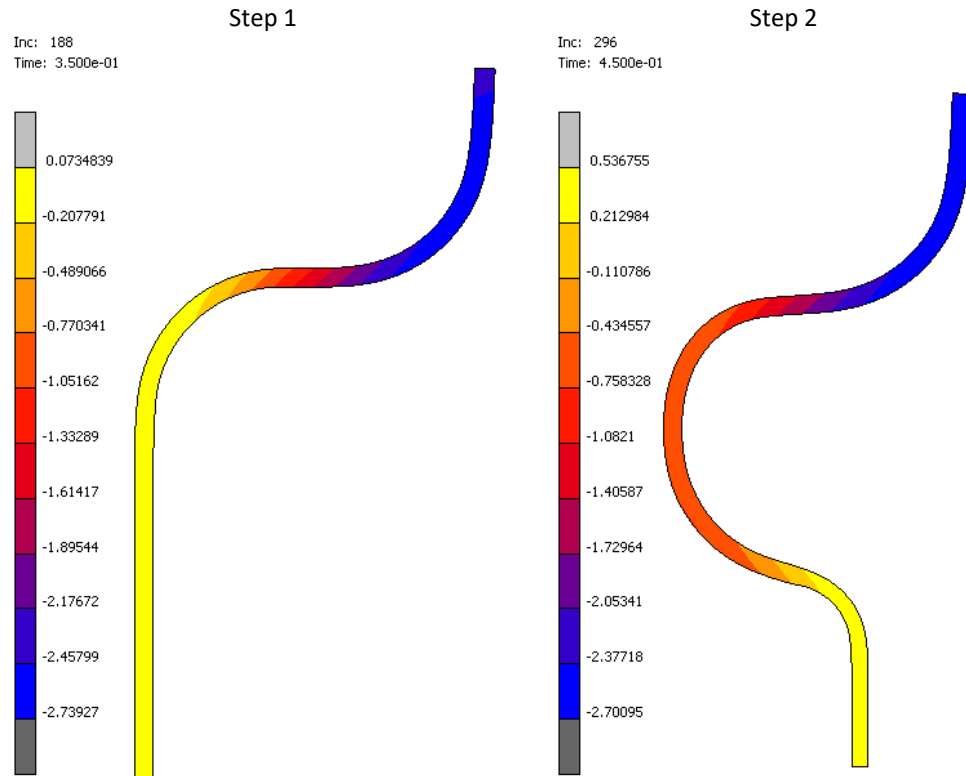
1 – Coulomb Arctangent



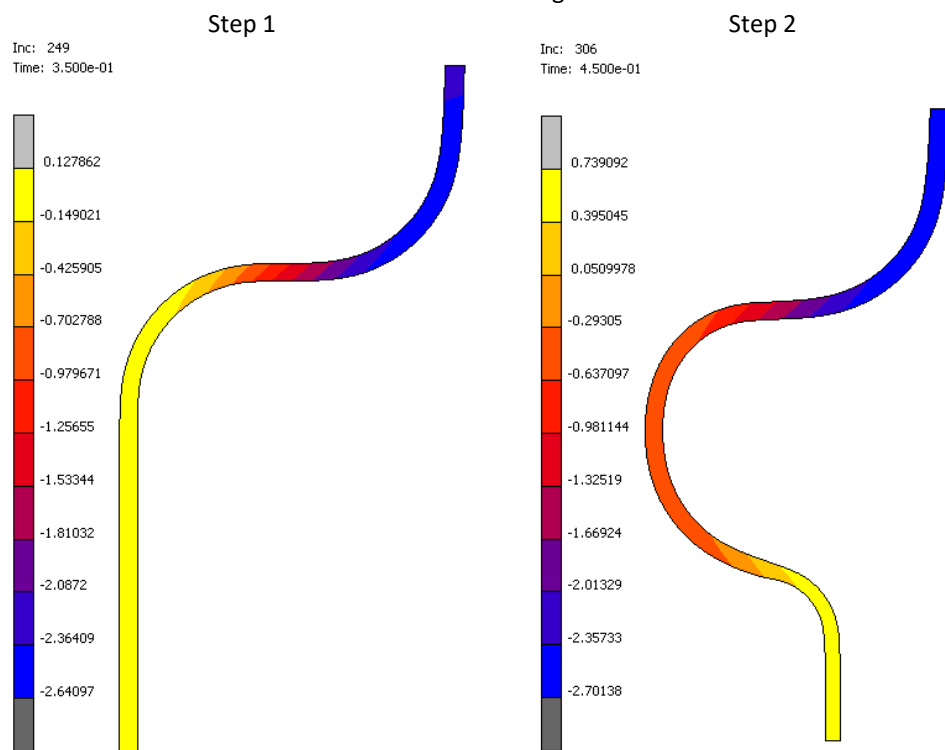
2 – Coulomb Bilinear



3 – Coulomb Stick-Slip



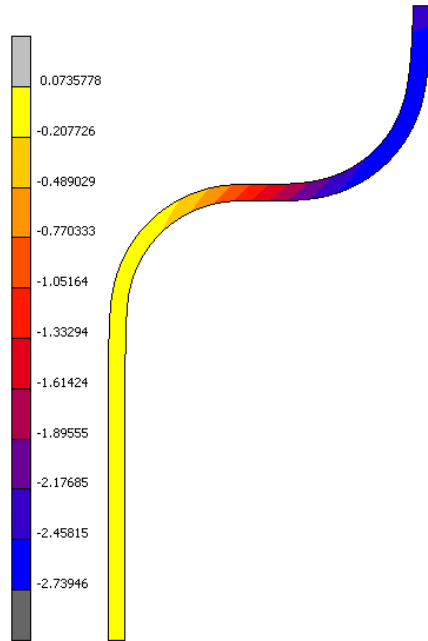
4 – Shear Arctangent



5 – Shear Bilinear

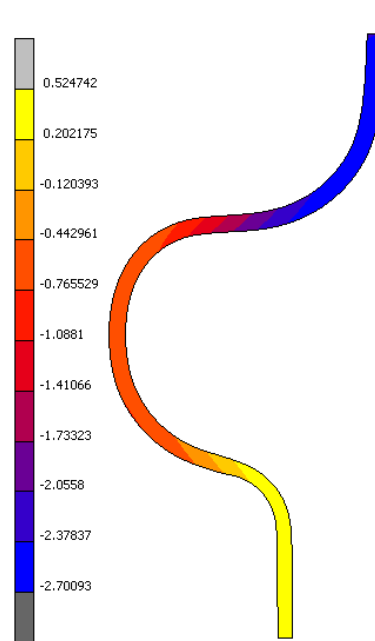
Step 1

Inc: 180
Time: 3.500e-01



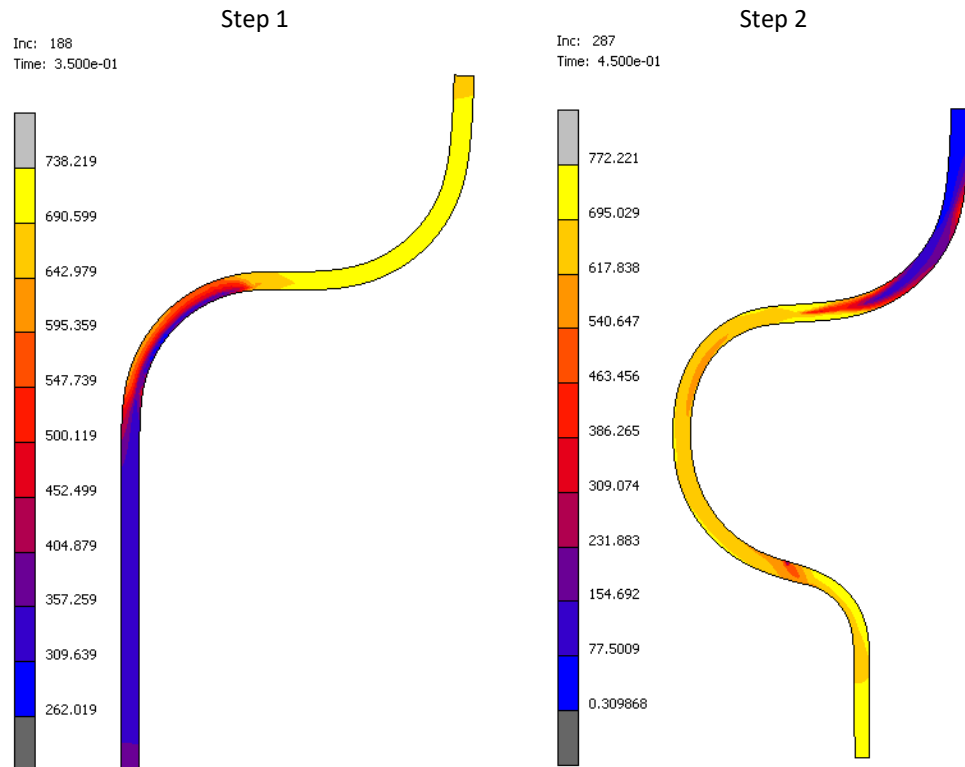
Step 2

Inc: 290
Time: 4.500e-01

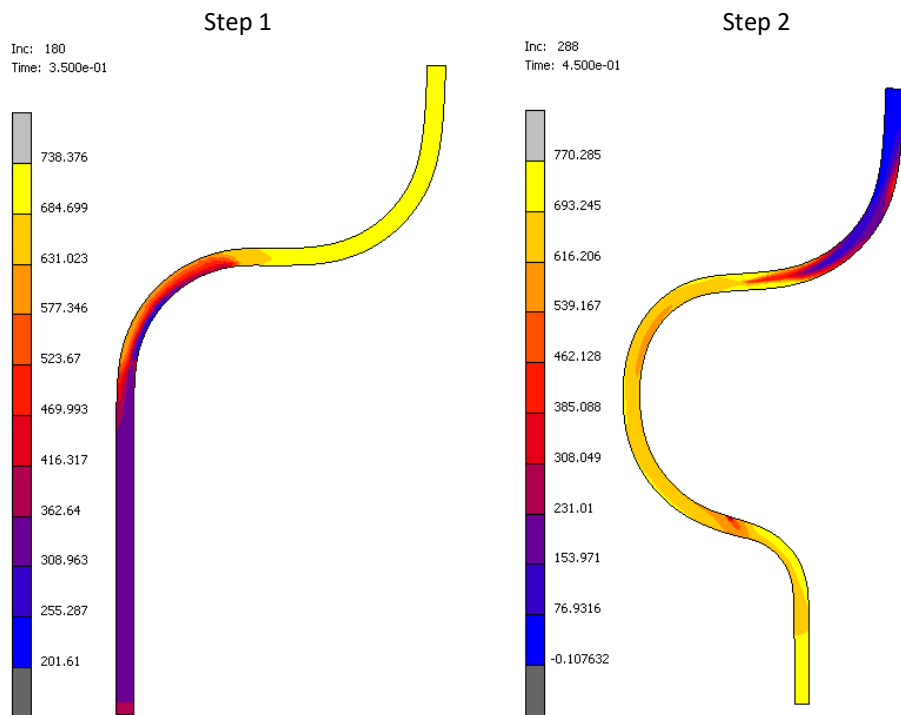


Equivalent Cauchy Stress Development Workpiece

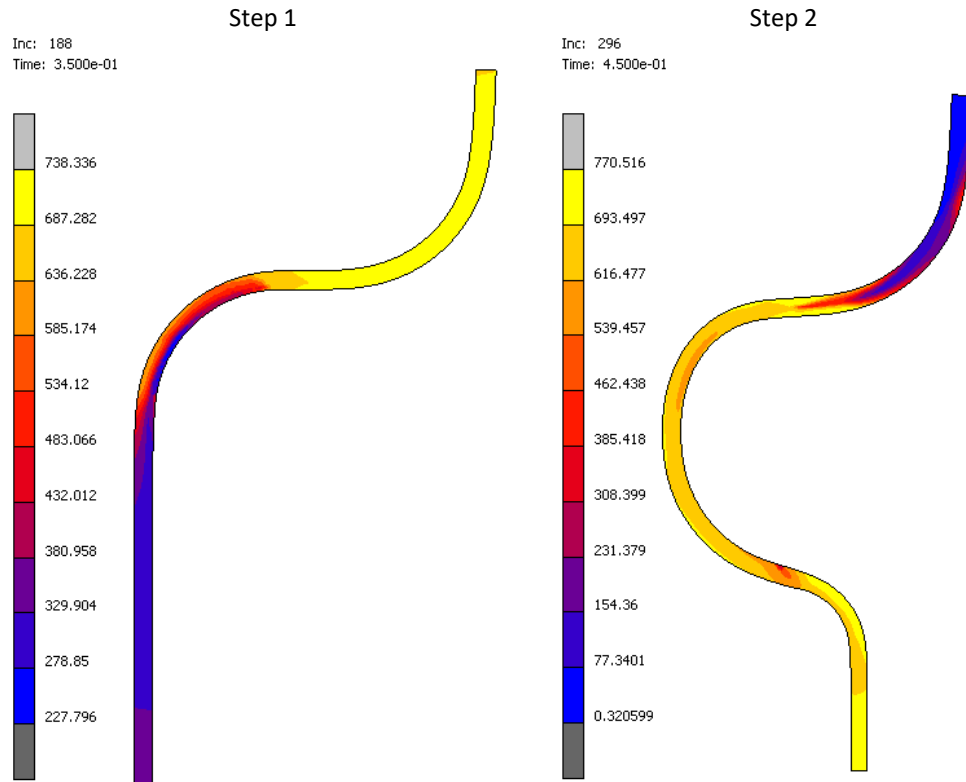
1 – Coulomb Arctangent



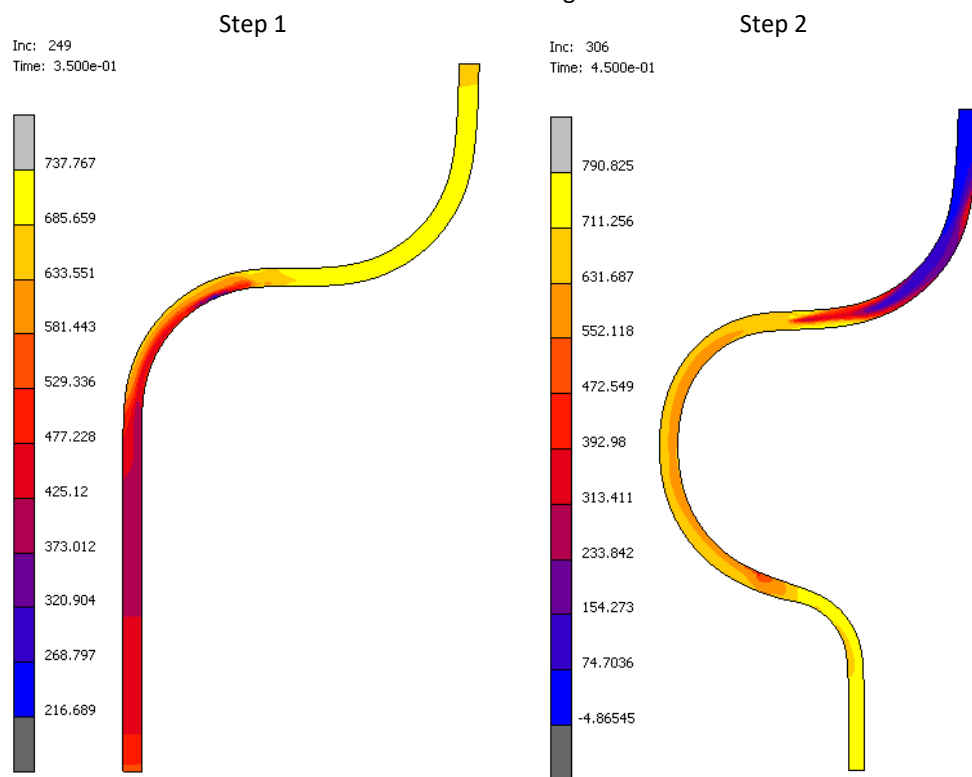
2 – Coulomb Bilinear



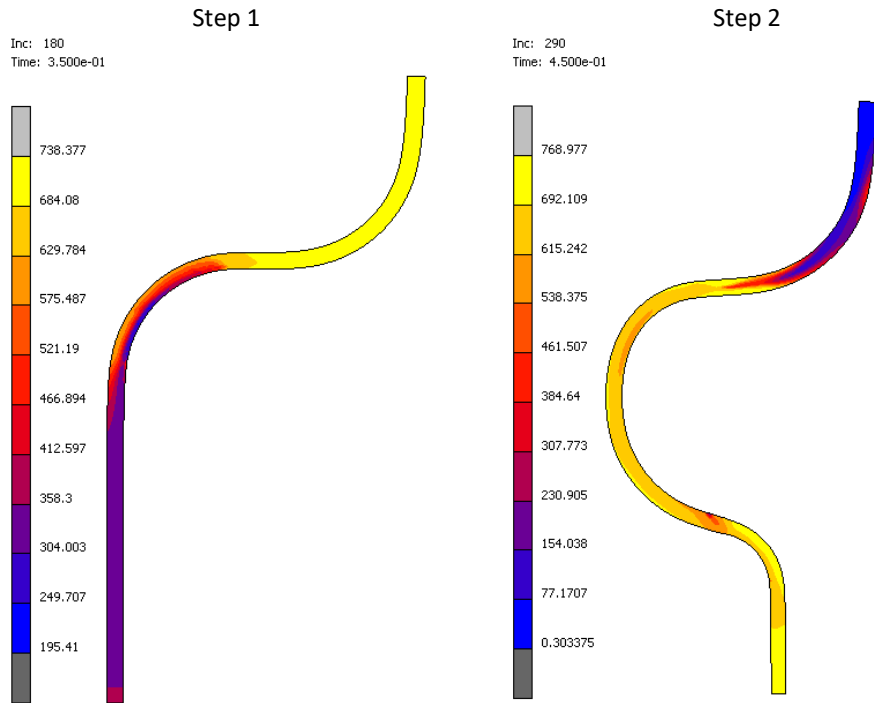
3 – Coulomb Stick-Slip



4 – Shear Arctangent



5 – Shear Bilinear

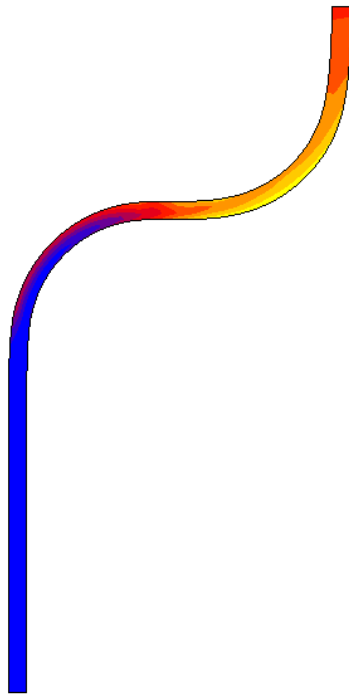
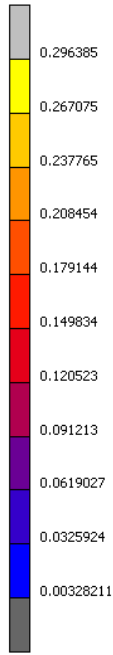


Total Equivalent Strain Development Workpiece

1 – Coulomb Arctangent

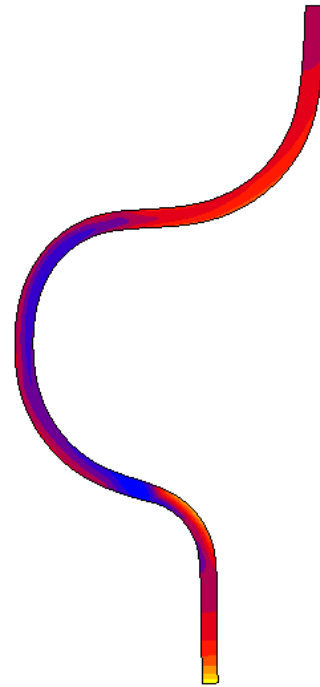
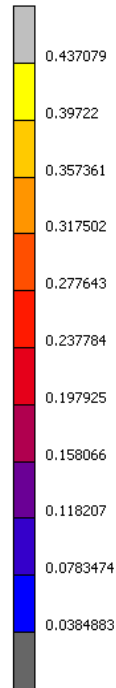
Step 1

Inc: 423
Time: 5.600e+00



Step 2

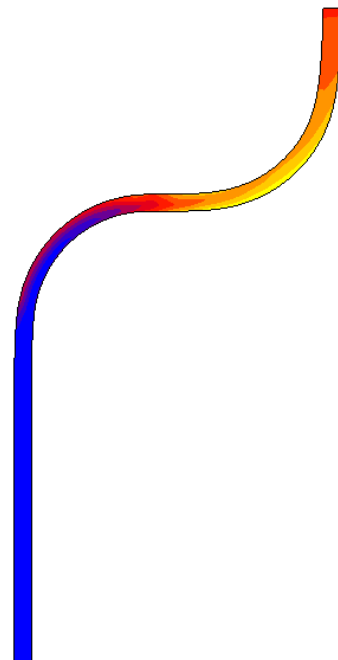
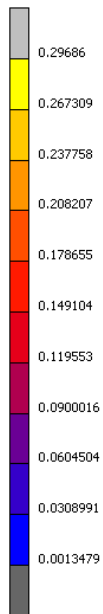
Inc: 531
Time: 7.000e-01



2 – Coulomb Bilinear

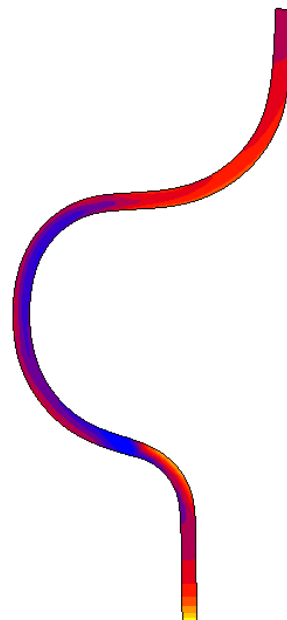
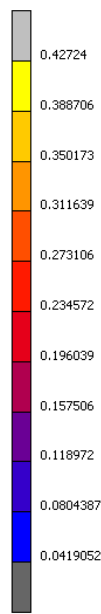
Step 1

Inc: 416
Time: 5.600e+00

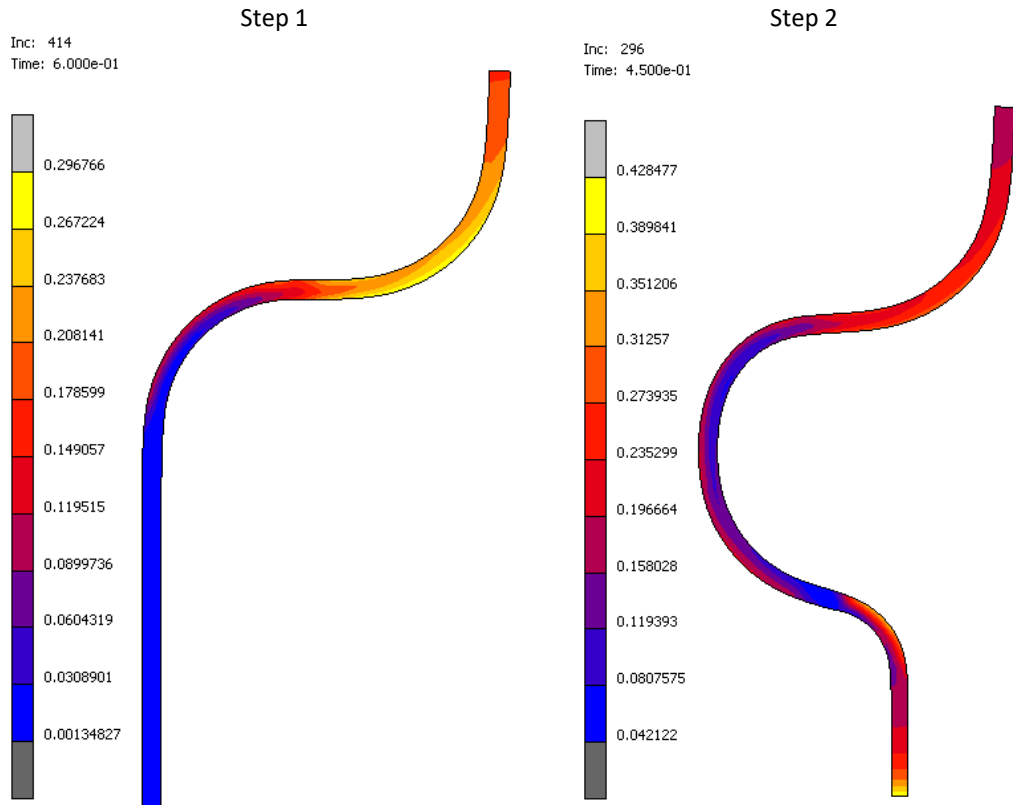


Step 2

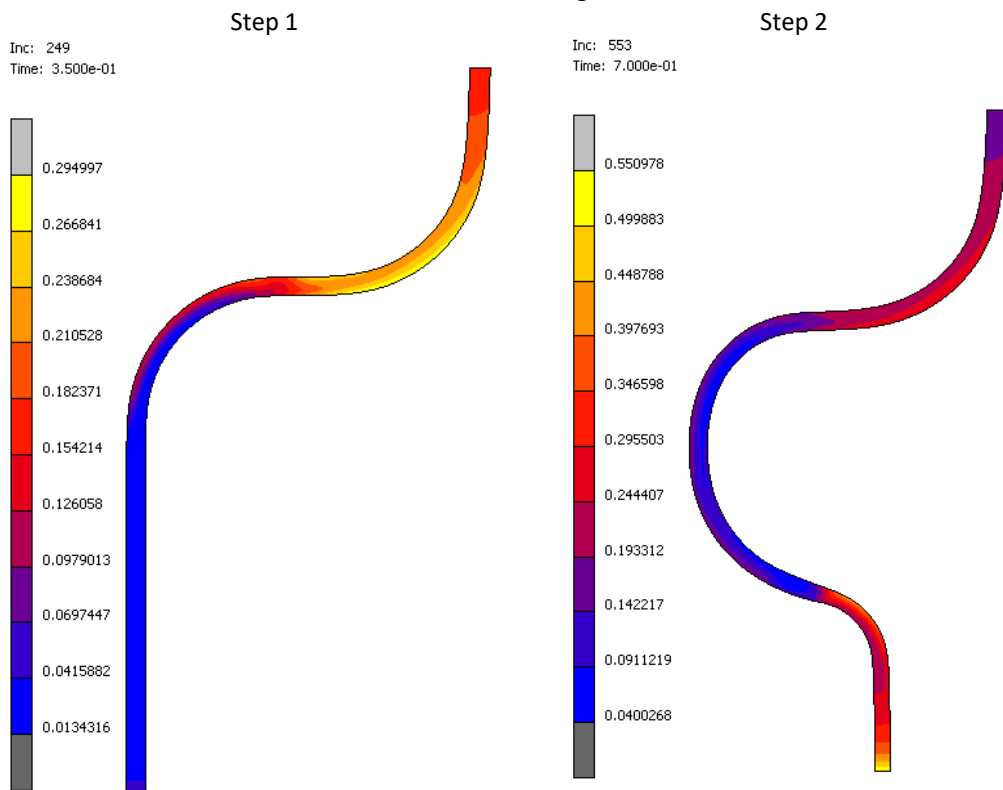
Inc: 533
Time: 7.000e-01



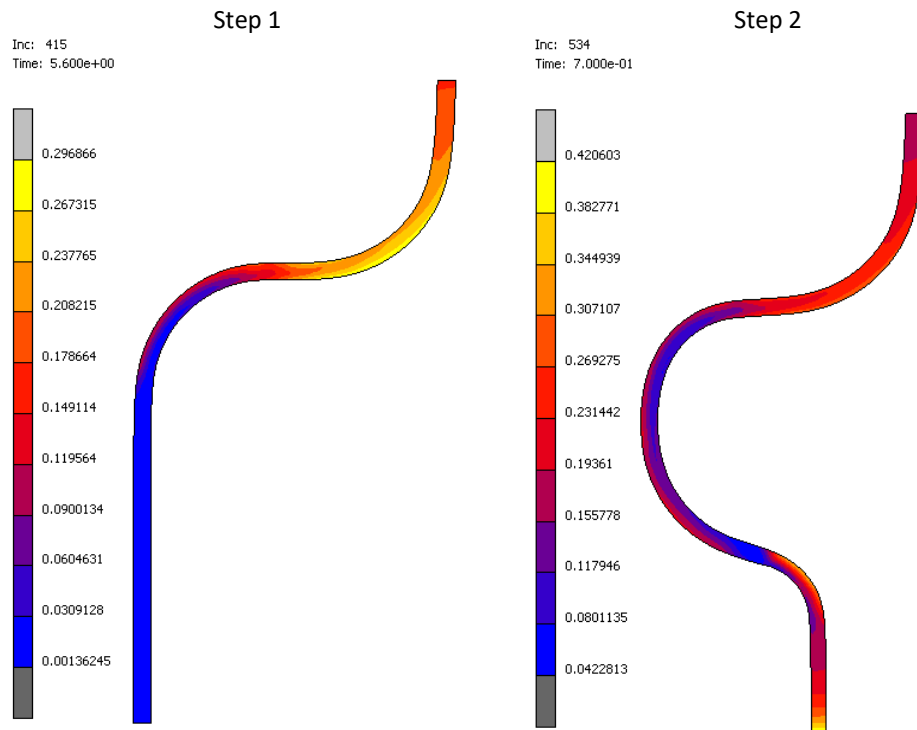
3 – Coulomb Stick-Slip



4 – Shear Arctangent



5 – Shear Bilinear



Appendix 12 – FEM Study 2 – Sensitivity Analysis

The end hole and flange development (at the end of step 2) for each variation in the sensitivity analyses of the two-step deep draw process is provided below:

Bergström van Liempt, $\mu=LUP(P_{nom}, T, \epsilon_p, V_{rel})$		
Temperature [K]	Hole Diameter [mm]	Flange Diameter [mm]
293	4.250	25.203
303	4.235	25.205
313	4.211	25.206
323	4.186	25.208
333	4.161	25.210
343	4.126	25.212
353	4.076	25.214
363	4.018	25.217
373	3.957	25.219

No Bergström-Van Liempt, $\mu=LUP(P_{nom}, T, \epsilon_p, V_{rel})$		
Temperature [K]	Hole Diameter [mm]	Flange Diameter [mm]
293	4.199	25.187
303	4.176	25.189
313	4.144	25.191
323	4.126	25.194
333	4.100	25.196
343	4.055	25.199
353	3.995	25.202
363	3.935	25.205
373	3.871	25.208

Bergström-Van Liempt, $\mu=0.1$		
Temperature [K]	Hole Diameter [mm]	Flange Diameter [mm]
293	4.242	25.217
313	4.248	25.215
333	4.254	25.214
353	4.256	25.213
373	4.261	25.211

Bergström-Van Liempt, $\mu=LUP(P_{nom})$		
Temperature [K]	Hole Diameter [mm]	Flange Diameter [mm]
293	4.318	25.196
313	4.322	25.195
333	4.327	25.194
353	4.337	25.193
373	4.345	25.191

Bergström-Van Liempt, $\mu=LUP(T)$

Temperature [K]	Hole Diameter [mm]	Flange Diameter [mm]
293	4.304	25.189
313	4.266	25.192
333	4.210	25.195
353	4.147	25.200
373	4.077	25.205

Bergström-Van Liempt, $\mu=LUP(Pnom,T)$

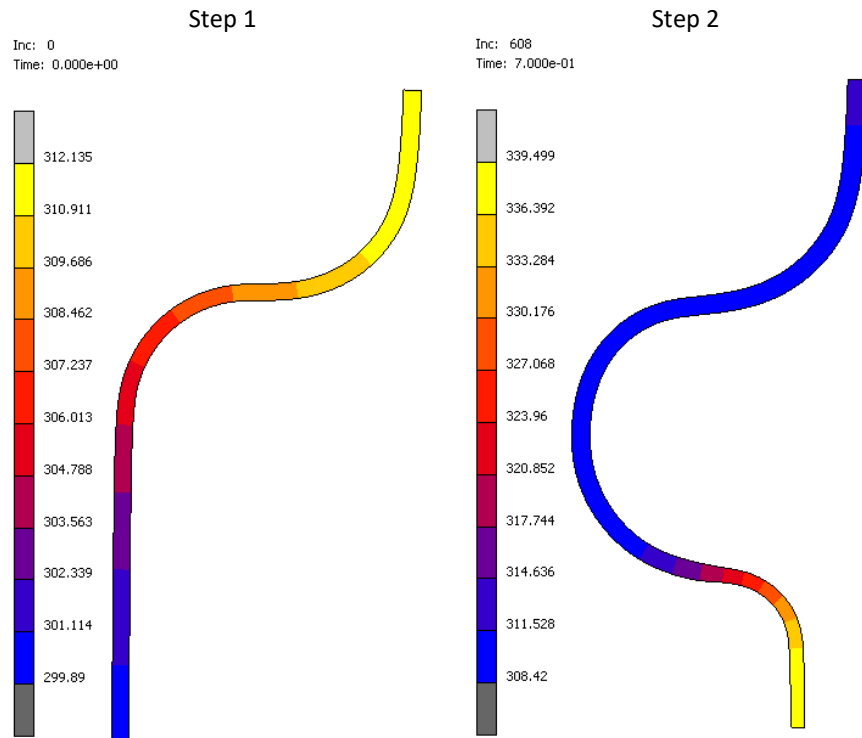
Temperature [K]	Hole Diameter [mm]	Flange Diameter [mm]
293	4.315	25.189
313	4.276	25.192
333	4.217	25.196
353	4.158	25.201
373	4.088	25.206

Appendix 13 – FEM Study 3 – Bergström van Liempt Model

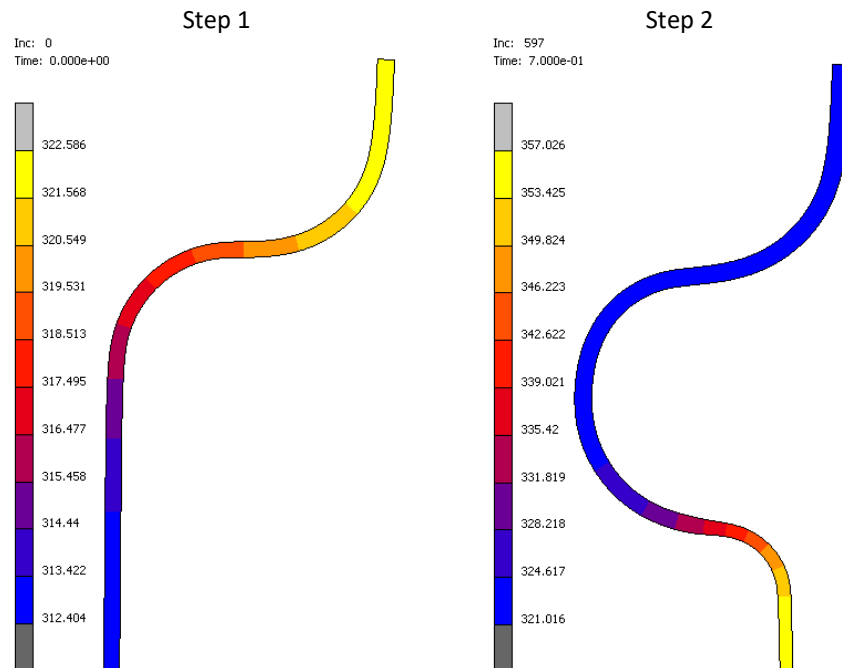
Original Parameters - SaS0.7um_Lub7gm2_SaT0.02um

Temperature Development Workpiece

293 K



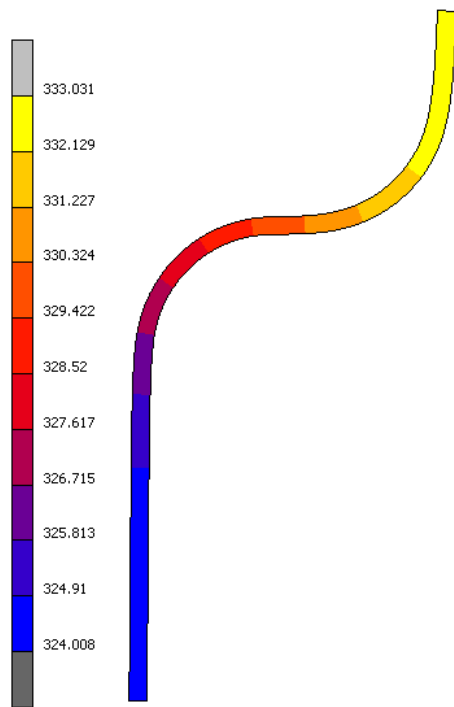
313 K



333 K

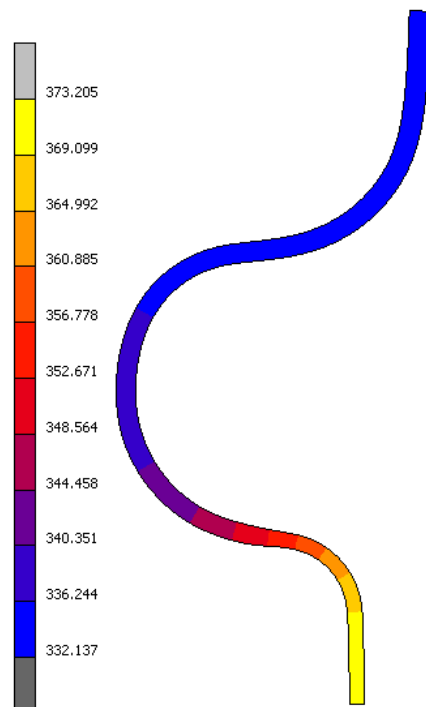
Step 1

Inc: 0
Time: 0.000e+00



Step 2

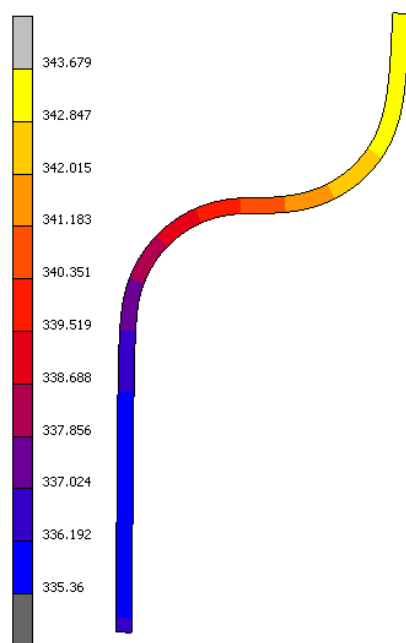
Inc: 597
Time: 7.000e-01



353 K

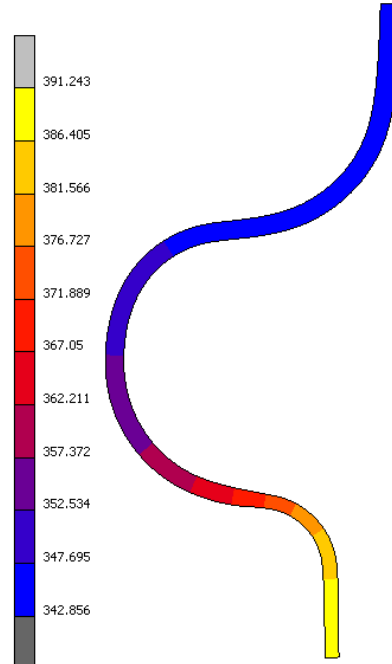
Step 1

Inc: 0
Time: 0.000e+00



Step 2

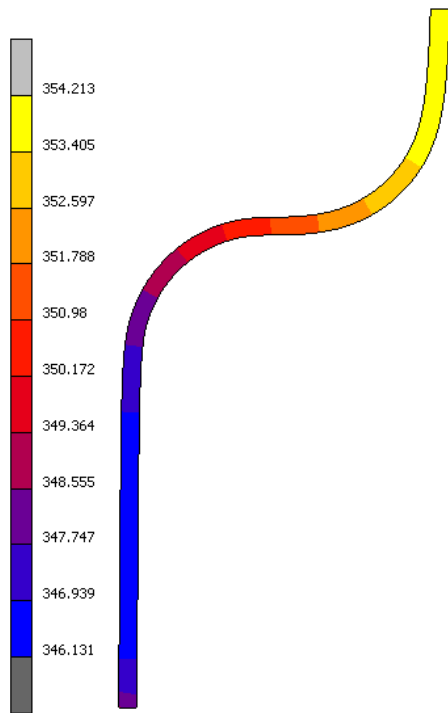
Inc: 544
Time: 6.500e-01



373 K

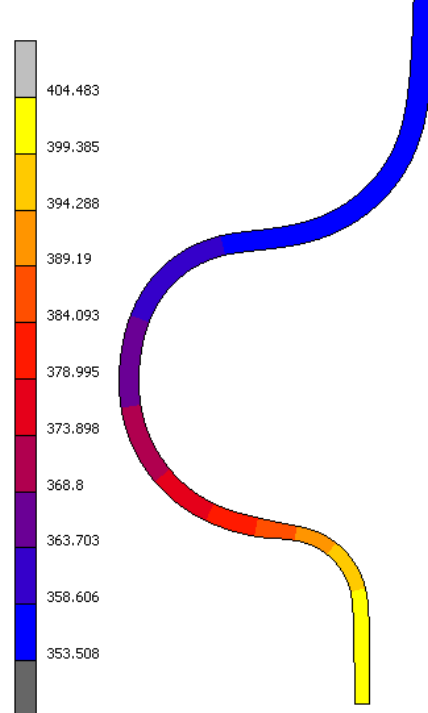
Step 1

Inc: 0
Time: 0.000e+00



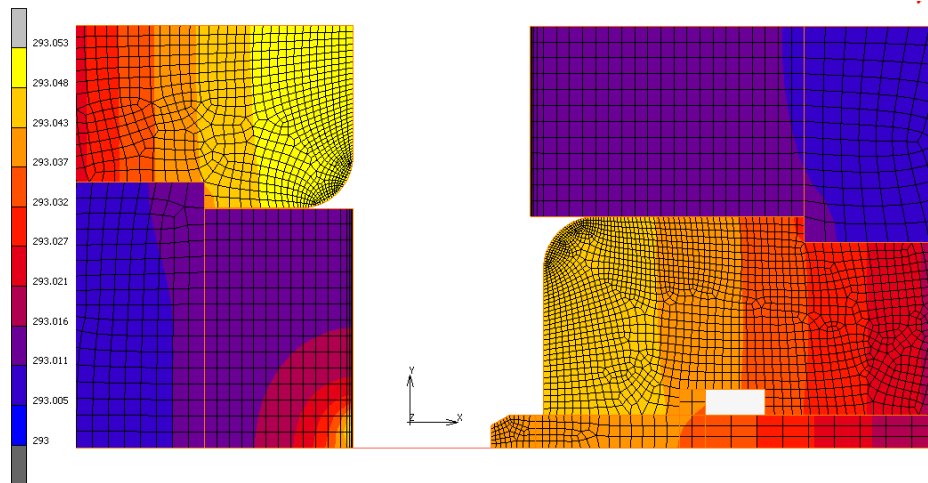
Step 2

Inc: 593
Time: 7.000e-01

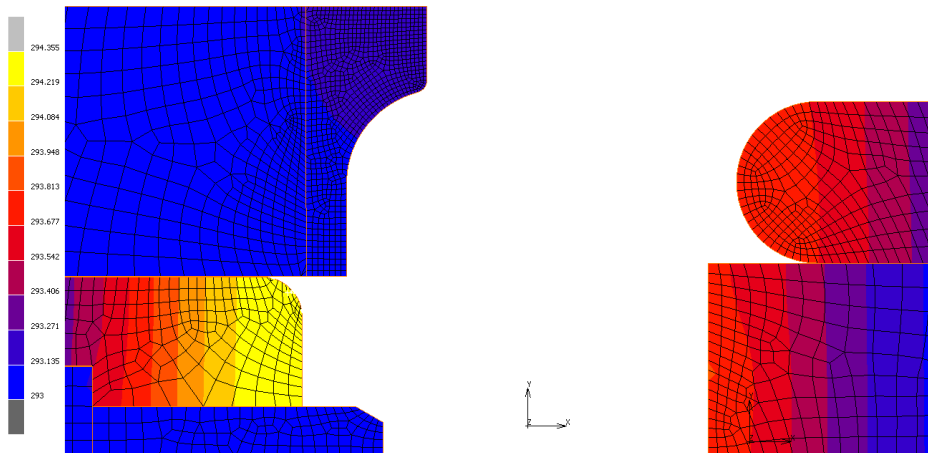


Temperature Development Tooling

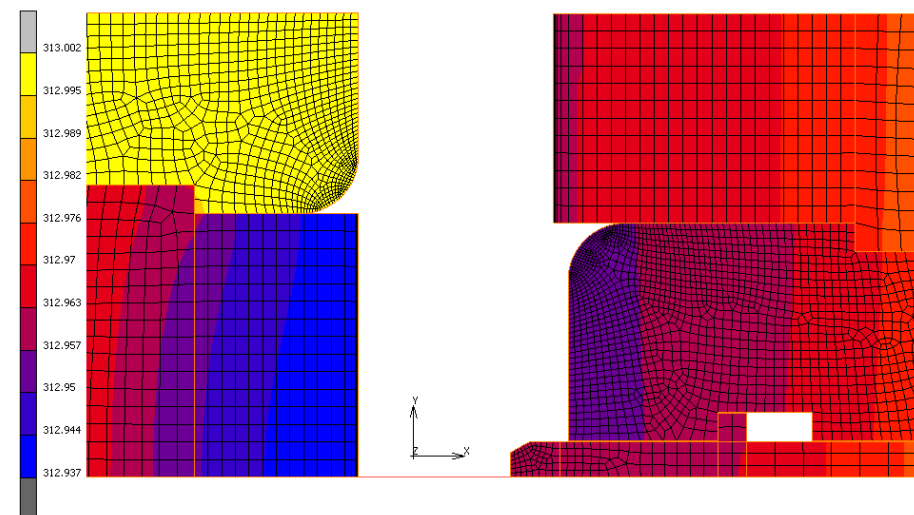
293 K - Step 1



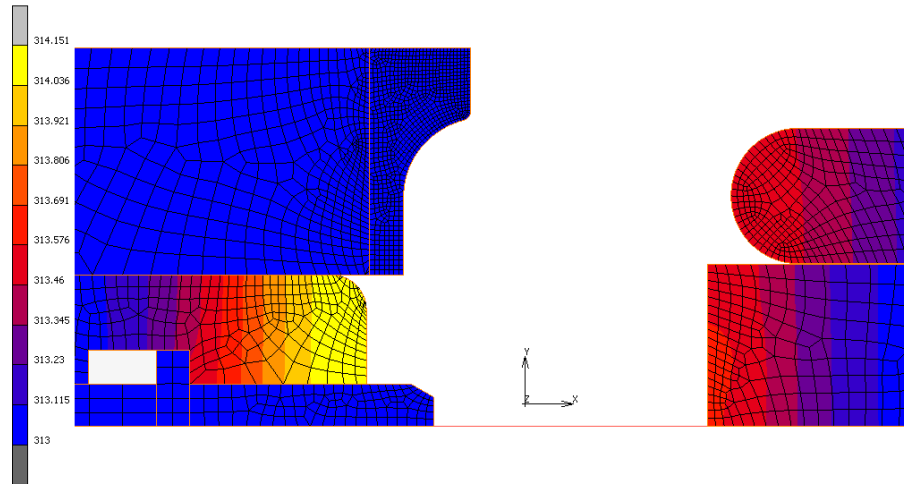
293 K - Step 2



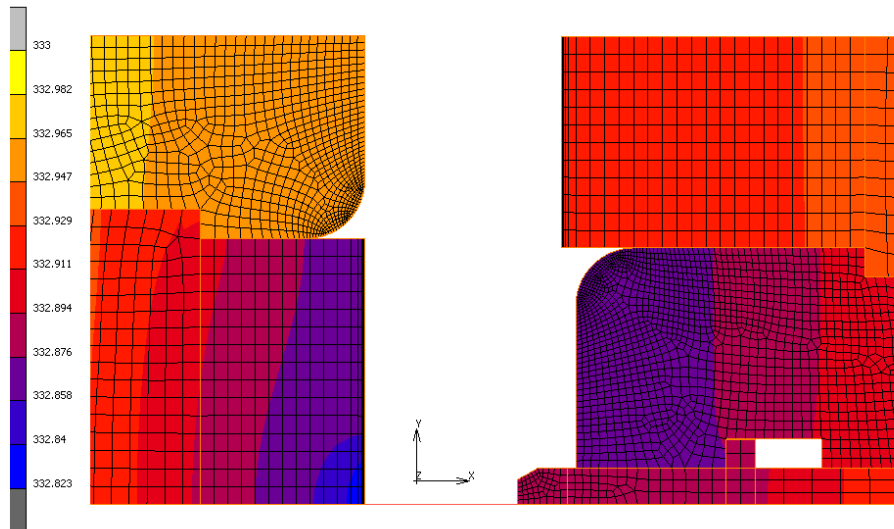
313 K - Step 1



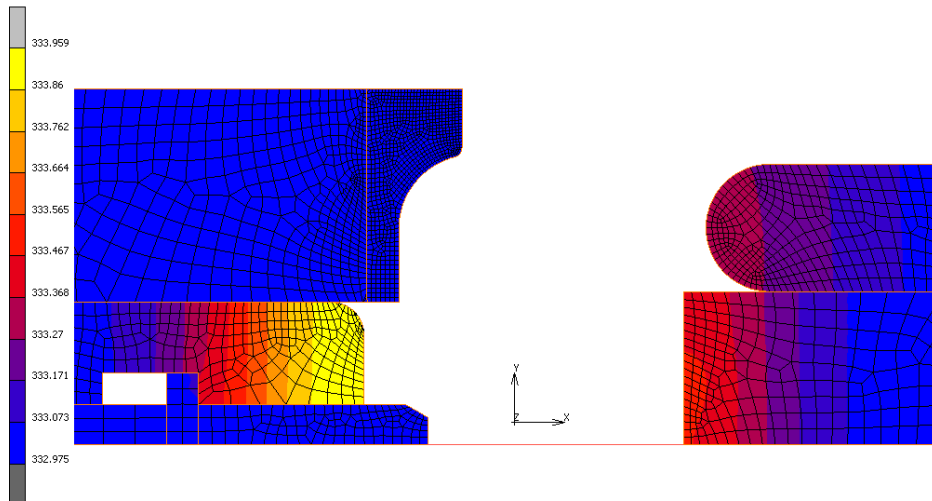
313 K - Step 2



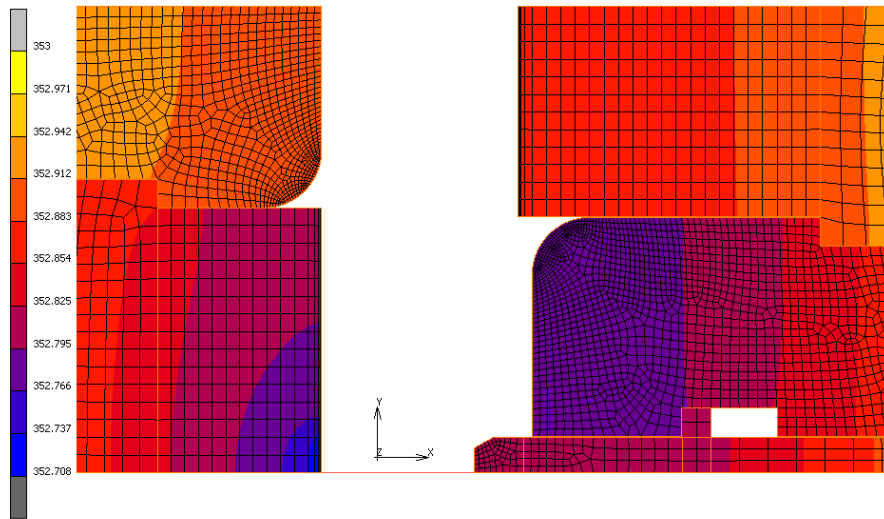
333 K - Step 1



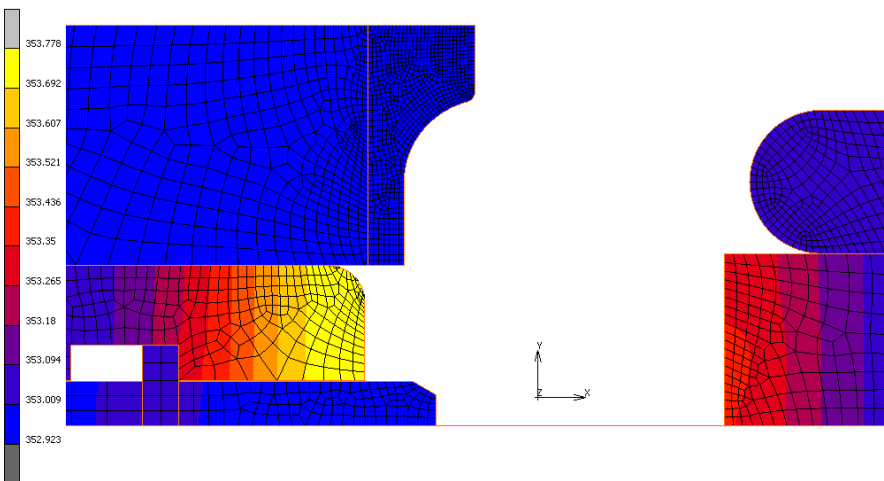
333 K - Step 2



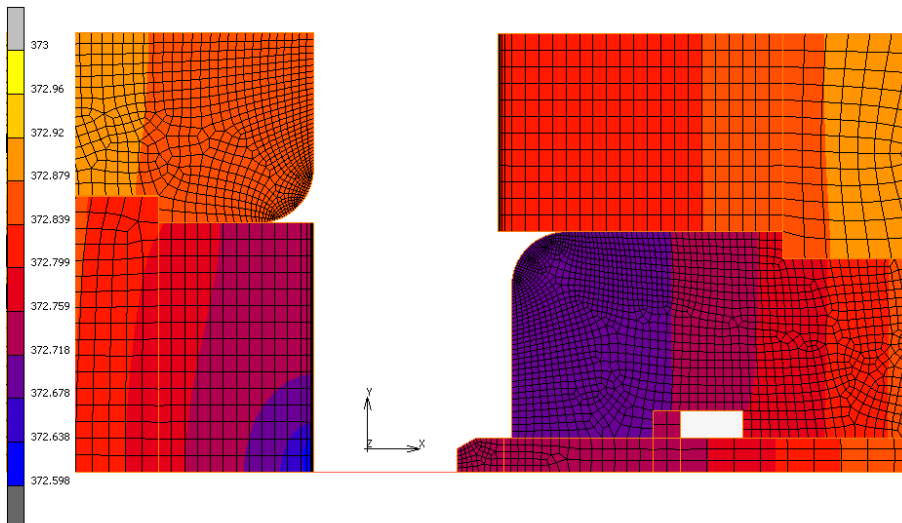
353 K - Step 1



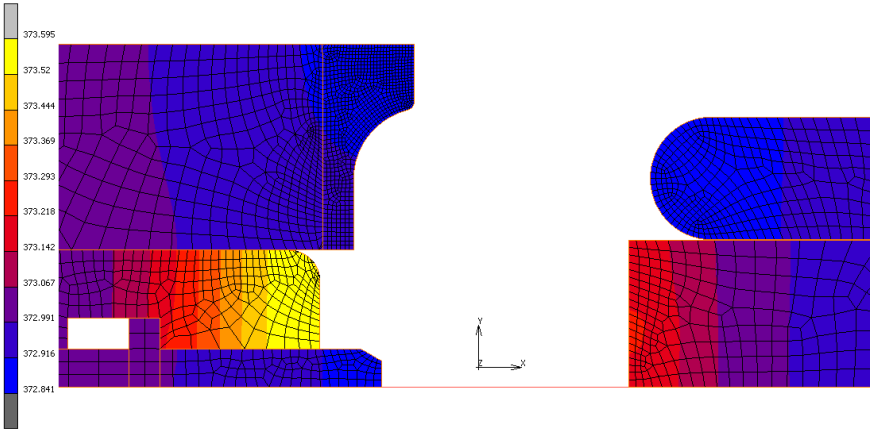
353 K - Step 2



373 K - Step 1



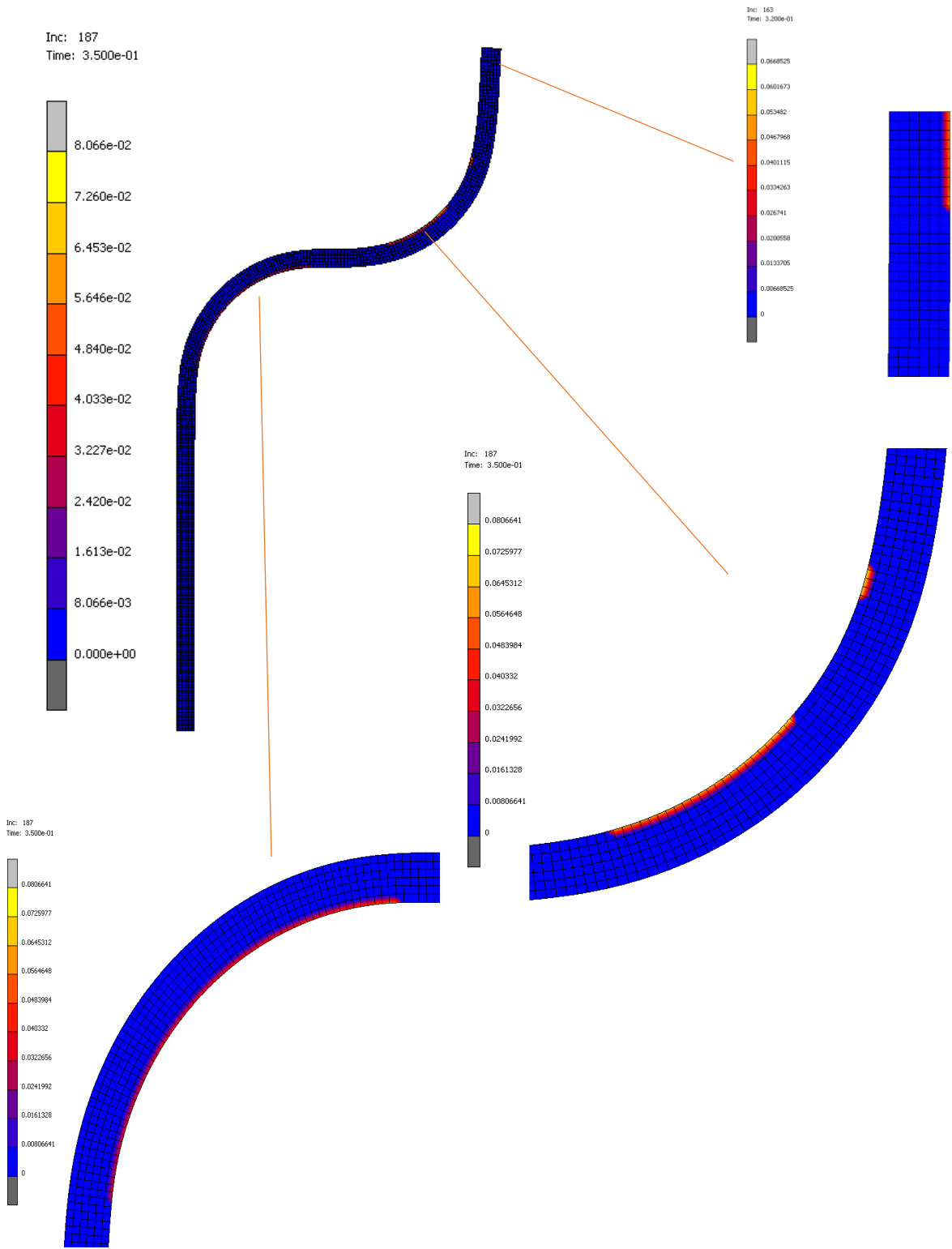
373 K - Step 2



Frictional Contact Workpiece – Tooling

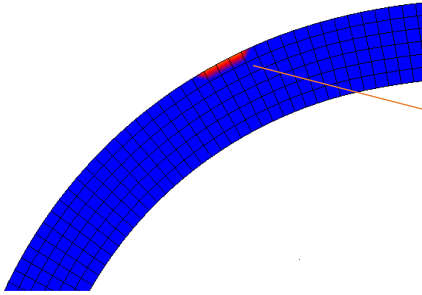
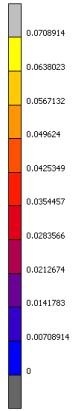
293 K

Step 1

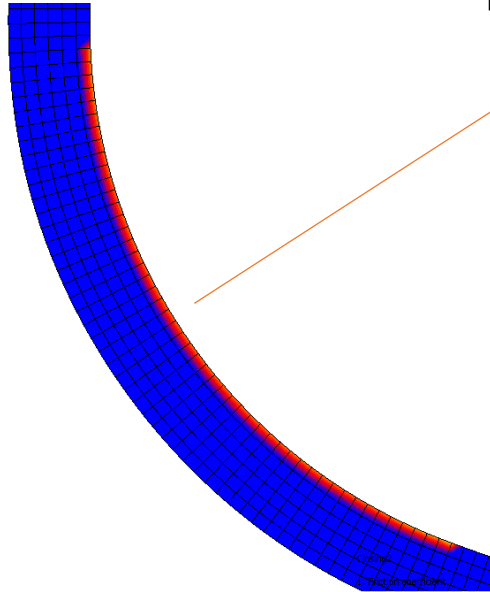
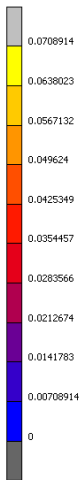


293 K
Step 2

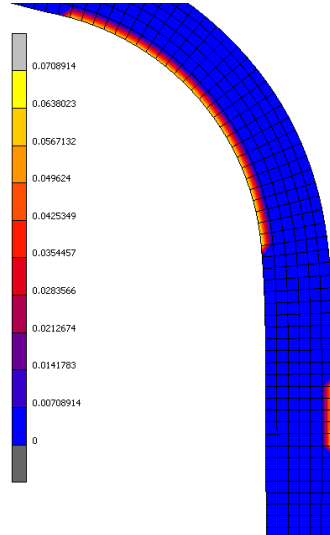
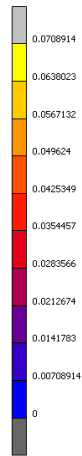
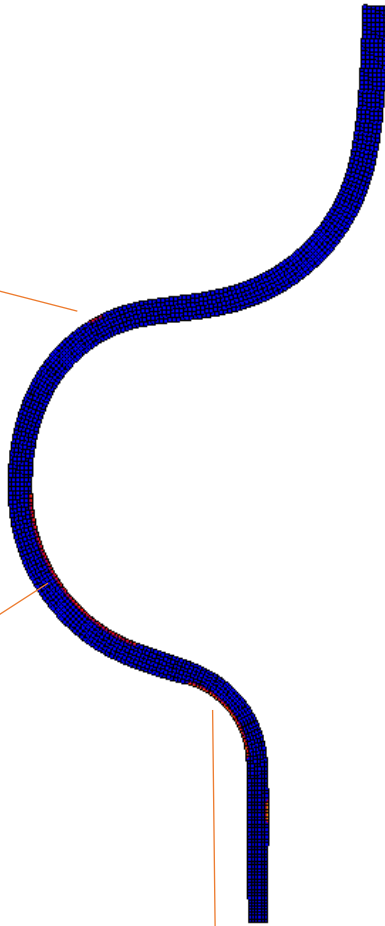
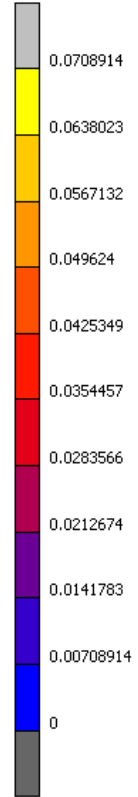
Inc: 282
Time: 4.125e-01



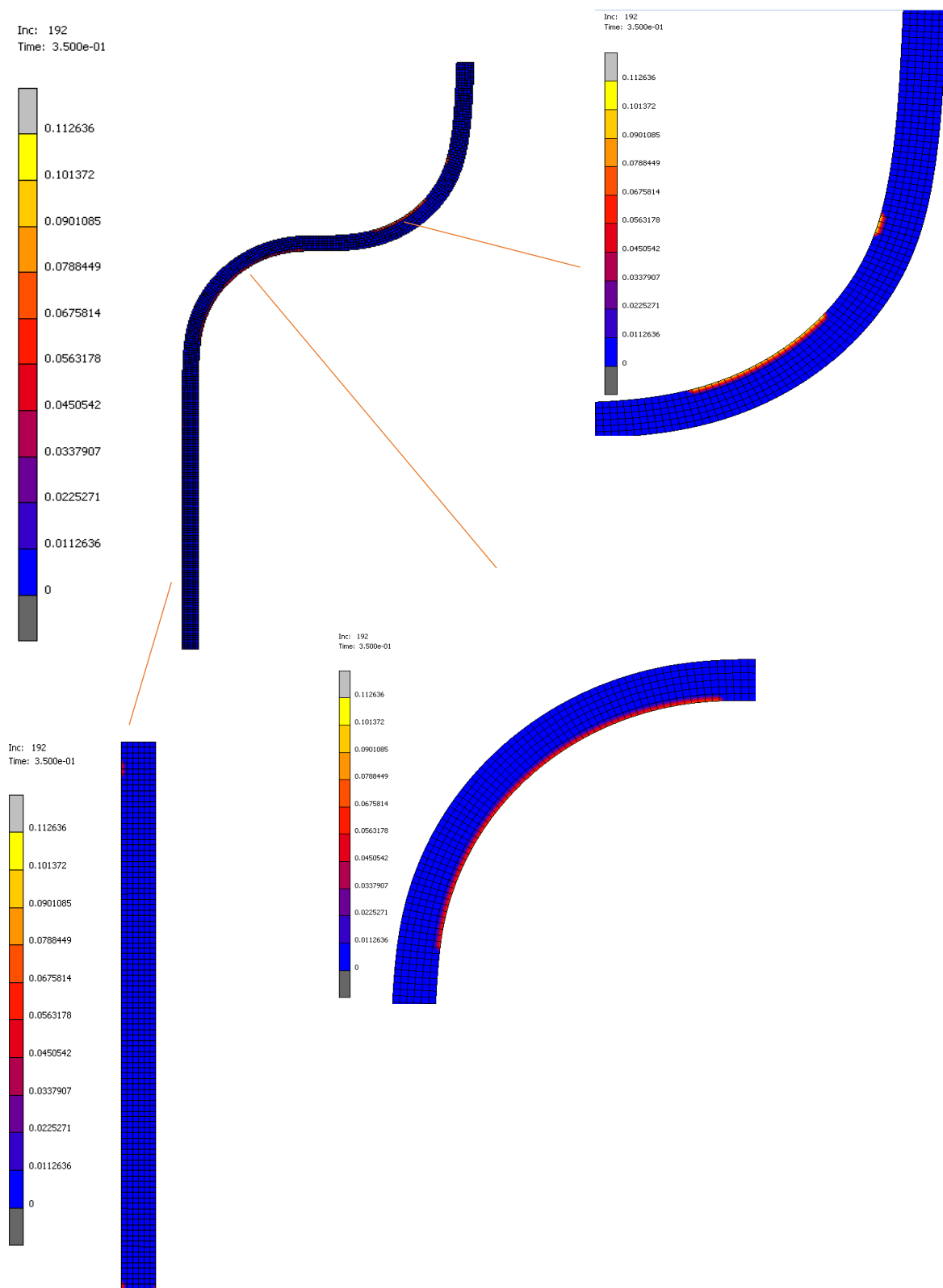
Inc: 282
Time: 4.125e-01



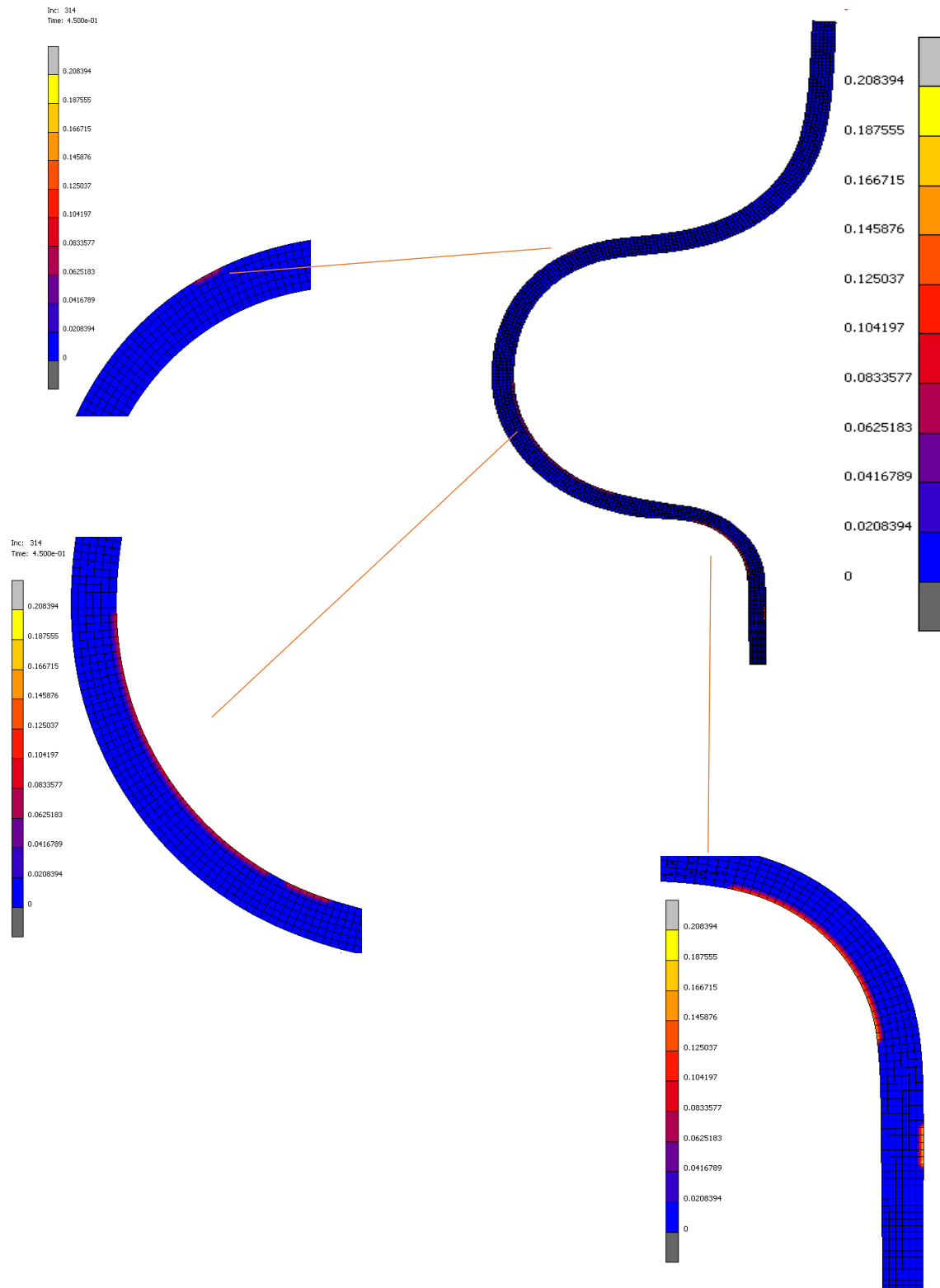
Inc: 282
Time: 4.125e-01



333 K
Step 1

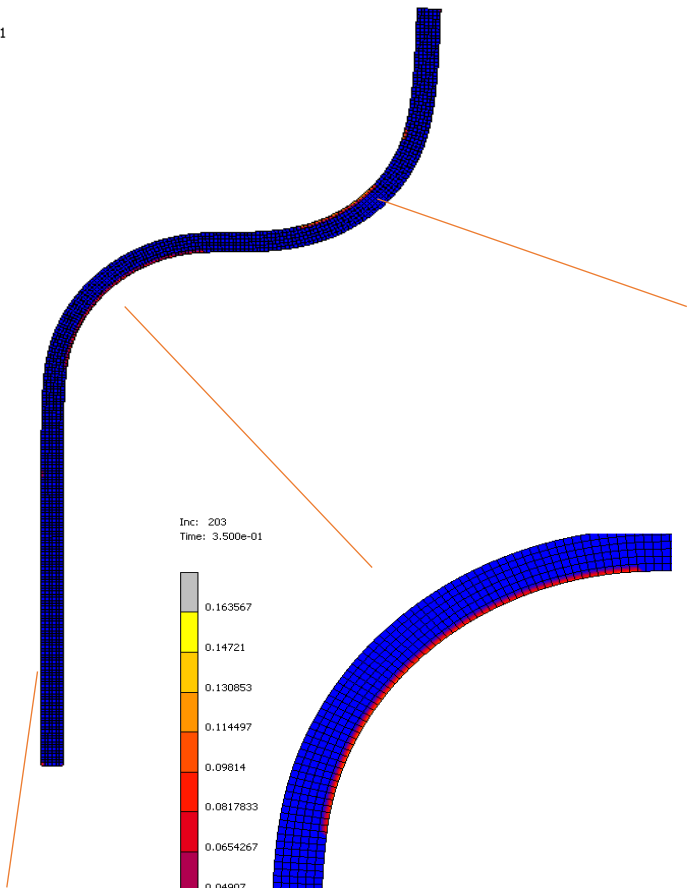
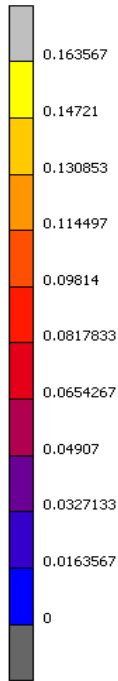


333 K
Step 2

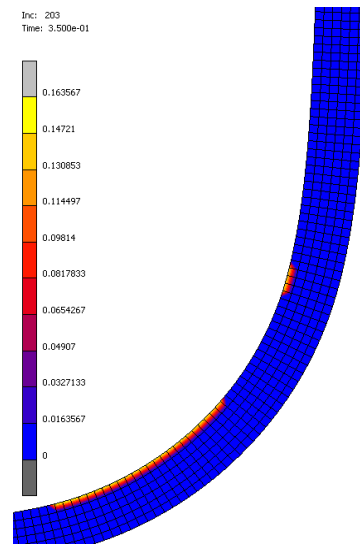
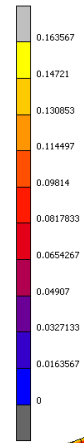


373 K
Step 1

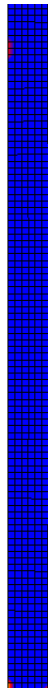
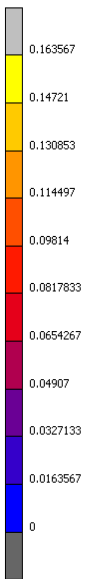
Inc: 203
Time: 3.500e-01



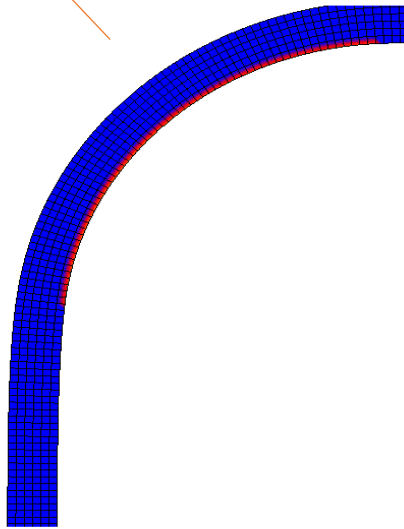
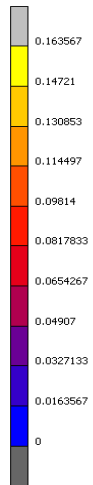
Inc: 203
Time: 3.500e-01



Inc: 203
Time: 3.500e-01

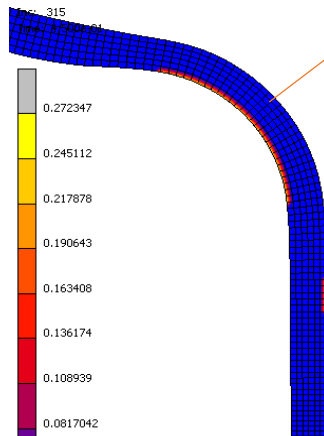
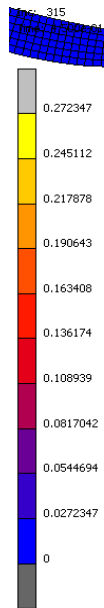
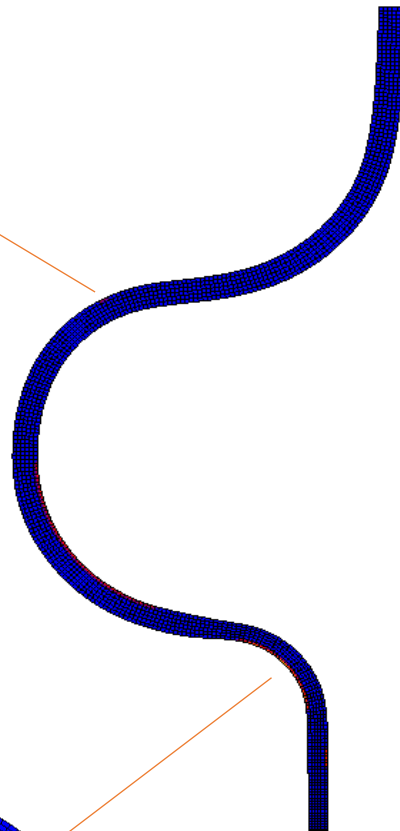
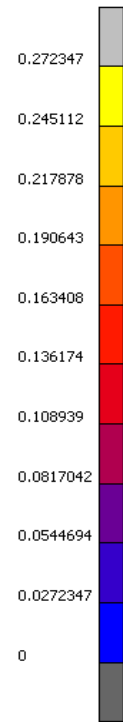
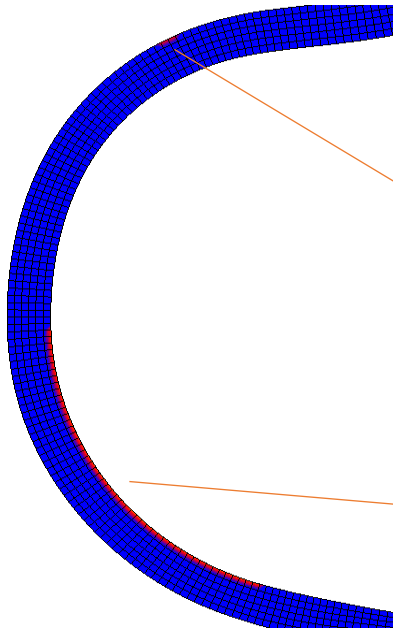
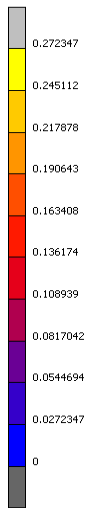


Inc: 203
Time: 3.500e-01



373 K
Step 2

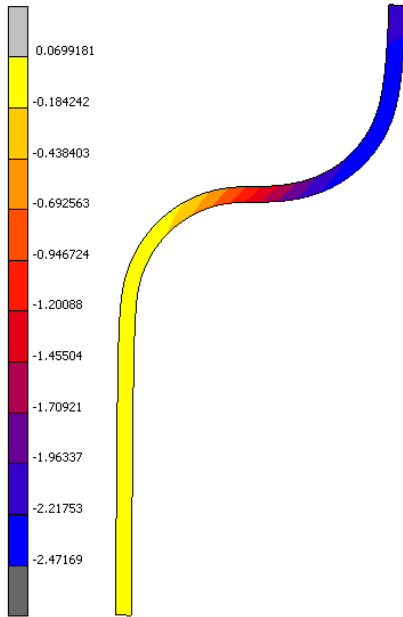
Inc: 315
Time: 4.500e-01



Total Displacement Y-Direction Workpiece

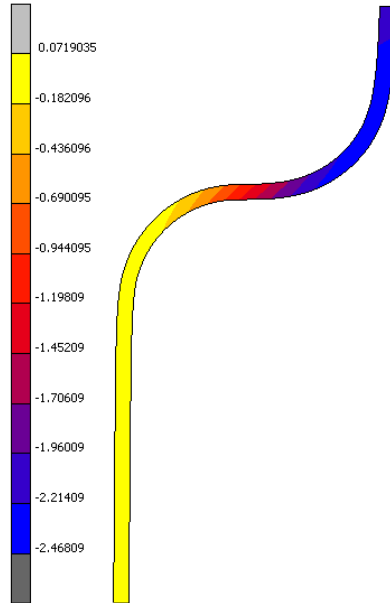
**293 K
Step 1**

Inc: 0
Time: 0.000e+00



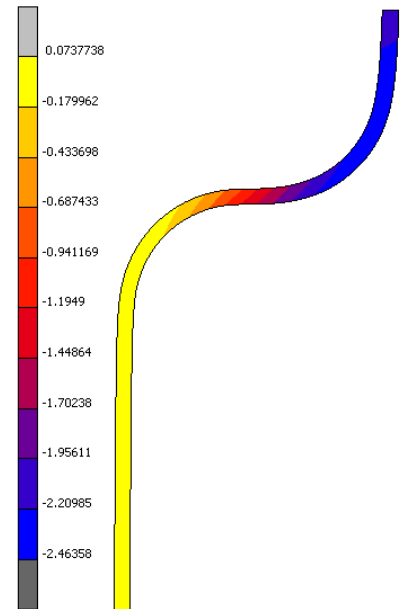
**333 K
Step 1**

Inc: 0
Time: 0.000e+00



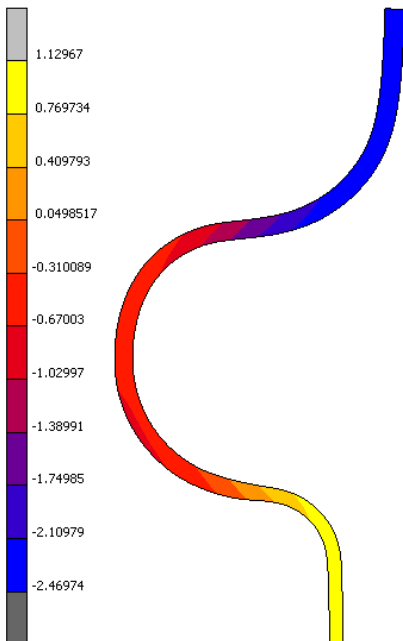
**373 K
Step 1**

Inc: 0
Time: 0.000e+00



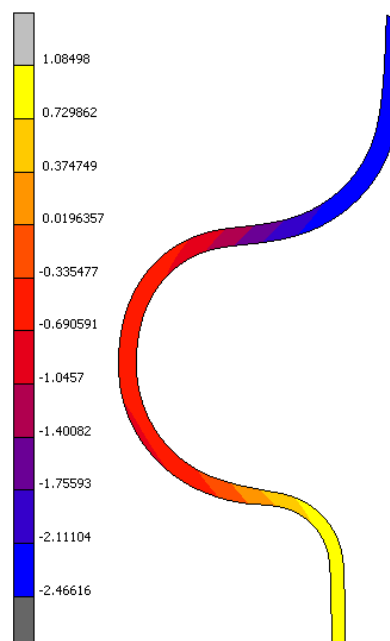
**293 K
Step 2**

Inc: 608
Time: 7.000e-01



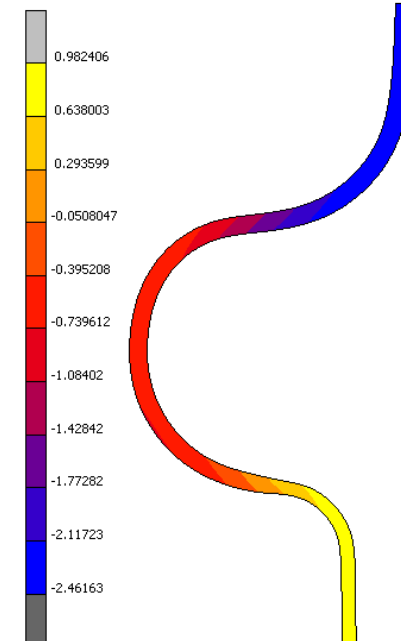
**333 K
Step 2**

Inc: 597
Time: 7.000e-01



**373 K
Step 2**

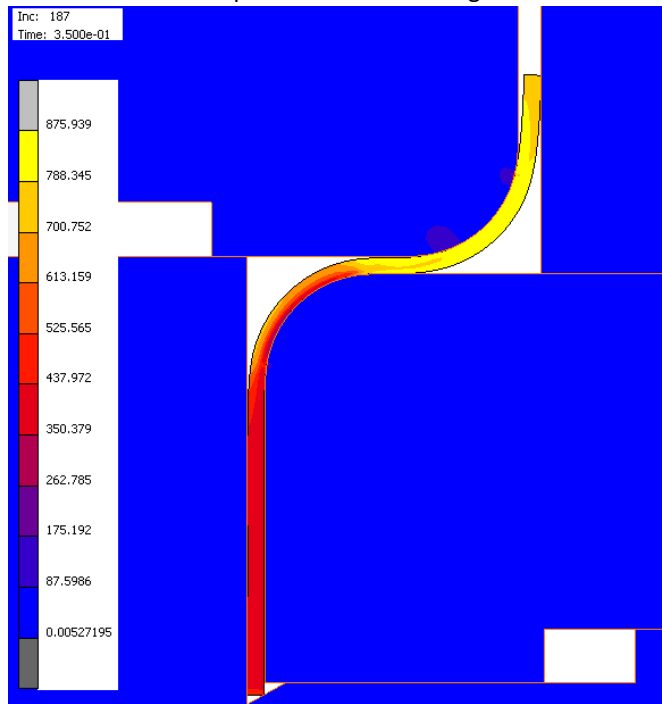
Inc: 593
Time: 7.000e-01



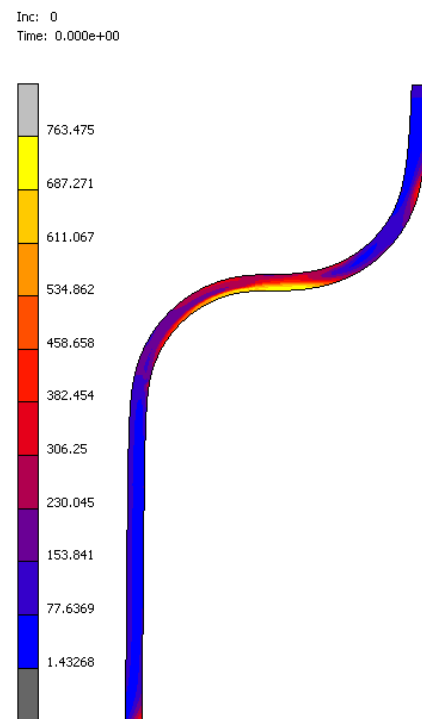
Equivalent Cauchy Stress Development Workpiece

293 K

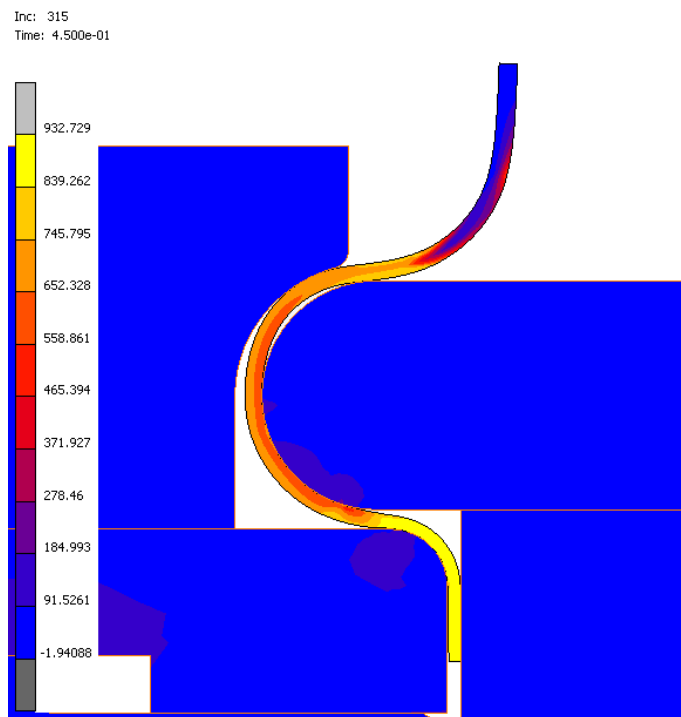
Step 1 – Before Unloading



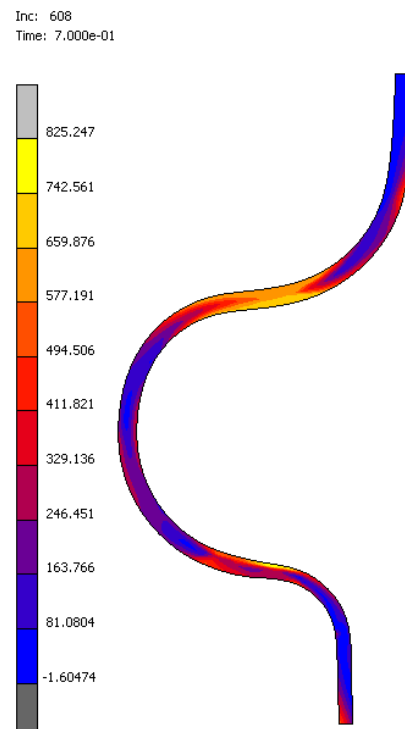
Step 1 – After Unloading



Step 2 – Before Unloading

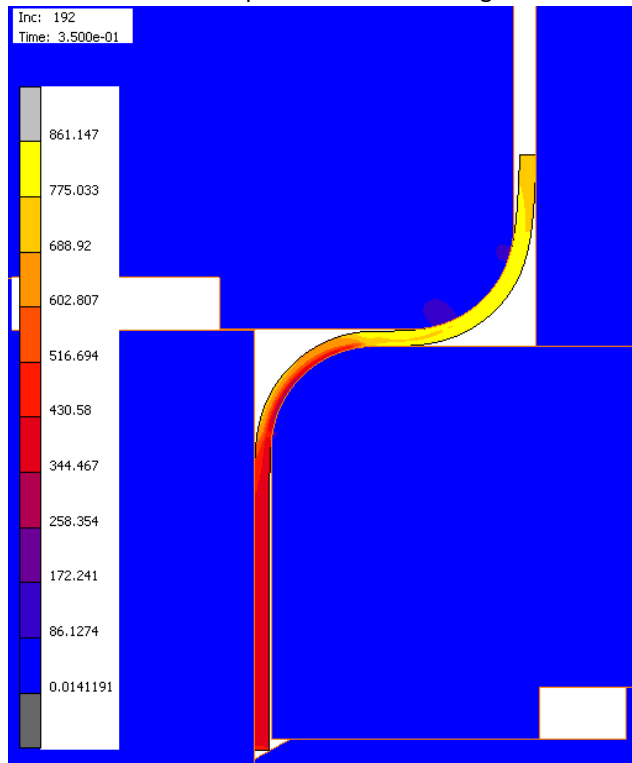


Step 2 – After Unloading

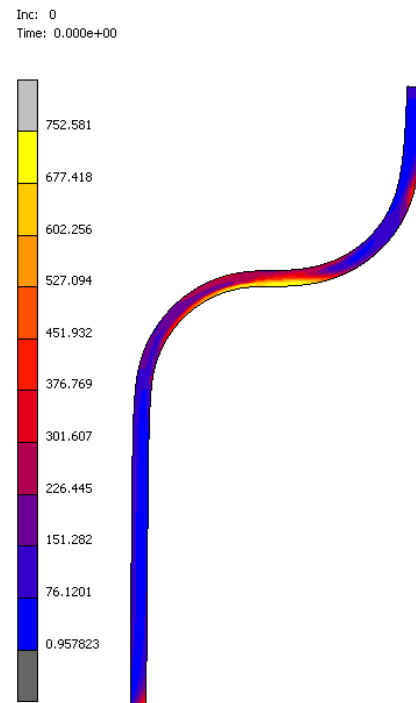


333 K

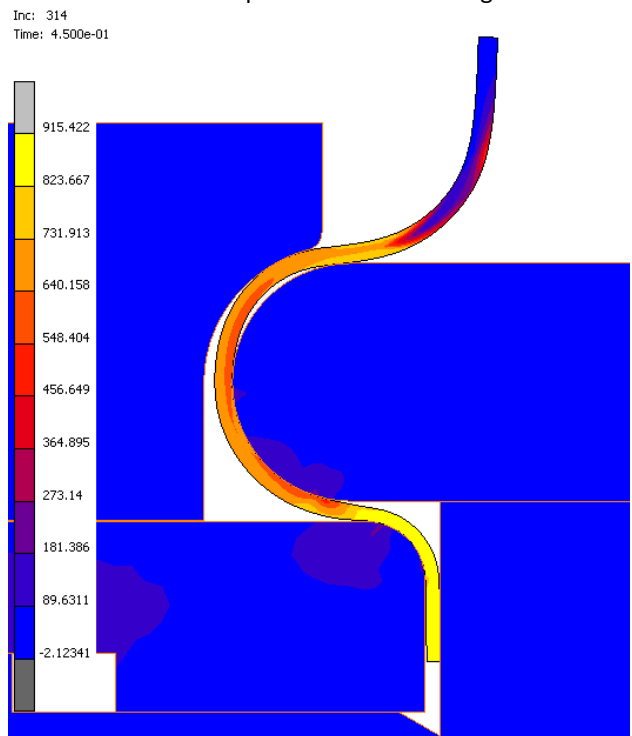
Step 1 – Before Unloading



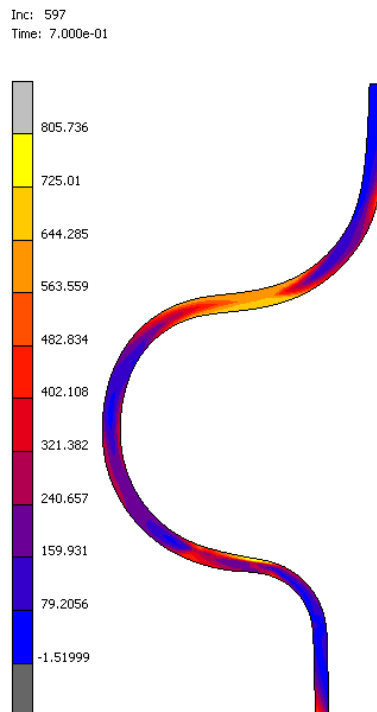
Step 1 – After Unloading



Step 2 – Before Unloading

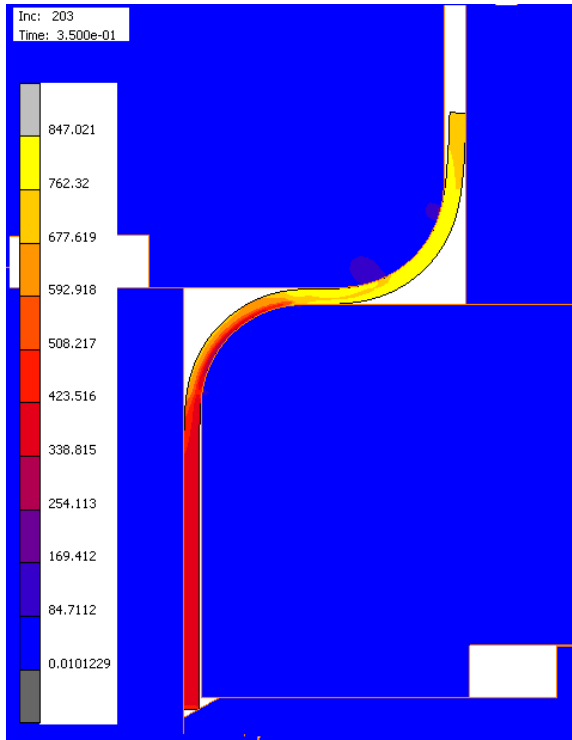


Step 2 – After Unloading

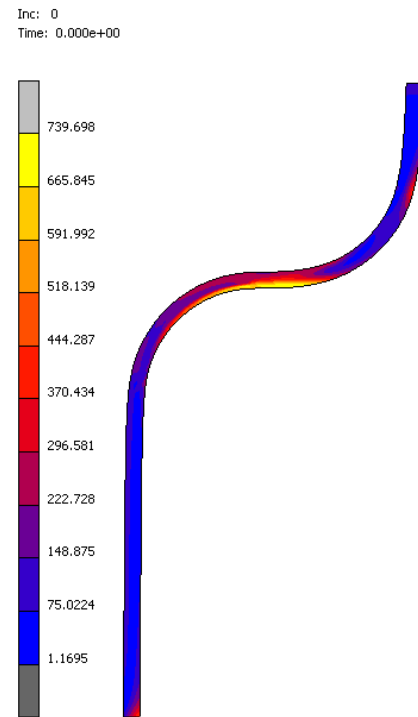


373 K

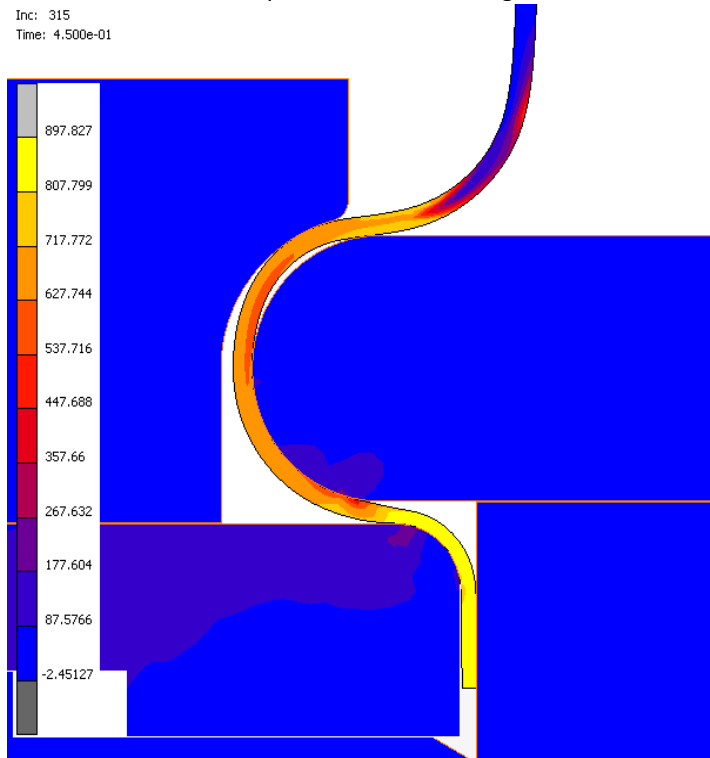
Step 1 – Before Unloading



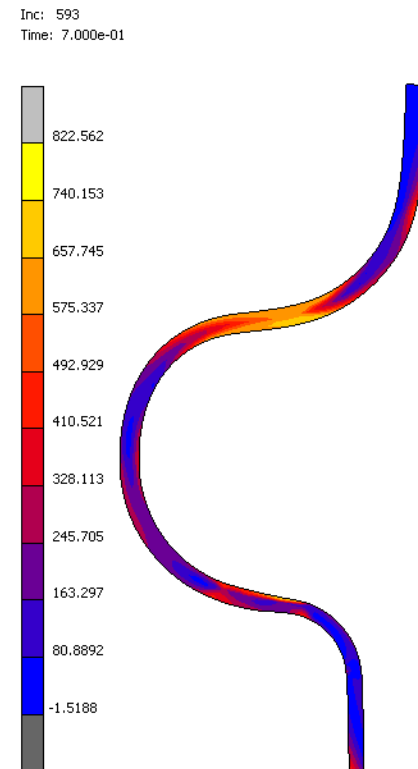
Step 1 – After Unloading



Step 2 – Before Unloading



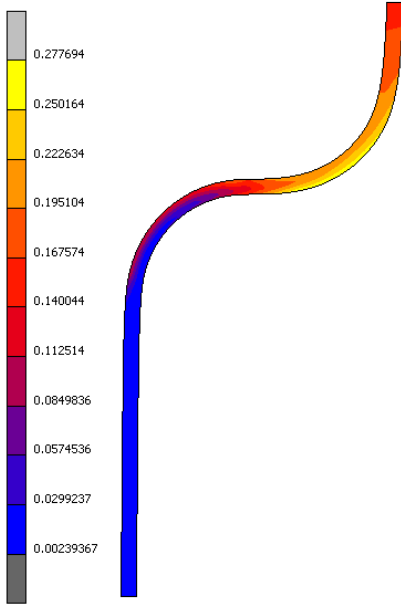
Step 2 – After Unloading



Total Equivalent Strain Development Workpiece

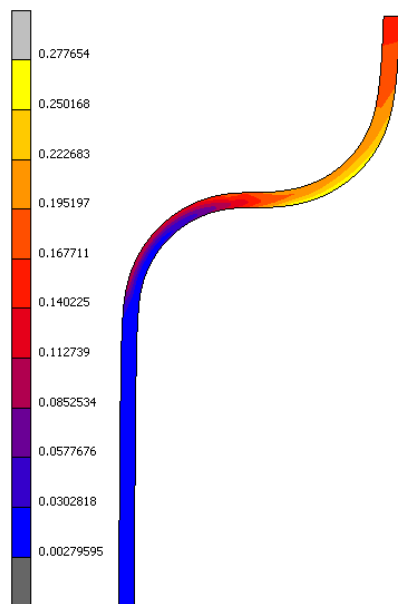
293 K
Step 1

Inc: 0
Time: 0.000e+00



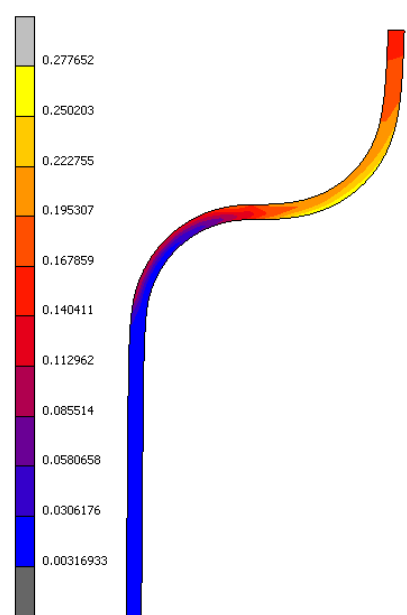
333 K
Step 1

Inc: 0
Time: 0.000e+00



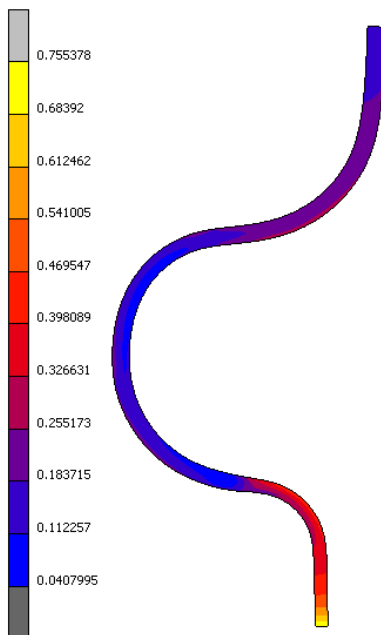
373 K
Step 1

Inc: 0
Time: 0.000e+00



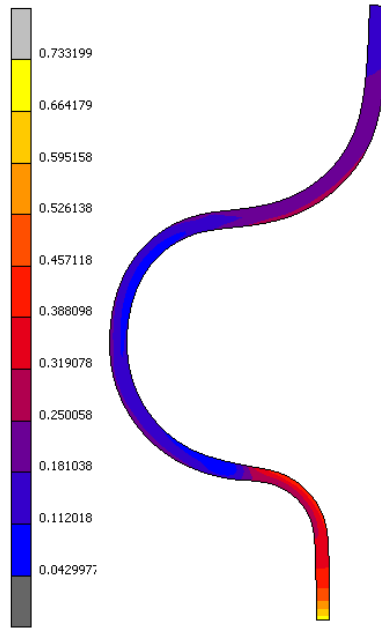
293 K
Step 2

Inc: 608
Time: 7.000e-01



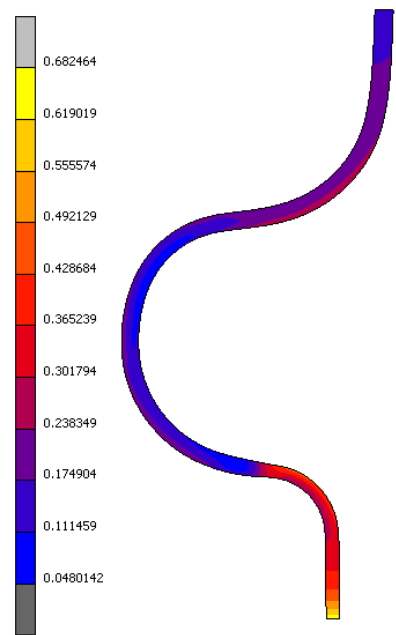
333 K
Step 2

Inc: 597
Time: 7.000e-01



373 K
Step 2

Inc: 315
Time: 4.500e-01



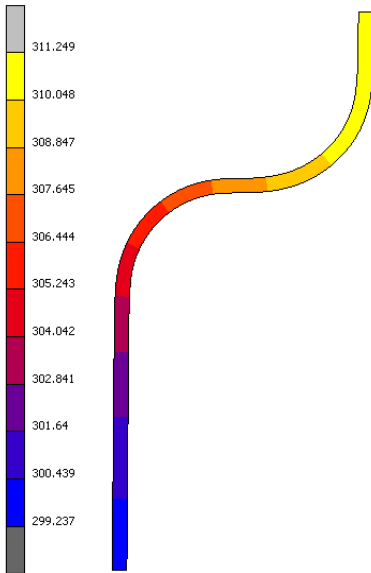
Appendix 14 – FEM Study 4 – Bergström Variations

Sa0.35um_Lub2gm2_SaT0.02um

Temperature Development Workpiece

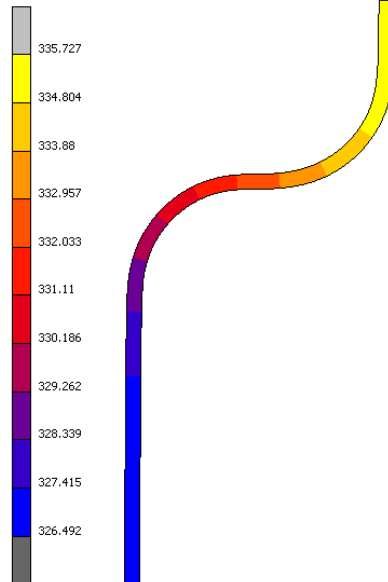
293 K
Step 1

Inc: 0
Time: 0.000e+00



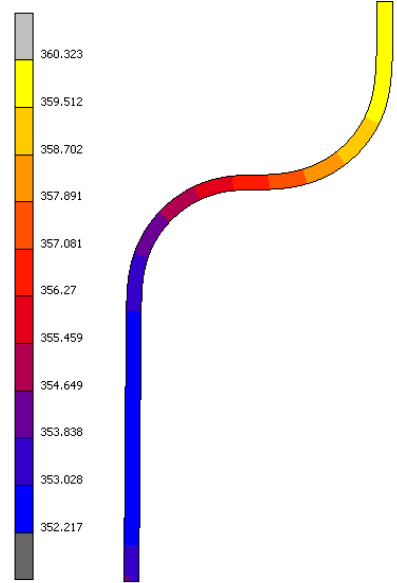
333 K
Step 1

Inc: 0
Time: 0.000e+00



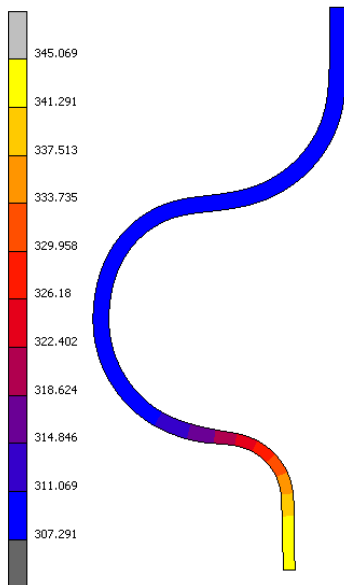
373 K
Step 1

Inc: 0
Time: 0.000e+00



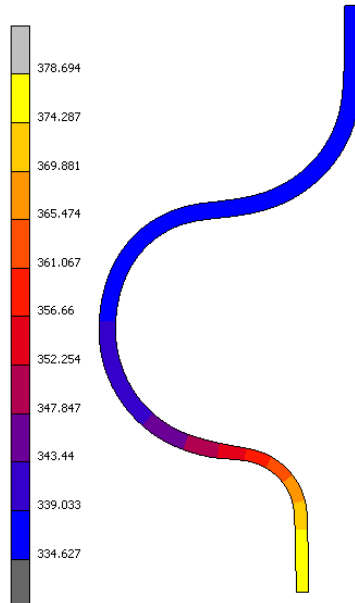
293 K
Step 2

Inc: 595
Time: 7.000e-01



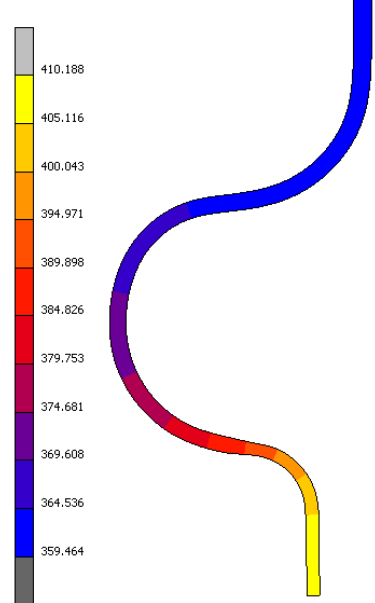
333 K
Step 2

Inc: 591
Time: 7.000e-01



373 K
Step 2

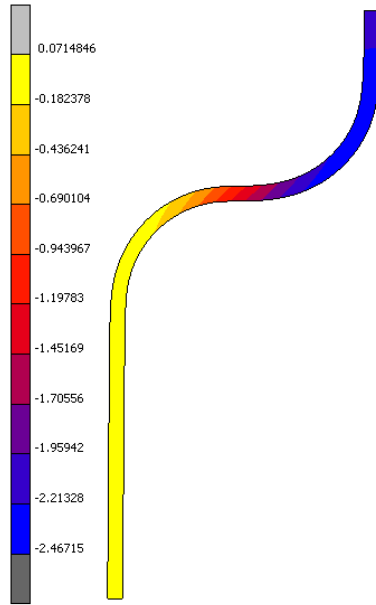
Inc: 590
Time: 7.000e-01



Total Displacement Y-Direction

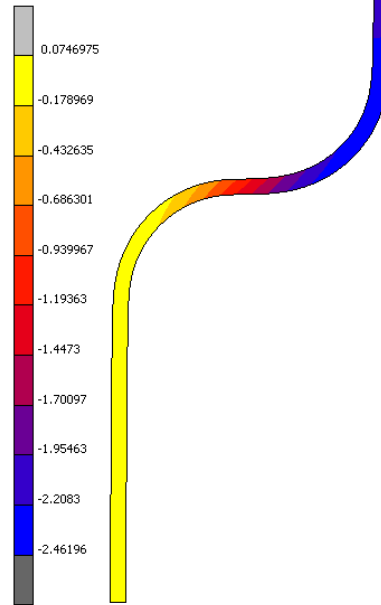
293 K
Step 1

Inc: 0
Time: 0.000e+00



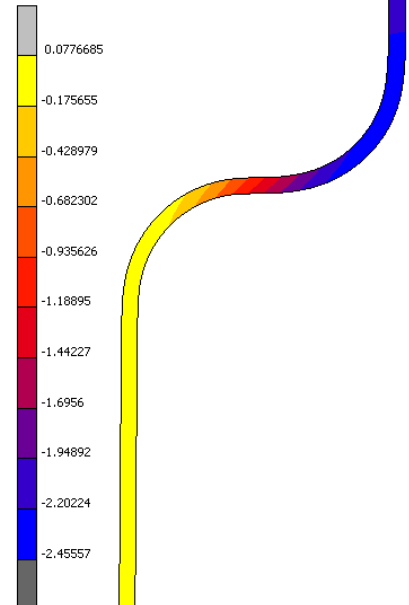
333 K
Step 1

Inc: 0
Time: 0.000e+00



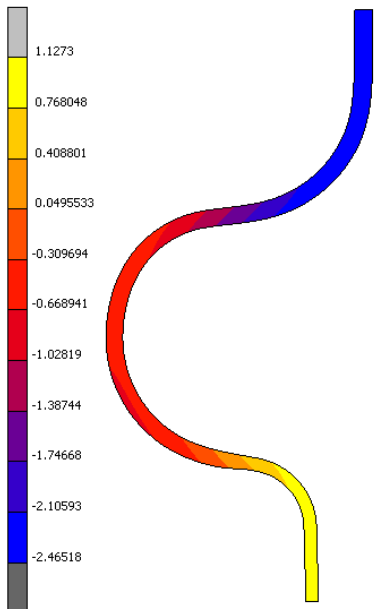
373 K
Step 1

Inc: 0
Time: 0.000e+00



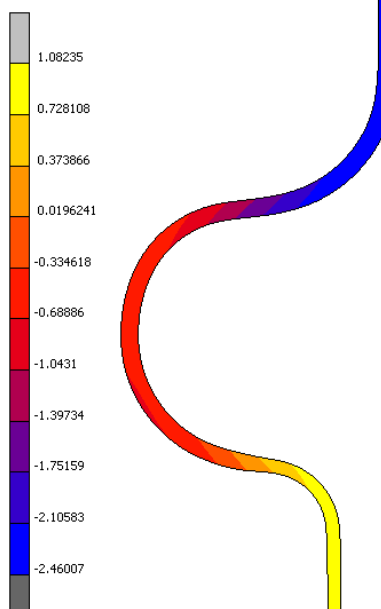
293 K
Step 2

Inc: 595
Time: 7.000e-01



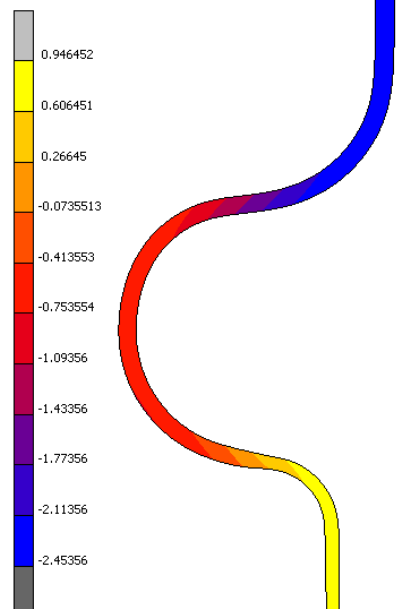
333 K
Step 2

Inc: 591
Time: 7.000e-01



373 K
Step 2

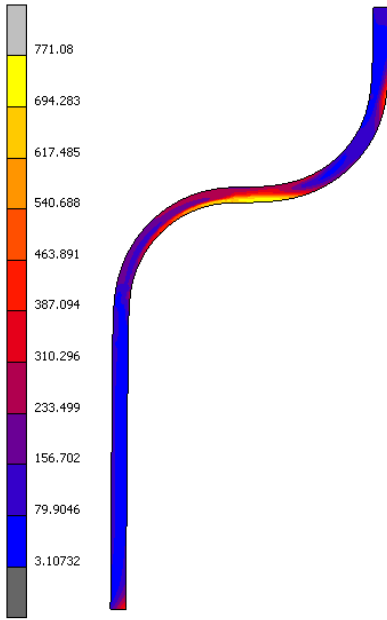
Inc: 590
Time: 7.000e-01



Equivalent Cauchy Stress Development

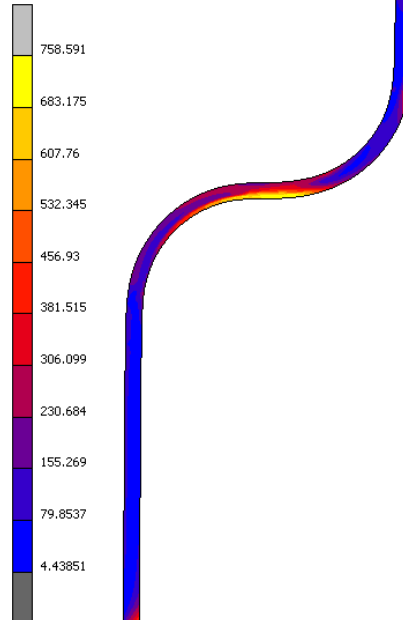
293 K
Step 1

Inc: 0
Time: 0.000e+00



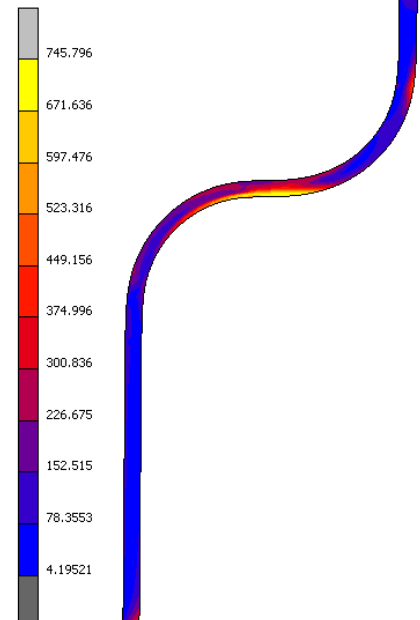
333 K
Step 1

Inc: 0
Time: 0.000e+00



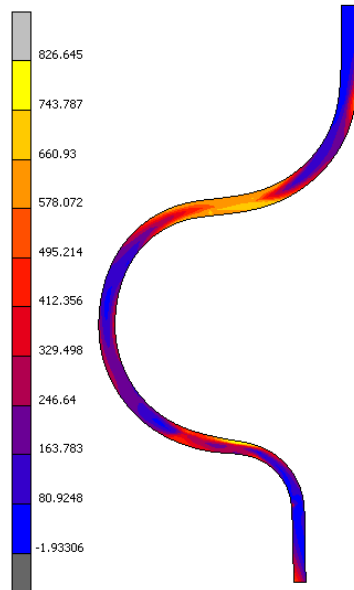
373 K
Step 1

Inc: 0
Time: 0.000e+00



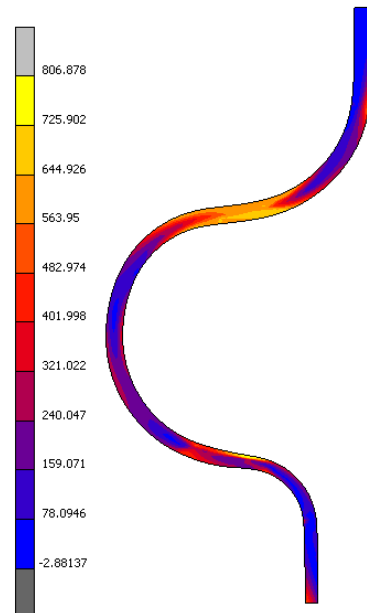
293 K
Step 2

Inc: 595
Time: 7.000e-01



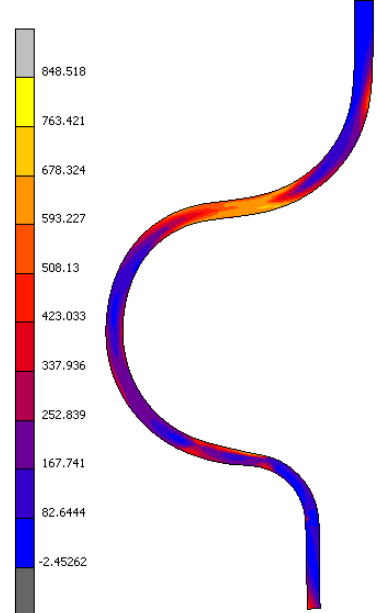
333 K
Step 2

Inc: 591
Time: 7.000e-01



373 K
Step 2

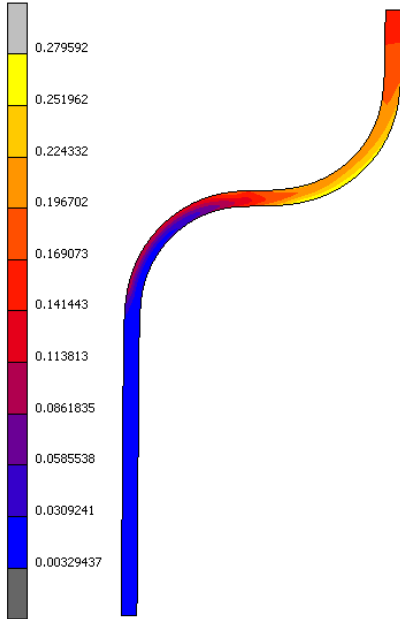
Inc: 590
Time: 7.000e-01



Equivalent Strain Development

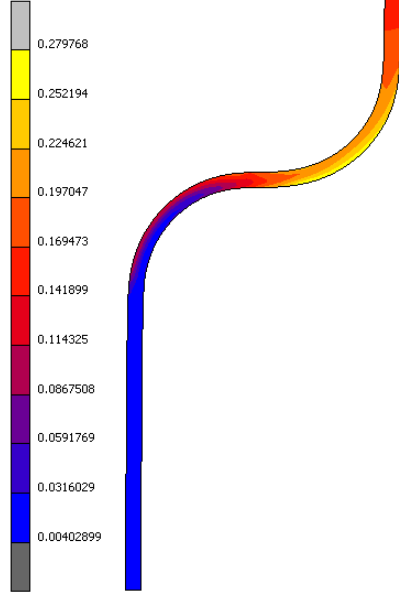
293 K
Step 1

Inc: 0
Time: 0.000e+00



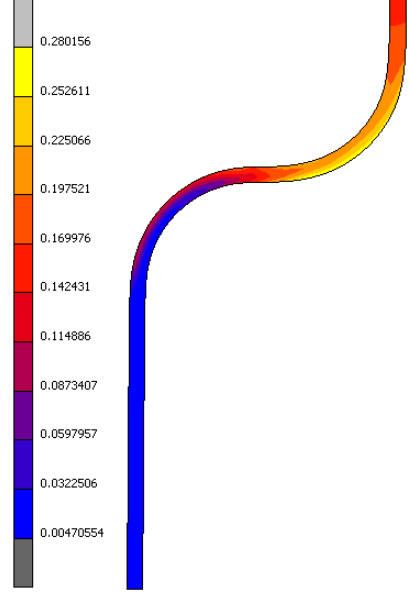
333 K
Step 1

Inc: 0
Time: 0.000e+00



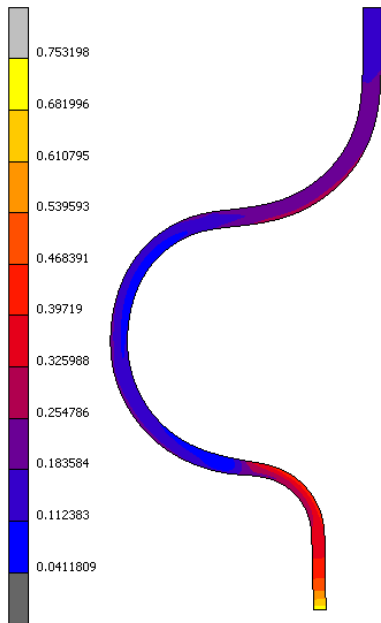
373 K
Step 1

Inc: 0
Time: 0.000e+00



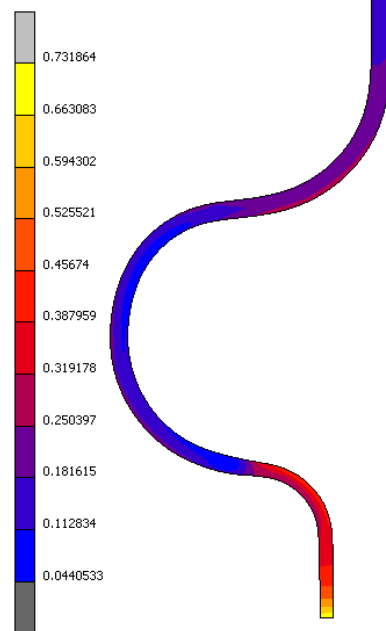
293 K
Step 2

Inc: 595
Time: 7.000e-01



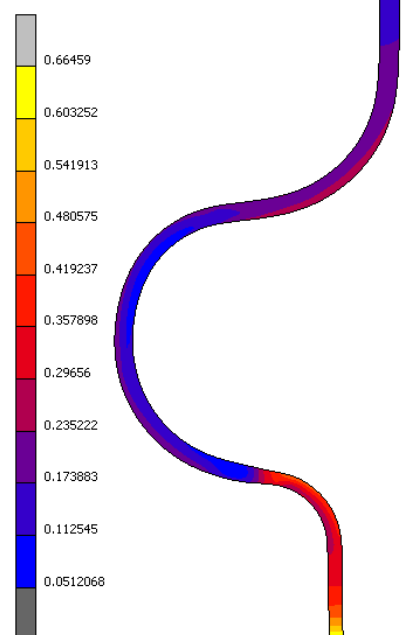
333 K
Step 2

Inc: 591
Time: 7.000e-01



373 K
Step 2

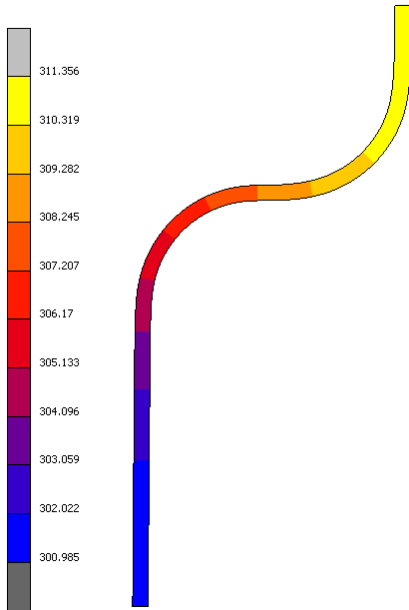
Inc: 590
Time: 7.000e-01



SaS0.35um_Lub2gm2_SaT0.05um Temperature Development Workpiece

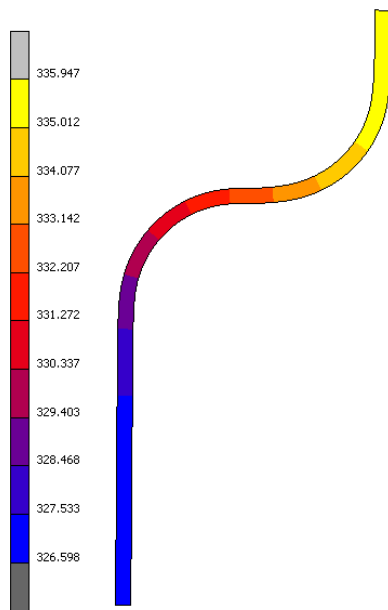
293 K
Step 1

Inc: 0
Time: 0.000e+00



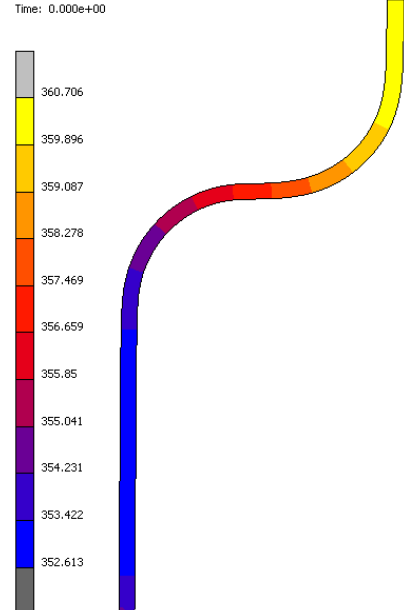
333 K
Step 1

Inc: 0
Time: 0.000e+00



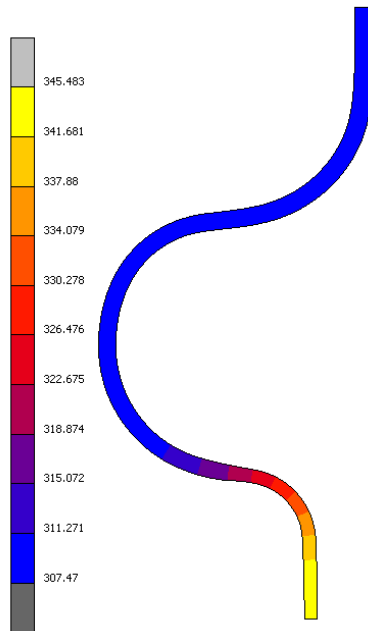
373 K
Step 1

Inc: 0
Time: 0.000e+00



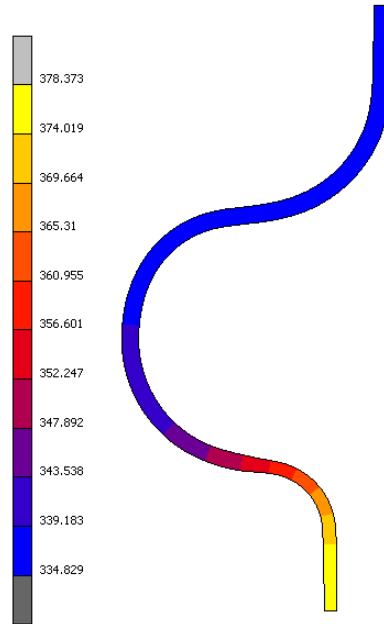
293 K
Step 2

Inc: 596
Time: 7.000e-01



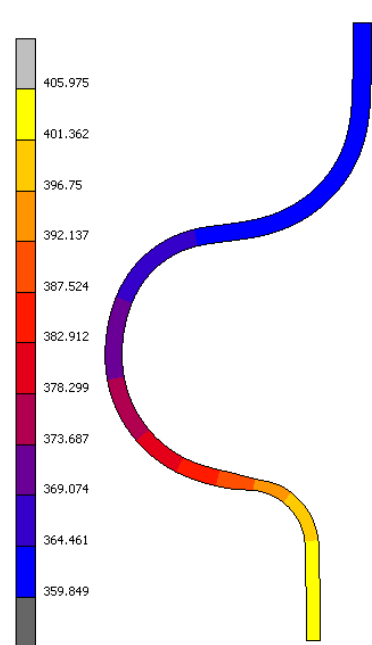
333 K
Step 2

Inc: 595
Time: 7.000e-01



373 K
Step 2

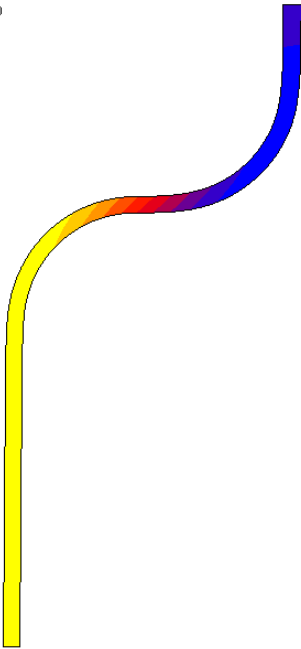
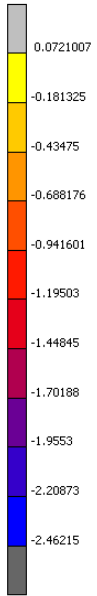
Inc: 606
Time: 7.000e-01



Total Displacement Y-Direction

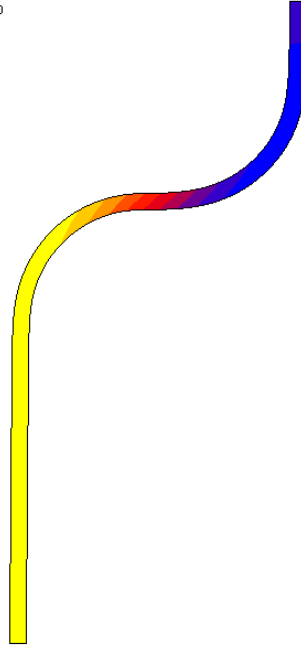
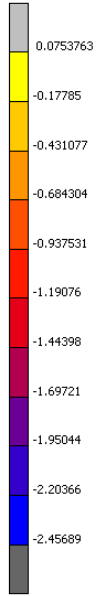
293 K
Step 1

Inc: 0
Time: 0.000e+00



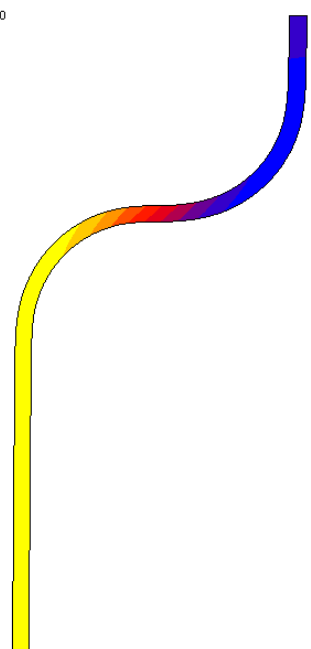
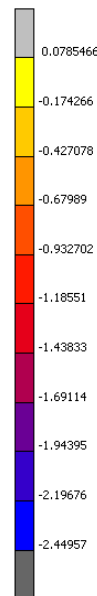
333 K
Step 1

Inc: 0
Time: 0.000e+00



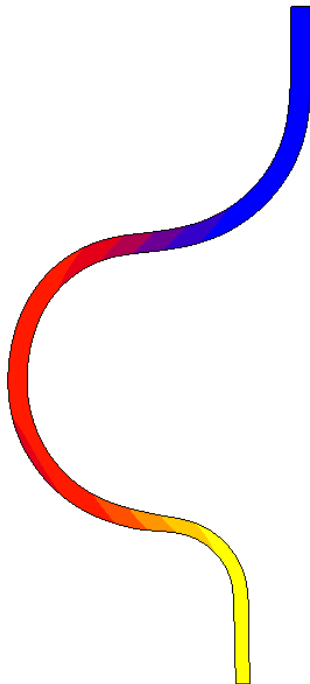
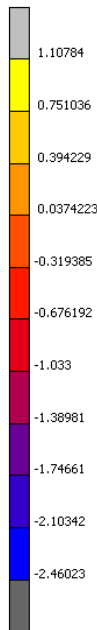
373 K
Step 1

Inc: 0
Time: 0.000e+00



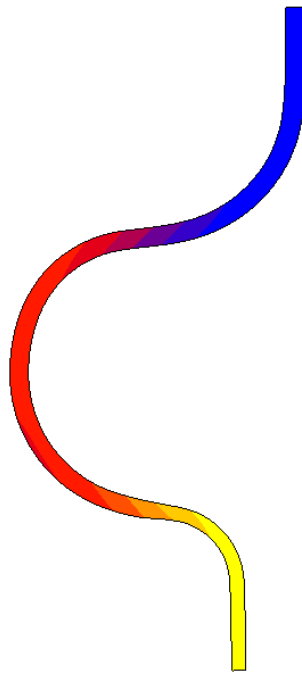
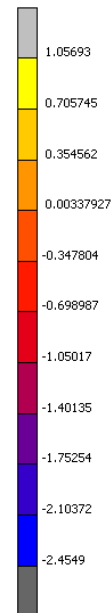
293 K
Step 2

Inc: 596
Time: 7.000e-01



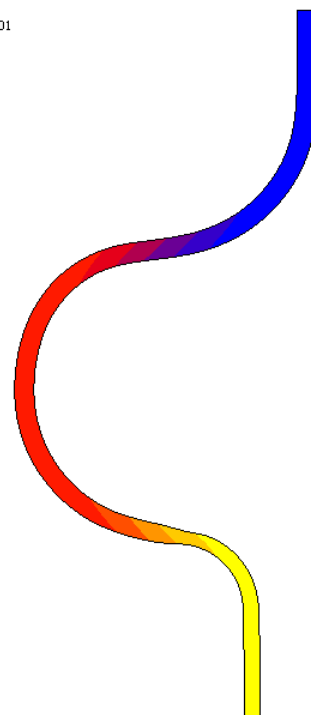
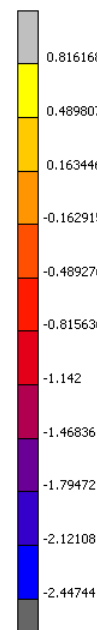
333 K
Step 2

Inc: 595
Time: 7.000e-01



373 K
Step 2

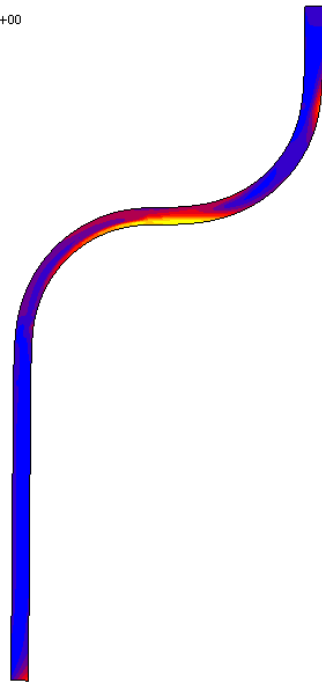
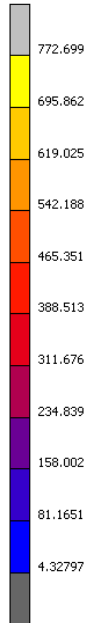
Inc: 606
Time: 7.000e-01



Equivalent Cauchy Stress Development

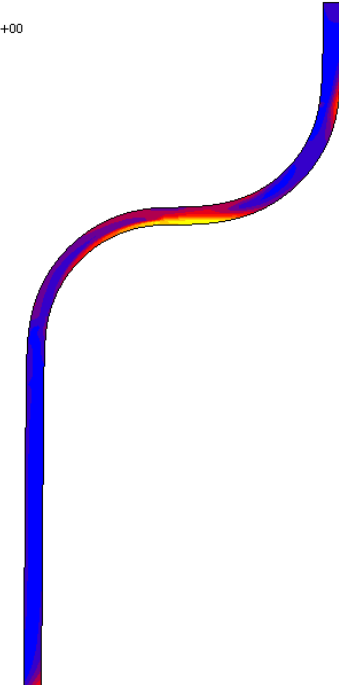
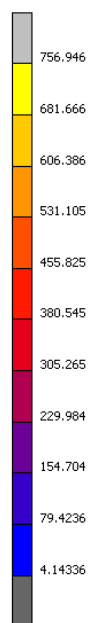
293 K
Step 1

Inc: 0
Time: 0.000e+00



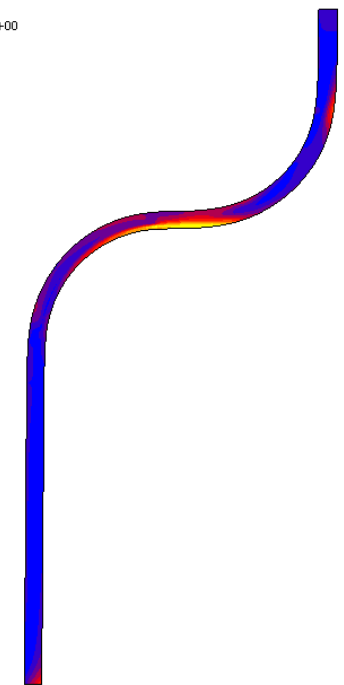
333 K
Step 1

Inc: 0
Time: 0.000e+00



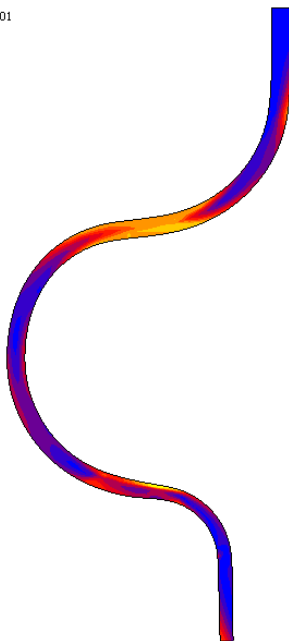
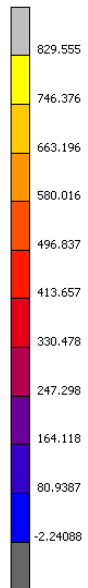
373 K
Step 1

Inc: 0
Time: 0.000e+00



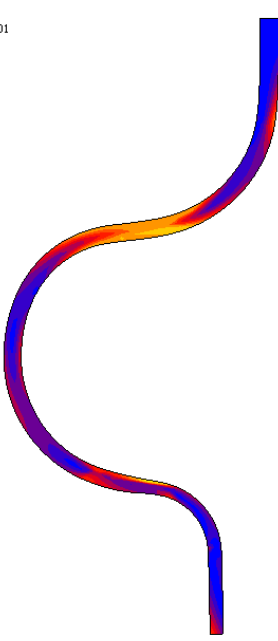
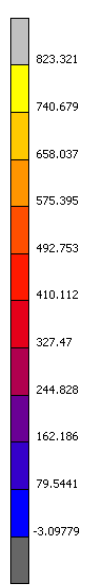
293 K
Step 2

Inc: 596
Time: 7.000e-01



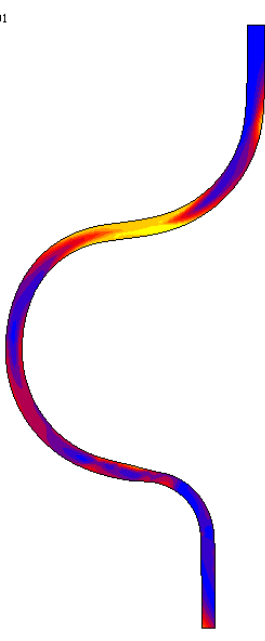
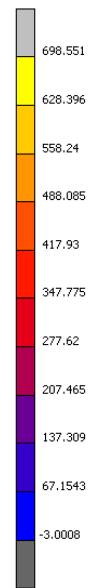
333 K
Step 2

Inc: 595
Time: 7.000e-01



373 K
Step 2

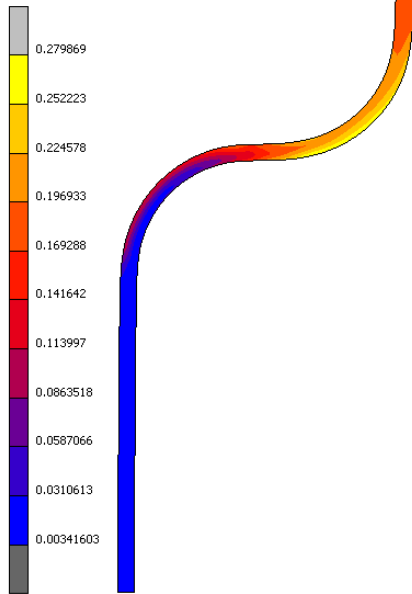
Inc: 606
Time: 7.000e-01



Equivalent Strain Development

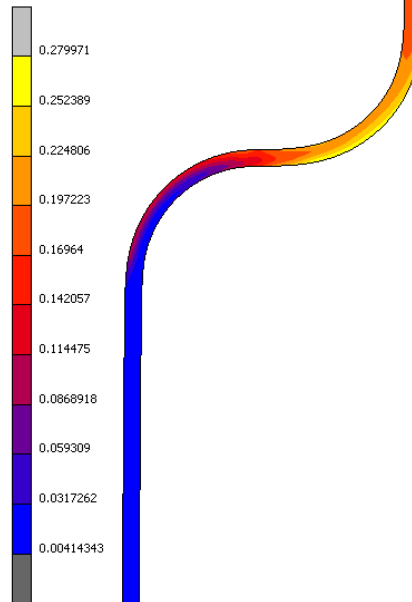
293 K
Step 1

Inc: 0
Time: 0.000e+00



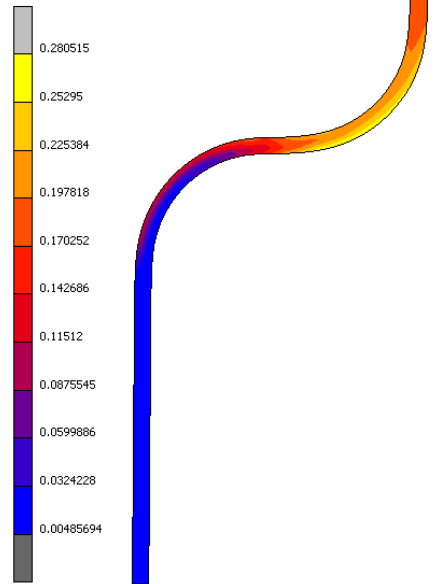
333 K
Step 1

Inc: 0
Time: 0.000e+00



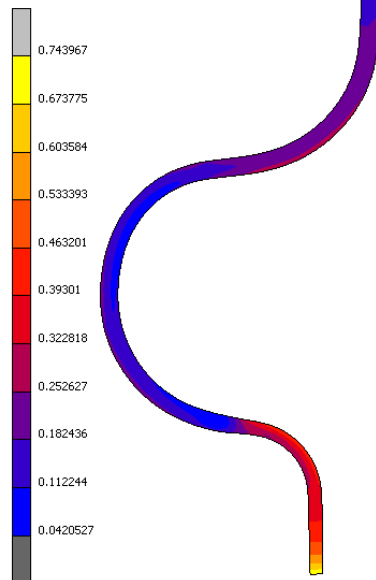
373 K
Step 1

Inc: 0
Time: 0.000e+00



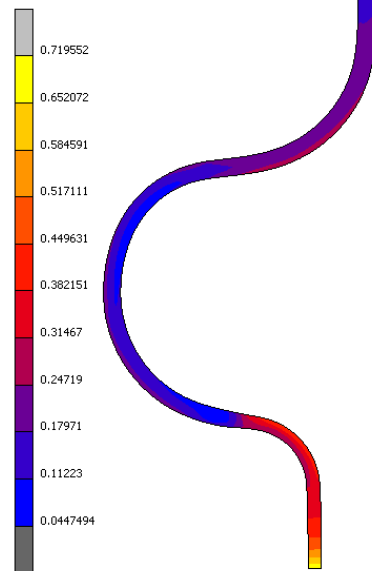
293 K
Step 2

Inc: 596
Time: 7.000e-01



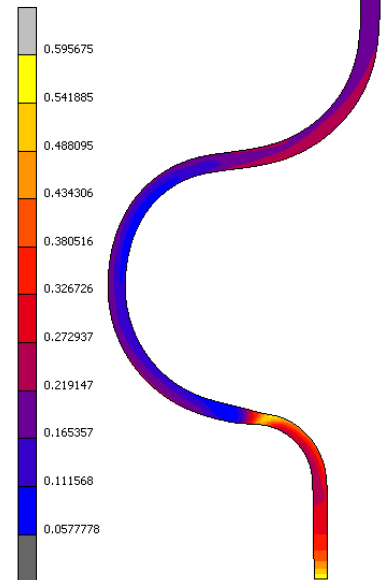
333 K
Step 2

Inc: 595
Time: 7.000e-01



373 K
Step 2

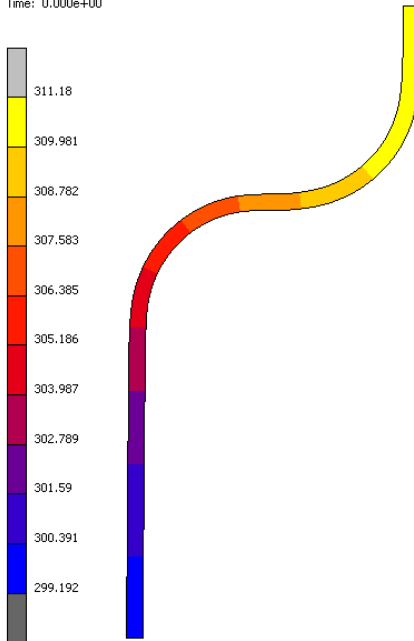
Inc: 606
Time: 7.000e-01



SaS0.35um_Lub7gm2_SaT0.02um Temperature Development Workpiece

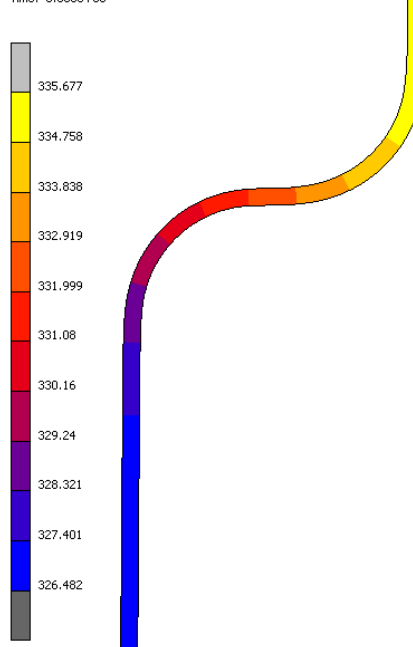
293 K
Step 1

Inc: 0
Time: 0.000e+00



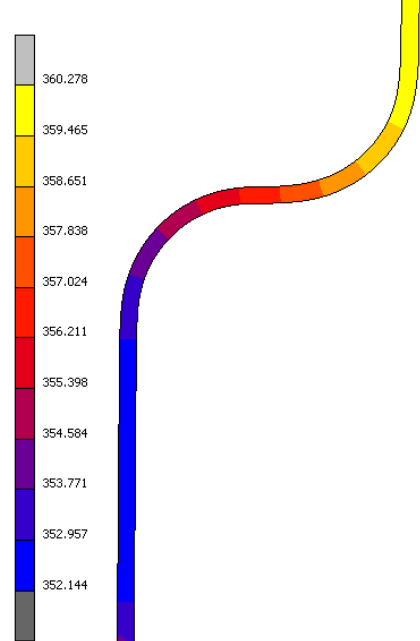
333 K
Step 1

Inc: 0
Time: 0.000e+00



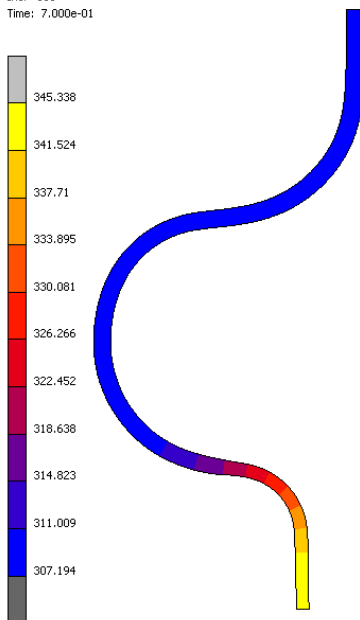
373 K
Step 1

Inc: 0
Time: 0.000e+00



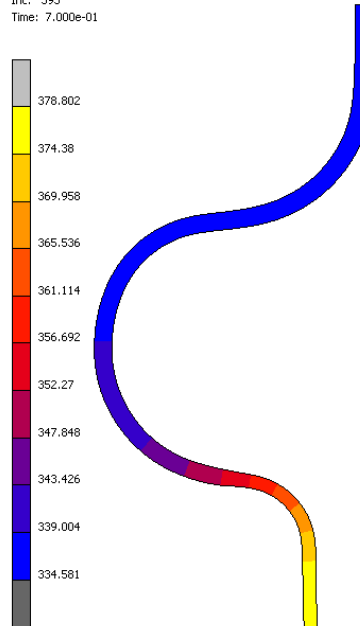
293 K
Step 2

Inc: 600
Time: 7.000e-01



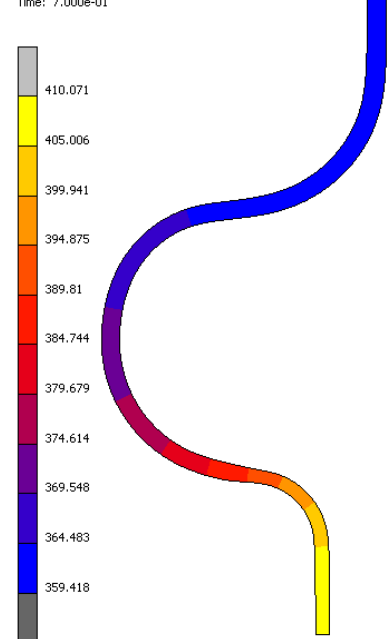
333 K
Step 2

Inc: 593
Time: 7.000e-01



373 K
Step 2

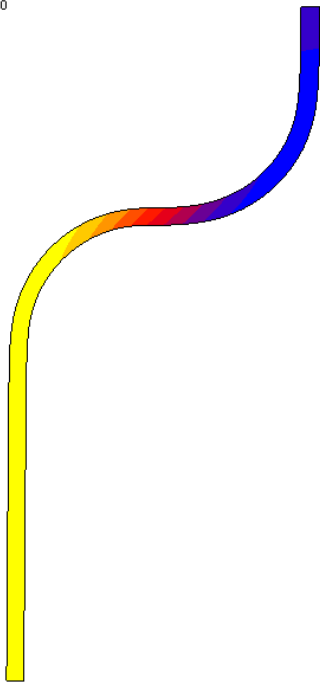
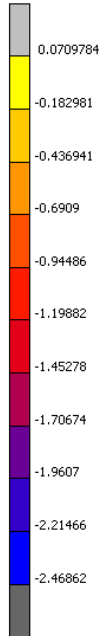
Inc: 590
Time: 7.000e-01



Total Displacement Y-Direction

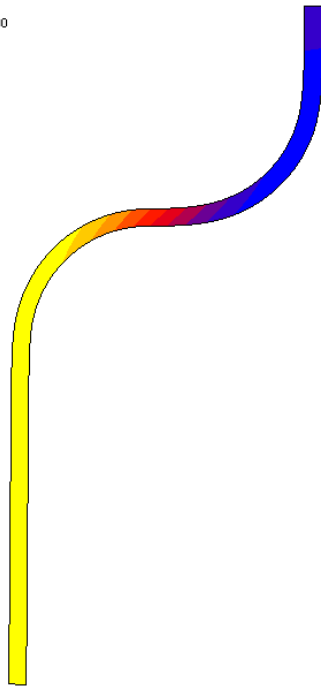
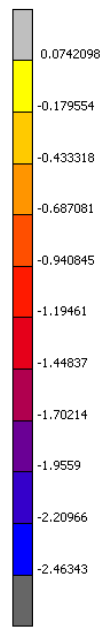
293 K
Step 1

Inc: 0
Time: 0.000e+00



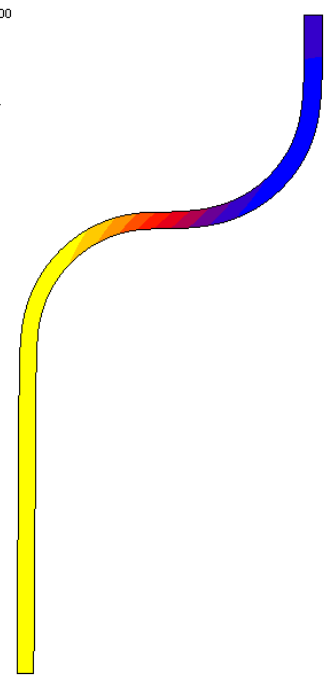
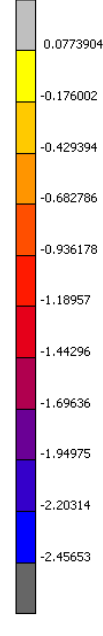
333 K
Step 1

Inc: 0
Time: 0.000e+00



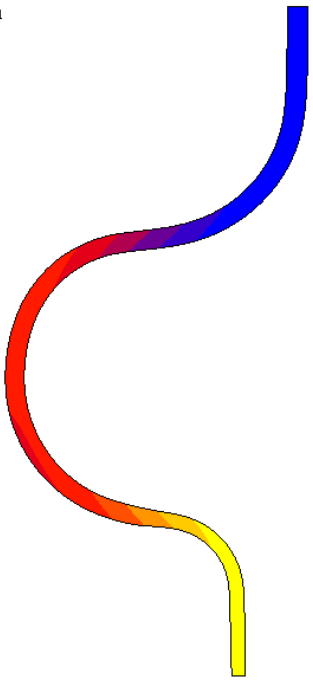
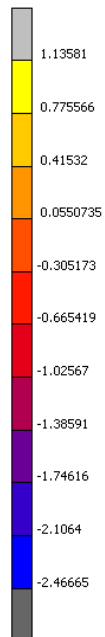
373 K
Step 1

Inc: 0
Time: 0.000e+00



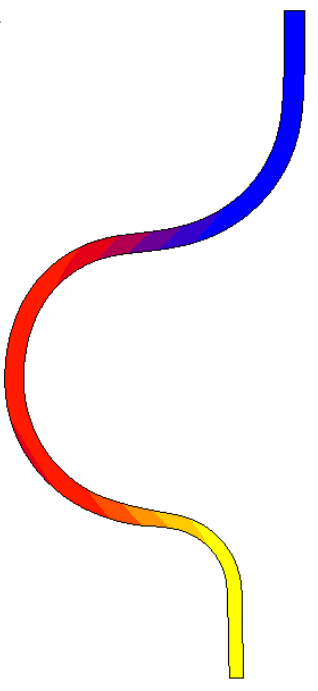
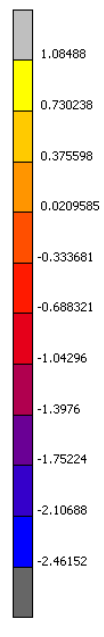
293 K
Step 2

Inc: 600
Time: 7.000e-01



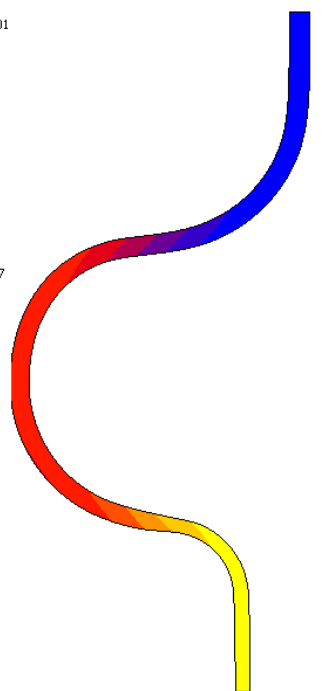
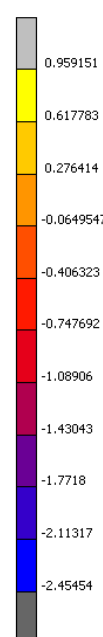
333 K
Step 2

Inc: 593
Time: 7.000e-01



373 K
Step 2

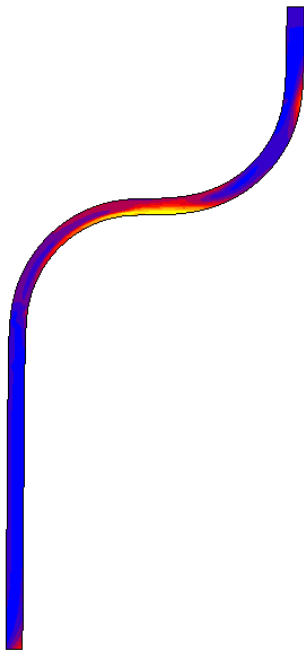
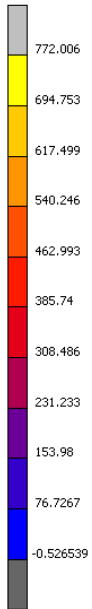
Inc: 590
Time: 7.000e-01



Equivalent Cauchy Stress Development

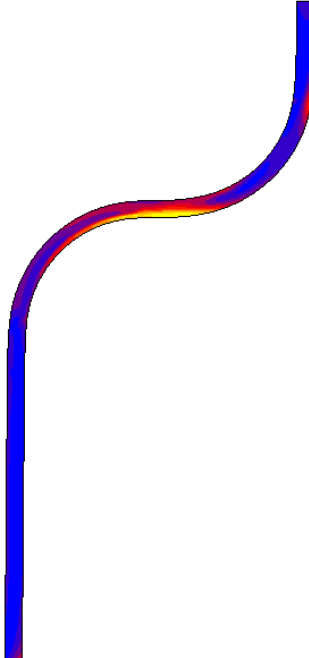
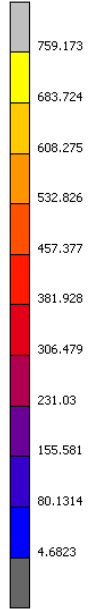
293 K
Step 1

Inc: 0
Time: 0.000e+00



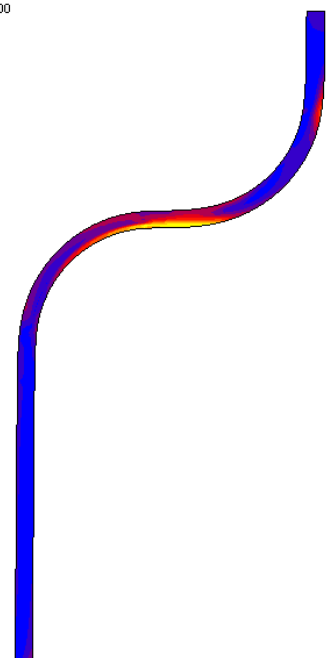
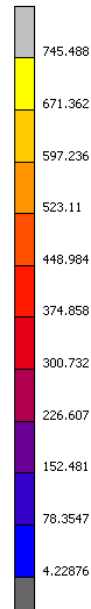
333 K
Step 1

Inc: 0
Time: 0.000e+00



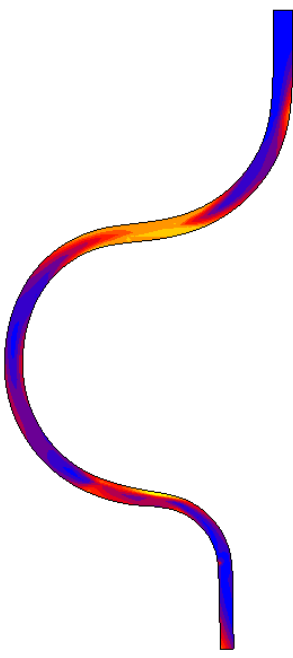
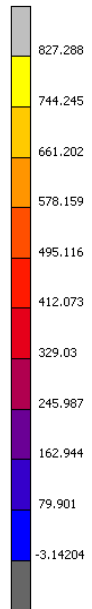
373 K
Step 1

Inc: 0
Time: 0.000e+00



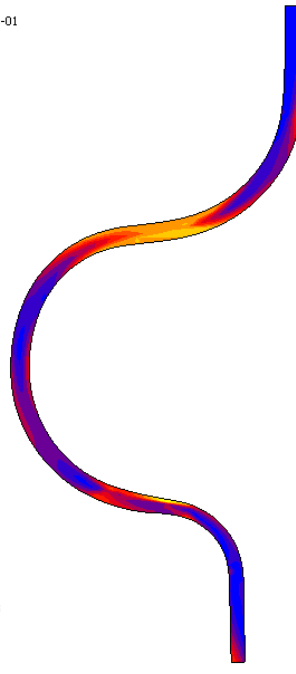
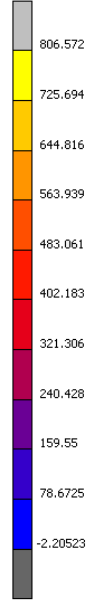
293 K
Step 2

Inc: 600
Time: 7.000e-01



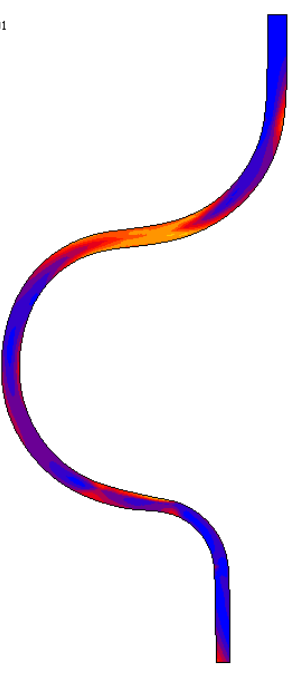
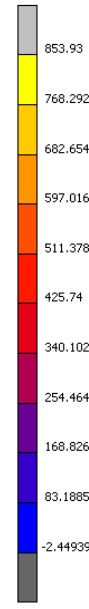
333 K
Step 2

Inc: 593
Time: 7.000e-01



373 K
Step 2

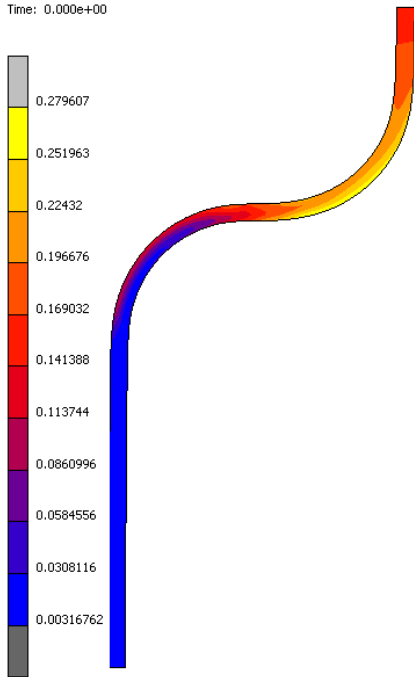
Inc: 590
Time: 7.000e-01



Equivalent Strain Development

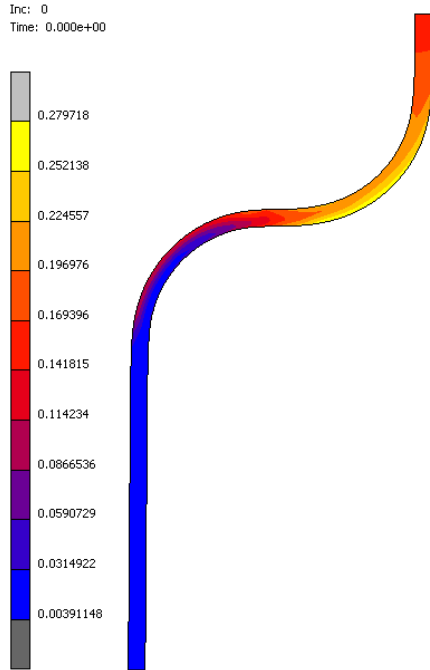
293 K
Step 1

Inc: 0
Time: 0.000e+00



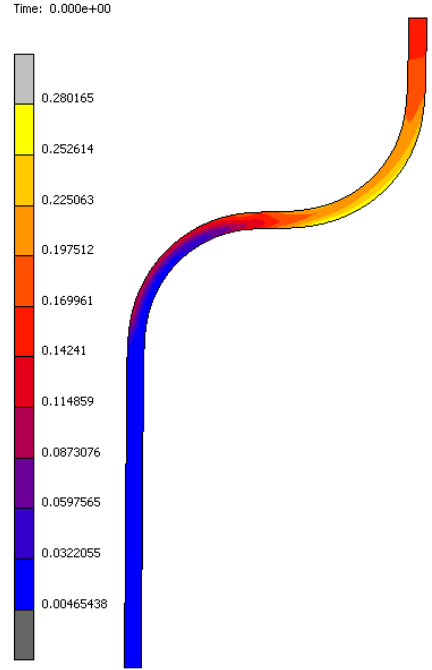
333 K
Step 1

Inc: 0
Time: 0.000e+00



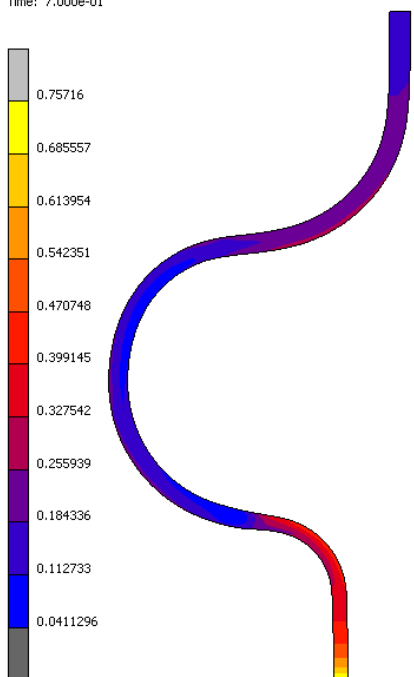
373 K
Step 1

Inc: 0
Time: 0.000e+00



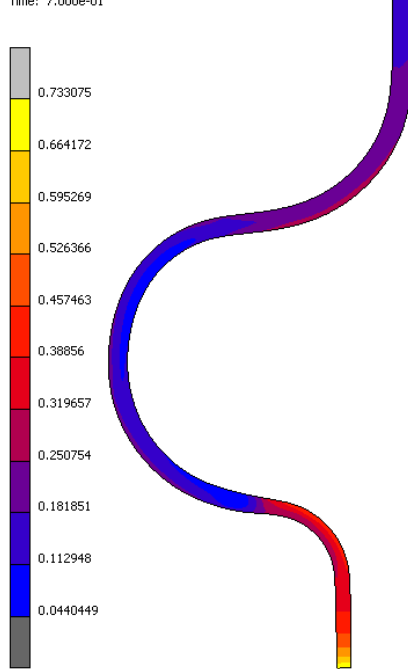
293 K
Step 2

Inc: 600
Time: 7.000e-01



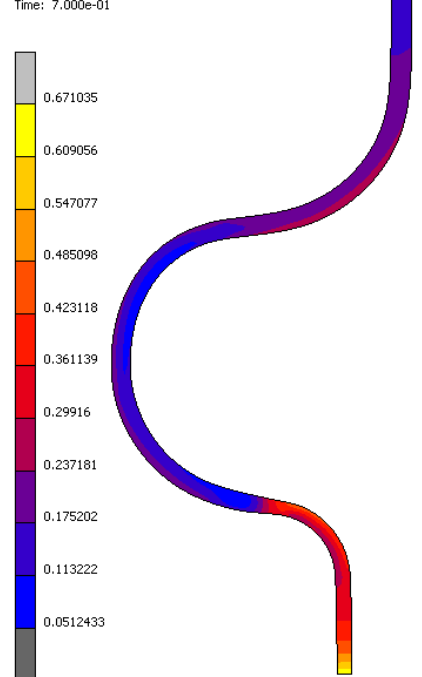
333 K
Step 2

Inc: 593
Time: 7.000e-01



373 K
Step 2

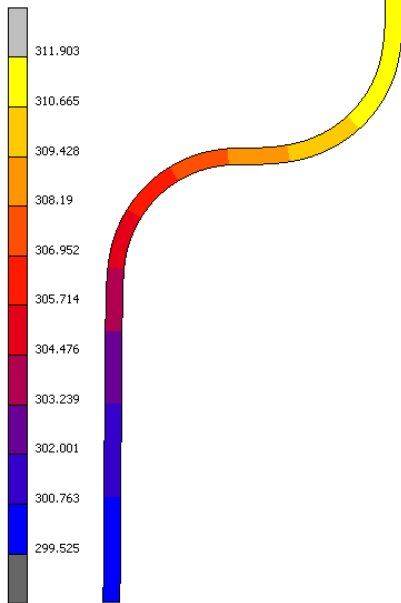
Inc: 590
Time: 7.000e-01



SaS0.35um_Lub7gm2_SaT0.02um-ContactHeatTransf Temperature Development Workpiece

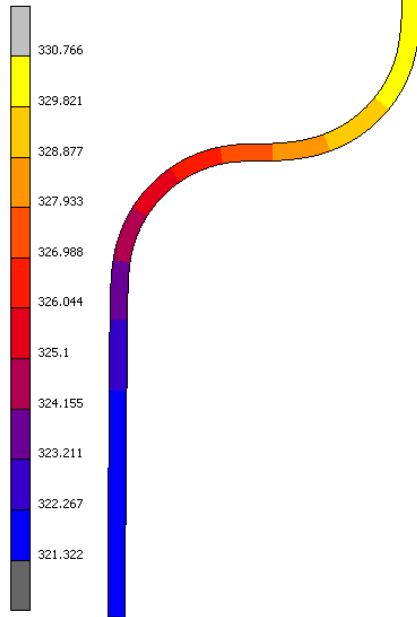
293 K
Step 1

Inc: 0
Time: 0.000e+00



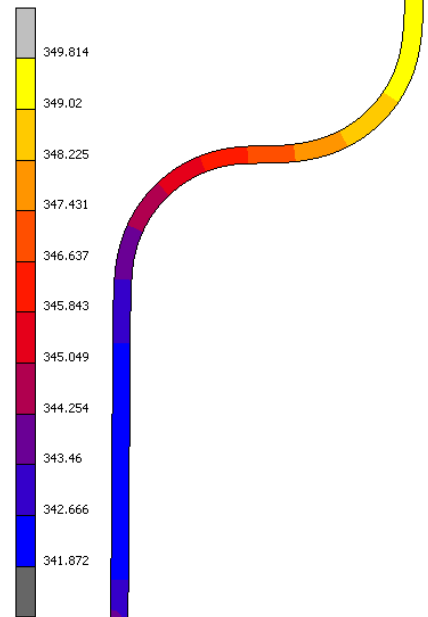
333 K
Step 1

Inc: 0
Time: 0.000e+00



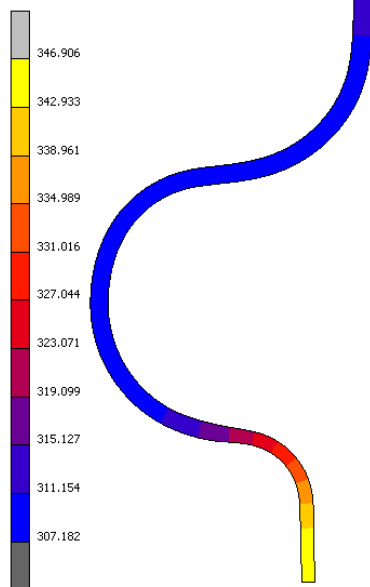
373 K
Step 1

Inc: 0
Time: 0.000e+00



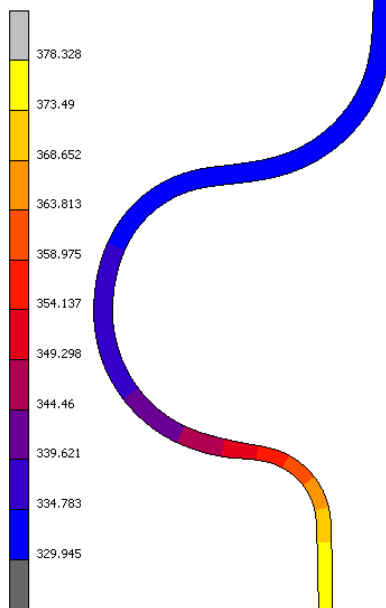
293 K
Step 2

Inc: 601
Time: 7.000e-01



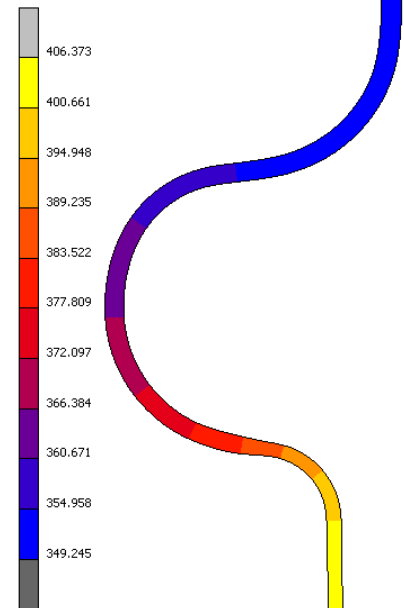
333 K
Step 2

Inc: 590
Time: 7.000e-01



373 K
Step 2

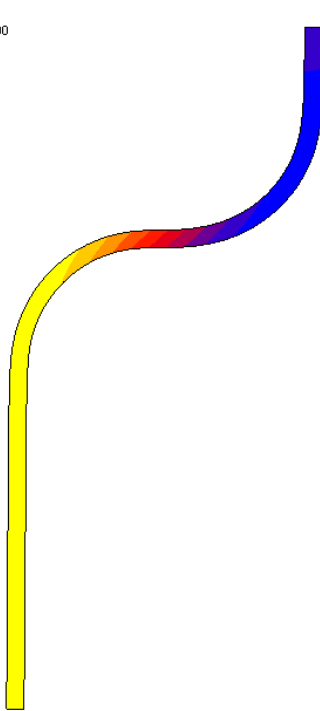
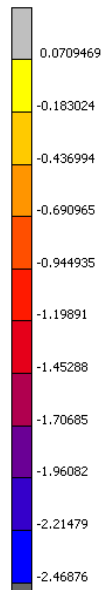
Inc: 591
Time: 7.000e-01



Total Displacement Y-Direction

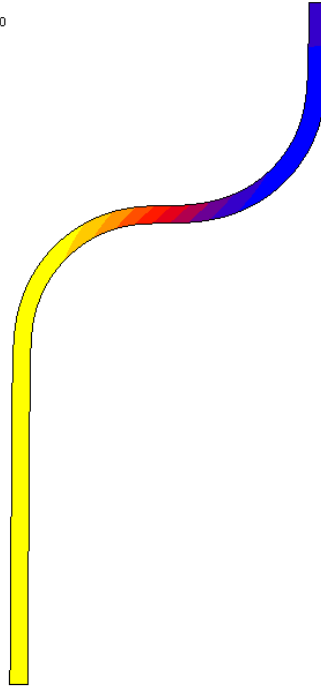
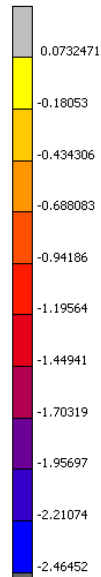
293 K
Step 1

Inc: 0
Time: 0.000e+00



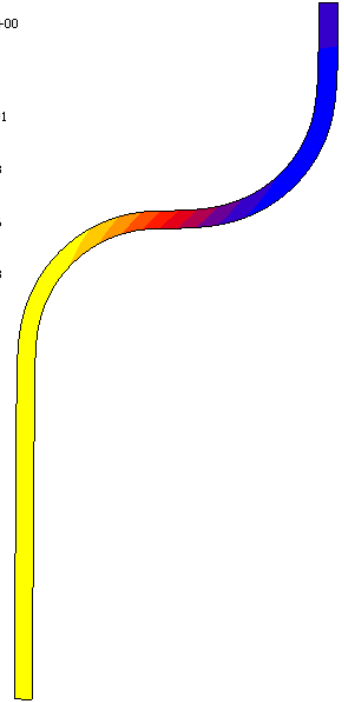
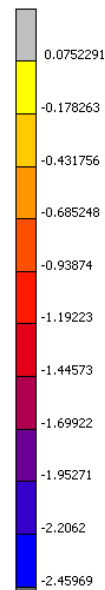
333 K
Step 1

Inc: 0
Time: 0.000e+00



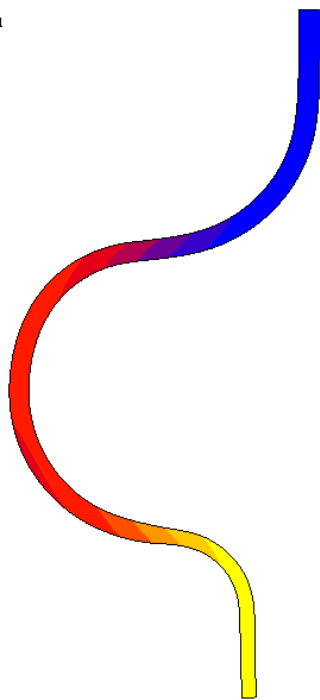
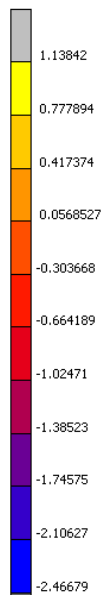
373 K
Step 1

Inc: 0
Time: 0.000e+00



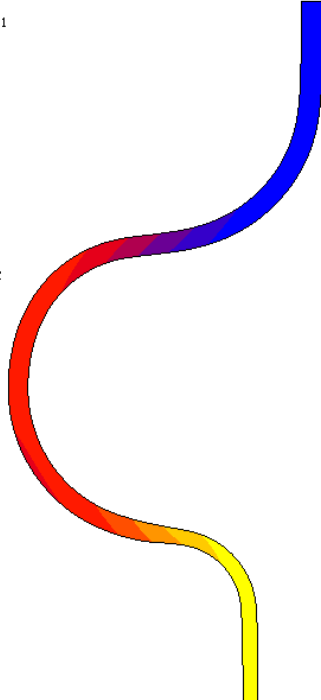
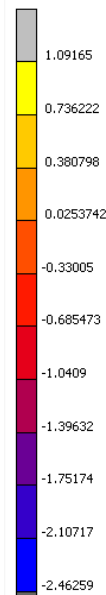
293 K
Step 2

Inc: 601
Time: 7.000e-01



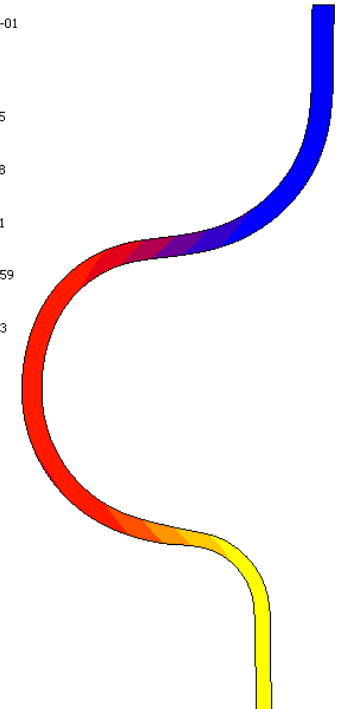
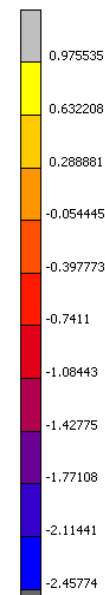
333 K
Step 2

Inc: 590
Time: 7.000e-01



373 K
Step 2

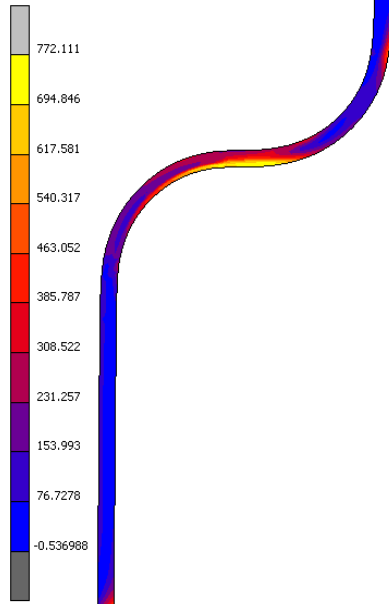
Inc: 591
Time: 7.000e-01



Equivalent Cauchy Stress Development

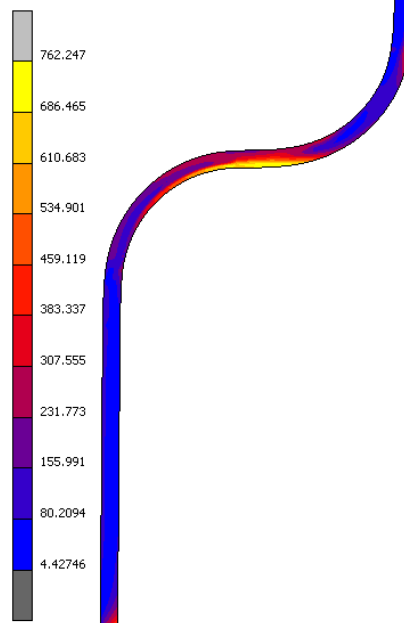
293 K
Step 1

Inc: 0
Time: 0.000e+00



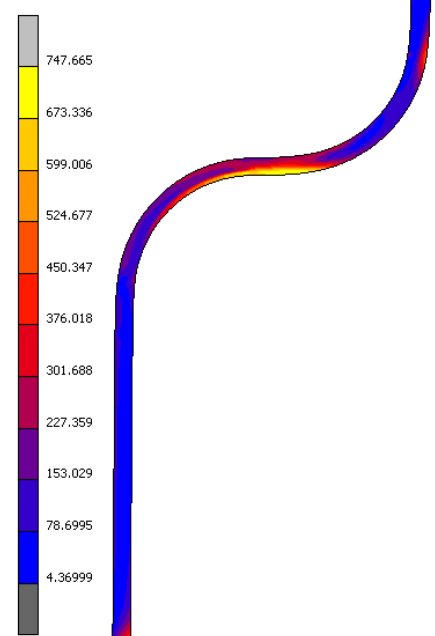
333 K
Step 1

Inc: 0
Time: 0.000e+00



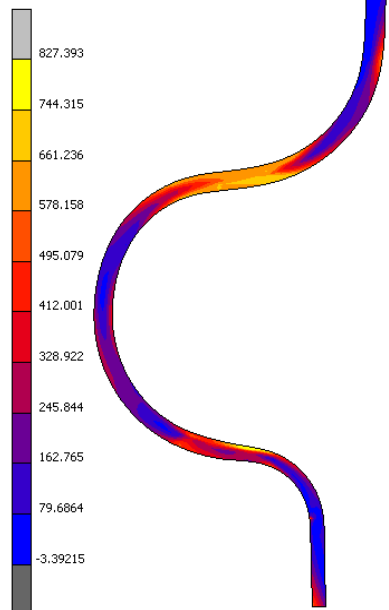
373 K
Step 1

Inc: 0
Time: 0.000e+00



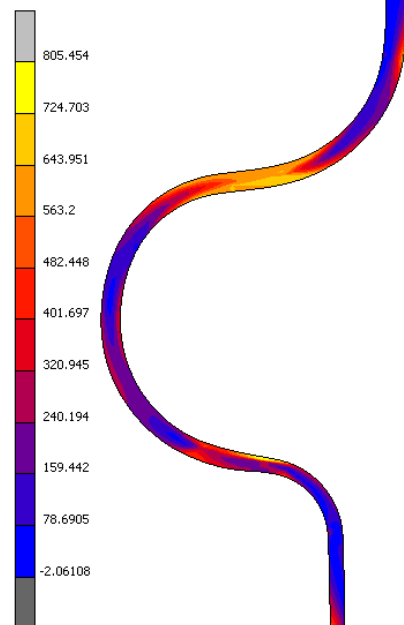
293 K
Step 2

Inc: 601
Time: 7.000e-01



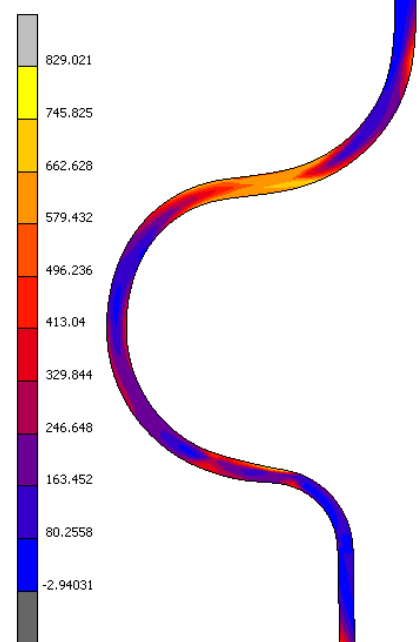
333 K
Step 2

Inc: 590
Time: 7.000e-01



373 K
Step 2

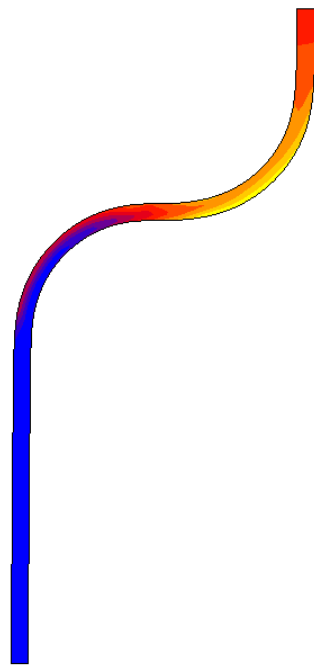
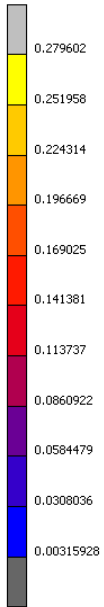
Inc: 591
Time: 7.000e-01



Equivalent Strain Development

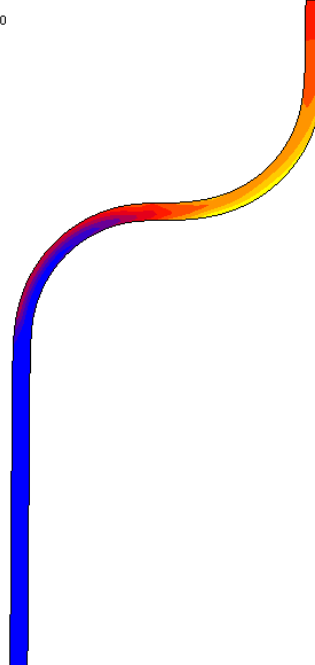
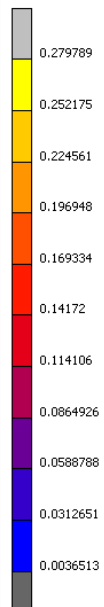
293 K
Step 1

Inc: 0
Time: 0.000e+00



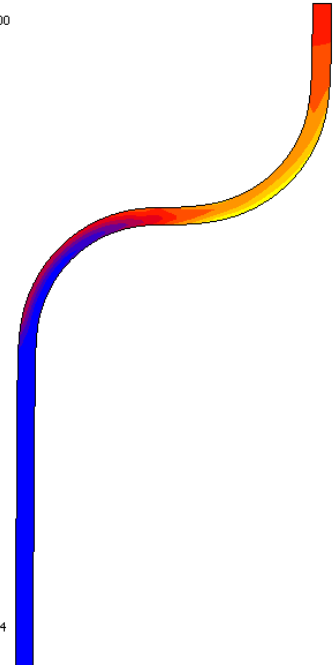
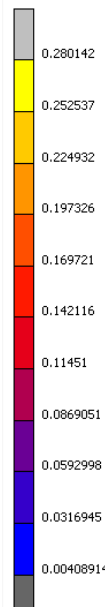
333 K
Step 1

Inc: 0
Time: 0.000e+00



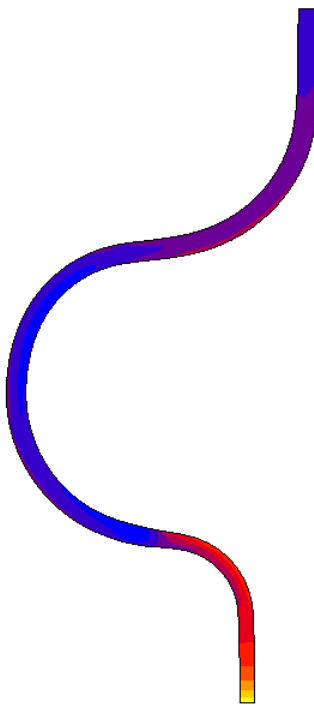
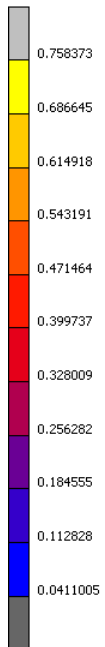
373 K
Step 1

Inc: 0
Time: 0.000e+00



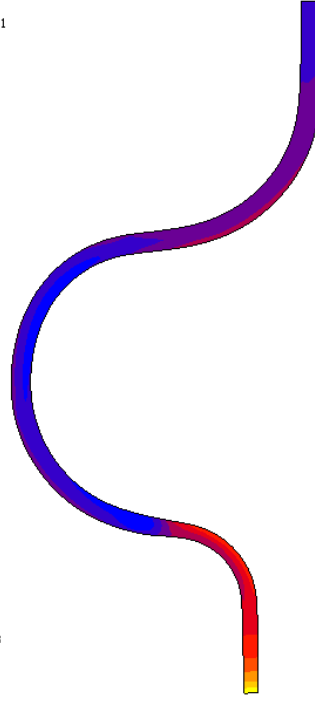
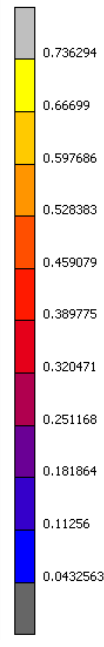
293 K
Step 2

Inc: 601
Time: 7.000e-01



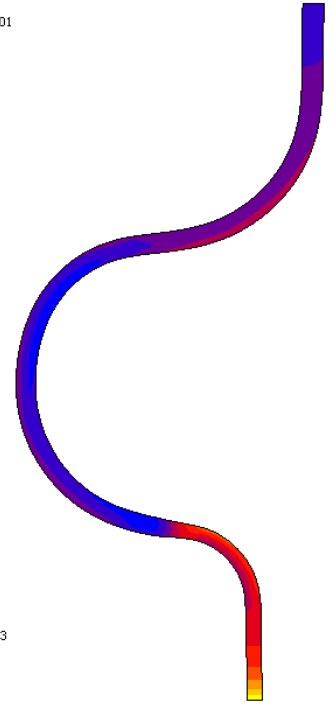
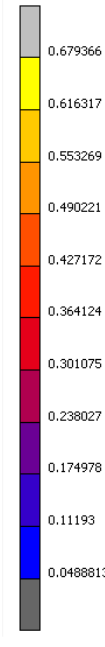
333 K
Step 2

Inc: 590
Time: 7.000e-01



373 K
Step 2

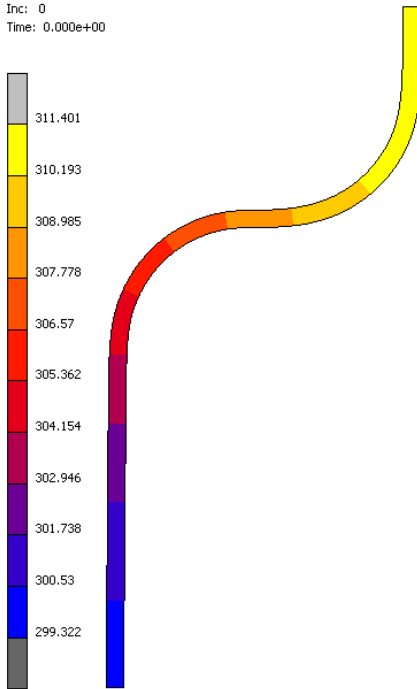
Inc: 591
Time: 7.000e-01



SaS0.35um_Lub7gm2_SaT0.05um Temperature Development Workpiece

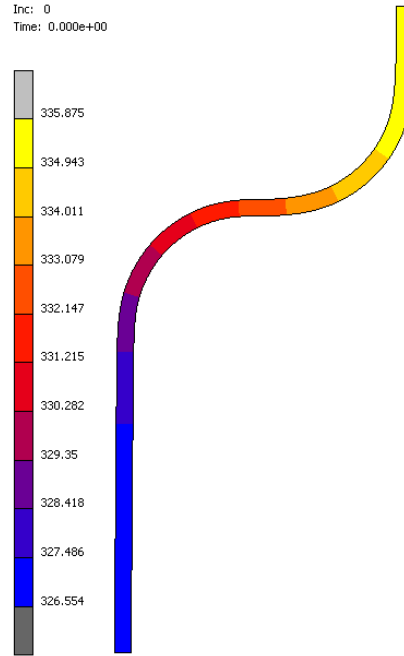
293 K
Step 1

Inc: 0
Time: 0.000e+00



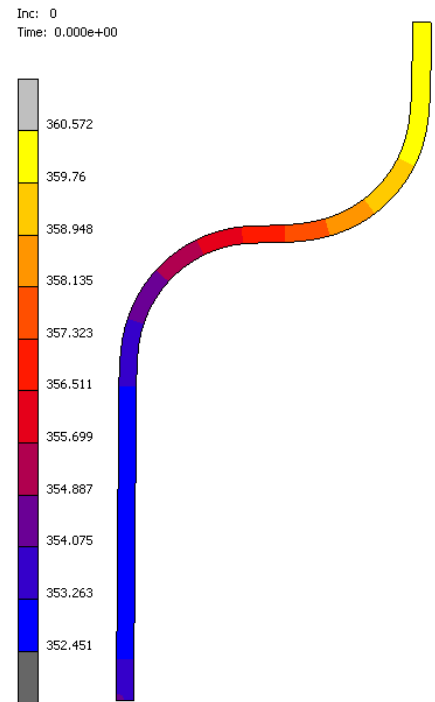
333 K
Step 1

Inc: 0
Time: 0.000e+00



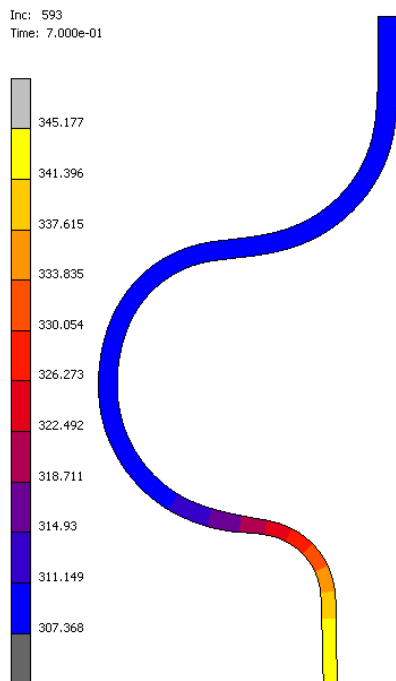
373 K
Step 1

Inc: 0
Time: 0.000e+00



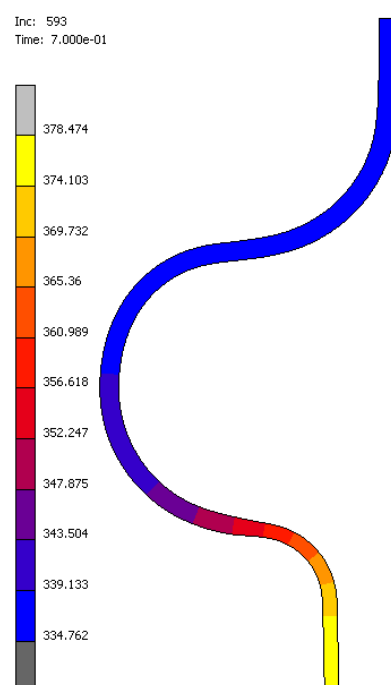
293 K
Step 2

Inc: 593
Time: 7.000e-01



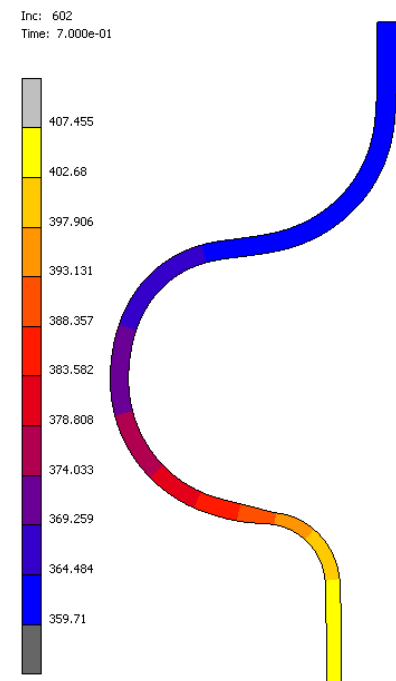
333 K
Step 2

Inc: 593
Time: 7.000e-01



373 K
Step 2

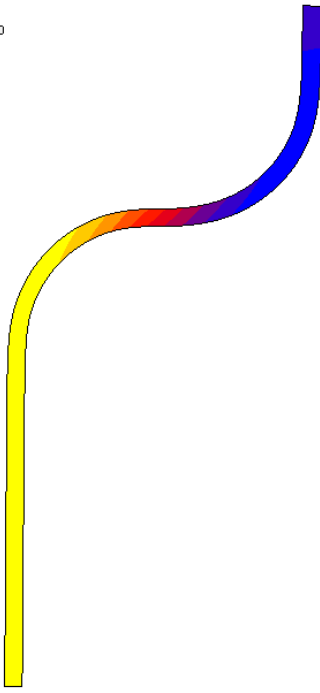
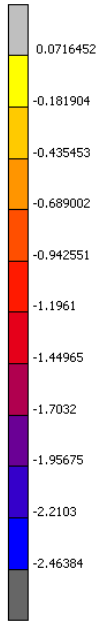
Inc: 602
Time: 7.000e-01



Total Displacement Y-Direction

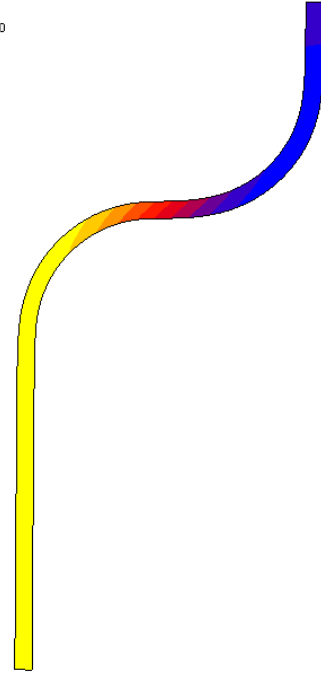
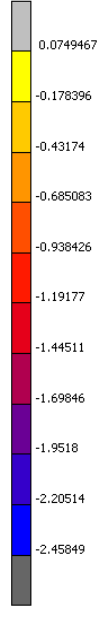
293 K
Step 1

Inc: 0
Time: 0.000e+00



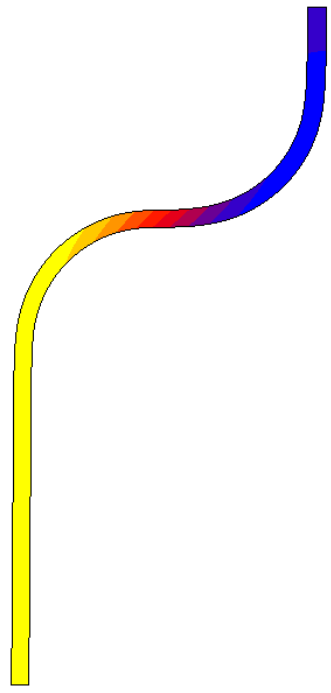
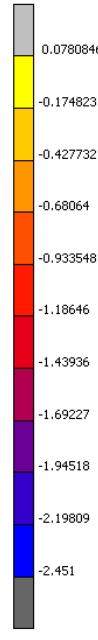
333 K
Step 1

Inc: 0
Time: 0.000e+00



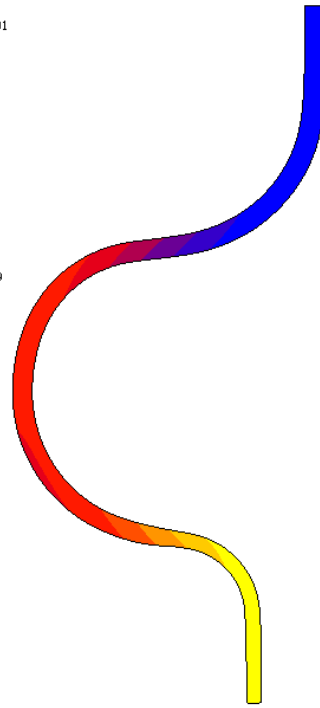
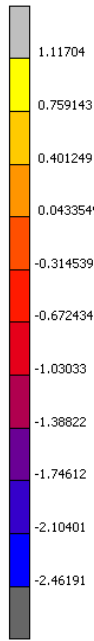
373 K
Step 1

Inc: 0
Time: 0.000e+00



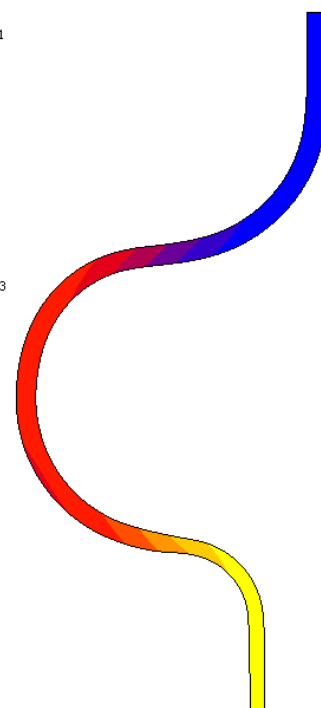
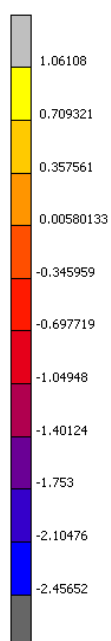
293 K
Step 2

Inc: 593
Time: 7.000e-01



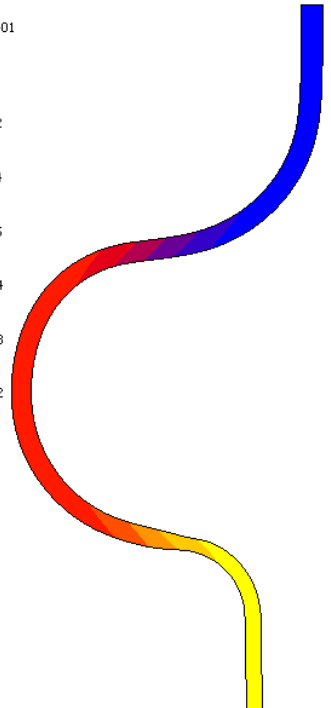
333 K
Step 2

Inc: 593
Time: 7.000e-01



373 K
Step 2

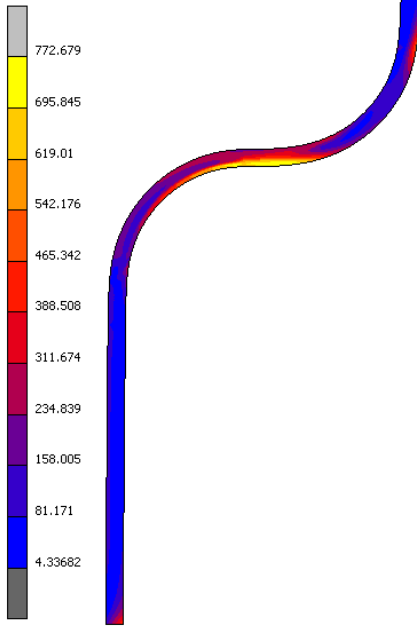
Inc: 602
Time: 7.000e-01



Equivalent Cauchy Stress Development

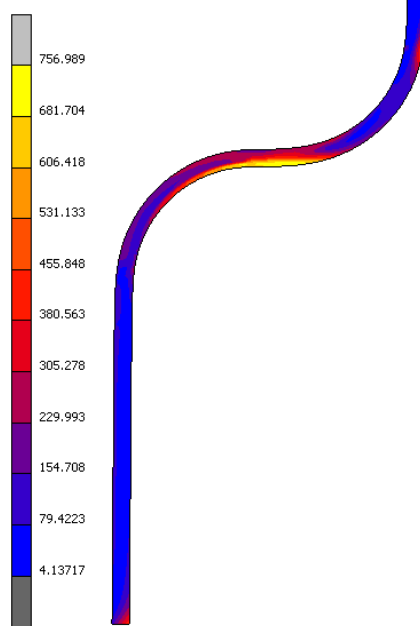
293 K
Step 1

Inc: 0
Time: 0.000e+00



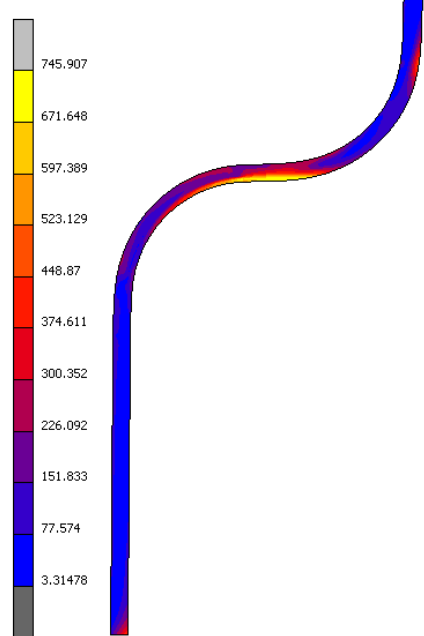
333 K
Step 1

Inc: 0
Time: 0.000e+00



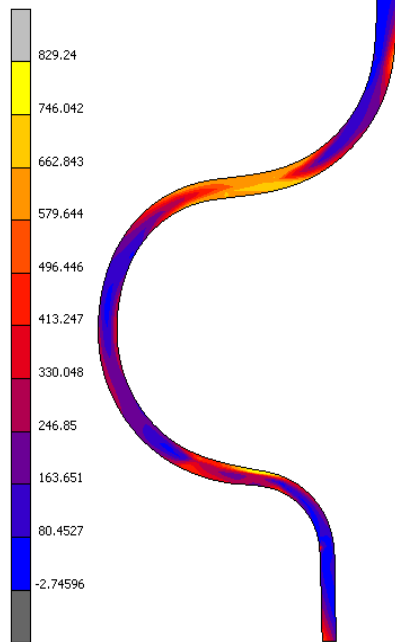
373 K
Step 1

Inc: 0
Time: 0.000e+00



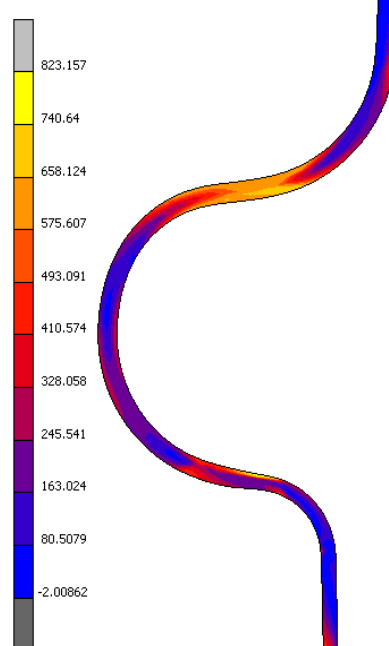
293 K
Step 2

Inc: 593
Time: 7.000e-01



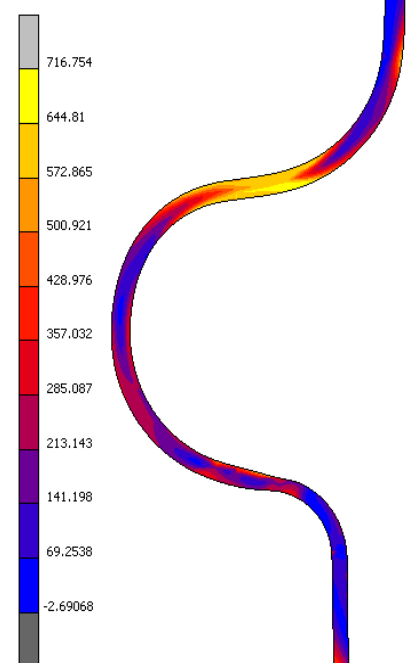
333 K
Step 2

Inc: 593
Time: 7.000e-01



373 K
Step 2

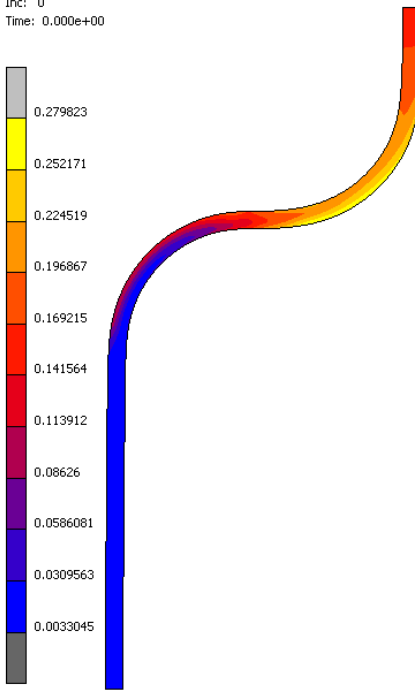
Inc: 602
Time: 7.000e-01



Equivalent Strain Development

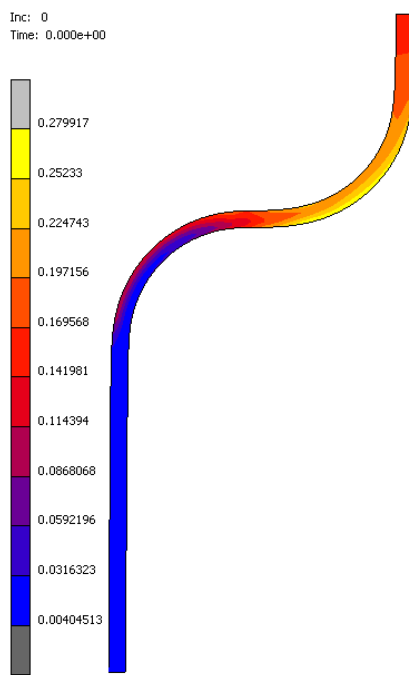
293 K
Step 1

Inc: 0
Time: 0.000e+00



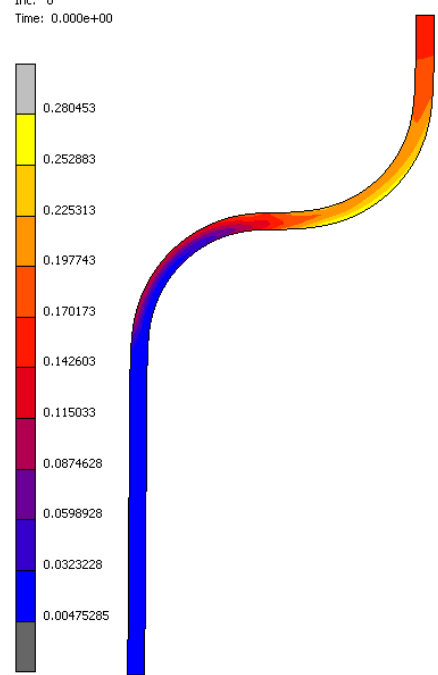
333 K
Step 1

Inc: 0
Time: 0.000e+00



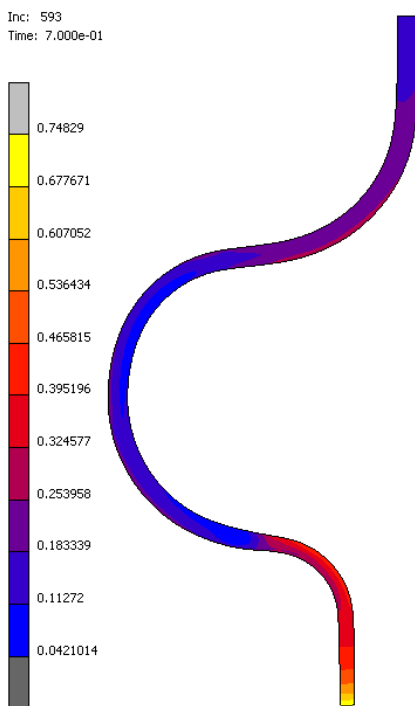
373 K
Step 1

Inc: 0
Time: 0.000e+00



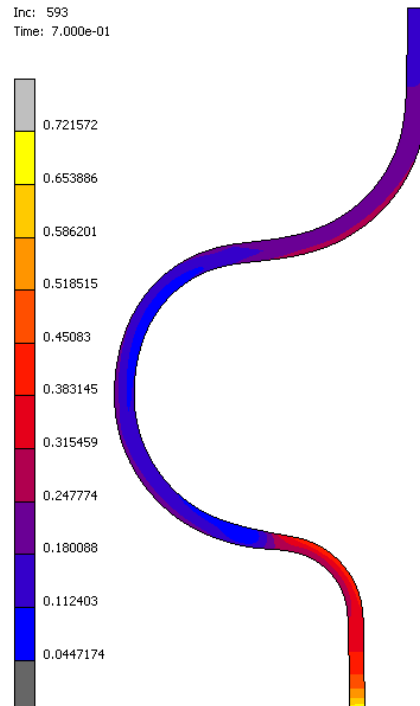
293 K
Step 2

Inc: 593
Time: 7.000e-01



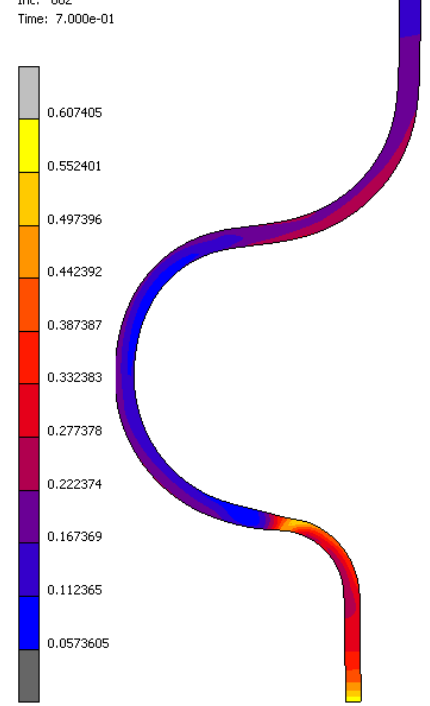
333 K
Step 2

Inc: 593
Time: 7.000e-01



373 K
Step 2

Inc: 602
Time: 7.000e-01



Appendix 15 – Pressto Case – Alternative Point Validation

Due to confidentiality issues, this page cannot be viewed.

For more information, please contact: r.m.nienhuis@student.rug.nl

References

- [1] Interreg, "Advanced Simulation and control of tribology in metal forming Processes for the North-West European Consumer goods and Transport sectors (ASPECT)," Stichting Materials Innovation Institute, 2016. [Online]. Available: <http://www.nweurope.eu/projects/project-search/advanced-simulation-and-control-of-tribology-in-metal-forming-processes-for-the-north-west-european-consumer-goods-and-transport-sectors-aspect/>.
- [2] P. University of Groningen, "Research Proposal," 2018.
- [3] M. Veldhuis, "Design of Temperature and Friction depending demonstrator process for ASPECT," Philips, 2017.
- [4] C. A. Coulomb, "Théorie des machines simples, Mémoires de Mathématique et de Physique de l'Academie de Sciences," pp. 161-331, 1785.
- [5] Interreg, "ASPECT Project Presentation," ASPECT Interest Group, 2017.
- [6] J. Hol, M. Alfaro, M. B. de Rooij and T. Meinders, "Multi-scale friction modeling for sheet metal forming," University of Twente, Enschede, 2013.
- [7] Y. Bergström, "A dislocation model for the stress-strain behaviour of polycrystalline α -Fe with special emphasis on the variation of the densities of mobile and immobile dislocations," *Materials Science and Engineering*, vol. 5, no. 4, pp. 193-200, 1970.
- [8] P. Van Liempt, "Workhardening and substructural geometry of metals," *Journal of Materials Processing Technology*, vol. 45, no. 1-4, pp. 459-464, 1994.
- [9] H. Vegter and A. H. van den Boogaard, "A plane stress yield function for anisotropic sheet material by interpolation of biaxial stress states," *International journal of plasticity*, vol. 22, no. 3, pp. 557-580, 2006.
- [10] R. Stribeck, "Kugellager für beliebige Belastungen (Ball Bearings for any Stress)," *Zeitschrift des Vereins Deutscher Ingenieure*, vol. 45, 1901.
- [11] R. Stribeck, "Die wesentlichen Eigenschaften der Gleit- und Rollenlager (Characteristics of Plain and Roller Bearings)," *Zeit. des VDI*, vol. 46, 1902.
- [12] U. o. Twente, Falzek and FILZEK, "Deliverable 1 - Temperature-dependent material properties," Interreg North-West Europe, 2017.
- [13] M2i, "Deliverable 2 - Tribological model predicting variation of friction," Interreg North-West Europe, 2017.

- [14] R. G. Longoria, "PID Control for Motor Speed and Position Control and for Vehicle Cruise Control Trials," The University of Texas at Austin, 2015. [Online]. Available: <https://www.me.utexas.edu/~longoria/CyVS/Lab2/index.html>.
- [15] R. J. Wieringa, Design science methodology for information systems and software engineering, Springer, 2014.
- [16] J. E. Aken, J. J. Berends and J. D. Bij, Problem solving in organizations: A methodological handbook for business and management students, ambridge University Press, 2012.
- [17] S. Heusinkveld and H. A. Reijers, "Reflections on a Reflective Cycle: Building Legitimacy in Design Knowledge Development," *Organization studies*, vol. 30, no. 8, pp. 865-886, 2009.
- [18] J. Dul and T. Hak, Case study methodology in business research, Routledge, 2007.
- [19] J. Hol, C. Alfaro, T. Meinders and J. Huetink, "Advanced friction modeling in sheet metal forming," *Trans Tech Publications*, vol. 473, pp. 715-722, 2011.
- [20] Engineering-AutoForm, "Sheet Metal Forming," AutoForm Engineering GmbH, 2018. [Online]. Available: <https://www.autoform.com/en/glossary/sheet-metal-forming/>.
- [21] J. D. Westeneng, Modelling of contact and friction in deep drawing processes, FEBO druk b.v., 2001.
- [22] T. Cwiekala, A. Brosius and A. E. Tekkaya, "Accurate deep drawing simulation by combining analytical approaches," *International Journal of Mechanical Sciences*, vol. 53, no. 5, pp. 374-386, 2011.
- [23] DIN-8584, "Manufacturing Processes Forming Under Combination Of Tensile And Compressive Conditions - Part 1-4: Spinning - Classification, Subdivision, Terms And Definitions," German Institute for Standardisation, 2003.
- [24] A. Mahkamov, "Tribology in Sheet Metal Forming," Departamento de Engenharia Mecânica, Porto, 2017.
- [25] A. I. O. Zaid, "Deep drawing mechanism, parameters, defects and recent results: state of the art," *Materials Science and Engineering*, vol. 146, no. 1, pp. 1-9, 2016.
- [26] P. Carlsson, "Surface engineering in sheet metal forming," Acta Universitatis - Faculty of Science and Technology, Upsaliensis, 2005.
- [27] ME-Mechanical, "Defects in Sheet Metal Drawing," ME Mechanical, 2017. [Online]. Available: <https://me-mechanicalengineering.com/defects-sheet-metal-drawing/>.
- [28] Library-of-Manufacturing, "Deep Drawing," The Library of Manufacturing, 2018. [Online]. Available: http://thelibraryofmanufacturing.com/deep_drawing.html.

- [29] R. Patel, H. Dave and H. Raval, "Study of Earing Defect during Deep Drawing Process with Finite Element Simulation In Key Engineering Materials," *rans Tech Publications*, vol. 639, pp. 91-98, 2015.
- [30] M. Veldhuis, "Cold Forming Process Parameters," Philips, 2010.
- [31] R. V. Reddy, D. T. J. Reddy and D. G. Reddy, "Effect of various parameters on the wrinkling in deep drawing cylindrical cups," *International Journal of Engineering Trends and Technology*, vol. 3, no. 1, pp. 53-58, 2012.
- [32] J. N. Mistri, K. D. Kothari and G. K. Sharma, "Experimental and Simulation study of Deep drawing process," *International Journal of Advance Engineering and Research Development*, vol. 1, no. 6, pp. 1-12, 2014.
- [33] C. P. Singh and G. Agnihotri, "Study of deep drawing process parameters: a review," *International Journal of Scientific and Research Publications*, vol. 5, no. 2, pp. 1-15, 2015.
- [34] H. Z. Poor, H. Moosavi, H. G. Menghari and R. A. de Sousa, "Investigation of Punch Nose Radius and Punch-Die Clearance on Thinning and Puckering in Hydro-Mechanical Deep Drawing Process," *International Journal of Mechanic Systems Engineering*, vol. 4, no. 2, pp. 16-21, 2014.
- [35] A. Jaisingh, K. Narasimhan, P. P. Date, S. K. Maiti and U. P. Singh, "Sensitivity analysis of a deep drawing process for miniaturized products," *Journal of materials processing technology*, vol. 147, no. 3, pp. 321-327, 2004.
- [36] P. Kováč and V. Tittel, "Blank holder force optimization of hemispherical product using numerical simulation," *Materials science and technology*, pp. 5-10, 2010.
- [37] M. C. Oliveira, R. Padmanabhan, A. J. Baptista, J. L. Alves and L. F. Menezes, "Sensitivity study on some parameters in blank design," *Journal of Material & Design*, vol. 30, no. 4, pp. 1223-1230, 2009.
- [38] V. D. Nguyen, P. A. Adragna and P. Lafon, "Predicting the effects of material and process parameters on springback by fem numerical simulation in sheet metal forming," in *10ème Conférence Francophone de Modélisation*, Nancy, 2014.
- [39] R. Chandramouli, "Cup drawing or deep drawing syllabus," NPTEL - Mechanical Engineering - Forming, 2013.
- [40] Y. S. Khairnar, D. Deshmukh, K. Dhembre, G. Sawant and A. Bhosale, "Review on Optimization of process parameter in square shaped components in deep drawing process," in *1st National Conference On Recent Innovations in Mechanical Engineering*, 2018.

- [41] G. M. Kakandikar and V. M. Nandedkar, "Optimization of forming load and variables in deep drawing process for automotive cup using Genetic Algorithm," in *n IISc Centenary-International Conference on Advances in Mechanical Engineering ICICAME*, Bangalor, 2005.
- [42] N. Ramesha and A. Hiremath, "The Significant Variables that Affect Metal During Deep Drawing Process in Sheet Metal Work," *International Journal of Engineering Research & Technology*, vol. 4, no. 5, pp. 1-4, 2015.
- [43] R. J. J. M. Sniekers, *Friction in deep drawing*, Eindhoven: Technische Universiteit Eindhoven, 1996.
- [44] S. Subramonian, "Evaluation of lubricants for stamping deep draw quality sheet metal in industrial environment," Doctoral dissertation, The Ohio State University, Athens, 2009.
- [45] B. Bhushan, *Introduction to tribology*, John Wiley & Sons, 2013.
- [46] P. Bergmann and F. Grün, "Modeling Wear of Journal Bearings," in *COMSOL Conference*, Munich, 2016.
- [47] M. D. Hersey, "The Laws of Lubrication of Horizontal Journal Bearings," *J. Wash. Academy*, vol. 4, pp. 542-552, 1914.
- [48] T. Tekkaya and A. E. Altan, "Friction and Lubrication," in *Sheet Metal Forming Fundamentals*, ASM International, 2012, pp. 89-98.
- [49] M. D. Bryant, "ME 383S Lubrication, Wear & Bearing Technology," Mechanical Engineering Department The University of Texas at Austin, [Online]. Available: <http://www.me.utexas.edu/~bryant/courses>.
- [50] L. I. U. Qiang, "Friction in mixed and elastohydrodynamic lubricated contacts including thermal effects," Doctoral dissertation, PhD Thesis, University of Twente, Enschede, 2002.
- [51] Tribonet, "Friction," in *TriboBR - Third International Brazilian Conference on Tribology*, Brasil, 2018.
- [52] J. A. Schey, "Tribology in metal working," in *ASM, Metals Park*, Ohio, 1983.
- [53] M. P. F. Sutcliffe, "Surface finish and friction in cold metal rolling," in *Metal Forming Science and Practice*, Oxford, Elsevier, 2002, pp. 19-59.
- [54] J. Wojewoda, A. Stefański, M. Wiercigroch and T. Kapitaniak, "Hysteretic effects of dry friction: modelling and experimental studies," *Philosophical Transactions of the Royal Society of London A: Mathematical, Physical and Engineering Sciences*, vol. 366, pp. 747-765, 2008.
- [55] G. Amontons, "On the Resistance Originating in Machines," *Proceedings of the French Royal Academy of Sciences*, pp. 206-222, 1734.

- [56] H. Olsson, K. J. Åström, C. C. de Wit, M. Gäfvert and P. Lischinsky, "Friction models and friction compensation," *European Journal of Control*, vol. 4, no. 3, pp. 176-195, 1998.
- [57] H. Olsson, K. J. Åström, C. C. de Wit, M. Gäfvert and P. Lischinsky, "Friction models and friction compensation," *European Journal of Control*, vol. 4, no. 3, pp. 176-195, 1998.
- [58] C. S. Gillmor, *Coulomb and the Evolution of Physics and Engineering in Eighteenth-century France*, vol. 4965, Princeton University Press, 2017.
- [59] P. Korondi, J. Halas, K. Samu, A. Bojtos and T. Péter, "Robot Applications," European Social Fund, 2014.
- [60] Y. F. Liu, J. Li, Z. M. Zhang, X. H. Hu and W. J. Zhang, "Experimental comparison of five friction models on the same test-bed of the micro stick-slip motion system," *Mechanical Sciences*, vol. 6, no. 1, pp. 15-28, 2015.
- [61] W. Wang, Y. Zhao, Z. Wang, M. Hua and X. Wei, "A study on variable friction model in sheet metal forming with advanced high strength steels," *Tribology International*, vol. 93, pp. 17-28, 2016.
- [62] V. van Geffen, "A study of friction models and friction compensation," Department Mechanical Engineering, Eindhoven, 2009.
- [63] A. J. Morin, "Nouvelles experiences faites a Metz en 1833 sur le frottement, sur la transmission due mouvement par le choc, sur le resistance des milieun imparfaits a le penetration des projectiles, et sur le frottement pendant le choc," *Mem. Savans Et rang*, Paris, 1835.
- [64] O. Reynolds, "On the theory of lubrication and its application to Mr. Beauchamp tower's experiments, including an experimental determination of the viscosity of olive oil," *Philosophical Transactions of the Royal Society of London*, vol. 177, pp. 157-234, 1886.
- [65] L. Chiou, S. Chebrolu, M. de Zorzi, R. Android, J. Silverman and J. Khim, "Friction," Brilliant, 2018. [Online]. Available: <https://brilliant.org/wiki/friction/>.
- [66] S. Cohn, "Dynamic friction measurement, modeling, and compensation for precise motion control," Doctoral dissertation, New Jersey Institute of Technology, New Jersey, 1998.
- [67] Mathworks, "Translational Friction," Mathworks, 2007. [Online]. Available: <https://nl.mathworks.com/help/phymod/simscape/ref/translationalfriction.html>.
- [68] M. P. N. Rajapakshe, "Physically Meaningful Harmonization of Tire/Pavement Friction Measurement Devices," Civil and Environmental Engineering, University of South Florida, Tampa, 2011.
- [69] S. Andersson, "Seminar at the Department of Automatic Control," in *Lund Institute of Technology*, Lund, 1993.

- [70] B. Armstrong-Hélouvry, P. Dupont and C. C. de Wit, "A survey of models, analysis tools and compensation methods for the control of machines with friction," *Automatica*, vol. 30, no. 7, pp. 1083-1138, 1994.
- [71] H. S. Muddana, R. R. Gullapalli, E. Manias and P. J. Butler, "Atomistic simulation of lipid and DiI dynamics in membrane bilayers under tension," *Physical Chemistry Chemical Physics*, vol. 13, no. 4, pp. 1368-1378, 2011.
- [72] I. B. Tijani and R. Akmeiliawati, "Support vector regression based friction modeling and compensation in motion control system," *Engineering Applications of Artificial Intelligence*, vol. 25, no. 5, pp. 1043-1052, 2012.
- [73] M. Yang, J. Yang and H. Ding, "A two-stage friction model and its application in tracking error pre-compensation of CNC machine tools," *Precision Engineering*, vol. 51, pp. 426-436, 2018.
- [74] J. Čerkala and A. Jadoslavská, "Mobile Robot Dynamics with Friction in Simulink," *TECHNICOM for Innovation Applications Supported by Knowledge Technology*, Slovakia, 2015.
- [75] K. Erkorkmaz and Y. Altintas, "High speed CNC system design. Part II: modeling and identification of feed drives," *International Journal of Machine Tools and Manufacturing*, vol. 41, no. 10, pp. 1487-1509, 2001.
- [76] T. Engineering, "Deliverable 3 - Metamodel describing the temperature-dependent micro-mechanical tribological behaviour," *TriboForm Engineering*, 2017.
- [77] Opel, "Deliverable 4 - Description of the Opel demonstrator process: components, interfaces, tools," Opel, 2017.
- [78] Philips, "Deliverable 5 - Metamodel for the Philips demonstrator process windows of the selected applications," Philips, 2017.
- [79] A. Vishtal and E. Retulainen, "Deep-drawing of paper and paperboard: The role of material propertie," *BioResources*, vol. 7, no. 2, pp. 4424-4450, 2012.
- [80] S. S. Panicker and S. K. Panda, "Improvement in Material Flow During Nonisothermal Warm Deep Drawing of Nonheat Treatable Aluminum Alloy Sheet," *Journal of Manufacturing Science and Engineering*, vol. 139, no. 3, pp. 1-8, 2017.
- [81] M. Rowland, T. N. Tozer, H. Derendorf and G. Hochhaus, *Clinical pharmacokinetics and pharmacodynamics: concepts and applications*, Philadelphia: Wolters Kluwer Health/Lippincott William & Wilkins, 2011.
- [82] M. Geiger, M. Merklein and M. Kerausch, "Finite element simulation of deep drawing of tailored heat treated blanks," *CIRP Annals-Manufacturing Technology*, vol. 53, no. 1, pp. 223-226, 2004.

- [83] P. Stoyanov and R. R. Chromik, "Scaling effects on materials tribology: from macro to micro scale," *Materials*, vol. 10, no. 5, pp. 1-47, 2017.
- [84] A. I. Vakis, V. A. Yastrebov, J. Scheibert, C. Minfray, L. Nicola, D. Dini, A. Almqvist, M. Paggi, S. Lee, G. Limbert and J. F. Molinari, "Modeling and simulation in tribology across scales: An overview," *Tribology International*, vol. 125, pp. 169-199, 2018.
- [85] Lehigh-University, "Materials Tribology," Tribology Laboratory - Lehigh University, 2013. [Online]. Available: <https://www.lehigh.edu/~intribos/materialtribology.html>.
- [86] D. Ananthapadmanaban, "Mechanisms of friction and their correlation to bond strength of friction welded Ti-6Al-4V similar welds, Low Carbon steel-Stainless steel and Aluminium-Copper dissimilar welds," *International Journal of Innovations in Engineering and Technology*, vol. 9, no. 3, p. 2018, 14-20.
- [87] K. G. Budinski and M. K. Budinski, *Engineering materials*, Nature, 2009.
- [88] E. M. Kopalinsky and P. L. B. Oxley, "Explaining the mechanics of metallic sliding friction and wear in terms of slipline field models of asperity deformation," *Wear*, vol. 190, no. 2, pp. 145-154, 1995.
- [89] D. F. Moore, *Principles and Applications of Tribology: Pergamon International Library of Science, Technology, Engineering and Social Studies: International Series in Materials Science and Technology*, Elsevier, 2013.
- [90] E. Broitman, "The nature of the frictional force at the macro-, micro-, and nano-scales," *Friction*, vol. 2, no. 1, pp. 40-46, 2014.
- [91] J. T. Desaguliers, "Some experiments concerning the cohesion of lead, by the same," *Philosophical Transactions*, vol. 33, no. 389, pp. 345-347, 1724.
- [92] G. A. Tomlinson, "Molecular cohesion," *The London, Edinburgh, and Dublin Philosophical Magazine and Journal of Scienc*, vol. 6, no. 37, pp. 695-712, 1928.
- [93] F. P. Bowden and D. Tabor, *The friction and lubrication of solids*, Oxford university press, 1950.
- [94] B. Townsend, "Static and Kinetic Friction," University of Alaska-Fairbanks, 2002. [Online]. Available: http://ffden-2.phys.uaf.edu/211_fall2002.web.dir/ben_townsend/staticandkineticfriction.htm.
- [95] X. Liu, M. Liewald and D. Becker, "Effects of rolling direction and lubricant on friction in sheet metal forming," *Journal of tribology*, vol. 131, no. 4, pp. 1-8, 2009.
- [96] S. Wen and P. Huang, *Principles of tribology*, John Wiley & Sons, 2012.

- [97] D. Kopeliovich, "Mechanisms of wear," Substech Substances and Technologies, [Online]. Available: http://www.substech.com/dokuwiki/doku.php?id=mechanisms_of_wear.
- [98] ASM, Friction, Lubrication, and Wear Technology, ASM International, 1992-2018.
- [99] H. Yoshizawa, Y. L. Chen and J. Israelachvili, "Fundamental mechanisms of interfacial friction - I, Relation between adhesion and friction," *The Journal of Physical Chemistry*, vol. 97, no. 16, pp. 4128-4140, 1993.
- [100] D. H. Buckley, Surface effects in adhesion, friction, wear, and lubrication (, Elsevier, 1981.
- [101] P. Kumar, A. Shenoy and S. Joshi, "The effect of various surface contaminants on the microleakage of two different generation bonding agents: A stereomicroscopic study. Journal of conservative dentistry: JCD," *Journal of conservative dentistry*, vol. 5, no. 3, pp. 1-4, 2012.
- [102] R. C. Dante, Handbook of friction materials and their applications, Woodhead Publishing, 2015.
- [103] P. Z. Zhu, Y. Z. Hu, T. B. Ma and H. Wang, "Molecular dynamics study on friction due to ploughing and adhesion in nanometric scratching process," *Tribology Letters*, vol. 41, no. 1, pp. 41-46, 2011.
- [104] M. Akkök, B. Acar and E. Açmaz, "Experimental analysis and wear modeling for mechanical components of a typical rail launcher," *Wear*, vol. 306, no. 1-2, pp. 1-9, 2013.
- [105] R. C. Hibbeleer, Mechanics of Materials, New Jersey USA: Pearson Education, 2004.
- [106] M. Torbacke, Å. K. Rudolphi and E. Kassfeldt, "Lubricants: Introduction to properties and performance," John Wiley & Sons, 2014.
- [107] E. Nøst, "Flow in pipes," University of Oslo, Oslo, 2004.
- [108] H. Kudela, "Application of the Vortex-In-Cell method for the simulation of two-dimensional viscous flow," *Task Quarterly*, vol. 3, no. 3, pp. 343-360, 1999.
- [109] H. Kudela, "Turbulent flow," Department of Numerical Flow Modeling, 2011.
- [110] A. Agrawal, "Fundamentals of Surface Tension / Wettability," Nanotechnology and Interdisciplinary Research Initiative - NIRT, 2005. [Online]. Available: <http://web.mit.edu/nnf/education/wettability/index1.html>.
- [111] G. Biswas and S. K. Som, "Fluid Mechanics," National Programme on Technology Enhanced Learning - NPTEL, 2009. [Online]. Available: <https://nptel.ac.in/courses/112104118/>.
- [112] Isel-Staff, "Viscosity," Isel, 2018. [Online]. Available: <https://iselinc.com/questions-answers/viscosity-qa/>.

- [113] B. R. Munson, T. H. Okiishi, W. W. Huebsch and A. P. Rothmayer, Fluid mechanics, Singapore: Wiley, 2013.
- [114] M. Engineering, "Fluid Mechanics," Mechanical Engineering, 2015. [Online]. Available: <https://mechaengineerings.wordpress.com/2015/05/25/viscosity/>.
- [115] Database-CROW, "Newtonian Fluids," Polymer Properties Database, 2015. [Online]. Available: <http://polymerdatabase.com/polymer%20physics/Viscosity.html>.
- [116] Toolbox-Engineering, "Absolute, Dynamic and Kinematic Viscosity," Engineering Toolbox, [Online]. Available: https://www.engineeringtoolbox.com/dynamic-absolute-kinematic-viscosity-d_412.html.
- [117] S. Kazemian, A. Prasad and B. B. Huat, "Review of Newtonian and non-Newtonian fluids behaviour in the context of grouts," *Geotechnical Aspects of Underground Construction in Soft Ground*, pp. 321-326, 2012.
- [118] B. Gharaibeh, "Surfaces and surface roughness measurement," University of Jordan, Amman, 2011.
- [119] B. N. J. Persson, O. Albohr, U. Tartaglino, A. I. Volokitin and E. Tosatti, "On the nature of surface roughness with application to contact mechanics, sealing, rubber friction and adhesion," *Journal of Physics: Condensed Matter*, vol. 17, no. 1, 2004.
- [120] W. D. Callister and D. G. Rethwisch, Materials science and engineering, New York: John Wiley & Sons, 2011.
- [121] A. S. Wadhwa and E. H. S. Dhaliwal, A Textbook of Engineering Material and Metallurgy, Firewall Media, 2008.
- [122] P. Kelly, "Engineering Solid Mechanics," Engineering Solid Mechanics, The University of Auckland, 2018.
- [123] P. Burnley, "Tensors: Stress, Strain and Elasticity," University of Nevada Las Vegas, [Online]. Available: https://serc.carleton.edu/NAGTWorkshops/mineralogy/mineral_physics/tensors.html.
- [124] R. Hill, "A theory of the yielding and plastic flow of anisotropic metals," *Proc. R. Soc. Lond. A*, vol. 193, no. 1033, pp. 281-297, 1948.
- [125] W. T. Lankford, S. C. Snyder and J. A. Bausher, "New criteria for predicting the press performance of deep drawing sheets," *Trans. ASM*, vol. 42, p. 1197–1205, 1950.
- [126] H. Vegter, Y. An, C. H. L. J. ten Horn, E. H. Atzema and M. E. Roelofsen, "Advancing Material Models for Automotive Forming Simulations," in *AIP Conference Proceedings*, 2005.

- [127] A. Nadai, "Plastic behavior of metals in the strain-hardening range. Part I," *Journal of Applied Physics*, vol. 8, no. 3, pp. 205-213, 1937.
- [128] P. Van Liempt, "Workhardening and substructural geometry of metals," *Journal of Materials Processing Technology*, vol. 45, no. 1-4, pp. 459-464, 1994.
- [129] H. Vegter, "Modelling of Metal Forming Processes," in *A Finite Difference Model as A Basis for Developing New Constitutive Equations for the Sheet Forming Process*, Dordrecht, Springer, 1988, pp. 111-121.
- [130] H. H. Pijlman, J. Huétink, T. Meinders and B. D. Carleer, "The implementation of the Vegter yield criterion and a physically based hardening rule in finite elements," in *Proceedings of Conference of the International Association of Computational Mechanics, IACM*, 1998.
- [131] H. Vegter, "On the plastic behaviour of steel during sheet forming," University of Twente, Enschede, 1991.
- [132] A. Dahl and W. Krabiell, "Zum einfluss von Temperatur und Dehngeschwindigkeit auf die Streckgrenze von Baustählen unterschiedlicher Festigkei," *Archiv für das Eisenhüttenwesen*, vol. 52, no. 11, pp. 429-436, 1981.
- [133] J. A. Greenwood and J. B. P. Williamson, "Contact of nominally flat surfaces," *Proceedings of the Royal Society of London. Series A, Mathematical and Physical sciences*, vol. 295, pp. 300-319, 1966.
- [134] D. Tabor, "Junction growth in metallic friction: The role of combined stresses and surface contamination," *Proceedings of the Royal Society of London*, vol. 251, p. 378–393, 1959.
- [135] M. Challen and P. L. B. Oxley, "An explanation of the different regimes of friction wear using asperity deformation models," *Wear*, vol. 53, p. 229–243, 1979.
- [136] X. Ma, M. de Rooij and D. J. Schipper, "A load dependent friction model for fully plastic contact conditions," *Wear*, vol. 269, p. 790–796, 2012.
- [137] M. Challen and P. L. B. Oxley, "Slip-line fields for explaining the mechanics of polishing and related processes," *International Journal of Mechanical Siences*, vol. 26, pp. 403-418, 1984.
- [138] P. K. Saha and W. R. D. Wilson, "Influence of plastic strain on friction in sheet metal forming," *Wear*, vol. 172, p. 167–173, 1994.
- [139] M. P. F. Sutcliffe, "Surface asperity deformation in metal forming processes," *International Journal of Mechanical Sciences*, vol. 30, p. 847–868, 1988.
- [140] W. R. D. Wilson and S. Sheu, "Real area of contact and boundary friction in metalforming," *International Journal of Mechanical Science*, vol. 30, p. 475–489, 1988.

- [141] K. Hokkirigawa and K. Kato, "An experimental and theoretical investigation of ploughing, cutting and wedge formation during abrasive wear," *Tribology*, vol. 57, p. 51–57, 1988.
- [142] J. Raphson, "Analysis aequationum universalis seu ad aequationes algebraicas resolvendas methodus generalis, & expedita, ex nova infinitarum serierum methodo, deducta ac demonstrata," typis Tho. Braddyll, ad insigne Navis in Coemeterio D. Pauli, 1702.
- [143] E. Chatzi, "The Finite Element Method for the Analysis of Non-Linear and Dynamic Systems," Swiss Federal Institute of Technology, Zurich, 2014.
- [144] MSC-Marc, "Volume A: Theory and User Information," MSCX Software, 2017.
- [145] V. L. Popov, Contact mechanics and friction, Berlin: Springer Berlin Heidelberg, 2010, pp. 231-253.
- [146] F. Findik, "Latest progress on tribological properties of industrial materials," *Materials & Design*, vol. 57, pp. 218-244, 2014.
- [147] K. Ankur, "Friction," Gautam Buddha University, 2015.
- [148] P. J. Blau, Friction science and technology: from concepts to applications, CRC press, 2008.
- [149] A. Marmi, "ASPECT subroutine - Technical report," M2i, 2018.
- [150] H. S. Cheng, "Introduction to Lubrication," ASM International, 1992.
- [151] S. Cupillard, "Lubrication of conformal contacts with surface texturing," Doctoral dissertation, Luleå tekniska universitet, 2007.
- [152] C. Iurian, F. Ikhoulane, J. Rodellar Benedé and R. Griñó Cubero, "Identification of a system with dry friction," Institut d'Organització i Control de Sistemes Industrials, 2005.
- [153] P. C. Nautiyal and J. A. Schey, "Transfer of aluminum to steel in sliding contact: effects of lubricant. Journal of tribology," *Journal of tribology*, vol. 112, no. 2, pp. 282-287, 1990.
- [154] Alicat, "Difference between turbulent and laminar flow," Alicat Scientific, 2018. [Online]. Available: <https://www.alicat.com/knowledge-base/what-is-laminar-flow/>.
- [155] Glenn-Research, "Similarity Parameter," NASA, 2018. [Online]. Available: <https://www.grc.nasa.gov/www/k-12/airplane/airsim.html>.
- [156] O. Reynolds, "An experimental investigation of the circumstances which determine whether the motion of water shall be direct or sinuous, and of the law of resistance in parallel channels," *Philosophical Transactions of the Royal Society of London*, vol. 174, pp. 935-982, 1883.

- [157] V. Kulkarni and N. Sahoo, "Module 5 - Viscous Incompressible Flow," National Programme on Technology Enhanced Learning - NPTEL, 2013. [Online]. Available: <https://nptel.ac.in/courses/101103004/module5/lec1/2.html>.